Dynamically Motivated Spectroscopy of Small Polyatomic Molecules

by

G. Barratt Park

S.B., Davidson College (2006)

Submitted to the Department of Chemistry
in partial fulfillment of the requirements for the degree of

Doctor of Philosophy

at the

MASSACHUSETTS INSTITUTE OF TECHNOLOGY

February 2015

Author . . . .
Department of Chemistry
January 8, 2015

Certified by . . . .
Robert W. Field
Haslam and Dewey Professor of Chemistry
Thesis Supervisor

Accepted by . . . .
Robert W. Field
Chairman, Departmental Committee on Graduate Students

Dynamically Motivated Spectroscopy of Small Polyatomic Molecules

by

G. Barratt Park

Submitted to the Department of Chemistry
on January 8, 2015, in partial fulfillment of the
requirements for the degree of
Doctor of Philosophy

Abstract

Molecular vibrational dynamics far from equilibrium, or in the vicinity of saddle points, are of utmost importance in chemistry. However, most of the standard models used by chemists only perform well near local minima in the potential energy surface. Several spectroscopic techniques are developed and applied to the study of molecules in excited states, including chirped-pulse millimeter wave spectroscopy and adaptations of millimeter-wave optical double resonance. Models for Franck-Condon factors in the linear-to-bent S_1–S_0 transition of acetylene elucidate the dynamics of bright states observed in the fluorescence spectrum and provide insight for the design of spectroscopic schemes for accessing barrier-proximal vibrational levels. IR-UV double resonance spectroscopy enables characterization of the source of staggering in the antisymmetric stretch progression of the $\tilde{\mathrm{C}}$ state of SO_2, which arises due to vibronic interactions that lead to non-equivalent equilibrium SO bond lengths.

Thesis Supervisor: Robert W. Field
Title: Haslam and Dewey Professor of Chemistry

Acknowledgments

First, I would like to thank my thesis advisor, Bob Field. Bob is an incredibly supportive and generous leader among his students and colleagues. Bob has infected me with his love of developing profound understanding of “simple” things. He is uninterested in collecting line lists and spectroscopic constants of important molecules for the sake of collecting line lists and spectroscopic constants of important molecules. Instead, Bob inspires his students and his colleagues to seek the narrative behind the spectrum, and always to approach high-resolution spectroscopy from the perspective of dynamics. I am humbled to receive Bob’s encouragement and support, and I could not be prouder than to be a part of Bob’s legacy.

During my (somewhat lengthy) Ph.D., I have had a wide range of colleagues and collaborators from near and far—it would be impossible to mention them all in this brief section. I would like to thank Adam Steeves and Hans Bechtel for showing me the singlet project ropes. Wilton Virgo, Jeff Kay, Vladimir Petrovic, and Bryan Wong were also very supportive of me during my early years in the Field lab. I will never forget Jessica Lam, who showed everyone always the merit of taking the bull by the horns, whatever the bull may be. Yan Zhou, Tony Colombo, and Josh Middaugh overlapped with me for much of my graduate career. Yan, in particular, impresses me with his intelligence, diligence, and graciousness. David Grimes has been a terrific colleague as well, and Tim Barnum, an impressive new student, must be commended for promoting gregariousness and cohesion within the research group.

I had substantially beneficial collaborations with Kirill Prozument and Josh Baraban, which are still continuing, and I hope will be fruitful for years to come. Bryan Changala was a particularly advanced UROP from whom I also learned a great deal. Towards the end of my graduate career, I collaborated substantially with JJ Jiang and Carrie Womack, both extremely talented scientists. JJ did a substantial amount of collaboration on the SO_2 IR-UV double resonance project reported in this thesis. The reader should expect great work to come from him. The SO_2 project was started as a collaboration with Andrew Whitehill of the Shuhei Ono group. Although

I don't think my work ended up directly addressing their research interests, which are on anomalous sulfur isotope fractionation in pre-Cambrian rocks, he introduced me to an electronic state that I found very interesting and became the focus of a very fruitful project. I would like to thank John Stanton in advance for a collaboration that we have recently started on vibronic coupling in the $\tilde{\mathrm{C}}$ state of SO_2. Catherine Saladrigas and Peter Richter also contributed to the project.

I am indebted to Brooks Pate and his research group—particularly Justin Neill—for teaching me the ropes of chirped-pulse microwave and millimeter-wave spectroscopy as a second year graduate student. They are both extremely generous colleagues. I am grateful to Arthur Suits for his support, and for inviting me to participate on his group's project to introduce chirped-pulse Fourier transform microwave spectroscopy to the world of kinetics. Key players in this project include Chamara Abeysekera, James Oldham, Lindsay Zack, Baptiste Joalland, and Ian Sims. I am grateful to Hua Guo for valuable discussions on both acetylene and SO_2, and Georg Melau for stimulating discussions on spectroscopy of isomerizing systems (and German lessons!). I would like to thank Matt Nava, Kit Cummins, Celina Bermudez, and Bryan Lynch for involving me in very interesting microwave experiments on unusual conformations of molecules generated from intelligently designed precursors. I hope the kinks get sorted out in the near future, because from the hands of such insightful researchers, beautiful results will be no surprise. John Muenter, Anthony Merer, and Steve Coy have been very supportive of my work. All three are extremely knowledgeable in the field of molecular spectroscopy and I have learned a great deal from discussions with them. I would also like to mention my advisor at Davidson College, Merle Schuh, who first introduced me to dynamics and spectroscopy, and my sister, Margaret Park, who inspires me as a scientist.

When I arrived at MIT, I was surprised to be presented with a nametag that said "Barratt Park." At every other school I visited, I got a nametag that said "George," which resulted in a lot of awkward conversations explaining that I don't go by George. The credit belongs to Susan Brighton, whose attention to personal detail always made me feel welcomed. Brooke Podgurski was also very supportive of the graduate students during my first year. Peter Guinta is an extremely competent administrator who goes above the call of duty to support our research group. I would like to thank Claudia in Cafe 4 for brightening each day as I purchase coffee. ("You're *still* a student?")

I am grateful to Bob for allowing me to continue to pursue my interest in classical music during my graduate school career. As with my scientific collaborators, I have far too many musical collaborators to name. I am grateful to Adam Boyles, Keeril Makan, Elena Ruehr, and Donald Wilkinson for their mentorship. As a composer, I would like to thank Dustin Damonte and Roderick Phipps-Kettlewell for recording my song cycle, Krista Buckland Reisner and her colleagues for playing my string quartet, and MITSO for playing my suite. I am indebted to Gil Rose for giving me the opportunity to perform with Opera Boston, Boston Modern Opera Project, and Odyssey Opera. I am grateful to Lidiya Yankovskaya for inviting me to perform in two world-premiere operas. Thank you to Jess Rucinski for her work at St. John the Evangelist Church in Boston, and to the MIT G&S Players for allowing me quite by accident to become a conductor.

I would like to thank Ethan A. Klein, Senior Field Group UROP, for entrusting me to serve as his Executive Administrative Assistant.

This doctoral thesis has been examined by a Committee of the
Department of Chemistry as follows:

Professor Keith A. Nelson...
Chairman, Thesis Committee
Professor of Chemistry

Professor Robert W. Field...
Thesis Supervisor
Haslam and Dewey Professor of Chemistry

Professor Moungi G. Bawendi...
Member, Thesis Committee
Lester Wolfe Professor of Chemistry

Contents

List of Figures

List of Tables

Chapter 1

Design and evaluation of a pulsed-jet chirped-pulse millimeter-wave spectrometer for the 70–102 GHz region

Abstract

Chirped-pulse millimeter-wave (CPmmW) spectroscopy is the first broadband (multi-GHz in each shot) Fourier-transform technique for high-resolution survey spectroscopy in the millimeter-wave region. The design is based on chirped-pulse Fourier-transform microwave (CP-FTMW) spectroscopy [G.G. Brown *et al.*, Rev. Sci. Instrum. **79**, 053103 (2008)], which is described for frequencies up to 20 GHz. We have built an instrument that covers the 70–102 GHz frequency region and can acquire up to 12 GHz of spectrum in a single shot. Challenges to using chirped-pulse Fourier-transform spectroscopy in the millimeter-wave region include lower achievable sample polarization, shorter Doppler dephasing times, and problems with signal phase stability. However, these challenges have been partially overcome and preliminary tests indicate a significant advantage over existing millimeter-wave spectrometers in the time required to record survey spectra. Further improvement to the sensitivity is expected as more powerful broadband millimeter-wave amplifiers become affordable. The ability to acquire broadband Fourier-transform millimeter-wave spectra enables rapid measurement of survey spectra at sufficiently high resolution to measure diagnostically important electronic properties such as electric and magnetic dipole moments and hyperfine coupling constants. It should also yield accurate relative line strengths across a broadband region. Several example spectra are presented to demonstrate initial

applications of the spectrometer.[a]

1.1 Introduction

Microwaves and millimeter waves are powerful tools for the spectroscopic study and state-specific detection of gas-phase molecules. The advantage of these spectral regions derives primarily from the extremely high resolution and accompanying high frequency accuracy that they provide. The millimeter-wave region has proven particularly important for measurements on small molecules with large rotational constants,[1–3] studies of pure-electronic Rydberg-Rydberg transitions,[4–9] sensitive detection of molecules at room temperature,[10–12] and detection of astronomical molecules.[13]

Much recent progress has been made in the development of methodology for gas-phase millimeter-wave spectroscopy. Traditional frequency-domain spectrometers must be scanned one frequency element at a time, which makes the acquisition of broadband chemically-relevant spectra expensive and time-consuming, especially when used in conjunction with 10–20 Hz repetition rate supersonic jet molecule sources and Nd:YAG-pumped tunable lasers. A tremendous advantage has been obtained in frequency-domain millimeter and sub-millimeter spectroscopy by using fast sweeps, which can measure up to 5×10^5 resolved spectral features per second (typically 50-500 GHz/s).[14–18] Efforts have also been made to apply fast sweep techniques to pulsed nozzle experiments.[19,20] However, because the pulse durations in those experiments are typically not more than 10–100 times longer than the ~ 1 μs time constant of the bolometer detectors used, such methods cover no more than approximately 100 resolution elements (typically 10 MHz) per gas pulse. Furthermore, the method is not suited for spectroscopy on laser-excited states with lifetimes that are short relative to the time constant of the detector.

Cavity-enhanced Fourier-transform microwave spectrometers caused a major

---

[a] This chapter is reprinted with permission from G. B. Park, A. H. Steeves, K. K. Kuyanov, J. L. Neill, and R. W. Field, *J. Chem. Phys.* **135**, 24202 (2011). Copyright 2011, AIP Publishing LLC.

breakthrough starting in the early 1980's.[21–25] A few cavity-enhanced Fourier transform spectrometers have been reported above 50 GHz.[26–31] However, the high quality factor of the Fabry-Perot cavity used in such spectrometers limits each Fourier-transform acquisition to a few MHz. While these spectrometers can be used to cover wide frequency ranges at high resolution and high sensitivity, they must do so in a sequence of many narrowband acquisitions, and the cavity resonance frequency must be mechanically tuned at each step.

The recent invention by Pate and coworkers of chirped-pulse Fourier-transform microwave (CP-FTMW) spectroscopy has made possible acquisition of truly broadband (> 10 GHz per pulse) Fourier-transform spectra in the microwave region (∼8–18 GHz).[32–34] The invention makes use of recent advances in broadband microwave electronics. In the University of Virginia implementation, a 24 GS/s arbitrary waveform generator is used to generate a broadband, frequency-chirped pulse, which is up-converted and amplified to ∼300 W in a traveling wave tube amplifier. The resulting high-power chirped pulse interacts with a molecular sample, polarizing all the transitions that lie within the bandwidth of the chirp. The sample emits a broadband free induction decay (FID) signal, which is detected directly by a fast 20 GHz oscilloscope. Further work at the University of Virginia has been done to implement the technique at frequencies up to 40 GHz.[35]

We have built a chirped-pulse millimeter-wave (CPmmW) spectrometer that operates in the 70–102 GHz region. CPmmW spectroscopy takes advantage of recent advances in broadband millimeter-wave amplifiers and heterodyne receivers. The design is similar to that of Pate and coworkers, but the output of the arbitrary waveform generator is up-converted and multiplied to millimeter-wave frequencies. After the FID is collected, it is down-converted to the broadband DC–12 GHz region so that it can be detected directly and averaged in the time domain by a fast oscilloscope. In spite of the advantages that are offered by CPmmW spectroscopy, there are also several challenges associated with operating at higher frequency, particularly lower available power and faster dephasing. Here, we address some of these challenges and demonstrate the abilities of our current spectrometer.

1.2 Spectrometer Design

The spectrometer is based on the CP-FTMW spectrometer of Pate and co-workers.[32] A schematic of the CPmmW spectrometer design is shown in Fig. 1-1. A 4.2 GS/s arbitrary waveform generator (AWG) is used to generate chirped pulses at frequencies in the range of 0.2–2 GHz. These pulses are up-converted by mixing with a phase-locked 10.7 GHz oscillator, and one of the sidebands is selected using a bandpass filter. Access to the millimeter-wave region is achieved by active multiplication (×8) of the resulting chirped microwave pulse. Because frequency multipliers multiply both the carrier frequency and the bandwidth of a chirped pulse, it is possible to generate chirped millimeter-wave pulses with ∼15 GHz bandwidth starting with a 0.2–2 GHz microwave pulse. As a result, the bandwidth of the AWG used in the experiment may be much narrower than that of the desired millimeter-wave chirped pulse. This was noted by Brown *et al.* in the bandwidth extension scheme designed for the FT-CPMW spectrometer.[32]

Unlike the spectrometer of Pate and coworkers, which uses a traveling wave tube amplifier (TWTA) to achieve peak pulse powers of up to 300 W, the CPmmW spectrometer power is limited by the capabilities currently available of broadband E- and W-band amplifiers, which can attain peak powers of only ∼10–100 mW. Our system uses an active frequency doubler with an output power of 30 mW. Because the millimeter-wave power is low, horn antennas can be safely located outside of the molecular beam chamber. Teflon optics are used to focus the millimeter-wave radiation into the chamber through a set of teflon windows.

The molecular FID must be down-converted to microwave frequencies for direct detection on a fast oscilloscope. This is achieved by mixing the collected signal with the output of a W-band Gunn oscillator. The detection bandwidth is limited by the 12 GHz oscilloscope [Tektronix model TDS6124C] used in the experiment. As in the design of Pate and coworkers, all oscillators and clocks used in the experiment are phase-locked to the same 10 MHz frequency standard. The experiment is repeated at an exact integer multiple of the period of the 10 MHz reference. This ensures that

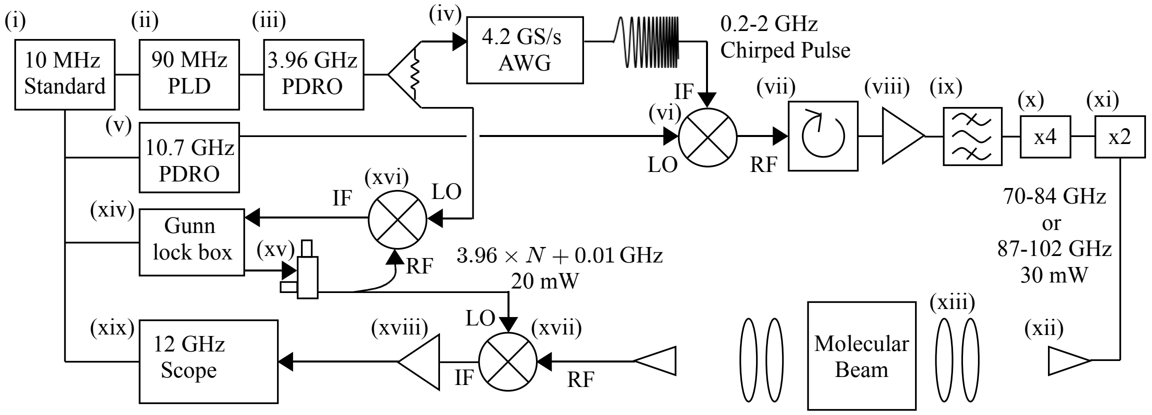

Figure 1-1: Schematic diagram of the CPmmW instrument. For a full list of parts, see Section 1.10. All components of the experiment are phase locked to the same 10 MHz Rubidium Frequency Standard (i). A 4.2 GS/s AWG [Tektronix model AWG710B] (iv), operating at the 3.96 GHz rate of an external clock (iii), is used to generate a linearly-chirped pulse, which is up-converted (vi) by mixing with the output of a fixed-frequency 10.7 GHz oscillator (v). The resultant signal is isolated (vii) and amplified (viii). The desired sideband is then selected using a bandpass filter (ix) and actively frequency-multiplied by a factor of 8 (x and xi) to produce a chirped pulse that covers the 70–84 GHz or the 87–102 GHz frequency range with a peak power of 30 mW. The millimeter-wave pulse is coupled into free space using a 24 dBi standard gain horn (xii) and focused into a molecular beam chamber by a pair of teflon lenses (xiii). After the chirped excitation pulse has polarized the molecular sample, the FID is collected and down-converted (xvii) by mixing with the output of a Gunn oscillator (xv). The resultant signal is input to a low-noise amplifier (xviii) and averaged in the time domain on a 12 GHz oscilloscope (xix).

the phase of the chirped pulse and the resultant FID is constant from pulse to pulse so that the signal can be phase-coherently averaged on an oscilloscope in the time domain.

1.3 Power Limitation

1.3.1 Measurement of Effective Power

The available power for the CPmmW spectrometer is currently limited to about 30 mW by the capabilities of commercially-available broadband millimeter-wave amplifiers. As millimeter-wave technology develops, more power is expected to become available in broadband solid-state devices. However, because of power limitations, it is important to achieve efficient coupling of power into the molecular beam chamber so that the *E*-field of the radiation that interacts with the molecules is as high as possible. In order to evaluate the effective *E*-field in the interaction region, test measurements were performed on the $6_{06} \leftarrow 5_{15}$ *b*-type pure rotational transition in SO_2 at 72.758 GHz, for which the transition dipole moment (averaged over M_J componenets) is 0.83 D. A resonant single-frequency pulse of varying duration was used to excite the transition.

The results, shown in Fig. 1-2, can be compared to an exponentially-damped Rabi oscillator. The detected signal, S, is the *E*-field radiated by the molecules, which is proportional to the magnitude of the quantum coherence, $|a_0 a_1|$, evaluated at time t_p, the pulse duration:

$$S \propto |a_0(t_p)a_1(t_p)| = \exp\left(\frac{-t_p}{\tau}\right)|\sin(\omega_R t_p)| \tag{1.1}$$

In Eq. 1.1, $\omega_R = \mu\mathcal{E}/\hbar$ is the on-resonance Rabi frequency, and $1/\tau$ is the decay rate of the coherence.

The data shown in Fig. 1-2 were fit to Eq. 1.1 to obtain best-fit parameters of 2.3 ± 0.2 μs for τ and 1.11 ± 0.04 MHz for ω_R. The fit parameter for τ agrees with the measured 2.1 μs $1/e$ dephasing time of the transition, which is dominated by the Doppler effect. The measured Rabi frequency corresponds to an effective *E*-field of 42 V/m. The measured diameter of the millimeter-wave focus (containing 90% of the integrated *E*-field) from the teflon lenses is ∼2.5 cm. If 30 mW of power were ideally focused onto a $(2.5\text{ cm})^2$ area, it would result in a 195 V/m *E*-field. Part of the loss of effective *E*-field is due to power loss. There are unavoidable losses due to reflections in the horn antenna and from the surfaces of the lenses and chamber windows. However, horn-to-horn transmission loss is only ∼3 dB (corresponding to a loss of 30% in *E*-field). The remaining loss of effective *E*-field can be attributed to imperfections in the profile and focussing of the millimeter-wave beam.

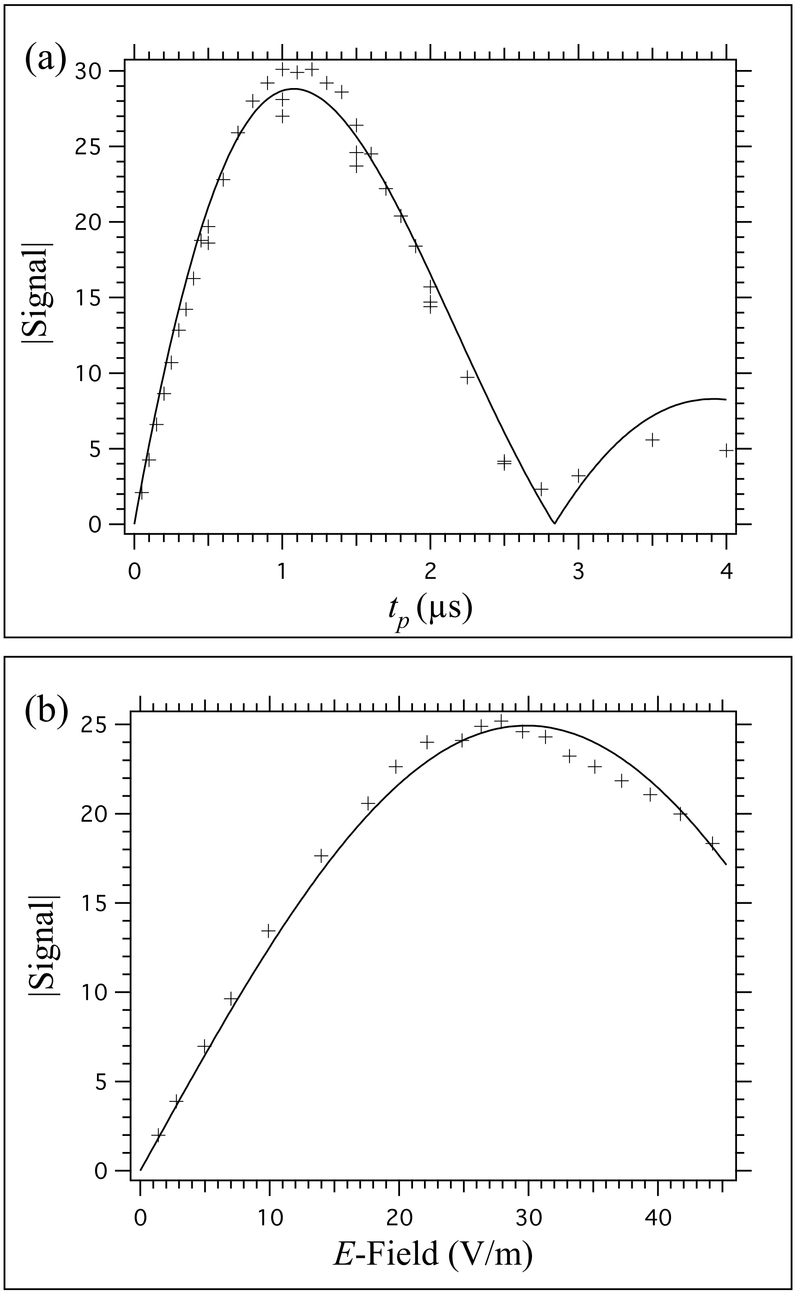

Figure 1-2: a) The amplitude of the FID signal from the SO_2 $6_{06} \leftarrow 5_{15}$ transition is plotted as a function of the duration of the single frequency excitation pulse. The data were fit to Eq. 1.1 to obtain best-fit parameters $\tau = 2.3 \pm 0.2$ μs and $\omega_R = 1.11 \pm 0.04$ MHz. b) The signal amplitude from the same transition is plotted as a function of millimeter-wave pulse power attenuation, for a constant pulse duration of $t_p = 2$ μs. The solid curve is the signal amplitude predicted by Eq. 1.1 with the best-fit parameters from above. The E-field plotted on the x-axis was calculated from the best-fit value of ω_R at zero attenuation and scaled according to the variable attenuation.

1.3.2 Power Requirements for Broadband Chirped Pulses

To calculate the achievable polarization of a two-level system excited by a broadband chirped millimeter-wave pulse, we integrate the optical Bloch equations for the case of a linearly-chirped pulse, as given by McGurk *et al.*[36] We define the polarization in the form

$$P = (P_r + iP_i)e^{i(\omega t - kz)} + \text{c.c.} \tag{1.2}$$

The time-dependent E-field of the excitation pulse is

$$\begin{aligned} E &= 2\mathcal{E}\cos\left(\omega_i t + \frac{1}{2}\alpha t^2\right) \\ &= 2\mathcal{E}\cos\{[\omega_0 - \Delta\omega(t)]\,t\}, \end{aligned} \tag{1.3}$$

where we define α as the linear frequency sweep rate and $\Delta\omega$ as the detuning of the excitation pulse from the two-level system resonance, ω_0. The Bloch equations can be written for the polarization in terms of $\Delta\omega$[36]

$$\begin{aligned} \alpha\frac{dP_r}{d(\Delta\omega)} + \Delta\omega P_i + \frac{P_r}{T_2} &= 0 \\ \alpha\frac{dP_i}{d(\Delta\omega)} - \Delta\omega P_r + \frac{\mu^2\mathcal{E}}{2\hbar}\Delta N + \frac{P_i}{T_2} &= 0 \\ \frac{\alpha\hbar}{4}\frac{d(\Delta N)}{d(\Delta\omega)} - \frac{\mathcal{E}}{2}P_i + \frac{\hbar}{4}\frac{(\Delta N - \Delta N_0)}{T_1} &= 0. \end{aligned} \tag{1.4}$$

In Eq. 1.4, T_1 and T_2 are the familiar decay lifetimes of the population and coherence, respectively, and ΔN is the population difference. Equation 1.4 was numerically integrated and the results are shown in Fig. 1-3.

Figure 1-3 demonstrates that the polarization achievable in a typical small molecule across a bandwidth of 10 GHz with a 42 V/m electric field is only 1% of the maximum polarization that would be achievable if higher chirped-pulse power were available. A qualitative difference between the polarization achieved with a broadband chirped pulse and that achieved with a single-frequency excitation pulse (Figure 1-2) is that even in the absence of relaxation effects, recurrence of the polarization does not take place at high E-field in the chirped-pulse case. This is a well known

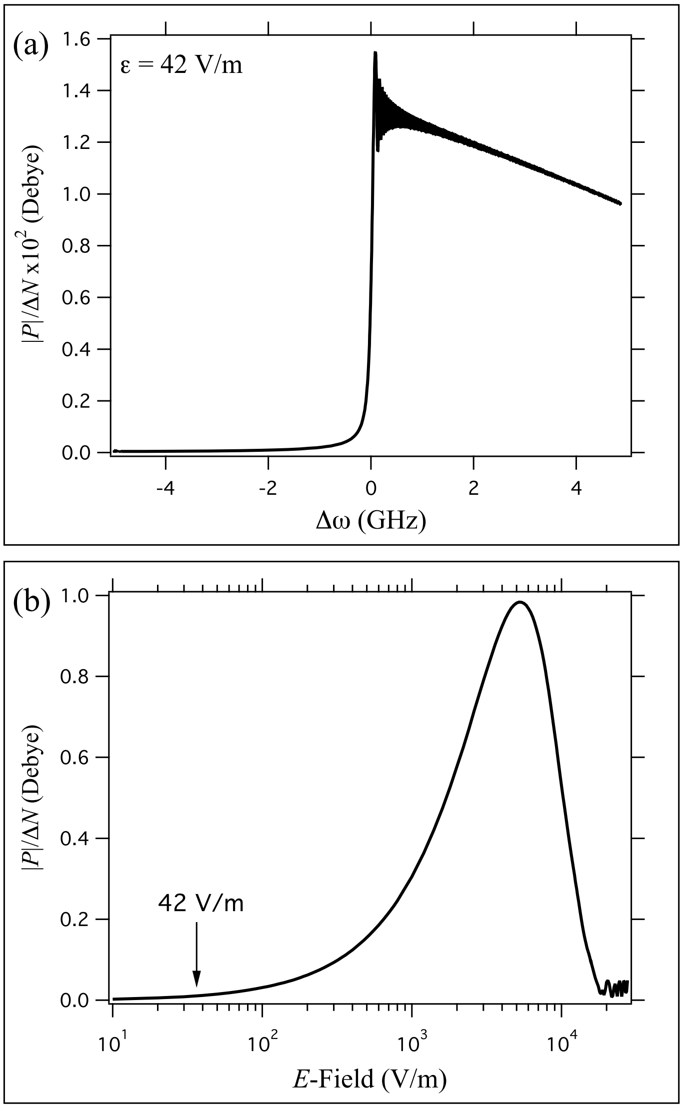

Figure 1-3: Equation 1.4 was numerically integrated for the case of a 10 GHz bandwidth chirped pulse of 1 μs duration exciting a 1 D dipole moment with T_1 and T_2 of 10 μs and 2 μs, respectively. The two level system resonance is assumed to occur at the center of the excitation pulse bandwidth. (a) The integration of Eq. 1.4 is shown for the above parameters with an E-field of 42 V/m, which is the available E-field in the current spectrometer. The magnitude of the polarization is plotted. (b) The E-field ($\mathcal{E}$) was varied and the resultant polarization after the excitation pulse is plotted. Optimal polarization occurs at an E-field of ~4000 V/m. The polarization never quite reaches its maximum value of 1 D because a small amount of dephasing occurs during the excitation pulse. Note that the polarization achieved at 42 V/m corresponds to only ~1.5% of the maximum achievable polarization.

phenomenon in the adiabatic fast passage regime. When $\mu\mathcal{E}/\hbar\sqrt{\alpha} \gg 1$, the effective E-field vector in the Bloch polarization picture is very strong and moves slowly relative to the Rabi precession. The polarization vector precesses tightly around the E-field vector as it is swept through 180°, and the system is swept slowly through resonance until population inversion is achieved.[37]

In the weak field case ($\mu\mathcal{E}/\hbar\sqrt{\alpha} \ll 1$), the signal scaling has been solved by McGurk *et al.*[36] They found that

$$P \propto \frac{\mu^2\mathcal{E}\Delta N}{\sqrt{\alpha}}. \tag{1.5}$$

The polarization will also decay at a rate proportional to $T_1^{-1} + T_2^{-1}$. Therefore, the excitation must occur on a timescale short compared to these time constants. Given that the excitation pulse duration is constrained, the obtainable signal is proportional to the reciprocal square root of the bandwidth. As pointed out by Brown *et al.*,[32] this means that the chirped-pulse signal scales favorably as bandwidth is increased. In contrast, the signal obtained from a Fourier-transform limited pulse scales as the reciprocal of the bandwidth to the first power. It is possible to achieve more polarization from a given transition by decreasing the bandwidth of the chirped pulse. However, this is rarely an advantageous strategy for increasing the efficiency of spectral acquisition, because the increase in signal is only proportional to $\Delta\omega^{1/2}$. Breaking up a spectrum into more than one frequency region therefore does not decrease the averaging time needed to obtain a specified signal-to-noise level over a given frequency region, since the noise reduction also scales as the square root of the number of averages, and there is a cancelation between the signal increase and the required number of averages.

In the strong power regime (where $\mu\mathcal{E}/\hbar\sqrt{\alpha}$ is no longer $\ll 1$), the maximum achievable polarization is limited by $P_{max} = \mu\Delta N$. The maximum obtainable polarization from a given sample does not scale with the chirp bandwidth or the E-field, and only scales as μ to the first power.

1.4 Shorter Dephasing times

In addition to low power availability, another challenge that faces chirped-pulse spectroscopy in the millimeter-wave region is that the dephasing time of the molecular transitions tends to be much shorter than in the centimeter-wave region. In a supersonic expansion, the most significant contributor to the lifetime of the FID is usually the Doppler-limited T_2 broadening. Since the Doppler effect is proportional to the emitted frequency, the dephasing times for the millimeter-wave FIDs are an order of magnitude shorter than those measured with centimeter waves. Pate and coworkers report FID lifetimes of ∼10 μs below 20 GHz,[32,33] while we encounter lifetimes of ∼2 μs. As a result of the shorter dephasing time, the millimeter-wave chirped pulse must have a shorter duration in order to minimize the dephasing that occurs during the polarizing pulse. This faster dephasing is combined with the additional problem of low available millimeter-wave power, and as a result the CPmmW spectrometer must operate in the low power limit when used to study rotational spectra of molecules with ∼1 D dipole moments.

One way to overcome Doppler dephasing in millimeter wave molecular beam experiments is to change the experimental geometry to reduce the Doppler profile. This has been employed with our CPmmW spectrometer by using a rooftop reflector and a wire-grid polarizer to propagate the millimeter-wave radiation parallel and antiparallel with the molecular beam in a manner similar to that used previously to obtain high-resolution spectra with our sequential scanning millimeter-wave absorption spectrometer.[38] The co-propagating geometry removes most of the Doppler effect caused by the component of the molecular velocity perpendicular to the molecular beam direction. In Fig. 1-4, a comparison is made between the signal obtainable with and without the rooftop reflector geometry. The linewidth was reduced from 350 kHz to 66 kHz. Because the FID lifetime is lengthened by a factor of 5, it is possible to extend the chirp duration without loss due to dephasing. This leads to stronger polarization of the sample and more signal. Additional advantage in the signal-to-background-noise ratio arises from the fact that the line is narrower.

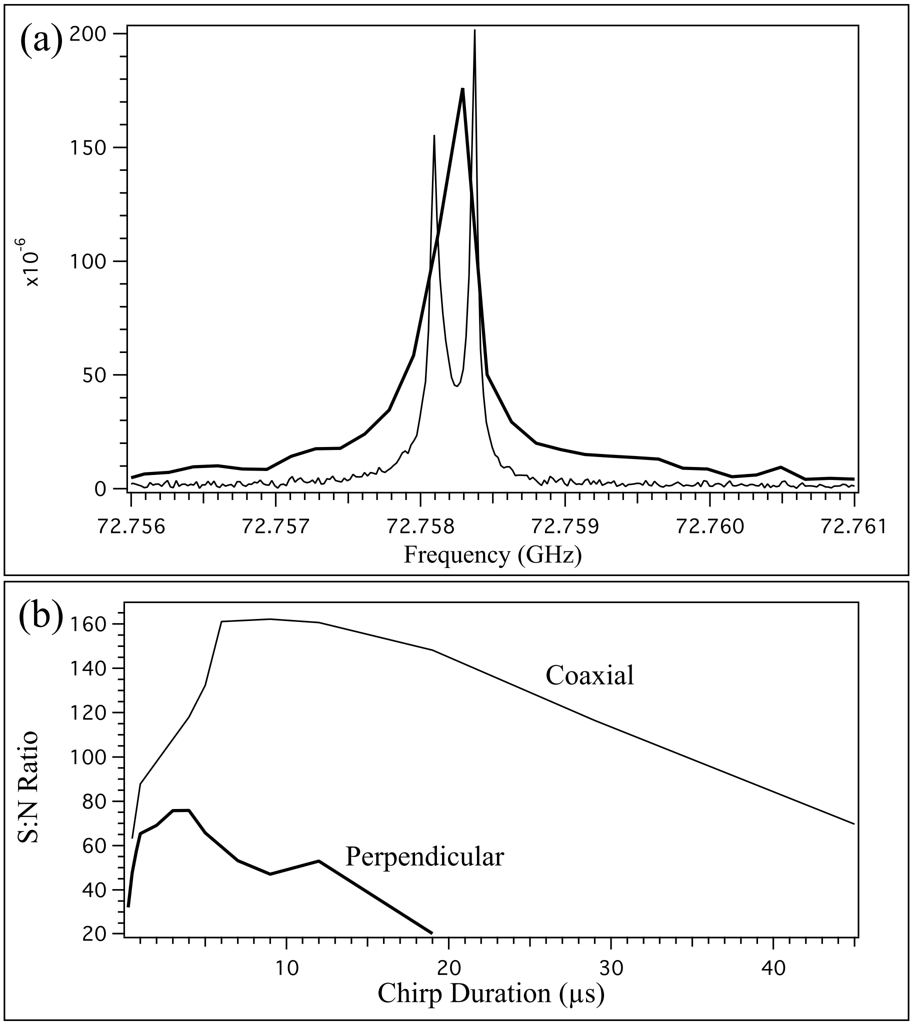

Figure 1-4: A comparison is made between the signal obtained from the $6_{06} \leftarrow 5_{15}$ transition of SO_2 in the perpendicular millimeter wave/molecular beam geometry (thick curve) and coaxial geometry obtained using a rooftop reflector (thin curve). The Doppler-limited linewidth is narrower in the coaxial geometry. The line is split into its two Doppler components when this double-pass configuration is used (a). Because the FID lifetime is longer when the Doppler dephasing is minimized, the duration of the excitation chirp can be extended to achieve further improvement in signal strength. In panel (b), the signal-to-background-noise ratio is plotted as a function of the chirp duration for both geometries. The millimeter-wave power, gas expansion characteristics, and other parameters were held constant.

The colinear geometry can also be used to improve the resolution, as demonstrated in the case of the $J = 5 \leftarrow 4$, $K = 0$ transition of acetonitrile with resolved hyperfine structure due to the ^{14}N quadrupole moment (Fig. 1-5).

1.5 Phase Stability

Another difficulty with up-converting the chirped-pulse technique into the millimeter-wave region is that the experiment becomes more sensitive to phase instabilities. When the signal is frequency-multiplied by 8, any phase jitter is also multiplied by 8. Phase jitter might be attributed to to temperature fluctuations and mechanical vibrations in the laboratory, or to phase jitter characteristics of electrical components.

When using chirped-pulse techniques, two types of phase jitter are possible: t-jitter as illustrated in Eq. 1.6a or ϕ-jitter, as illustrated in Eq. 1.6b.

$$I \propto \sin\left[\omega_0(t+\Delta t) + \frac{1}{2}\alpha(t+\Delta t)^2 + \phi\right] \tag{1.6a}$$

$$I \propto \sin\left[\omega_0 t + \frac{1}{2}\alpha t^2 + (\phi + \Delta\phi(\omega))\right] \tag{1.6b}$$

We find that when the phase of the FID is unstable from one acquisition to the next, the instability can be corrected by rotating the phases of the Fourier transforms relative to one another (and not by shifting the FIDs in time). Furthermore, we find that the rotation angle that maximizes the overlap between the two Fourier transforms is independent of the frequency. That is, in Eq. 1.6b, $\Delta\phi(\omega) = \Delta\phi$. Thus, Eq. 1.7 can be used to rotate the phase of the Fourier transform to correct for phase instabilities:

$$\begin{pmatrix} \Re\{F'(\omega)\} \\ \Im\{F'(\omega)\} \end{pmatrix} = \begin{pmatrix} \cos\Delta\phi & \sin\Delta\phi \\ -\sin\Delta\phi & \cos\Delta\phi \end{pmatrix} \begin{pmatrix} \Re\{F(\omega)\} \\ \Im\{F(\omega)\} \end{pmatrix}, \tag{1.7}$$

where $\Re\{F(\omega)\}$ and $\Im\{F(\omega)\}$ refer to the real and imaginary parts of the Fourier transform, respectively.

The frequency-independence of the correction indicates that the source of the

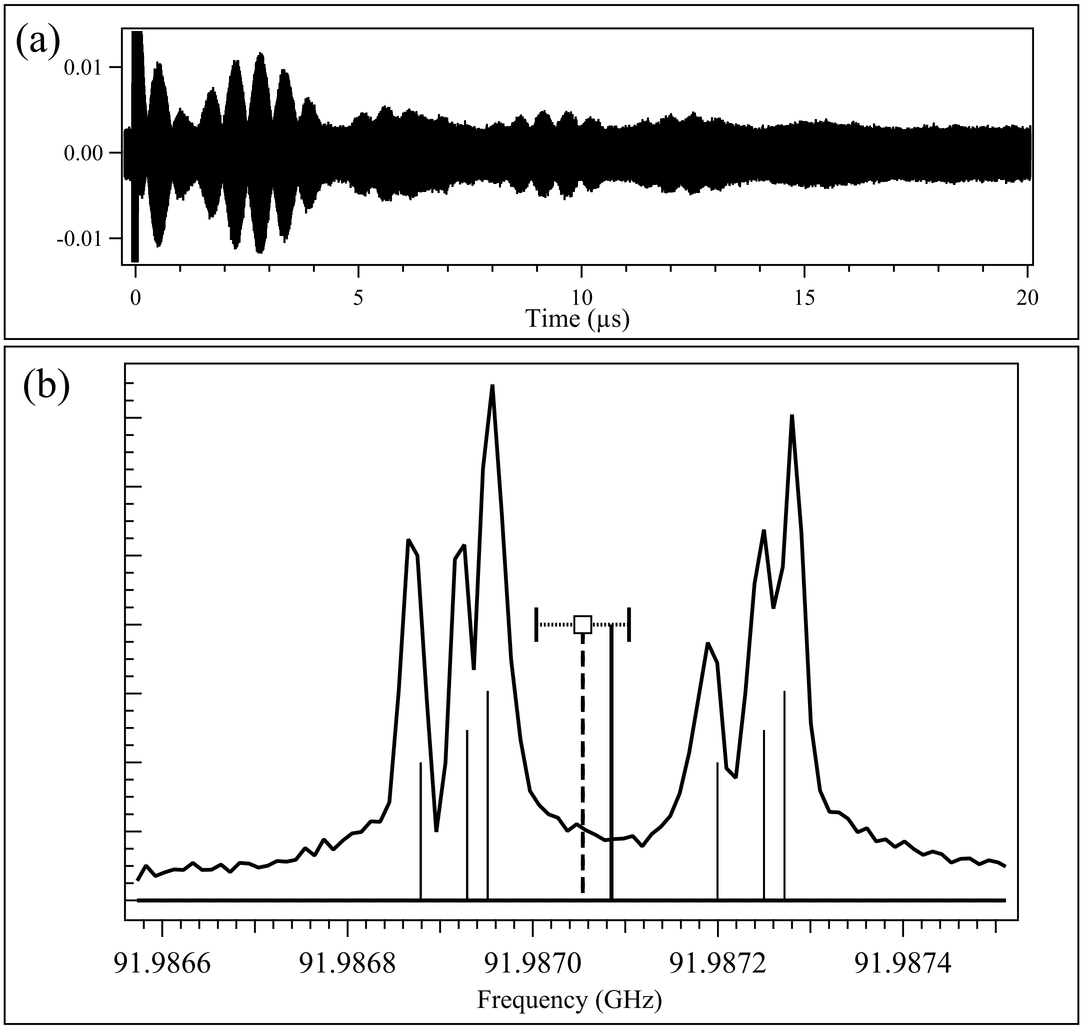

Figure 1-5: High-resolution CPmmW spectrum of the acetonitrile $J = 5 \leftarrow 4$, $K = 0$ transition with resolved ^{14}N quadrupole moment hyperfine structure. The FID (a) has a decay constant of $\sim$17 μs. The Hamming window function was used in the Fourier Transform. The spectrum (b) is Doppler-doubled as a result of the rooftop reflector geometry. The line spectrum represents the calculated spectrum obtained using the accepted nuclear quadrupole coupling constant, -4.2244 MHz,[39] and a best-fit molecular beam velocity of 508 m/s. The thick central line is the measured central line frequency and the dotted line is the unresolved line position reported by Boucher *et al.*[40] The measured line frequency agrees to within the 60 kHz reported uncertainty.

phase instability is likely to be in one of the single-frequency local oscillators. If the phase jitter were generated in a component that passes a chirped pulse, there would likely be frequency dependence to the phase jitter, since different frequencies accumulate phase at different rates. In future generations of our spectrometer, we plan to replace the Gunn oscillator with a multiplied phase-locked microwave oscillator as the local oscillator for the down-conversion. This will allow us to determine whether the Gunn oscillator is the source of phase instability.

Long-term drifts in phase of the type discussed above have been efficiently corrected in signal processing. This type of instability can be corrected by rotating the phase of the Fourier transform of each acquisition (Eq. 1.7) by the angle $\Delta\phi$ that maximizes the overlap of the strongest line in the spectrum. Because of the frequency independence of $\Delta\phi$, this rotation maximizes the phase overlap of all molecular lines, regardless of how far apart they are in frequency. When it is necessary to perform a long average over the course of an hour or more, the averaging can be performed in shorter 5–10 minute acquisitions over which time the phase of the FID is stable. These shorter acquisitions can then be phase corrected with signal processing tools before being averaged together. The overall time required for the acquisition of the long average is affected negligibly because the data must be Fourier-transformed and stored only once every 5–10 minutes when this scheme is implemented.

A disadvantage of this method is that it is only efficient when there is a strong line that is visible above the baseline noise after a 5–10 minute acquisition. If necessary, the phase correction can be achieved by introducing into the sample mixture a standard that has a strong transition. The phase-correction algorithm can be applied automatically in the LabView program that is used to collect and average the data.

As an example, we have acquired 87–92 GHz spectra of the 193 nm photolysis products of acrylonitrile. We collected 28,000 averages in acquisitions of 500–2000 averages each. In Fig. 1-6 we present a comparison between the spectra obtained when each acquisition is phase corrected and when each acquisition is not phase corrected. Note that the levels of background noise in the two spectra are similar, but the signal in the phase-corrected spectrum is several times stronger, because signal is destroyed when individual FIDs are averaged out of phase. In the phase-corrected spectrum, the signal-to-background ratio increases as the square root of the number of acquisitions out to the longest measurement of 28,000 acquisitions.

1.6 Evaluation

1.6.1 Spectroscopy of Ground States

We used the frequency region surrounding the 72,976.7794 MHz OCS $J = 6 \leftarrow 5$ transition to compare the CPmmW spectrometer to the supersonic jet W-band bolometer-detected absorption spectrometer used previously in the Field laboratory (Fig. 1-7).[38,41] The older absorption spectrometer was used primarily for measuring hyperfine structure surrounding lines with known positions and was not designed for broadband spectral acquisition. With the absorption spectrometer, only a narrow 100 MHz region containing the main OCS $J = 6 \leftarrow 5$ transition could be scanned during the 100 minute experiment (Fig. 1-7.a). However, with the CPmmW spectrometer, a 4 GHz spectral region could be surveyed at improved signal-to-background-noise ratio in approximately half the time. The strong OCS $J = 6 \leftarrow 5$ transition is visible above the background noise after only seconds of averaging. After 5 minutes of averaging, the spectrum reaches a signal-to-background-noise ratio comparable to that obtained with the absorption spectrometer. The spectrum shown in Fig. 1-7.b was obtained in 50 minutes and exhibits greater than two-fold improvement in signal-to-background-noise ratio over the spectrum shown in Fig. 1-7.a. Because the broadband Fourier-transform capabilities of the CPmmW spectrometer can be used to survey a broad spectral region, it is possible not only to find the strong OCS $J = 6 \leftarrow 5$ transition after mere seconds of averaging, but also to observe simultaneously the weaker satellite transitions, which are assigned to isotopologues and vibrationally excited states of OCS. From the signal to background noise ratio of the $O^{13}CS$ peak, we estimate that for the bandwidth and acquisition time used in this experiment, the limit of detection for OCS $J = 6 \leftarrow 5$ transition is approximately

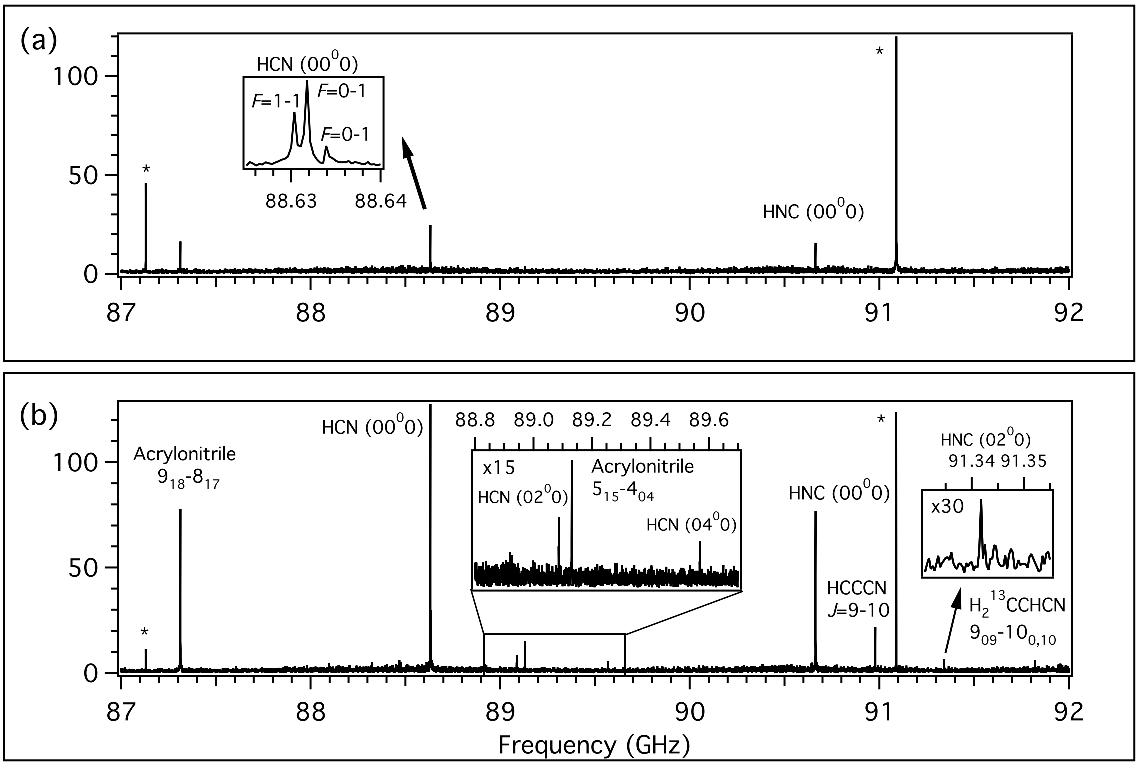

Figure 1-6: A 5-GHz bandwidth spectrum of the 193 nm photolysis products of acrylonitrile was acquired in a supersonic jet expansion. A total of 28,000 averages were recorded in short acquisitions of 500–2000 averages each. Without phase correction (a), only the acrylonitrile $J_{K_aK_c} = 9_{18} \leftarrow 9_{17}$, the HCN $(\nu_1\,\nu_2^\ell\,\nu_3) = (0\,0^0\,0)$, $J = 1 \leftarrow 0$ line, and the HNC $(0\,0^0\,0)$, $J = 1 \leftarrow 0$ lines are detected above the noise. When the phase of each spectrum is shifted to maximize the overlap of the HCN $(0\,0^0\,0)$ line (b), the signal-to-background-noise ratio increases dramatically and more lines become visible: HCN $(0\,2^0\,0)$, $J = 1 \leftarrow 0$; HCN $(0\,4^0\,0)$, $J = 1 \leftarrow 0$; HNC $(0\,2^0\,0)$, $J = 1 \leftarrow 0$; acrylonitrile $5_{15} \leftarrow 4_{04}$; HCCCN, $J = 10 \leftarrow 9$ and a ^{13}C-substituted acrylonitrile line at 91,821.43 MHz. Artifact lines corresponding to local oscillator frequencies are labeled with asterisks.

10^{11} molecules/cm^3.

The CPmmW spectrometer has also been used in millimeter wave-optical double resonance (mmODR) experiments. In the first such implementation, the millimeter-wave beam was crossed with the frequency-doubled output of a pulsed dye laser. The supersonic jet expansion was directed at a right angle to the millimeter-wave and laser beams. The $6_{06} \leftarrow 5_{15}$ transition in ground-state SO_2 was excited by the millimeter waves and the laser frequency was scanned across the $\tilde{\mathrm{C}}\ {}^1\mathrm{B}_2(1,3,2) \leftarrow \tilde{\mathrm{X}}\ {}^1\mathrm{A}_1(0,0,0)$ band centered at 45336 cm^{-1}. The $\sim$10 ns laser pulse arrived 500 ns after the start of the millimeter-wave FID, so that it causes a decrease in the magnitude of the millimeter-wave coherence if it is resonant with one of the two states involved. The method is similar to the cavity Fourier-transform microwave-optical double resonance technique of Nakajima *et al.*[42] The double resonance spectrum was obtained by recording the normalized ratio of the FID intensity before and after the laser pulse. The double resonance spectrum is plotted along with the laser induced fluorescence (LIF) spectrum in Fig 1-8. Rotational assignments for this band have been made previously by Yamanouchi *et al.*[43] The double resonance peak at 45332.65(2) cm^{-1} agrees to within experimental uncertainty with the peak assigned to the $4_{14} \leftarrow 5_{15}$ transition. We have assigned the other peak at 45332.79(2) cm^{-1} to the $5_{05} \leftarrow 6_{06}$ transition, which was not assigned by Yamanouchi *et al.* due to spectral congestion and complications caused by Coriolis effects. Both of our assignments are confirmed by the existence of combination difference peaks in the LIF spectrum.

The successful implementation of mmODR with our spectrometer suggests that the technique could be used to generate two dimensional Chirped-Pulse mmODR spectra in order to decongest LIF spectra and provide rotational assignments. The technique will provide the most information for molecules with sufficiently small rotational constants such that the chirped pulse will cover several rotational transitions. The laser spectrum can be scanned while many ground-state rotational transitions are probed, and the Fourier transform of the FID dip will provide information about which ground-state rotational level is involved in each LIF transition.

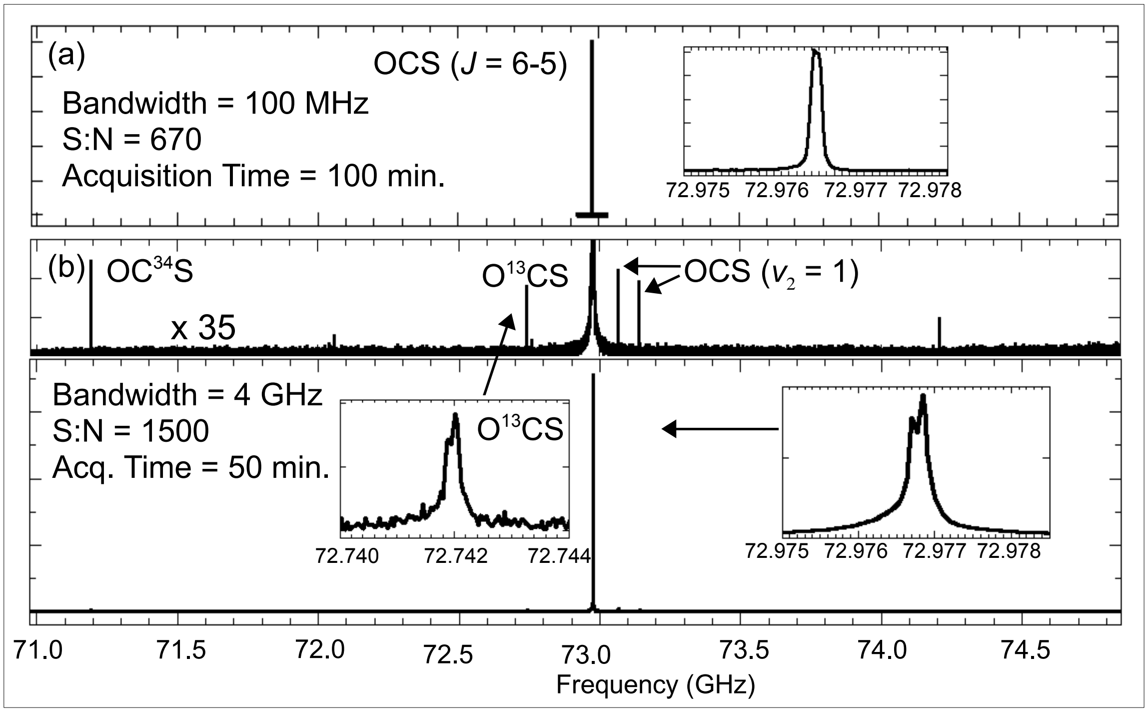

Figure 1-7: For comparison, the spectrum of OCS in the region surrounding the $J = 6 \leftarrow 5$ region was measured with (a) the scanned absorption spectrometer previously used in the Field group and (b) the CPmmW spectrometer. The CPmmW spectrometer was able to cover 40 times the bandwidth in half the time with better signal-to-background-noise ratio. Differences in line profile are due primarily to the fact that the CPmmW spectrometer detects electric field, which is proportional to the square root of power.

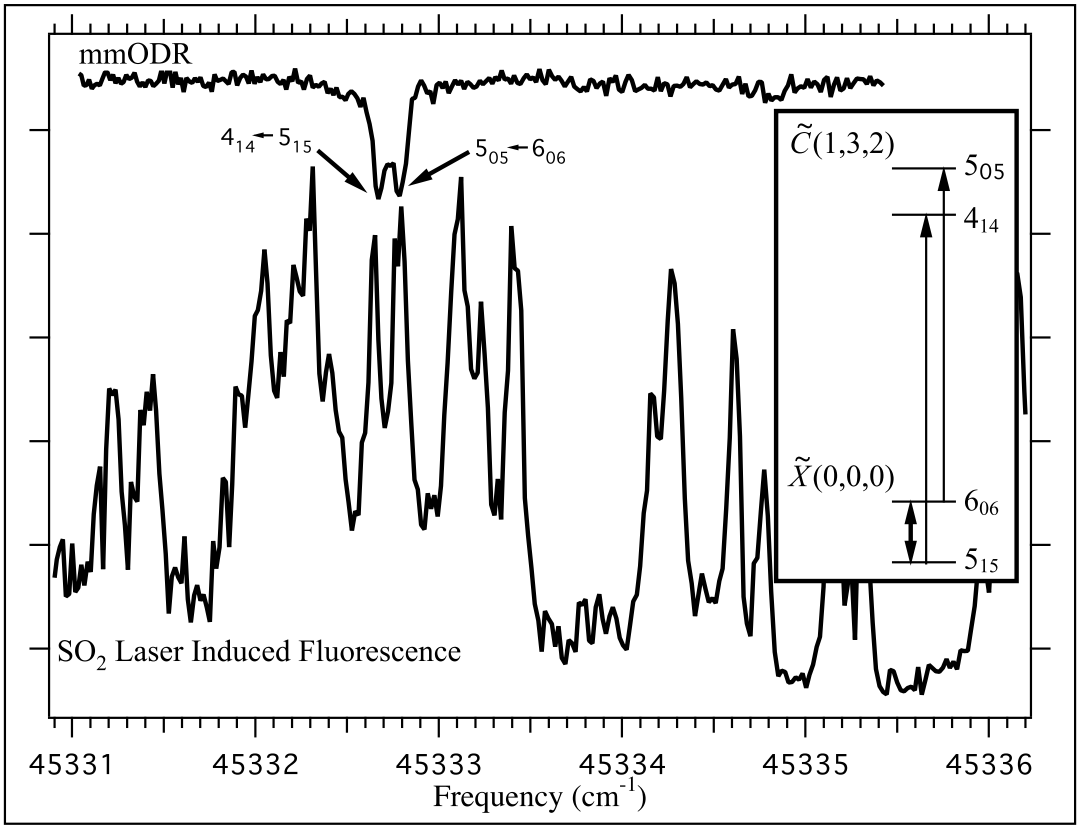

Figure 1-8: The LIF spectrum of SO_2 (lower trace) to the $(1, 3, 2)$ level of the $\tilde{C}$ state is shown along with a millimeter wave-optical double resonance spectrum to the same band (upper trace). The scheme for the double resonance experiment is shown in the inset. The thick double arrow represents the millimeter-wave coherence that was generated between the 6_{06} and 5_{15} rotational levels of the $\tilde{X}(0, 0, 0)$ state. The double resonance signal was obtained by measuring the dip in the millimeter-wave FID intensity as the laser was scanned.

1.6.2 Spectroscopy of Laser-Excited States

CPmmW spectroscopy is particularly advantageous as a tool for probing laser-excited states since it is designed for pulsed operation and can be easily coupled to pulsed supersonic jets and tunable pulsed laser systems. The duty cycle of such experiments is necessarily low. In our laboratory, the pulsed dye lasers operate at 10 Hz and the chirped-pulse experiment lasts ∼5 μs or less. Thus the fraction of time when microwave observations can be made is less than 10^{-4}, when compared with traditional non-pulsed absorption measurements. CPmmW spectroscopy is well suited to this case since it can record a broad spectral region during the short radiative lifetime and the time between gas pulses can be used for digital averaging of the FID.

As a demonstration that CPmmW spectroscopy can be used to probe laser-excited states, we measured the $(J' = 2, N' = 2) \leftarrow (J' = 1, N' = 1)$ transition in the excited triplet electronic state e $^3\Sigma^-$ $(\nu = 2)$ of CS using a 1 GHz bandwidth chirped pulse (Fig. 1-9). Because the uncertainty in laser transitions is typically ~1 GHz, it may be necessary to cover a broad spectral range when probing for rotational transitions of laser-excited states. The CS line could be seen above the noise after about 100 averages (10 seconds). We estimate that this signal came from a total of $\sim 4.8 \times 10^{10}$ excited CS molecules in a single quantum state.

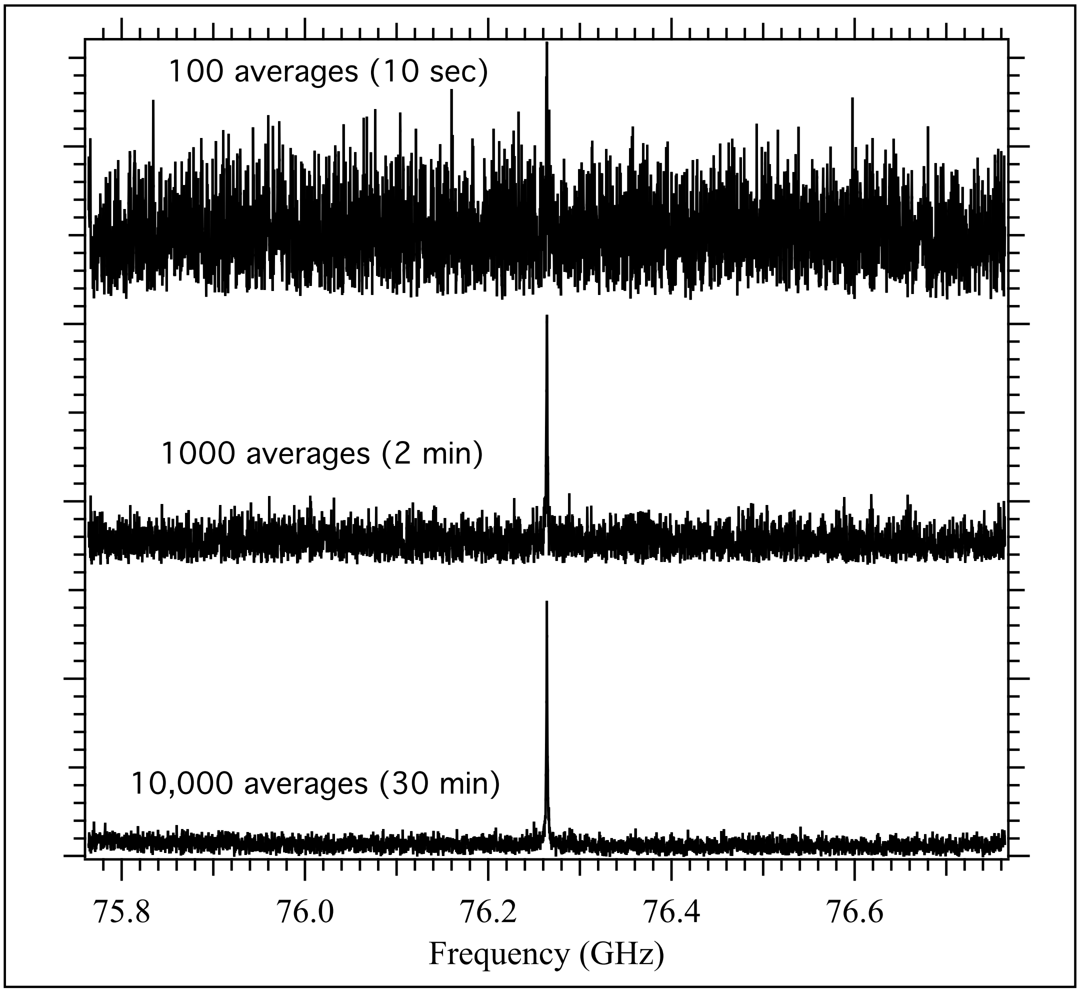

Figure 1-9: The e $^3\Sigma^-$ $(\nu = 2)$ state of CS was populated using the frequency-doubled output of a tunable Nd:YAG-pumped dye laser at ~39910 cm^{-1}. The $(J' = 2, N' = 2) \leftarrow (J' = 1, N' = 1)$ transition in the excited state was then probed using a 1 GHz bandwidth chirped pulse centered on the transition.

The transition frequency was previously reported as 76,229.027(20) MHz.[44] In the current work, we correct this frequency to 76,263.89(10). The FWHM is 1.1 MHz and is attributable to the radiative lifetime of the e $^3\Sigma^-$ state. The difference between the previously reported frequency and the current value is almost exactly 35 MHz, which was the reference frequency used in the original measurement to stabilize the Gunn oscillator. This suggests that the oscillator may have been erroneously locked to the second harmonic of the reference.

The CPmmW technique has also been recently applied to pure electronic Rydberg-Rydberg transitions in calcium atoms.[9]

1.7 Instrument Noise Floor

In our current spectrometer, the noise level is set by the noise output of the source amplifier. We experimentally measure the noise level at the receiver to be a factor of 9 in power above the thermal noise at the receiver. Fast, broadband PIN switches with insertion losses of ∼2 dB have recently become available for the W-band. We plan to place a switch after the source amplifier to eliminate source amplifier noise during detection of the FID. The noise encountered in the experiment will then be set by the noise figure of the detection arm. In the current spectrometer, the noise figure of the detection arm is set by a combination of a rather lossy downconverter (9 dB conversion loss) and the 2.3 dB noise figure of the low noise amplifier for the RF. The combined noise figure after the collection horn is therefore ∼11.3 dB (or a factor of 13.5). Recently, LNAs covering the full W-band with a noise figure of ∼5 dB have become available. Such an amplifier would need to be protected from the powerful excitation pulse by a switch (∼2 dB insertion loss). The combined noise figure of the detection arm would then be set by these two components to 7 dB (or a factor of 5.0). We therefore expect to be able to achieve an overall reduction in noise floor by a factor of $13.5 \times 9/5.0 = 24$ in power or 4.9 in electric field. The 2 dB insertion loss of the switch on the source will cause a 25% loss in signal, but this will be more than compensated by the reduction in noise floor.

1.8 Future Work

CPmmW spectroscopy is shown to be an advantageous method for spectroscopy in the 70–100 GHz region. However, future work is planned to improve the sensitivity of the method by taking full advantage of recent advances in millimeter-wave technology. Most importantly, we plan to obtain W-band low-noise amplifiers and switches to improve the noise floor of the detection arm, as discussed in Section 1.7. We also hope to obtain new power amplifiers to increase the strength of our excitation pulse.

Technology is rapidly progressing for broadband millimeter-wave power amplifiers. Powers up to 400 mW have been reported across the W-band.[45,46] Because signal scales with the square root of pulse power, such an amplifier (used in conjunction with a 2 dB insertion loss switch) would improve the signal strength in the CPmmW spectrometer by a factor of 3.

1.9 Acknowledgments

The authors are grateful for advice and support from Brooks Pate and his lab. This work was supported at MIT by DOE Grant No. DEFG0287ER13671 and by an NSF Graduate Research Fellowship.

1.10 Appendix: Part List

The following part list is labeled with Roman numerals corresponding to the labeling in Fig. 1-1. In cases where parts are swapped out depending on which sideband is being used, the parts are labeled “a” for the lower (70–85 GHz) sideband and “b” for the upper (87–102 GHz) sideband.

i. 10 MHz Rubidium Frequency Standard (Stanford Research Systems FS725)

ii. 90 MHz Phase-Locked Crystal Oscillator (Miteq PLD-10-90-15P)

iii. 3.96 GHz Phase-Locked Dielectic Resonator Oscillator (Microwave Dynamics PLO-2000-03.96)

iv. 4.2 GS/s Arbitrary Waveform Generator (Tektronix AWG710B)

v. 10.7 GHz Phase-Locked Dielectric Resonator Oscillator (Miteq PLDRO-10-10700-3-8P)

vi. Double-Balanced Mixer (Macom M79)

vii. 8–16 GHz circulator (Hitachi R3113110)

viii. 1.5–18 GHz amplifier (Armatek MH978141)

ix.a. 8.7–10.5 GHz bandpass filter (Spectrum Microwave C9680-1951-1355)

ix.b. 10.9–12.7 GHz bandpass filter (Spectrum Microwave C11800-1951-1355)

x. Q-Band Active Frequency Quadrupler (Phase One Microwave PS07-0153A R2)

xi.a. E-Band Active Frequency Doubler (Quinstar QMM-77151520)

xi.b. W-Band Active Frequency Doubler (Quinstar QMM-9314152ZI1)

xii. WR10 gain horn, 24 dBi gain mid-band (TRG 861W/387)

xiii Teflon circular lenses, 30 cm and 40 cm focal length at 80 GHz (custom)

xiv. Gunn Phase Lock Module (XL Microwave Model 800A)

xv. W-Band Gunn Oscillator (J.E. Carlstrom Co.)

xvi. W-Band Subharmonic Downconverter (Pacific Millimeter Products)

xvii.a. E-Band Downconverter (Ducommun Technologies FDB-12-01)

xvii.b. W-Band Downconverter (Ducommun Technologies FDB-10-01)

xviii. Low-Noise Amplifier (Miteq AMF-5D-00101200-23-10P)

xix. 12 GHz Digital Storage Oscilloscope (Tektronix TDS6124C)

Chapter 2

Edge effects in chirped-pulse Fourier transform microwave spectra

Abstract

Recent applications of chirped-pulse Fourier transform microwave and millimeter wave spectroscopy have motivated the use of short (10–50 ns) chirped excitation pulses. In this regime, individual transitions within the chirped pulse bandwidth do not all, in effect, experience the same frequency sweep through resonance from far above to far below (or vice versa), and "edge effects" may dominate the relative intensities. We analyze this effect and derive simplifying expressions for the linear fast passage polarization response in the limit of long and short excitation pulses. In the long pulse limit, the polarization response converges to a rectangular function of frequency, and in the short pulse limit, the polarization response morphs into a form proportional to the window function of the Fourier-transform-limited excitation pulse.[a]

2.1 Introduction

Chirped-pulse Fourier-transform microwave (CP-FTMW) spectroscopy, invented in Professor Brooks Pate's lab,[32,34] is rapidly becoming a mainstream technique for broadband (> 10 GHz) high-resolution microwave and millimeter-wave spectroscopy. Because the CP-FTMW technique allows rapid acquisition of broadband rotational spectra, it provides a wealth of chemical and physical information that was not previ-

---

[a] At the time of the submission of this thesis, the contents of this chapter have been submitted for publication in *The Journal of Molecular Spectroscopy.*

ously readily accessible. To zeroth order, the rotational spectrum is a direct function of the molecule's structure and the molecule-frame orientation of its dipole moment. Fine and hyperfine structure often provides additional information about the electronic wavefunction. Thus, the microwave spectrum of a gas-phase molecule provides information that is fundamental to the way a chemist thinks about the molecule at rest (with well-defined nuclear and electronic structure). Furthermore, the rotational spectrum is specific to different conformers and vibrational states, and may be used to study clusters and complexes.

Since its inception, CP-FTMW has also been a dynamically-relevant technique. Dian *et al.*[34] show that the spectral coalescence of the broadband rotational spectrum of a highly vibrationally-excited species can be used to extract dynamical information about intramolecular vibrational energy redistribution (IVR) and chemical isomerization. Fine structure in the chirped-pulse spectrum of the prism isomer of the water hexamer enables the measurement of hydrogen-bond network rearrangement.[47] Prozument *et al.*[48] have used chirped-pulse millimeter wave spectroscopy to obtain meaningful product branching ratios and vibrational population distributions from a flash pyrolysis reactor. Recent work in the A. G. Suits lab[49,50] has demonstrated the use of time-domain CP-FTMW measurements to measure the vibrationally-specific rate of appearance of unimolecular and bimolecular reaction products in a cold uniform flow.

Because of growing interest in CP-FTMW as a tool for kinetics and dynamics, there is an increasing necessity for reliable, quantitatively accurate measurement of relative intensity across broadband spectral regions. At the same time, several factors are driving researchers to use chirped excitation pulses of shorter duration. First, there has been a push to extend chirped-pulse spectroscopy to higher millimeter-wave frequencies, where Doppler dephasing times become short.[51–53] Next, the use of CP-FTMW by Abeysekera *et al.*[50] to study bimolecular reactions at pressures as high as ∼0.2 mbar leads to a regime where the coherence time is shortened by pressure broadening. Indeed, the authors of Ref. 50 found that when using 1 μs long excitation pulses, dephasing phenomena had a significant effect on the relative intensities. As a result of dephasing during the excitation pulse, intensities of transitions that were excited early in the chirped pulse were weakened relative to those of transitions excited later in the pulse. The problem was mitigated by decreasing the pulse duration to 250 ns, or by taking the frequency-domain average between spectra from "up-chirp" and "down-chirp" excitation pulses. (See Figure 2 of Ref. 50.) Proposed experiments to probe pure-electronic transitions in Rydberg molecules rely on chirped pulse schemes for rapidly populating non-core-penetrating high-l states before predissociation occurs.[9,54] Finally, kinetic schemes involving time-resolved broadband microwave spectroscopy[50] motivate fast excitation pulses to achieve the best time-resolution for monitoring state-resolved reactant and product populations.

References 48 and 55 discuss the need for the chirped excitation pulse to be in the weak-field (fast-passage) limit rather than the strong-field (adiabatic rapid passage) limit in order to avoid saturation effects on the relative intensities. References 50, 56 and others discuss the need for the duration of the excitation pulse to be short relative to the coherence decay time in order to achieve accurate relative intensities. However, most authors have ignored "edge effects" on relative intensities in chirped-pulse spectra. Therefore, we will discuss these effects briefly. These effects become pronounced as one uses shorter excitation pulses. It is important to point out that we do not derive any novel physics in this paper. Our results may all be obtained from analysis of the equations presented in Refs. 57 and 36 and reviewed in detail in Ref. 58.

2.2 Polarization from a linearly chirped pulse in the weak coupling limit

The response of a two-level system to a linearly swept excitation pulse in the weak coupling limit was reported by McGurk *et al.*[36,57] and is also discussed in Ref. 56 and reviewed in detail in Ref. 58. We will therefore provide only a brief summary in Appendix B. The dynamics driven by a slowly varying excitation pulse of the form

$E = 2\mathcal{E}\cos(\omega t - kz)$ can be described by the master equations,

$$\frac{\partial P_r}{\partial t} + \Delta\omega P_i = 0 \tag{2.1}$$

$$\frac{\partial P_i}{\partial t} - \Delta\omega P_r + \frac{|\mu_{ab}|^2 \mathcal{E}\Delta N}{\hbar} = 0 \tag{2.2}$$

$$\frac{\partial}{\partial t}\Delta N - \frac{4\mathcal{E}}{\hbar}P_i = 0, \tag{2.3}$$

where P_r and P_i are the real and imaginary components of the polarization, $\Delta\omega = \omega_0 - \omega$ is the detuning of the driving frequency (ω) from the resonance frequency (ω_0), μ_{ab} is the transition dipole moment, and $\Delta N = N_a - N_b$ is the difference in population density of the two levels. Our notation is defined in more detail in Appendix B, where we provide a derivation of Eqs. (2.1–2.3). We have omitted the phenomenological T_1 and T_2 decay terms included by McGurk *et al.*

Assume a linearly chirped pulse with sweep rate α that crosses through a molecular resonance at time $t = 0$, so that

$$\Delta\omega(t) = \omega_0 - \omega(t) = \alpha t.$$

Assume also that the experiment is performed in the weak power limit so that the population transfer, $\Delta N - \Delta N_0$, is negligible. In that case, we may ignore (2.3) and we may set ΔN in (2.2) to a constant, ΔN_0, equal to the initial difference in population density. Our assumption that the population transfer is negligible also implies that the power absorbed by the sample is negligible, so we can take $\mathcal{E}$ to be a constant over the space occupied by the molecular sample. Finally, since $\Delta\omega$ is proportional to t, we may write the differential equations with respect to $\Delta\omega$ instead of t. The result is

$$\alpha\frac{\partial P_r}{\partial(\Delta\omega)} + \Delta\omega P_i = 0 \tag{2.4}$$

$$\alpha\frac{\partial P_i}{\partial(\Delta\omega)} - \Delta\omega P_r + \frac{|\mu_{ab}|^2 \mathcal{E}\Delta N_0}{\hbar} = 0. \tag{2.5}$$

McGurk *et al.*[36] have shown that (2.4–2.5) is an exactly solvable system of differential equations. The solution is given by

$$P_r = \frac{|\mu_{ab}|^2 \mathcal{E} \Delta N_0}{\hbar} \sqrt{\frac{\pi}{\alpha}} \left\{ \sin\left(\frac{(\Delta\omega_f)^2}{2\alpha}\right) \left[-C\left(\frac{\Delta\omega_i}{(\pi\alpha)^{1/2}}\right) + C\left(\frac{\Delta\omega_f}{(\pi\alpha)^{1/2}}\right) \right] \right.$$
$$\left. - \cos\left(\frac{(\Delta\omega_f)^2}{2\alpha}\right) \left[-S\left(\frac{\Delta\omega_i}{(\pi\alpha)^{1/2}}\right) + S\left(\frac{\Delta\omega_f}{(\pi\alpha)^{1/2}}\right) \right] \right\} \tag{2.6}$$

$$P_i = -\frac{|\mu_{ab}|^2 \mathcal{E} \Delta N_0}{\hbar} \sqrt{\frac{\pi}{\alpha}} \left\{ \cos\left(\frac{(\Delta\omega_f)^2}{2\alpha}\right) \left[-C\left(\frac{\Delta\omega_i}{(\pi\alpha)^{1/2}}\right) + C\left(\frac{\Delta\omega_f}{(\pi\alpha)^{1/2}}\right) \right] \right.$$
$$\left. + \sin\left(\frac{(\Delta\omega_f)^2}{2\alpha}\right) \left[-S\left(\frac{\Delta\omega_i}{(\pi\alpha)^{1/2}}\right) + S\left(\frac{\Delta\omega_f}{(\pi\alpha)^{1/2}}\right) \right] \right\}, \tag{2.7}$$

where $C(a)$ and $S(a)$ are the Fresnel integrals,

$$C(a) = \int_0^a \cos(\pi x^2/2)\mathrm{d}x, \quad S(a) = \int_0^a \sin(\pi x^2/2)\mathrm{d}x,$$

and $\Delta\omega_i$ and $\Delta\omega_f$ are the initial and final values of the the detuning. We have simplified the expression derived by McGurk *et al.*, noting that the Fresnel integrals are odd functions, $C(-a) = -C(a)$ and $S(-a) = -S(a)$, which allows us to remove the absolute values and the ± choices.

The solutions (2.6–2.7) seem complicated, but the form is simplified by the assumptions

$$|\Delta\omega_i| \gg (\pi\alpha)^{1/2}, \qquad |\Delta\omega_f| \gg (\pi\alpha)^{1/2}. \tag{2.8}$$

With this assumption, we can use the limiting behavior of the Fresnel integrals,

$$\lim_{a\to-\infty} C(a) = -0.5 \qquad \lim_{a\to-\infty} S(a) = -0.5$$
$$\lim_{a\to+\infty} C(a) = +0.5 \qquad \lim_{a\to+\infty} S(a) = +0.5,$$

We assume the case where $\Delta\omega$ is swept through resonance from negative to positive ($\Delta\omega_i < 0$, $\Delta\omega_f > 0$, and $\alpha > 0$). From assumption (2.8), we obtain

$$P_r \approx \frac{|\mu_{ab}|^2 \mathcal{E} \Delta N_0}{\hbar} \sqrt{\frac{\pi}{\alpha}} \left\{ \sin\left(\frac{(\Delta\omega_f)^2}{2\alpha}\right) - \cos\left(\frac{(\Delta\omega_f)^2}{2\alpha}\right) \right\} \tag{2.9}$$

$$P_i \approx -\frac{|\mu_{ab}|^2 \mathcal{E} \Delta N_0}{\hbar} \sqrt{\frac{\pi}{\alpha}} \left\{ \cos\left(\frac{(\Delta\omega_f)^2}{2\alpha}\right) + \sin\left(\frac{(\Delta\omega_f)^2}{2\alpha}\right) \right\}. \tag{2.10}$$

In the case where $\Delta\omega$ is swept in the other direction, the phase of Eqs. (2.9–2.10) will change, but the magnitude will remain the same. Assumption (2.8) will hold for most chirped pulse experiments as long as the sweep rate is not too fast and the molecular resonance is not too close in frequency to the initial or final frequency of the linearly swept excitation pulse—i.e., if the transition is not too close to the high- or low-frequency edge of the spectrum. For a typical chirped pulse experiment, the excitation pulse sweeps through a bandwidth of ~10 GHz during a time interval of ~1 μs, so $\alpha \approx 10^{16}$ s^{-2} and $(\pi\alpha)^{1/2} \approx 180$ MHz. Furthermore, in this case, the values of

$$\left[-C\left(\frac{\Delta\omega_i}{(\pi\alpha)^{1/2}}\right) + C\left(\frac{\Delta\omega_f}{(\pi\alpha)^{1/2}}\right)\right]$$

and

$$\left[-S\left(\frac{\Delta\omega_i}{(\pi\alpha)^{1/2}}\right) + S\left(\frac{\Delta\omega_f}{(\pi\alpha)^{1/2}}\right)\right]$$

will be within ~20% of unity for any transition not within 30 MHz of the boundaries $\Delta\omega_i$ or $\Delta\omega_f$, so the approximation in Eqs. (2.9–2.10) will usually apply. For a typical chirped pulse experiment, the approximation will be invalid only for transitions located in the outer 0.3% wings of the frequency span of the applied pulse.

Equations (2.9–2.10) may be simplified even further to give the magnitude of the oscillating polarization. Noting the definitions of P_r and P_i from Eq. (B.14), we see that the bracketed sin and cos terms in Eqs. (2.9–2.10) merely describe the rapid oscillation of the polarization in the rotating frame of the applied electromagnetic field. Because the polarization of the molecular resonance will oscillate at a frequency ω_0 in the non-rotating frame, we may write

$$P \approx \frac{2|\mu_{ab}|^2\mathcal{E}\Delta N_0}{\hbar}\sqrt{\frac{\pi}{\alpha}}\sin(\omega_0 t + \phi), \tag{2.11}$$

where ϕ is a phase that may be determined from Eqs. (2.9–2.10), and the prefactor, $2|\mu_{ab}|^2\mathcal{E}\Delta N_0/\hbar$ gives the magnitude of the oscillating polarization.

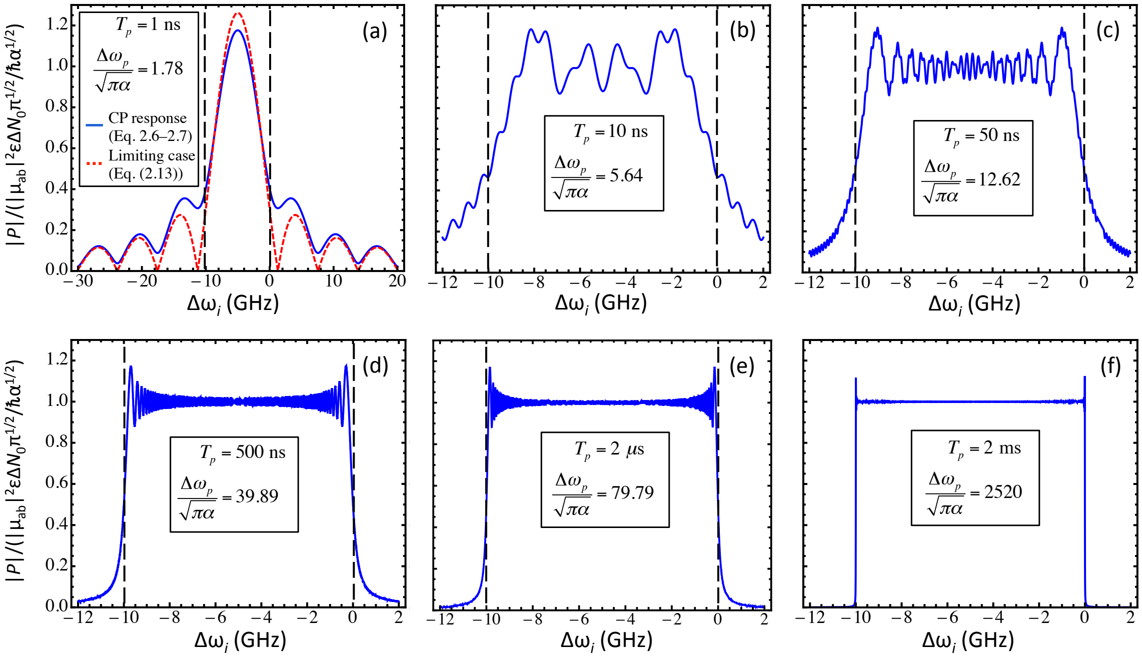

Figure 2-1: The magnitude of the polarization from Eqs. (2.6–2.7), normalized to the prefactor as indicated, is plotted against the initial detuning frequency $\Delta\omega_i$ for a $\Delta\omega_p = 10$ GHz bandwidth chirped pulse as a function of pulse duration, T_p. In panel (a), the limiting sinc function behavior from Eq. 2.13 is plotted for comparison as a dotted curve, normalized to the same prefactor. As the pulse duration increases, the frequency dependence of the polarization response morphs from the window-function-limited behavior of Eq. 2.13 to the rectangular response function of Eq. 2.12.

2.3 Limiting behavior of the polarization response with respect to pulse duration

For very short excitation pulses, assumption 2.8 is invalid. Therefore, it is useful to examine the limiting behavior of Eqs. (2.6–2.7) as $\alpha \to \infty$ and $\alpha \to 0$. The evolution of the polarization response from a 10 GHz bandwidth excitation pulse as a function of pulse duration is shown in Fig. 2-1. We define the nominal bandwidth, $\Delta\omega_\text{p}$, and duration, T_p, of the chirped excitation pulse such that

$$\Delta\omega_\text{p} = \Delta\omega_f - \Delta\omega_i$$

$$T_p = \frac{\Delta\omega_p}{\alpha}.$$

2.3.1 Long pulse limit

In the limit of very long pulse duration, ($\alpha \to 0$), assumption (2.8) applies and the limiting behavior of the Fresnel integrals is relevant. Note that the signs of the Fresnel integrals in Eqs. (2.6–2.7) depend on the signs of $\Delta\omega_i$ and $\Delta\omega_f$. Assuming $\Delta\omega_f > \Delta\omega_i$, there are three cases:

$$\lim_{\substack{\alpha\to 0\\ \mu\mathcal{E}\to 0}} |P| = \begin{cases} 0 & \Delta\omega_f < 0 \text{ and } \Delta\omega_i < 0 \\ \frac{2|\mu_{ab}|^2\mathcal{E}\Delta N_0}{\hbar}\sqrt{\frac{\pi}{\alpha}} & (\Delta\omega_i < 0 \text{ and } \Delta\omega_f > 0) \text{ or } (\Delta\omega_i > 0 \text{ and } \Delta\omega_f < 0) \\ 0 & \Delta\omega_f > 0 \text{ and } \Delta\omega_i > 0. \end{cases} \tag{2.12}$$

The first and third cases of Eq. (2.12) apply when the resonance is below or above the excitation pulse bandwidth and the second case applies when the resonance is within the excitation bandwidth. Thus, we see that in the $\alpha \to 0$ limit of an infinitely long excitation pulse, Eqs. (2.6–2.7) become a rectangular wave excitation with a completely flat polarization response. (See Fig. 2-1(f).) Of course, Eqs. (2.6–2.7) also assume the weak field limit ($\mu\mathcal{E}/\hbar \ll \alpha^{1/2}$, i.e. the Rabi frequency is slower than the sweep rate) and neglects dephasing. Thus, to obtain this result we have also implicitly assumed an infinitesimal $\mu\mathcal{E}$ and $1/T_2$ coherence dephasing rate. (In the strong-field case where $\mu\mathcal{E}/\hbar \gg \alpha^{1/2}$, we expect to enter the adiabatic rapid passage regime, where the Bloch vector precesses tightly around the driving vector $\mathbf{\Omega}$ as the frequency is swept, and the result is a population inversion rather than a coherent polarization.[55,58]) Therefore, panel (f) of Fig. 2-1 is not intended to represent a physically realistic regime for most experiments—it is merely intended to illustrate the limiting behavior of Eqs. (2.6–2.7).

2.3.2 Short pulse limit

In the limit of very short pulse duration ($\alpha \to \infty$), assumption (2.8) does not apply. However, in the limit where the bandwidth of the excitation pulse window function, $\mathcal{E}(t)$, becomes broader than the nominal chirp bandwidth, the polarization response becomes dominated by the Fourier transform of the window function. For a rectangular window function, it is possible to show that Eqs. (2.6–2.7) approach the limit

$$\lim_{\alpha\to\infty}|P| = \frac{|\mu_{ab}|^2\mathcal{E}\Delta N_0}{\sqrt{2}\hbar}\frac{T_p\sin\left[\frac{1}{2}(\Delta\omega_i+\Delta\omega_p/2)T_p\right]}{\frac{1}{2}(\Delta\omega_i+\Delta\omega_p/2)T_p}. \tag{2.13}$$

Eq. 2.13 is simply a sinc function centered at the middle of the chirped pulse bandwidth. Note that the $\sqrt{\alpha}$ scaling has disappeared and that the prefactor depends instead on the excitation pulse duration T_p. Thus, when the window function bandwidth becomes much broader than the chirp, the sample no longer behaves as if it is being excited by a chirped pulse. Instead, the polarization response morphs into what would be obtained from a rectangular excitation pulse with a carrier frequency at the center of the chirped pulse bandwidth. This limiting behavior is illustrated in Fig. 2-1(a). Note that in most chirped-pulse spectrometers, it is difficult to generate a 1 ns excitation pulse due to limitations of currently available microwave components. Therefore, the case illustrated in Fig. 2-1(a) is not intended to represent an experimentally realistic regime—it is merely shown to illustrate the limiting behavior of Eqs. (2.6–2.7).

In conclusion, there are three primary considerations that are necessary in order to ensure a flat polarization response across a broadband chirped-pulse spectrum:

$$T_p \ll T_2 \tag{2.14a}$$

$$|\mu_{ab}|\mathcal{E}/\hbar \ll \alpha^{1/2} \tag{2.14b}$$

$$|\Delta\omega_i|, |\Delta\omega_f| \gg (\pi\alpha)^{1/2} \tag{2.14c}$$

Condition (2.14a) ensures that the transition intensities will not be attenuated by dephasing of the coherence during the excitation pulse, as illustrated in Fig. 2-2. As shown in Ref. 50, dephasing effects can lead to anomalies in the relative intensities because transitions excited early in the excitation pulse will undergo more dephasing than transitions excited later in the excitation pulse. Condition (2.14b) ensures that the excitation pulse will be in the weak field limit so that saturation effects will be avoided and Eqs. (2.6–2.7) will be valid. Finally, condition (2.14c) ensures that the transition is not too close in frequency to either edge of the chirped-pulse bandwidth, where edge effects can dominate the relative intensities.

In the Bloch sphere picture, both Eqs. (2.14b) and (2.14c) are necessary to ensure that the transitions are excited in the linear fast passage regime. In the standard Cartesian representation of the rotating-frame optical Bloch equations,[58] the axes (u, v, w) are proportional to $(P_r, P_i, \Delta N)$ of Eqs. (2.1–2.3). In the absence of damping terms, the dynamics of the system are succinctly described by the Bloch vector picture,

$$\frac{\mathrm{d}\boldsymbol{\Theta}}{\mathrm{d}t} = \boldsymbol{\Omega} \times \boldsymbol{\Theta}, \tag{2.15}$$

where $\boldsymbol{\Theta} = (u, v, w)$ describes the state of the system and $\boldsymbol{\Omega} = (-\mu_{ab}\mathcal{E}/\hbar, 0, \Delta\omega(t))$ is the driving vector. When condition (2.14c) is satisfied, the initial and final detuning is large and $\boldsymbol{\Omega}$ is, in effect, swept 180° in the u, w plane from the $+w$ to the $-w$ axis. The initial detuning must be large compared to $\sqrt{\alpha}$ in order to ensure that the Bloch vector, $\boldsymbol{\Theta}$, precesses tightly around $\boldsymbol{\Omega}$ during the initial sweep toward resonance. However, in order to avoid the adiabatic rapid passage regime, the sweep rate must be sufficiently fast so that condition (2.14b) also applies. This ensures that the Bloch vector does not follow the driving vector all the way to a population inversion. Instead, as resonance is approached and the Rabi frequency decreases, the Bloch vector is no longer able to “keep up” with the driving vector, and the tight precession disappears. The final detuning must also be sufficiently large to ensure that the driving vector effectively sweeps through the full 180° and we are left with a polarization given by Eq. (2.11). A Bloch sphere illustration of the linear fast passage regime is given in Fig. 4 of Ref. 55. Most authors in the chirped-pulse spectroscopy community have emphasized the importance of conditions (2.14a) and (2.14b), but there has been very little discussion of condition (2.14c) in the literature, which is also important in achieving linear fast passage dynamics and meaningful relative intensities provided by the flat frequency response in the limiting case where Eq. (2.12) applies.

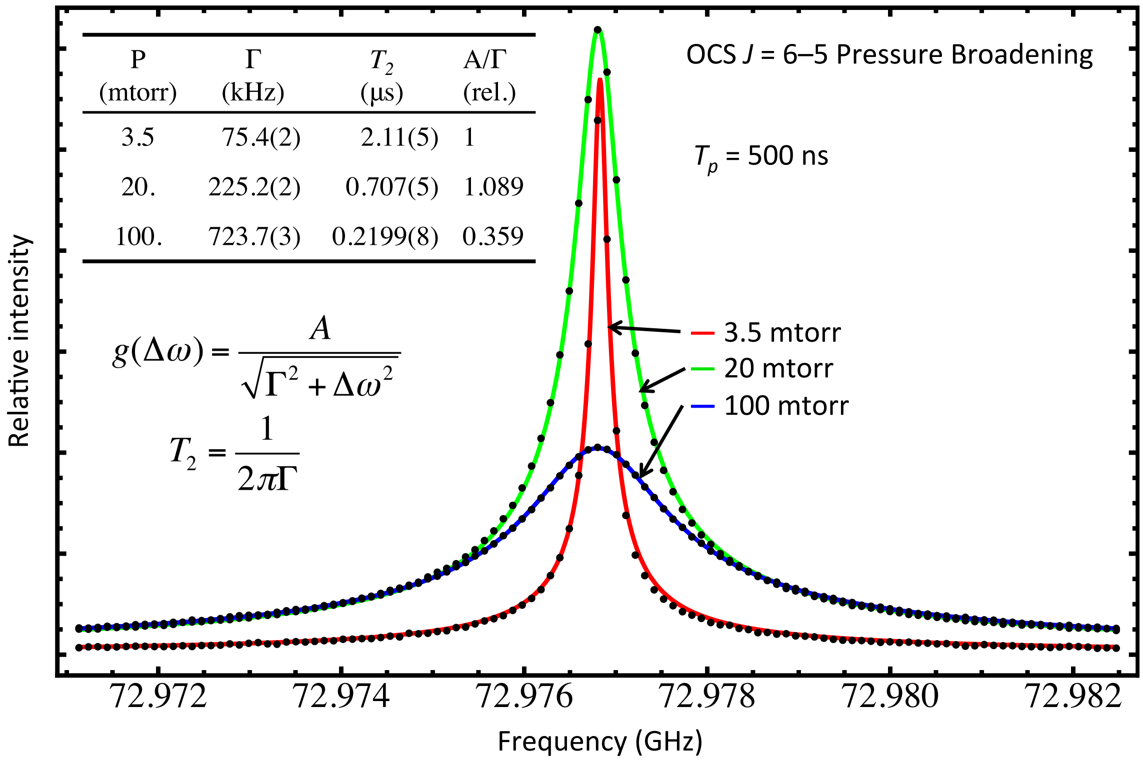

Figure 2-2: The $J = 6$–5 transition of the OCS molecule was observed using the chirped-pulse millimeter-wave spectrometer described in Ref. 51 at room temperature, as a function of pressure. The spectra were obtained using a $T_p = 500$ ns excitation pulse duration. The magnitude Fourier-transform of a 20 μs FID window is plotted. The lineshape $g(\Delta\omega)$ is proportional to the square root of a Lorentzian since the electric field radiated is proportional to the square root of the power absorption. The width parameter, Γ, and coherence lifetime, T_2, defined in the figure, were obtained from a least-squares fit to $g(\Delta\omega)$ at each pressure (see inset—values in parentheses are the 2σ statistical uncertainty of the last digit). As the pressure is increased, the peak height, A/Γ first increases due to increased number density, but then decreases as T_2 becomes faster than the excitation pulse duration, $T_p = 500$ ns.

2.4 Conclusions

We have briefly described the impact of "edge effects" on the polarization response in linear fast passage experiments. In order to obtain a flat frequency response over the full bandwidth of the chirped excitation pulse, it is important for the initial and final detuning frequencies to be much greater than $\alpha^{1/2}$. This is because the linear fast passage regime relies on a Bloch vector, $\boldsymbol{\Theta}$, that follows the driving vector, $\boldsymbol{\Omega}$, adiabatically when it is far away from resonance, but becomes decoupled from the driving vector along the approach to resonance. If $|\omega_i|$ and $|\omega_f|$ are too small or α is too fast, the sample will not effectively experience a frequency sweep through resonance from far away, and the relative intensities will be affected by the window function of the chirped excitation pulse.

In the usual implementations of CP-FTMW, typically the bandwidth is not broader than 10–20 GHz and the pulse duration is 1 μs or longer, so that these effects are unimportant. However, new directions in chirped pulse microwave and millimeter wave spectroscopy have motivated the use of shorter excitation pulses, where the polarization response loses its flatness. We have therefore analyzed the long-pulse and short-pulse limits of the linear fast passage response, and we have derived the appropriate simplifying expressions for these extreme cases.

2.5 Acknowledgements

GBP would like to thank Arthur Suits for an insightful discussion that led to the current work. This paper is based upon work supported by the U.S. Department of Energy, Office of Science, Chemical Sciences Geosciences and Biosciences Division of the Basic Energy Sciences Office, under Award Number DE-FG0287ER13671.

Chapter 3

Full Dimensional Franck-Condon Factors for the Acetylene $\tilde{\mathrm{A}}\ {}^1\mathrm{A_u}$—$\tilde{\mathrm{X}}\ {}^1\Sigma_g^+$ Transition. I. Method for Calculating Polyatomic Linear—Bent Vibrational Intensity Factors and Evaluation of Calculated Intensities for the *gerade* Vibrational Modes in Acetylene

Abstract

Franck-Condon vibrational overlap integrals for the $\tilde{\mathrm{A}}\ {}^1\mathrm{A}_u$—$\tilde{\mathrm{X}}\ {}^1\Sigma_g^+$ transition in acetylene have been calculated in full dimension in the harmonic normal mode basis. The calculation uses the method of generating functions first developed for polyatomic Franck-Condon factors by Sharp and Rosenstock [*J. Chem. Phys.* **41**(11), 3453–3463 (1964)], and previously applied to acetylene by Watson [*J. Mol. Spectrosc.* **207**(2), 276–284 (2001)] in a reduced-dimension calculation. Because the transition involves a

large change in the equilibrium geometry of the electronic states, two different types of corrections to the coordinate transformation are considered to first order: corrections for axis-switching between the Cartesian molecular frames and corrections for the curvilinear nature of the normal modes at large amplitude. The angular factor in the wavefunction for the out-of-plane component of the trans bending mode, ν_4'', is treated as a rotation, which results in an Eckart constraint on the polar coordinates of the bending modes. To simplify the calculation, the other degenerate bending mode, ν_5'', is integrated in the Cartesian basis and later transformed to the constrained polar coordinate basis, restoring the conventional v and l quantum numbers. An updated Ã-state harmonic force field obtained recently in the R. W. Field research group is evaluated. The results for transitions involving the *gerade* vibrational modes are in qualitative agreement with experiment. Calculated results for transitions involving *ungerade* modes are presented in Chapter 4.[a]

3.1 Introduction

The $\tilde{\mathrm{A}}\ {}^1\mathrm{A}_u(\mathrm{C}_{2\mathrm{h}})$—$\tilde{\mathrm{X}}\ {}^1\Sigma_g^+(\mathrm{D}_{\infty\mathrm{h}})$ transition in acetylene has been the subject of extensive spectroscopic and theoretical investigation. In the 1950s Ingold and King[59,60]—and later Innes[61]—performed the first detailed analysis of the band structure. They showed that a linear to trans-bent geometry change takes place upon excitation from the $\mathrm{D}_{\infty\mathrm{h}}$ ground state to the $\mathrm{C}_{2\mathrm{h}}$ excited state. Acetylene was the first molecular system in which a qualitative change in geometry and symmetry accompanying an electronic excitation was proven by spectroscopic methods. Since that time, both the $\tilde{\mathrm{X}}$ and $\tilde{\mathrm{A}}$ states of acetylene have been spectroscopically characterized in great detail.[62–95]

In spite of the wealth of data available, it has been challenging to make quantitative predictions for $\tilde{\mathrm{A}}$—$\tilde{\mathrm{X}}$ spectral intensities. Although the Franck-Condon principle has long guided the interpretation of vibrational intensity factors, the calculation of FC factors for polyatomic molecules remains challenging—especially in cases where there is a large change in equilibrium geometry and a qualitative change in symmetry between the states in question. The multidimensional nature of the polyatomic vibrational problem not only introduces interactions between the degrees of freedom

---

[a] This chapter is reprinted with permission from G. Barratt Park, *J. Chem. Phys.* **141**, 134304 (2014). Copyright 2014, AIP Publishing LLC.

on each potential energy surface, but it also complicates the transformation between the coordinates of the two states. So, in addition to the shift of origin and frequency scaling that are familiar from diatomic molecules, polyatomic molecules also exhibit Duschinsky rotation,[96] as a result of the non-diagonal (and in general nonlinear) transformation between the normal mode coordinates. Furthermore, for transitions involving a change from linear to bent reference configurations, there is an inherent interplay between vibrational and rotational degrees of freedom, because vibrational angular momentum of the linear state correlates with rotation in the bent state, and the number of vibrational degrees of freedom typically used to describe the linear and bent configurations is different.

Due to the importance of FC factors in polyatomic molecules, numerous approaches have been taken by various authors. Reference 97 provides a list of citations. There is no consensus on the best general formulation of the problem and most authors have tailored their methods to the molecular transition at hand. The most common approaches involve variations on the method introduced by Sharp and Rosenstock,[98] which involves direct integration of harmonic wavefunctions obtained by the method of generating functions.

Relatively little attention has been paid to the calculation of FC factors for systems involving linear to bent geometry changes. Smith and Warsop[99] pointed out the need for inclusion of rotational coordinates in linear to bent transitions, but they did not address the problem further. Kovner *et al.*[100] calculated Franck-Condon factors for the $^1\mathrm{B}_2 \to ^1\Sigma_g^+$ transition in CO_2 in full dimension. For the degenerate bending mode of the linear molecule, these authors use degenerate bending wavefuctions, which are separable into a radial factor (a generalized Laguerre polynomial that depends on v, l, and the radial coordinate ρ) and an angular factor (depending on l and the polar angle ϕ). They include the radial factor in the vibrational integral, but they treat the angular factor as part of the rotational integral, and they successfully calculate rovibrational intensity factors by approximating the bent state as a symmetric top. The research groups of Vaccaro, Iachello, and collaborators have successfully applied methods, based on Lie algebra formalisms,[101] to the bent-linear transition in HCP.[102]

After the pioneering works of Ingold, King, and Innes, several authors considered the one-dimensional Franck-Condon factors for the trans-bending progression of the acetylene $\tilde{\mathrm{A}}$—$\tilde{\mathrm{X}}$ transition.[60,99,103] More recently, Watson has calculated reduced-dimension Franck-Condon overlaps for the three *gerade* vibrational modes by extending the method of Sharp and Rosenstock[98] to treat a linear-to-bent transition, including axis-switching effects.[104] Watson's treatment of the vibrational and rotational degrees of freedom are analogous to those used by Kovner *et al.*,[100] but in the case of linear molecules with more than three atoms, more than one pair of degenerate modes contributes to out-of-plane vibration. In general, one of the vibrational degrees of freedom may be treated as a rotation, but factoring out this degree of freedom rotates the angular coordinate of each degenerate vibration. We will discuss this problem in detail in Section 3.2.4, and consequences for the full-dimensional Franck-Condon propensities will be discussed in Chapter 4. Weber and Hohlneicher[105] have calculated multi-dimensional Franck-Condon factors for the acetylene $\tilde{\mathrm{A}}$—$\tilde{\mathrm{X}}$ transition, but their calculation constrains the molecule to planarity, so they have not considered a number of the symmetry properties and propensity rules that we investigate here in our full-dimensional treatment. They have also rotated the linear molecule to the CC-axis of the trans-bent configurations, so their calculation is inconsistent with Watson's treatment of axis-switching effects.[104,106] To our knowledge, the work presented here is the first publication of a full-dimensional Franck-Condon calculation for a tetra-atomic molecule undergoing a linear-to-bent geometry change.

3.2 Methodology for the calculations

3.2.1 Vibrational Intensity Factors: Dependence of the electronic transition dipole moment on nuclear coordinates

In the Born-Oppenheimer approximation, the intensity factor S_{ev} accompanying a dipole-allowed vibronic transition is proportional to

$$S_{\mathrm{ev}} \propto \sum_{\alpha=a,b,c} \left|\langle \Psi'_{\mathrm{vib}} | \langle \Psi'_{\mathrm{el}} | \mu_\alpha | \Psi''_{\mathrm{el}} \rangle | \Psi''_{\mathrm{vib}} \rangle\right|^2 . \tag{3.1}$$

In Eq. (3.1), the rotational and spin contributions to the dipole transition moment are assumed to be separable and have been factored out of the integral. Ψ_{vib} and Ψ_{el} are the vibrational and electronic parts of wavefunction, and single and double primes are used to denote the upper and lower electronic state, respectively. The summation is over the a, b, and c molecular frame axis components of the dipole moment, $\boldsymbol{\mu}$. If we treat the electronic wavefunctions in the adiabatic Born-Oppenheimer basis, then the components of the integral over the electronic degrees of freedom may be written as

$$\langle \Psi'_{\mathrm{el}} | \mu_\alpha | \Psi''_{\mathrm{el}} \rangle = \int \mathrm{d}\mathbf{r}_{\mathrm{el}} \; \Psi'_{\mathrm{el}}(\mathbf{r}_{\mathrm{el}}, \mathbf{q}) \mu_\alpha \Psi''_{\mathrm{el}}(\mathbf{r}_{\mathrm{el}}, \mathbf{q}), \tag{3.2}$$

where $\mathbf{r}_{\mathrm{el}}$ represents the coordinates of the electrons and $\mathbf{q}$ represents the nuclear coordinates. It is important to note that the Born-Oppenheimer electronic wavefunctions $\Psi_{\mathrm{el}}(\mathbf{r}_{\mathrm{el}}, \mathbf{q})$ are functions of *both* the electronic *and* nuclear coordinates, because they are defined parametrically as functions of nuclear coordinates. Since the integral in (3.2) is performed only over the electronic degrees of freedom, but the integrand depends on both the electronic and nuclear degrees of freedom, the resulting electronic transition moment is a function of $\mathbf{q}$, and we may say that (3.2) is a "partial" integral rather than a complete overlap integral over all degrees of freedom. The electronic transition moment may be expanded in terms of the normal mode coordinates of one of the electronic states,

$$\langle\Psi'_{\text{el}}|\mu_\alpha|\Psi''_{\text{el}}\rangle = \mu_\alpha^{(0)}(\text{el}',\text{el}'') + \sum_k \mu_\alpha^{(k)}(\text{el}',\text{el}'')q_k + \frac{1}{2}\sum_{k,k'} \mu_\alpha^{(k,k')}(\text{el}',\text{el}'')q_k q_{k'} + \ldots\ , \quad (3.3)$$

where the subscript k labels the normal modes. In many cases, the integral in Eq. (3.1) accumulates over a limited range of nuclear geometries over which $\langle\Psi'_{\text{el}}|\mu_\alpha|\Psi''_{\text{el}}\rangle$ is approximately constant. In such a case, the contributions from higher-order terms in Eq. (3.3) are small compared to the contribution from $\mu_\alpha^{(0)}(\text{el}',\text{el}'')$ and may be ignored. The electronic transition dipole moment may then be separated from the vibrational part of the overlap integral in Eq. (3.1), and the intensity is proportional to the square of the familiar Franck-Condon overlap integral, multiplied by a constant electronic factor,

$$S_{\text{ev}} \propto \sum_\alpha |\mu_\alpha^{(0)}(\text{el}',\text{el}'')|^2 \, |\langle\Psi'_{\text{vib}}|\Psi''_{\text{vib}}\rangle|^2 \, . \quad (3.4)$$

Familiar symmetry arguments show that the integral in Eq. (3.2) has a non-zero leading term (i.e. the transition is "electronically allowed") if we set $\mathbf{q}$ to zero and see that $\Gamma(\Psi'_{\text{el}}) \otimes \Gamma(\Psi''_{\text{el}}) \supset \Gamma(\mu_\alpha)$.

In the case of acetylene, the Ã—X̃ transition is electronically allowed in the lower symmetry point group $\text{C}_{2\text{h}}$ common to both states, because $\Gamma(\Psi_{\tilde{\text{A}}}) \otimes \Gamma(\Psi_{\tilde{\text{X}}}) = \text{A}_u \otimes \text{A}_g$, which contains $\Gamma(\mu_c) = \text{A}_u$. However, the transition is electronically forbidden in the higher symmetry point group $\text{D}_{\infty\text{h}}$ of the ground electronic state, because the Ã $^1\text{A}_u$ state correlates with $^1\Sigma_u^-$ at the linear configuration and it does not have the correct symmetry to form a totally symmetric product with the X̃ $^1\Sigma_g^+$ state via any of the possible representations of the linear dipole moment operator (Π_u or Σ_u^+). Therefore, $\langle\Psi'_{\text{el}}|\boldsymbol{\mu}|\Psi''_{\text{el}}\rangle$ approaches zero at the linear configuration and its dependence on nuclear coordinates may *not* be ignored.

We may take the expansion in Eq. (3.3) about the linear X̃-state equilibrium geometry and employ the X̃-state normal mode coordinates, $\mathbf{q}''$. Since both sides of the equation must have the same symmetry, it is straightforward to determine which terms have the correct symmetry to be non-vanishing. The symmetry of the left hand side is (from Eq. (3.2))

$$\begin{aligned}\Gamma\left(\langle\Psi_{\tilde{\mathrm{A}}}|\mu_c|\Psi''_{\tilde{\mathrm{X}}}\rangle\right) &= \Gamma_{\mathrm{el}}(\tilde{\mathrm{A}})\otimes\Gamma(\mu_c)\otimes\Gamma_{\mathrm{el}}(\tilde{\mathrm{X}})\\ &= \Sigma_u^-\otimes\Pi_u\otimes\Sigma_g^+\\ &= \Pi_g. \end{aligned} \tag{3.5}$$

Since the trans-bending mode, ν''_4, is the only normal mode with π_g symmetry, $\mu_c^{(4'')}(\mathrm{el}',\mathrm{el}'')q''_4$ is the only first-order term in the expansion of the electric transition dipole moment about the linear geometry.

Higher-order terms in Eq. (3.3) with π_g symmetry may also contribute to the integral in Eq. (3.1), but *ab initio* calculations[107,108] have shown that over the range of geometries relevant to the Ã—X̃ transition, the electronic transition dipole moment is approximately linear in q''_4 and independent of displacement in other modes. The authors of Ref. 107 kindly shared the raw data from their reduced-dimension calculation, performed at the EOM-CCSD level of theory. The dependence of the electronic transition dipole moment on q''_2 and q''_4 obtained from the calculation is shown in Figure 3-1. From the reduced-dimension data, it was possible to estimate the dependence of $\langle\Psi_{\tilde{\mathrm{A}}}|\mu_c|\Psi_{\tilde{\mathrm{X}}}\rangle$ on the lowest-order terms in q''_2 and q''_4 (Table 3.1).

Table 3.1: Lowest-order contributions of q''_2 and q''_4 to the polynomial expansion of $\langle\Psi_{\tilde{\mathrm{A}}}|\mu_c|\Psi_{\tilde{\mathrm{X}}}\rangle = \sum_{n,m} c_{nm}(q''_2)^n(q''_4)^m$, obtained from a fit to the reduced-dimension calculation from Ref. 107, plotted in Figure 3-1. Second-order terms in q''_2 were omitted because their contribution was negligible. Values in parentheses represent 2 standard deviations in the uncertainty of the last digit of the fit parameter. The RMS error of the fit to the 256 grid points shown in Figure 3-1 was 0.0025 Debye.

n	m	c_{nm} (Debye)
0	1	0.0138(7)
1	1	−0.0026(2)
0	3	0.00109(7)
1	3	$8.3(6)\times 10^{-5}$

In the current work, we ignore higher-order vibrational corrections to the electronic transition dipole moment, and we assume that the vibrational intensity factors are

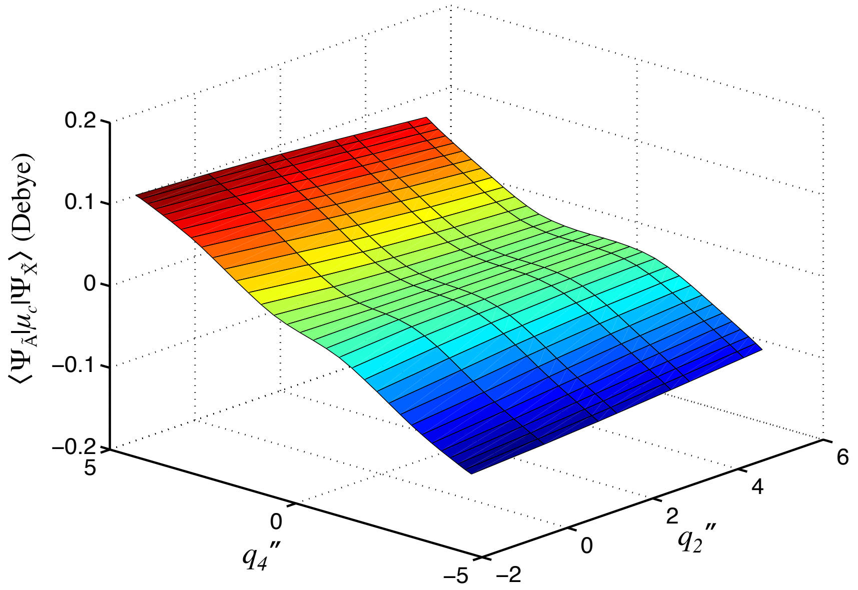

Figure 3-1: The value of $\langle \Psi_{\tilde{\mathrm{A}}} | \mu_c | \Psi_{\tilde{\mathrm{X}}} \rangle$ obtained from the reduced-dimension calculation in Ref. 107 is plotted as a function of q_2'' and q_4''. The normal mode coordinates shown are the dimensionless rectilinear coordinates described in Section 3.3. Because the reduced-dimension calculation held the CH bond length fixed to its equilibrium value in the $\tilde{\mathrm{A}}$ state, the projection of the data onto the q_2'' coordinate is an approximation that ignores the dependence of q_2'' on the CH bond length.

proportional to

$$S_{\mathrm{ev}} \propto \left| \langle \Psi'_{\mathrm{vib}} | q_4'' | \Psi''_{\mathrm{vib}} \rangle \right|^2 . \tag{3.6}$$

Watson has shown that including a factor of q_4'' in intensity calculations produces better agreement with experimental absorption data for the $\tilde{\mathrm{A}}(v_3') \leftarrow \tilde{\mathrm{X}}(0_0)$ progression. (See Table 1 of Ref. 104.)

3.2.2 Nuclear-coordinate dependence of the electronic transition dipole moment in the diabatic picture

It was pointed out to the author by Dr. Josh Baraban that there is an alternative way to describe the dependence of the electronic transition dipole moment on nuclear coordinates using electronic wavefunctions in the diabatic basis. Because the diabatic formulation provides additional insight into the origins of the transition strength, it is presented here briefly. Let Φ_{el} represent a diabatic electronic wavefunction with $\mathrm{D}_{\infty\mathrm{h}}$ symmetry. Φ_{el} has no explicit dependence on nuclear coordinates, but there may be vibronic interactions that couple electronic states of different symmetry. The $\tilde{\mathrm{X}}$ (Σ_g^+) state may have electronically allowed dipole transitions to states of Σ_u^+ or Π_u symmetry. There are no vibrational modes with the correct symmetry to allow a first-order vibronic interaction between the $\tilde{\mathrm{A}}$ (Σ_u^-) state and higher-lying Σ_u^+ states, but interactions between the $\tilde{\mathrm{A}}$ state and higher-lying Π_u states (such as the $\tilde{\mathrm{C}}$ state) may be vibronically mediated by the q_4'' (π_g) vibration. If we assume such an interaction takes place via a matrix element, $H_{12} \propto q_4'' + ...$, (the ellipsis indicates higher-order vibrational terms with π_g symmetry that we will ignore), then we may write

$$|\Psi_{\tilde{\mathrm{A}}}\rangle = a|\Phi(\Sigma_u^-)\rangle + bq_4''|\Phi(\Pi_u)\rangle, \tag{3.7}$$

where the a and b mixing coefficients are obtained from diagonalization of the vibronic interaction matrix, and the b coefficient also contains the proportionality of H_{12} to q_4''. The integral in Eq. 3.1 may then be written as

$$\begin{aligned} S_{\mathrm{ev}} &= \left|\langle\Psi'_{\mathrm{vib}}|\left(a^*\langle\Phi(\Sigma_u^-)| + b^*q_4''\langle\Phi(\Pi_u)|\right)\mu_c|\Phi_{\tilde{\mathrm{X}}}\rangle|\Psi''_{\mathrm{vib}}\rangle\right|^2 \\ &= b^2\left|\langle\Phi(\Pi_u)|\mu_c|\Phi_{\tilde{\mathrm{X}}}\rangle\right|^2\left|\langle\Psi'_{\mathrm{vib}}|q_4''|\Psi''_{\mathrm{vib}}\rangle\right|^2. \end{aligned} \tag{3.8}$$

Because the diabatic wavefunctions do not depend explicitly on nuclear coordinates, the electronic and vibrational parts of the integral are separable and the first term in the electronic integral vanishes by symmetry. The vibrational q_4'' term that mediates the vibronic transition is treated in the vibrational integral and we obtain the same result as in Eq. (3.6).

When viewed in the diabatic picture, it becomes clear that the vibronic mechanism by which the $\tilde{\mathrm{A}}$—$\tilde{\mathrm{X}}$ becomes electronically allowed is the *same* mechanism that causes the vibronic distortion of the $\tilde{\mathrm{A}}$-state equilibrium along the π_g trans-bend coordinate. The dependence of $\langle\Psi_{\tilde{\mathrm{A}}}|\mu_c|\Psi_{\tilde{\mathrm{X}}}\rangle$ on nuclear coordinates can be directly related to the vibronic distortion of the $\tilde{\mathrm{A}}$-state equilibrium because both effects arise from the same matrix element, H_{12}. In the literature, dependence of electronic transition strength on nuclear coordinates (Herzberg-Teller coupling) is often attributed to two seemingly different phenomena: (1) $\mathbf{q}$-dependence of the electronic transition dipole moment between the upper and lower electronic states, or (2) intensity borrowing from vibronic interactions. As illustrated by the above example, these two explanations are in fact equivalent descriptions of the same phenomenon, viewed in the basis of (1) adiabatic electronic wavefunctions, or (2) diabatic electronic wavefunctions.

3.2.3 Coordinate transformation

Because the normal mode coordinates in the ground and excited states ($\mathbf{q}''$ and $\mathbf{q}'$) are defined differently, $\Psi''_{\text{vib}}(\mathbf{q}'')$ and $\Psi'_{\text{vib}}(\mathbf{q}')$ are usually given as functions of different sets of variables. In order to evaluate (3.6) as an overlap integral, a coordinate transformation must be performed to convert the excited-state normal coordinates $\mathbf{q}'$ into ground state coordinates $\mathbf{q}''$. Because the $\tilde{\text{A}}$—$\tilde{\text{X}}$ transition in acetylene involves a large change in equilibrium geometry between the two electronic states, there are nonlinear contributions to the coordinate transformation. We will consider two different types of corrections. First, we will examine the effects of axis switching between the Cartesian molecular frames of the two states. Next, we examine effects that arise from the curvilinear nature of the normal modes. Either of these corrections might be expected to become important at large displacement along bending coordinates.

Axis-switching effects

In the case of acetylene, axis-switching effects[106] accompany the $\tilde{\text{A}}$—$\tilde{\text{X}}$ transition because the trans↔linear geometry change rotates the orientation of the principal axes about the *c*-axis, and rotation about the *c*-axis is totally symmetric in the $\text{C}_{2\text{h}}$ point group. Axis-switching effects are most familiar in cases where they give intensity to nominally forbidden rovibronic transitions. For example, axis switching in the $\tilde{\text{A}}$—$\tilde{\text{X}}$ transition of acetylene gives rise to nominally-forbidden *a*-type transitions.[109] However, because axis switching enters into the coordinate transformation, it also plays a role in vibrational intensity factors and its effects should be considered.[110]

In deriving the coordinate transformation appropriate to the acetylene $\tilde{\mathrm{A}}$—$\tilde{\mathrm{X}}$ transition, Watson includes the effects of axis switching through linear terms in $\mathbf{q}''$.[104] However, Watson's discussion is terse. Therefore, we include some detail about the effects of axis switching on the transformation. In general, the molecular coordinates obeying one set of Eckart conditions may be written in terms of another according to

$$\begin{aligned} \mathbf{r}'_{\mathbf{e}} + \boldsymbol{\rho}' &= \boldsymbol{\Lambda}(\mathbf{r}''_{\mathbf{e}} + \boldsymbol{\rho}'') \\ \boldsymbol{\rho}' &= \boldsymbol{\Lambda}\mathbf{r}''_{\mathbf{e}} - \mathbf{r}'_{\mathbf{e}} + \boldsymbol{\Lambda}\boldsymbol{\rho}'', \end{aligned} \tag{3.9}$$

where $\mathbf{r}_{\mathbf{e}}$ and $\boldsymbol{\rho}$ are length $3N$ vectors that give the equilibrium position of each nucleus and the displacement of each nucleus from equilibrium, respectively, expressed in the Cartesian principal axis system that satisfies the Eckart conditions for each respective electronic state. Single- and double-primes are used to label the upper and lower electronic states, respectively. The Eckart rotation matrix or "axis-switching" matrix $\boldsymbol{\Lambda}$ in Eq. (3.9) rotates the principal axis system that obeys the lower state Eckart conditions onto the axis system that obeys the upper state Eckart conditions. The Eckart conditions are satisfied by

$$\mathbf{Q}_{\mathbf{T}} \equiv \tilde{\mathbf{l}}_{\mathbf{T}}\mathbf{m}^{1/2}\boldsymbol{\rho} = M^{-1/2}\sum_i m_i\boldsymbol{\rho}_i = \mathbf{0} \tag{3.10}$$

$$\mathbf{Q}_{\mathbf{R}} \equiv \tilde{\mathbf{l}}_{\mathbf{R}}\mathbf{m}^{1/2}\boldsymbol{\rho} = \mathbf{I}^{-1/2}\sum_i m_i(\mathbf{r}_{\mathbf{e},i} \times \boldsymbol{\rho}_i) = \mathbf{0}, \tag{3.11}$$

where the subscript i labels the nuclei, $M = \sum_i m_i$ is the total mass, and $\mathbf{I}$ is the diagonal moment of inertia tensor for the principal axes. The $3N \times 3N$ diagonal matrix $\mathbf{m}$ weights the Cartesian coordinates by the nuclear masses, and $\tilde{\mathbf{l}}_{\mathbf{R}}$ and $\tilde{\mathbf{l}}_{\mathbf{T}}$ represent the linearized transformations from mass-weighted Cartesian displacements to rotational and translational coordinates, respectively. Throughout this chapter, we will use the tilde to denote matrix transposition. The translation of the center of mass may be rigorously separated from other degrees of freedom by condition (3.10), but the separation of rotational and vibrational coordinates provided by condition (3.11) is only approximate. Furthermore, because the Eckart conditions (3.10–3.11) that determine the principal axes are a function of the instantaneous geometry, $\mathbf{\Lambda}$ depends on $\mathbf{q}''$ and Eq. (3.9) is—in general—a nonlinear transformation.

We may write the transformation (3.9) in terms of vibrational normal mode coordinates using the standard coordinate transformations defined in Ref. 111,

$$\mathbf{Q} = \mathbf{L}_0^{-1}\mathbf{B_e}\boldsymbol{\rho}. \tag{3.12}$$

Here, $\mathbf{B_e} = (\partial\mathbf{S}/\partial\boldsymbol{\rho})|_{\boldsymbol{\rho}=\mathbf{0}}$ transforms Cartesian displacements to "linearized" internal coordinates, $\mathbf{S}$, and $\mathbf{L}_0^{-1}$ transforms the $\mathbf{S}$ coordinates to normal mode coordinates of dimension $\sqrt{\text{mass}} \cdot$ distance. Because the $\mathbf{B_e}$ matrix is defined in terms of infinitesimal curvilinear displacements from a reference equilibrium geometry, $\mathbf{Q}$ is a linear combination of Cartesian displacements for each nucleus. In this paper, we use scaled dimensionless normal mode vibrational coordinates $\mathbf{q}$ defined according to

$$\mathbf{q} = \boldsymbol{\gamma}^{1/2}\mathbf{Q}, \tag{3.13}$$

where $\boldsymbol{\gamma}$ is a diagonal scaling matrix with elements $\gamma_k = hc\omega_k/\hbar^2$. ($\omega_k$ is the harmonic frequency of the kth normal mode.) We insert (3.12) to obtain

$$\begin{aligned} \mathbf{q} &= \boldsymbol{\gamma}^{1/2}\mathbf{L}_0^{-1}\mathbf{B_e}\boldsymbol{\rho} \\ &= \boldsymbol{\gamma}^{1/2}\tilde{\mathbf{l}}\mathbf{m}^{1/2}\boldsymbol{\rho}. \end{aligned} \tag{3.14}$$

We have introduced the substitution $\mathbf{l} = \mathbf{m}^{-1/2}\tilde{\mathbf{B}}_{\mathbf{e}}\tilde{\mathbf{L}}_{\mathbf{0}}^{\mathbf{-1}}$. $\tilde{\mathbf{l}}$ is the $3N \times n_{\text{vib}}$ matrix that transforms mass-weighted Cartesian coordinates to normal mode vibrational coordinates, and n_{vib} is the number of vibrational degrees of freedom being considered.

The $3N \times 3N$ matrix that transforms Cartesian coordinates to the $3N$-dimensional vector of normal vibrational, rotational, and translational coordinates according to

$$\begin{bmatrix} \mathbf{Q} \\ \mathbf{Q_R} \\ \mathbf{Q_T} \end{bmatrix} = \begin{bmatrix} \tilde{\mathbf{l}} \\ \tilde{\mathbf{l}}_{\mathbf{R}} \\ \tilde{\mathbf{l}}_{\mathbf{T}} \end{bmatrix} \mathbf{m}^{1/2}\boldsymbol{\rho} \tag{3.15}$$

is a unitary transformation,[111] so

$$\begin{bmatrix} \mathbf{l} & \mathbf{l_R} & \mathbf{l_T} \end{bmatrix} \begin{bmatrix} \mathbf{Q} \\ \mathbf{Q_R} \\ \mathbf{Q_T} \end{bmatrix} = \mathbf{m}^{1/2}\boldsymbol{\rho}. \tag{3.16}$$

We may now write the coordinate transformation (3.9) in terms of normal coordinates by substituting (3.15) and (3.16) for $\boldsymbol{\rho'}$ and $\boldsymbol{\rho''}$ to obtain

$$\begin{bmatrix} \mathbf{Q}' \\ \mathbf{Q}'_\mathbf{R} \\ \mathbf{Q}'_\mathbf{T} \end{bmatrix} = \begin{bmatrix} \tilde{\mathbf{l}}' \\ \tilde{\mathbf{l}}'_\mathbf{R} \\ \tilde{\mathbf{l}}'_\mathbf{T} \end{bmatrix} \mathbf{m}^{1/2}(\boldsymbol{\Lambda}\mathbf{r}''_\mathbf{e} - \mathbf{r}'_\mathbf{e}) + \begin{bmatrix} \tilde{\mathbf{l}}'\boldsymbol{\Lambda}\mathbf{l}'' & \tilde{\mathbf{l}}'\boldsymbol{\Lambda}\mathbf{l}''_\mathbf{R} & \tilde{\mathbf{l}}'\boldsymbol{\Lambda}\mathbf{l}''_\mathbf{T} \\ \tilde{\mathbf{l}}'_\mathbf{R}\boldsymbol{\Lambda}\mathbf{l}'' & \tilde{\mathbf{l}}'_\mathbf{R}\boldsymbol{\Lambda}\mathbf{l}''_\mathbf{R} & \tilde{\mathbf{l}}'_\mathbf{R}\boldsymbol{\Lambda}\mathbf{l}''_\mathbf{T} \\ \tilde{\mathbf{l}}'_\mathbf{T}\boldsymbol{\Lambda}\mathbf{l}'' & \tilde{\mathbf{l}}'_\mathbf{T}\boldsymbol{\Lambda}\mathbf{l}''_\mathbf{R} & \tilde{\mathbf{l}}'_\mathbf{T}\boldsymbol{\Lambda}\mathbf{l}''_\mathbf{T} \end{bmatrix} \begin{bmatrix} \mathbf{Q}'' \\ \mathbf{Q}''_\mathbf{R} \\ \mathbf{Q}''_\mathbf{T} \end{bmatrix}. \tag{3.17}$$

We enforce the Eckart conditions by setting $\mathbf{Q_R} = \mathbf{Q_T} = \mathbf{0}$ for both states to obtain the set of equations

$$\mathbf{q}' = (\boldsymbol{\gamma}')^{1/2}\ \tilde{\mathbf{l}}'[\boldsymbol{\Lambda}\mathbf{m}^{1/2}\mathbf{r}''_\mathbf{e} - \mathbf{m}^{1/2}\mathbf{r}'_\mathbf{e}] + (\boldsymbol{\gamma}')^{1/2}\ \tilde{\mathbf{l}}'\boldsymbol{\Lambda}\mathbf{l}''(\boldsymbol{\gamma}'')^{-1/2}\mathbf{q}'' \tag{3.18}$$

$$\tilde{\mathbf{l}}'_\mathbf{R}\boldsymbol{\Lambda}\left[\mathbf{m}^{1/2}\mathbf{r}''_\mathbf{e} + \mathbf{l}''(\boldsymbol{\gamma}'')^{1/2}\mathbf{q}''\right] = \mathbf{0}. \tag{3.19}$$

We have used the fact that $\tilde{\mathbf{l}}'_\mathbf{R}\mathbf{m}^{\mathbf{1/2}}\mathbf{r}'_\mathbf{e} = \mathbf{0}$ because the equilibrium geometry satisfies the Eckart condition (3.11). Equation (3.18) is the desired (nonlinear) coordinate transformation. The first term in Eq. (3.18) accounts for the difference in equilibrium geometry of the upper and lower states and the second term accounts for displacement of molecular geometry away from the lower state equilibrium. Equation (3.19) enforces the rotational Eckart condition (3.11) for each state. Equation (3.19) may be used to define $\boldsymbol{\Lambda}$ as a function of $\mathbf{q}''$. We have omitted the equation for the translational Eckart condition, obtained from the third row of Eq. (3.17). It is trivially zero since condition (3.10) ensures that the origin of the principal axis system for each state is at the center of mass.

In order to expand the transformation (3.18) to first-order in $\mathbf{q}''$ we define

$$\boldsymbol{\Lambda} = \boldsymbol{\Lambda}_\mathbf{e}(\mathbf{E} + \boldsymbol{\Lambda}_\mathbf{1}(\mathbf{q}'')), \tag{3.20}$$

where $\mathbf{E}$ is the unit matrix. $\boldsymbol{\Lambda}_\mathbf{e}$ is the axis-switching matrix that satisfies (3.19) at the lower state equilibrium and the dependence of the axis rotation on $\mathbf{q}''$ is contained in $\boldsymbol{\Lambda}_\mathbf{1}$. For small displacements, we may use the infinitesimal rotation matrix,

$$\boldsymbol{\Lambda}_\mathbf{1} \approx \begin{bmatrix} 0 & \mathrm{d}\Omega_c & -\mathrm{d}\Omega_b \\ -\mathrm{d}\Omega_c & 0 & \mathrm{d}\Omega_a \\ \mathrm{d}\Omega_b & -\mathrm{d}\Omega_a & 0 \end{bmatrix}. \tag{3.21}$$

Note that the effect of $\boldsymbol{\Lambda}_\mathbf{1}$ operating on a vector $\mathbf{r}$ may be written as a cross product

$$\boldsymbol{\Lambda}_\mathbf{1}\mathbf{r} = \mathbf{r} \times \mathbf{d}\vec{\Omega}, \tag{3.22}$$

where $\mathbf{d}\vec{\Omega}$ is the vector $\langle \mathrm{d}\Omega_a\ \mathrm{d}\Omega_b\ \mathrm{d}\Omega_c \rangle$. Thus by the definition in (3.11), the rotation of the equilibrium Cartesian coordinates $\boldsymbol{\Lambda}_\mathbf{1}\mathbf{m}^{1/2}\mathbf{r}_\mathbf{e}$ is related to the rotation matrix $\tilde{\mathbf{l}}_\mathbf{R}$ by

$$\begin{aligned} \boldsymbol{\Lambda}_\mathbf{1}\mathbf{m}^{1/2}\mathbf{r}_\mathbf{e} &= \mathbf{m}^{1/2}\mathbf{r}_\mathbf{e} \times \mathbf{d}\vec{\Omega} \\ &= \mathbf{I}_\mathbf{e}{}^{1/2}\mathbf{l}_\mathbf{R}\mathbf{d}\vec{\Omega}, \end{aligned} \tag{3.23}$$

where $\mathbf{I}_\mathbf{e}$ denotes the moment of inertia tensor at the equilibrium configuration. We now substitute Eqs. (3.20), (3.22), and (3.23) into the Eckart condition (3.19) for the transformation and solve for $\mathbf{d}\vec{\Omega}$, noting that $\tilde{\mathbf{l}}'_\mathbf{R}\boldsymbol{\Lambda}_\mathbf{e}\mathbf{m}^{1/2}\mathbf{r}''_\mathbf{e} = \mathbf{0}$, because the $\boldsymbol{\Lambda}_\mathbf{e}$ rotation satisfies the upper state Eckart conditions for $\mathbf{q}'' = \mathbf{0}$.

$$\mathbf{d}\vec{\Omega} = -\left[\tilde{\mathbf{l}}'_\mathbf{R}\boldsymbol{\Lambda}_\mathbf{e}(\mathbf{I}_\mathbf{e}'')^{1/2}\mathbf{l}_\mathbf{R}''\right]^{-1}\left[\tilde{\mathbf{l}}'_\mathbf{R}\boldsymbol{\Lambda}_\mathbf{e}\mathbf{l}''(\boldsymbol{\gamma}'')^{1/2}\mathbf{q}'' + \tilde{\mathbf{l}}'_\mathbf{R}\boldsymbol{\Lambda}_\mathbf{e}\boldsymbol{\Lambda}_\mathbf{1}\mathbf{l}''(\boldsymbol{\gamma}'')^{1/2}\mathbf{q}''\right]. \tag{3.24}$$

The second term in (3.24) is $O[(\mathbf{q}'')^2]$ and may be ignored in the first-order expansion.

We now substitute (3.20) and (3.24) into the coordinate transformation (3.18), and use the relation (3.23) to obtain (noting that the factors of $(\mathbf{I}''_\mathbf{e})^{1/2}$ cancel)

$$\mathbf{q}' = \boldsymbol{\delta}^{(\text{a-s})} + \mathbf{D}^{(\text{a-s})}\mathbf{q}'' + O[(\mathbf{q}'')^2], \tag{3.25}$$

$$\boldsymbol{\delta}^{(\text{a-s})} = (\boldsymbol{\gamma}')^{1/2}\left[\tilde{\mathbf{l}}'\boldsymbol{\Lambda}_{\mathbf{e}}\mathbf{m}^{1/2}\mathbf{r}''_{\mathbf{e}} - \tilde{\mathbf{l}}'\mathbf{m}^{1/2}\mathbf{r}'_{\mathbf{e}}\right] \tag{3.26}$$

$$\mathbf{D}^{(\text{a-s})} = (\boldsymbol{\gamma}')^{1/2}\left[\tilde{\mathbf{l}}'\boldsymbol{\Lambda}_{\mathbf{e}}\mathbf{l}'' - \tilde{\mathbf{l}}'\boldsymbol{\Lambda}_{\mathbf{e}}\mathbf{l}''_{\mathbf{R}}(\tilde{\mathbf{l}}'_{\mathbf{R}}\boldsymbol{\Lambda}_{\mathbf{e}}\mathbf{l}''_{\mathbf{R}})^{-1}\tilde{\mathbf{l}}'_{\mathbf{R}}\boldsymbol{\Lambda}_{\mathbf{e}}\mathbf{l}''\right](\boldsymbol{\gamma}'')^{-1/2} \tag{3.27}$$

$$O[(\mathbf{q}'')^2] \approx (\boldsymbol{\gamma}')^{1/2}\tilde{\mathbf{l}}'\boldsymbol{\Lambda}_{\mathbf{e}}\left[\mathbf{E} + \mathbf{l}''_{\mathbf{R}}(\tilde{\mathbf{l}}'_{\mathbf{R}}\boldsymbol{\Lambda}_{\mathbf{e}}\mathbf{l}''_{\mathbf{R}})^{-1}\tilde{\mathbf{l}}'_{\mathbf{R}}\boldsymbol{\Lambda}_{\mathbf{e}}\right]\boldsymbol{\Lambda}_{\mathbf{1}}\mathbf{l}''(\boldsymbol{\gamma}'')^{-1/2}\mathbf{q}''. \tag{3.28}$$

The $\boldsymbol{\delta}^{(\text{a-s})}$ vector gives the upper state normal mode coordinates at the equilibrium geometry of the lower state (the shift of origin), and may have nonzero elements for totally symmetric normal modes in the point group common to both states. The $\mathbf{D}^{(\text{a-s})}$ matrix describes (to first order) the transformation of lower state normal mode coordinates to upper state normal mode coordinates. It is block-diagonal with respect to the symmetries of the normal modes. Off-diagonal elements allow "Duschinski rotation" between normal modes of the same symmetry.[96] The "(a-s)" superscript denotes that the transformation takes into account first-order corrections for axis-switching. The first term in (3.27) gives the zero-order projection of the ground-state normal modes onto the basis of the excited-state normal modes after rotating the equilibrium ground-state principal axes into the excited-state Eckart frame. The second term is a first-order correction term for the dependence of the Eckart conditions on the instantaneous geometry. Equations (3.25–3.27) are equivalent to Eqs. 8–10 of Ref. 104. Higher order corrections to the transformation arising from the terms in (3.28) are considered by Özkan,[110] but will be ignored in the present work.

Curvilinear effects

The normal mode coordinates $\mathbf{Q}$, defined by Eq. (3.12), are rectilinear in the sense that displacement along any given mode (all other normal mode displacements held constant), results in straight-line motion of each nucleus in the molecular coordinate frame. This is because each normal mode is defined as a linear combination of "linearized" internal coordinates, $\mathbf{S}$. A classic paper by Hoy, Mills, and Strey[112] describes the transformation to the true curvilinear internal coordinates (which we will denote $\bar{\mathbf{S}}$), defined in terms of the bond lengths and angles. As shown in Figure 3-2, the rectilinear bending coordinate $S_{\angle \mathrm{H_1C_1C_2}}$ stretches the C—H bond at large displacements from the linear equilibrium.

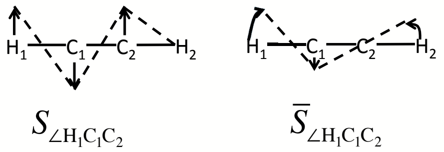

Figure 3-2: The rectilinear internal coordinate $S_{\angle \mathrm{H_1C_1C_2}}$ stretches the bond lengths in acetylene, while the curvilinear internal coordinate $\bar{S}_{\angle \mathrm{H_1C_1C_2}}$ changes only the HCC bond angle while other bond angles and lengths remain constant.

In many cases, it is useful to work with rectilinear normal coordinates because they provide a convenient simplification of the kinetic energy operator,

$$\begin{aligned} T_{\mathrm{kin}} &= \frac{1}{2}\frac{\mathrm{d}\tilde{\mathbf{S}}}{\mathrm{d}t}\left(\tilde{\mathbf{B}}_{\mathbf{e}}^{-\mathbf{1}}\mathbf{m}\mathbf{B}_{\mathbf{e}}^{-\mathbf{1}}\right)\frac{\mathrm{d}\mathbf{S}}{\mathrm{d}t} \\ &= \frac{1}{2}\frac{\mathrm{d}\tilde{\mathbf{Q}}}{\mathrm{d}t}\frac{\mathrm{d}\mathbf{Q}}{\mathrm{d}t}. \end{aligned}$$

As we will see below, curvilinear coordinates *do not* afford the same simplification and their use comes at the price of higher-order terms in the kinetic energy operator. Nevertheless, for problems involving large amplitude bending motion, it is sometimes simpler to work in the basis of curvilinear normal modes. For example, Borrelli and Peluso[113,114] have shown that the use of curvilinear coordinates has a profound simplifying effect on the coordinate transformation for the $V \leftarrow N$ transition in ethylene, which involves a 90° twist along the torsional coordinate. The reason for this simplification is that curvilinear coordinates reduce cross-anharmonicities introduced between stretching and bending coordinates, as illustrated in Figure 3-2.

The potential energy may be expanded in either coordinate system,

$$V = \frac{1}{2}\sum_{ij} f^{ij} S_i S_j + \frac{1}{6}\sum_{ijk} f^{ijk} S_i S_j S_k + \frac{1}{24}\sum_{ijkl} f^{ijkl} S_i S_j S_k S_l ... \tag{3.29}$$

$$= \frac{1}{2}\sum_{ij} \phi^{ij} \bar{S}_i \bar{S}_j + \frac{1}{6}\sum_{ijk} \phi^{ijk} \bar{S}_i \bar{S}_j \bar{S}_k + \frac{1}{24}\sum_{ijkl} \phi^{ijkl} \bar{S}_i \bar{S}_j \bar{S}_k \bar{S}_l .... \tag{3.30}$$

In general, the coefficients in the two expansions are different. However, because the leading quadratic terms that determine the harmonic force field depend only on infinitesimal displacements, for which $\mathbf{S}$ and $\bar{\mathbf{S}}$ are identical, $\phi^{ij} = f^{ij}$, and we see that in the harmonic limit the the coordinate systems are interchangeable and the distinction is moot. However, at large displacements from equilibrium, curvilinear coordinates often provide a simpler description of the potential energy because the potential energy surface of most molecules tends to be steepest along directions that stretch or contract the bond lengths. As a result the force field naturally tends to send nuclei along curved bending trajectories, and the curvilinear cross-anharmonicities $\phi^{ijk\ldots}$ may be much smaller in magnitude than $f^{ijk\ldots}$.

Several authors have discussed approximate methods for using curvilinear coordinates in the Franck-Condon coordinate transformation.[115–117] The transformation from curvilinear $\bar{\mathbf{S}}$ to rectilinear $\mathbf{Q}$ is nonlinear.

$$\bar{S}_i = L_i^r Q_r + \frac{1}{2} L_i^{rs} Q_r Q_s + \frac{1}{6} L_i^{rst} Q_r Q_s Q_t + \ldots, \tag{3.31}$$

where $L_i^r = (\partial \bar{S}_i / \partial Q_r)|_{\bar{S}=0}$ are elements of the $\mathbf{L_0}$ matrix defined in section 3.2.3, and higher-order components of the $\mathbf{L}$ tensor define the nonlinear transformation. We may define curvilinear normal coordinates, $\bar{\mathbf{Q}}$, by truncating the expansion in (3.31),

$$\bar{S}_i = L_i^r \bar{Q}_r, \quad \text{or} \qquad \bar{\mathbf{Q}} \equiv \mathbf{L}_0^{-1} \bar{\mathbf{S}}. \tag{3.32}$$

As shown by Capobianco and co-workers,[116] the quantum vibrational Hamiltonian may then be written as

$$\hat{H} = \hat{H}_0^{\text{(c-l)}} + \Delta T_{\text{kin}} + V_{\text{kin}}(\bar{\mathbf{Q}}) + \Delta V(\bar{\mathbf{Q}}), \tag{3.33}$$

where $\hat{H}_0^{\text{(c-l)}}$ is the harmonic Hamiltonian written in curvilinear normal coordinates,

$$\hat{H}_0^{\text{(c-l)}} = -\frac{\hbar^2}{2} \sum_r \frac{\partial^2}{\partial \bar{Q}_r^2} + \frac{1}{2} \sum_r \omega_r^2 \bar{Q}_r^2, \tag{3.34}$$

and the remaining terms are

$$\Delta T_{\text{kin}} = \frac{\hbar}{2}\sum_{jk}\frac{\partial^2}{\partial\bar{Q}_j\partial\bar{Q}_k} - \frac{\hbar^2}{2}\sum_{jk}\frac{\partial}{\partial\bar{Q}_j}g_{jk}(\bar{\mathbf{Q}})\frac{\partial}{\partial\bar{Q}_k} \tag{3.35}$$

$$V_{\text{kin}}(\bar{\mathbf{Q}}) = \frac{5\hbar}{32g^2}\sum_{jk}g_{jk}\frac{\partial g}{\partial\bar{Q}_j}\frac{\partial g}{\partial\bar{Q}_k} - \frac{\hbar^2}{8g}\sum_{jk}\frac{\partial g_{jk}}{\partial\bar{Q}_j}\frac{\partial g}{\partial\bar{Q}_k} - \frac{\hbar^2}{8g}\sum_{jk}g_{jk}\frac{\partial^2 g}{\partial\bar{Q}_j\partial\bar{Q}_k}, \tag{3.36}$$

and $\Delta V(\bar{\mathbf{Q}})$ collects the anharmonic potential energy terms. $g_{jk}(\bar{\mathbf{Q}})$ and g are the matrix elements and the determinant, respectively, of

$$\mathbf{g} = \mathbf{L}_0^{-1}\mathbf{B}(\bar{\mathbf{Q}})\mathbf{m}^{-\mathbf{1}}\tilde{\mathbf{B}}(\bar{\mathbf{Q}})\tilde{\mathbf{L}}_0^{-1}. \tag{3.37}$$

In (3.37), $\mathbf{B}(\bar{\mathbf{Q}})$ is the transformation $\mathbf{B}(\bar{\mathbf{Q}}) = (\partial\bar{\mathbf{S}}/\partial\boldsymbol{\rho})$, which depends on the instantaneous vibrational coordinates. The zero order expansion of $g_{jk}(\bar{\mathbf{Q}})$ in the second term of (3.35) is unity and cancels the first term, so that the leading term of ΔT_{kin} is third-order in the position and momentum operators.

In the basis set of the eigenfunctions of $\hat{H}_0^{(\text{c-l})}$, the coordinate transformation between $\bar{\mathbf{q}}'' = (\boldsymbol{\gamma}'')^{1/2}\bar{\mathbf{Q}}''$ and $\bar{\mathbf{q}}' = (\boldsymbol{\gamma}')^{1/2}\bar{\mathbf{Q}}'$ is given by

$$\bar{\mathbf{q}}' = \mathbf{D}^{(\text{c-l})}\bar{\mathbf{q}}'' + \boldsymbol{\delta}^{(\text{c-l})} \tag{3.38}$$

$$\mathbf{D}^{(\text{c-l})} = (\boldsymbol{\gamma}')^{1/2}(\mathbf{L}_0')^{-1}(\mathbf{L}_0'')(\boldsymbol{\gamma}'')^{-1/2} \tag{3.39}$$

$$\boldsymbol{\delta}^{(\text{c-l})} = (\boldsymbol{\gamma}')^{1/2}(\mathbf{L}_0')^{-1}(\boldsymbol{\zeta}_{\boldsymbol{e}}'' - \boldsymbol{\zeta}_{\boldsymbol{e}}'), \tag{3.40}$$

where $\boldsymbol{\zeta}_{\boldsymbol{e}}'$ and $\boldsymbol{\zeta}_{\boldsymbol{e}}''$ are the equilibrium values of the internal coordinates in the upper and lower state, respectively, about which the displacements $\bar{\mathbf{S}} = \boldsymbol{\zeta} - \boldsymbol{\zeta}_{\boldsymbol{e}}$ are defined, and the superscript (c-l) indicates that the transformation is performed in the basis of curvilinear harmonic oscillators. A transformation is given conveniently in terms of the Cartesian $\mathbf{l}$ matrices by Reimers,[115]

$$\boldsymbol{\delta}^{(\text{c-l})} = (\boldsymbol{\gamma}')^{1/2}\tilde{\mathbf{l}}'\mathbf{m}^{-1/2}\tilde{\mathbf{B}}_{\mathbf{0}}'(\mathbf{B}_{\mathbf{0}}'\mathbf{m}^{-\mathbf{1}}\tilde{\mathbf{B}}_{\mathbf{0}}')^{-1} \tag{3.41}$$

$$\mathbf{D}^{(\text{c-l})} = (\boldsymbol{\gamma}')^{1/2}\tilde{\mathbf{l}}'\mathbf{m}^{-1/2}\tilde{\mathbf{B}}_{\mathbf{0}}'(\mathbf{B}_{\mathbf{0}}'\mathbf{m}^{-\mathbf{1}}\tilde{\mathbf{B}}_{\mathbf{0}}')^{-1/2}(\mathbf{B}_{\mathbf{0}}''\mathbf{m}^{-\mathbf{1}}\tilde{\mathbf{B}}_{\mathbf{0}}'')^{-1/2}\tilde{\mathbf{B}}_{\mathbf{0}}''\mathbf{m}^{-1/2}\mathbf{l}''(\boldsymbol{\gamma}'')^{-1/2} \tag{3.42}$$

Both of the transformations that we have presented—(3.25–3.28) and (3.38–3.42)—are analogous to Eq. 10 of Sharp and Rosenstock,[98] in the limit of small displacements. If the displacement in equilibrium geometry between the two electronic states is small then $\mathbf{\Lambda} \approx \mathbf{E}$, and axis switching effects do not enter into the coordinate transformation. Similarly, if only small displacements along the normal mode coordinates are considered, then the curvilinear $\bar{\mathbf{q}}$ are equivalent to the rectilinear $\mathbf{q}$ and $\tilde{\mathbf{l}}'\mathbf{l}'' \approx (\mathbf{L}_0')^{-1}(\mathbf{L}_0'')$. The reader should be cautioned that the paper by Sharp and Rosenstock contains typographical errors. Care must be taken to correct the errors when applying equations from that paper. Some of the errata have been published in Ref. 118. Corrected versions of key equations from Ref. 98 are also printed in Ref. 105.

3.2.4 Coordinate transformation for bent—linear transitions

Some additional complications are presented by the Ã—X̃ transition in acetylene because the ground state has a linear equilibrium geometry while the electronically-excited Ã state is trans-bent. In the most familiar formulation of the rovibrational Hamiltonian, states with nonlinear equilibrium geometry are treated with 3 rotational degrees of freedom and $3N-6$ vibrational degrees of freedom, while states with linear equilibrium geometry are treated with 2 rotational degrees of freedom and $3N-5$ vibrational degrees of freedom. In this formulation for linear molecules, the three-dimensional moment of inertia tensor is singular and all angular momentum about the a-inertial axis arises from vibration.

For the current problem of full-dimensional Franck–Condon factors in the acetylene Ã—X̃ system, it is more convenient to formulate the X̃-state Hamiltonian in terms of 3 rotational degrees of freedom and $3N-6$ vibrational degrees of freedom. Watson has discussed in detail the formulation of the rovibrational kinetic energy operator for this case, and the reader is referred to Ref. 119.

The (x, y) sub-block of $\mathbf{I}$ is trivially diagonal in the linear configuration. Therefore, in the conventional treatment involving only two rotations, the χ Euler angle is not defined. Rotation of the molecular orientation around the z-axis is instead achieved by a rotation of the polar coordinates of each of the degenerate bending modes, q_t, which are defined relative to the x and y axes by

$$q^u_{tx} = \rho_t \cos\phi^u_t, \tag{3.43}$$

$$q^u_{ty} = \rho_t \sin\phi^u_t, \tag{3.44}$$

where t is an index that labels the bending vibrational modes, and the u superscript signifies that the polar coordinates are unconstrained. To add a third rotational degree of freedom (restoring χ), a constraint must be placed on the vibrational coordinates so that the total number of degrees of freedom remains constant. In general, the constraint may be accomplished by choosing a nonlinear reference configuration, $\mathbf{q}_{\text{ref}}$, and then restricting the polar coordinates ϕ_t of the degenerate bending modes to locate the x and y axes such that the (x, y) block of the moment of inertia tensor is diagonal. This allows reintroduction of the χ Euler angle to give constrained polar angles ϕ_t according to

$$\phi_t = \phi^u_t - \chi. \tag{3.45}$$

In the case of a linear—nonlinear transition, the natural choice of reference configuration is the equilibrium geometry of the nonlinear state, so for the current problem, we choose as the reference configuration the trans-bent Ã-state equilibrium geometry. The off-diagonal element of the (x, y) block of $\mathbf{I}$ is

$$I_{xy} = -\sum_i m_i r_{ix} r_{iy}, \tag{3.46}$$

where $(r_{ix},\ r_{iy})$ is the $(x,\ y)$ position of the i^{th} nucleus in the trans-bent reference configuration (and the orientation of the x and y axes are to be defined by the constraint). Only the trans- and cis-bending modes (ν''_4 and ν''_5, respectively) have amplitude in the (x, y) plane, and furthermore, the displacement along the *ungerade* cis bend, q''_5, is zero at the centrosymmetric Ã-state equilibrium. Therefore, q''_4 will be the only contribution to r_{ix} and r_{iy}. Since the requirement $I_{xy} = 0$ satisfies the Eckart conditions, we have from Eq. (3.16) $m_i^{1/2} r_{ix} = l''_{ix,4}(\gamma''_4)^{-1/2} q''_{4x}$ and $m_i^{1/2} r_{iy} =$

$l''_{iy,4}(\gamma''_4)^{-1/2}q''_{4y}$, so

$$I_{xy} = -q''_{4x}q''_{4y}\sum_i \left(\frac{l''_{ix,4}l''_{iy,4}}{\gamma''_4}\right) = 0, \tag{3.47}$$

or, from Eqs. (3.43) and (3.44)

$$-\frac{1}{2}\rho''_4 \sin 2\phi_4 = 0. \tag{3.48}$$

Equation (3.48) has more than one solution, but it is conventional to choose y to correspond with the out-of-plane c-axis in the trans C_{2h} configuration, so we choose the solution $\phi_4 = 0$, (or $q''_{4y} = 0$), which gives

$$\chi = \phi^u_4 \tag{3.49}$$

$$\phi_5 = \phi^u_5 - \chi. \tag{3.50}$$

The resulting constraint ensures that displacement along q''_4 must lie in the plane of the equilibrium geometry of the trans-bent Ã state. Note that constraining ϕ_4 to zero and restoring the χ Euler angle is equivalent to removing the $\exp(il_4\phi_4)$ factor from the two-dimensional harmonic oscillator wavefunction and including it instead in the the rotational integral. Hence, the $(v-l)/2$ radial nodes of the two-dimensional harmonic oscillator wavefunction for mode ν''_4 are included in the vibrational FC factor, but the angular factor is not. On the other hand, ϕ_5 is *not* constrained to zero, so it will contribute both a radial and angular factor to the vibrational integral. This leads to important propensity rules and symmetry considerations for the vibrational overlap integrals, which will be discussed in Chapter 4. Some of these considerations have been neglected by other authors because they have not considered the problem of linear-to-bent transitions in full dimension.

The rotational integral may be evaluated from the μ_c matrix elements. Formulas for rotational strength factors for linear to bent transitions are given in Ref. 120. In the current work, we ignore rovibrational interactions and we are primarily interested with the vibrational intensity factors rather than the distribution of that intensity between the rotational states within each vibrational band, so we have ignored the rotational integral.

3.2.5 Method of Generating Functions

General case for non-linear molecules

The method of generating functions used by Sharp and Rosenstock for calculating Franck-Condon overlap integrals makes use of the exponential generating function for Hermite polynomials (denoted $H_v(q)$)

$$\exp\left(2sq - s^2\right) = \sum_v \frac{H_v(q)s^v}{v!}. \tag{3.51}$$

To generate properly normalized wavefunctions $\langle q|v\rangle$ of the dimensionless variable $q = (hc\omega/\hbar^2)^{1/2}Q$, we use

$$\sum_v \frac{\langle q|v\rangle s^v}{\sqrt{v!}} = \pi^{-\frac{1}{4}} \exp\left(-\frac{1}{2}q^2 + \sqrt{2}sq - \frac{1}{2}s^2\right) \tag{3.52}$$

$$\langle q|v\rangle = \pi^{-\frac{1}{4}} \left(\frac{1}{2^v v!}\right)^{\frac{1}{2}} \exp\left(\frac{-q^2}{2}\right) H_v(q). \tag{3.53}$$

Equation (3.52) states that if we take the exponential function on the right hand side and expand it as a polynomial of the dummy variable s, then we obtain the Harmonic oscillator wavefunctions as coefficients. Any desired Harmonic oscillator wavefunction, $\langle q|v\rangle$, may be obtained by collecting the coefficient of s to the desired power. The factor of $\sqrt{v!}$ in the denominator is required in order to achieve the properly normalized wavefunction given in Eq. (3.53). Note that in Eq. (3.52), s has been scaled by a factor of $2^{-1/2}$ to achieve the factor of $2^{(-v/2)}$ in the normalization constant of Eq. (3.53).

To generate an n_{vib}-dimensional harmonic oscillator wavefunction in the product basis, $\langle \mathbf{q}|\mathbf{v}\rangle = \prod_k \langle q_k|v_k\rangle$, we may write Eq. (3.52) in terms of the vector $\mathbf{q}$ and use a dummy vector $\mathbf{s}$ of length n_{vib},

$$\sum_{\mathbf{v}} \frac{\langle \mathbf{q}|\mathbf{v}\rangle \prod\limits_k s_k^{v_k}}{\prod\limits_k (v_k!)^{1/2}} = \pi^{-n_{\text{vib}}/4} \exp\left(-\frac{1}{2}\tilde{\mathbf{q}}\mathbf{q} + \sqrt{2}\tilde{\mathbf{s}}\mathbf{q} - \frac{1}{2}\tilde{\mathbf{s}}\mathbf{s}\right), \tag{3.54}$$

where k is an index that labels each mode and the summation over $\mathbf{v}$ on the left hand side denotes summation over each v_k.

To obtain the overlap integral in Eq. (3.4), we wish to calculate

$$\langle \Psi'_{\text{vib}}|\Psi''_{\text{vib}}\rangle = \int \left|\frac{\partial \mathbf{q}'}{\partial \mathbf{q}''}\right|^{\frac{1}{2}} \mathrm{d}\mathbf{q}''\ \langle \mathbf{v}'|\mathbf{q}'\rangle\langle \mathbf{q}''|\mathbf{v}''\rangle, \tag{3.55}$$

where $\int \mathrm{d}\mathbf{q}''$ is shorthand for $\int_{-\infty}^{\infty} \ldots \int_{-\infty}^{\infty} \prod_k \mathrm{d}q''_k$. The $|\partial \mathbf{q}'/\partial \mathbf{q}''|$ represents the determinant of the matrix of partial derivatives with components $D_{ij} = \partial q'_i/\partial q''_j$. It is included because the transformation $\mathbf{q}' = \mathbf{D}\mathbf{q}'' + \boldsymbol{\delta}$ need not be unitary, and the wavefunction $\Psi'_{\text{vib}}(\mathbf{q}')$ must therefore be renormalized by the Jacobian determinant for integration with respect to $\mathbf{q}''$.

$$\int \mathrm{d}\mathbf{q}' |\Psi'_{\text{vib}}(\mathbf{q}')|^2 = 1 \tag{3.56}$$

$$\int \left|\frac{\partial \mathbf{q}'}{\partial \mathbf{q}''}\right| \mathrm{d}\mathbf{q}'' |\Psi'_{\text{vib}}(\mathbf{q}'')|^2 = 1 \tag{3.57}$$

$$\det(\mathbf{D}) \int \mathrm{d}\mathbf{q}'' |\Psi'_{\text{vib}}(\mathbf{q}'')|^2 = 1. \tag{3.58}$$

We define renormalized excited-state wavefunctions $\Psi'^{(\text{rn})}_{\text{vib}}(\mathbf{q}'') = \sqrt{\det(\mathbf{D})}\ \Psi'_{\text{vib}}(\mathbf{q}'')$, so that

$$\int \mathrm{d}\mathbf{q}'' |\Psi'^{(\text{rn})}_{\text{vib}}(\mathbf{q}'')|^2 = 1. \tag{3.59}$$

We obtain a generating function G for Eq. (3.55) by taking the product of Eq. (3.54) for the ground and excited states and performing the integral with respect to d$\mathbf{q}''$.

$$\begin{aligned}G = \sum_{\mathbf{v}',\mathbf{v}''} &\frac{\langle \mathbf{v}'|\mathbf{v}''\rangle \prod\limits_{k',k''} (s_{k'})^{v'_{k'}} (t_{k''})^{v''_{k''}}}{\prod\limits_{k',k''} [(v'_{k'}!)(v''_{k''}!)]^{1/2}} \\ &= \left(\frac{\det \mathbf{D}}{\pi^{n_{\mathrm{vib}}}}\right)^{\frac{1}{2}} \int \mathrm{d}\mathbf{q}'' \exp\left(-\frac{1}{2}\tilde{\mathbf{q}}'\mathbf{q}' + \sqrt{2}\,\tilde{\mathbf{s}}\mathbf{q}' - \frac{1}{2}\tilde{\mathbf{s}}\mathbf{s}\right) \\ &\times \exp\left(-\frac{1}{2}\tilde{\mathbf{q}}''\mathbf{q}'' + \sqrt{2}\,\tilde{\mathbf{t}}\mathbf{q}'' - \frac{1}{2}\tilde{\mathbf{t}}\mathbf{t}\right). \qquad (3.60)\end{aligned}$$

We have used $s_{k'}$ as the dummy variable for the excited state modes and $t_{k''}$ as the dummy variable for the ground state modes. We substitute $\mathbf{q}' = \mathbf{D}\mathbf{q}'' + \boldsymbol{\delta}$ to obtain

$$\begin{aligned}G = \left(\frac{\det \mathbf{D}}{\pi^{n_{\mathrm{vib}}}}\right)^{\frac{1}{2}} &\exp\left(-\frac{1}{2}\tilde{\boldsymbol{\delta}}\boldsymbol{\delta} + \sqrt{2}\tilde{\mathbf{s}}\boldsymbol{\delta} - \frac{1}{2}\tilde{\mathbf{s}}\mathbf{s} - \frac{1}{2}\tilde{\mathbf{t}}\mathbf{t}\right) \\ &\times \int \mathrm{d}\mathbf{q}'' \exp\left[-\tilde{\mathbf{q}}''\mathbf{A}\mathbf{q}'' + \left(\sqrt{2}\tilde{\mathbf{s}}\mathbf{D} + \sqrt{2}\,\tilde{\mathbf{t}} - \tilde{\boldsymbol{\delta}}\mathbf{D}\right)\mathbf{q}''\right]. \qquad (3.61)\end{aligned}$$

We have made the substitution $\mathbf{A} = \frac{1}{2}(\mathbf{E} + \tilde{\mathbf{D}}\mathbf{D})$, where $\mathbf{E}$ is the $n_{\mathrm{vib}} \times n_{\mathrm{vib}}$ identity matrix. The integral in Eq. (3.61) can be solved by changing coordinates to the basis that diagonalizes $\mathbf{A}$ and evaluating the resulting one-dimensional Gaussian integrals. Note that $\mathbf{A}$ is a symmetric matrix and therefore guaranteed to be diagonalizable by an orthogonal matrix. Let $\mathbf{V}$ be the orthogonal matrix that diagonalizes $\mathbf{A}$ such that $\tilde{\mathbf{V}}\mathbf{A}\mathbf{V} = \boldsymbol{\Theta}$, ($\boldsymbol{\Theta}$ is diagonal), and let $\mathbf{y}$ be the transformation of $\mathbf{q}''$ under $\mathbf{V}$ so that $\tilde{\mathbf{V}}\mathbf{q}'' = \mathbf{y}$. Since $\mathbf{V}$ is orthogonal (and unitary), the Jacobian determinant of the transformation is unity and d$\mathbf{q}''$ = d$\mathbf{y}$.

Substituting $\mathbf{q}'' = \mathbf{V}\mathbf{y}$, we obtain

$$G = \left(\frac{\det \mathbf{D}}{\pi^{n_{\mathrm{vib}}}}\right)^{\frac{1}{2}} \exp\left(-\frac{1}{2}\tilde{\boldsymbol{\delta}}\boldsymbol{\delta} + \sqrt{2}\tilde{\mathbf{s}}\boldsymbol{\delta} - \frac{1}{2}\tilde{\mathbf{s}}\mathbf{s} - \frac{1}{2}\tilde{\mathbf{t}}\mathbf{t}\right) \int \mathrm{d}\mathbf{y} \exp\left(-\tilde{\mathbf{y}}\boldsymbol{\Theta}\mathbf{y} + \tilde{\mathbf{w}}\mathbf{y}\right), \qquad (3.62)$$

where we have substituted $\tilde{\mathbf{w}} = (\sqrt{2}\tilde{\mathbf{s}}\mathbf{D} + \sqrt{2}\,\tilde{\mathbf{t}} - \tilde{\boldsymbol{\delta}}\mathbf{D})\mathbf{V}$. Since $\boldsymbol{\Theta}$ is diagonal, the integral in (3.62) may be evaluated as a product of one-dimensional Gaussian integrals:

$$\begin{aligned}
G &= \left(\frac{\det \mathbf{D}}{\pi^{n_{\mathrm{vib}}}}\right)^{\frac{1}{2}} \exp\left(-\frac{1}{2}\tilde{\boldsymbol{\delta}}\boldsymbol{\delta} + \sqrt{2}\tilde{\mathbf{s}}\boldsymbol{\delta} - \frac{1}{2}\tilde{\mathbf{s}}\mathbf{s} - \frac{1}{2}\tilde{\mathbf{t}}\mathbf{t}\right) \prod_i^{n_{\mathrm{vib}}} \int \mathrm{d}y_i \exp\left(-\Theta_{ii} y_i^2 + w_i y_i\right) \\
&= \left(\frac{\det \mathbf{D}}{\pi^{n_{\mathrm{vib}}}}\right)^{\frac{1}{2}} \exp\left(-\frac{1}{2}\tilde{\boldsymbol{\delta}}\boldsymbol{\delta} + \sqrt{2}\tilde{\mathbf{s}}\boldsymbol{\delta} - \frac{1}{2}\tilde{\mathbf{s}}\mathbf{s} - \frac{1}{2}\tilde{\mathbf{t}}\mathbf{t}\right) \prod_i^{n_{\mathrm{vib}}} \sqrt{\frac{\pi}{\Theta_{ii}}} \exp\left(\frac{w_i^2}{4\Theta_{ii}}\right) \\
&= \left(\frac{\det \mathbf{D}}{\det \boldsymbol{\Theta}}\right)^{\frac{1}{2}} \exp\left(-\frac{1}{2}\tilde{\boldsymbol{\delta}}\boldsymbol{\delta} + \sqrt{2}\tilde{\mathbf{s}}\boldsymbol{\delta} - \frac{1}{2}\tilde{\mathbf{s}}\mathbf{s} - \frac{1}{2}\tilde{\mathbf{t}}\mathbf{t}\right) \exp\left(\frac{1}{4}\tilde{\mathbf{w}}\boldsymbol{\Theta}^{-1}\mathbf{w}\right).
\end{aligned}$$

After some algebra, we find

$$\frac{1}{4}\tilde{\mathbf{w}}\boldsymbol{\Theta}^{-1}\mathbf{w} = \frac{1}{4}\left(\sqrt{2}\tilde{\mathbf{s}} - \tilde{\boldsymbol{\delta}}\right)\left(2\mathbf{E} - \mathbf{B}^{-1}\right)\left(\sqrt{2}\mathbf{s} - \boldsymbol{\delta}\right) + \frac{1}{\sqrt{2}}\left(\sqrt{2}\tilde{\mathbf{s}} - \tilde{\boldsymbol{\delta}}\right)\mathbf{X}^{-1}\mathbf{t} + \frac{1}{2}\tilde{\mathbf{t}}\mathbf{A}^{-1}\mathbf{t}, \tag{3.63}$$

where we have made the substitutions

$$\mathbf{B} = \frac{1}{2}\left(\mathbf{E} + \mathbf{D}\tilde{\mathbf{D}}\right) = \mathbf{D}\mathbf{A}\mathbf{D}^{-1} = (2\mathbf{E} - \mathbf{D}\mathbf{A}^{-1}\tilde{\mathbf{D}})^{-1} \tag{3.64}$$

$$\mathbf{X} = \frac{1}{2}\left(\tilde{\mathbf{D}} + \mathbf{D}^{-1}\right) = \mathbf{A}\mathbf{D}^{-1} = \mathbf{D}^{-1}\mathbf{B}, \tag{3.65}$$

and where $\mathbf{E}$ represents the $n_{\mathrm{vib}} \times n_{\mathrm{vib}}$ identity matrix. We also note that $\det \boldsymbol{\Theta} = \det \mathbf{A}$ because the determinant is invariant under a unitary transformation. The final expression for G is

$$\begin{aligned}
G &= \sum_{\mathbf{v}',\mathbf{v}''} \frac{\langle \mathbf{v}' | \mathbf{v}'' \rangle \prod\limits_{k',k''} (s_{k'})^{v'_{k'}} (t_{k''})^{v''_{k''}}}{\prod\limits_{k',k''} [(v'_{k'}!)(v''_{k''}!)]^{1/2}} \\
&= \left(\frac{1}{\det \mathbf{X}}\right)^{\frac{1}{2}} \exp\left(-\frac{1}{4}\tilde{\boldsymbol{\delta}}\mathbf{B}^{-1}\boldsymbol{\delta}\right) \\
&\quad \times \exp\left[\frac{1}{2}\tilde{\mathbf{s}}\left(\mathbf{E} - \mathbf{B}^{-1}\right)\mathbf{s} - \frac{1}{2}\tilde{\mathbf{t}}\left(\mathbf{E} - \mathbf{A}^{-1}\right)\mathbf{t} + \tilde{\mathbf{s}}\mathbf{X}^{-1}\mathbf{t} + \frac{1}{\sqrt{2}}\tilde{\mathbf{s}}\mathbf{B}^{-1}\boldsymbol{\delta} - \frac{1}{\sqrt{2}}\tilde{\boldsymbol{\delta}}\mathbf{X}^{-1}\mathbf{t}\right].
\end{aligned} \tag{3.66}$$

This is in agreement with the equation obtained by Watson[104] and the corrected version of the equation obtained by Sharp and Rosenstock[98,118].

Generating Function for the Full-Dimensional Acetylene Ã—X̃ System

Watson has derived a generating function for the *gerade* modes of the acetylene Ã—X̃ system.[104] It is our goal here to extend Watson's work to obtain a full-dimensional treatment. Watson treats the doubly-degenerate bending mode ν_4'' in the (v, l)-basis and integrates the wavefunction in polar coordinates, ρ_4, ϕ_4. He makes use of the generating function

$$\sqrt{\frac{\rho_t}{\pi}} \exp\left\{-\frac{1}{2}\rho_t + \frac{1}{\sqrt{2}}\rho_t e^{i\phi_t} su + \frac{1}{\sqrt{2}}\rho_t e^{-i\phi_t} su^{-1} - \frac{1}{2}s^2\right\} \\ = \sum_{v_t, l_t} \frac{\langle \rho_t \phi_t | v_t l_t \rangle s^{v_t} u^{l_t}}{\left\{2^{v_t}\left[\frac{1}{2}(v_t + l_t)\right]!\left[\frac{1}{2}(v_t - l_t)\right]!\right\}^{1/2}}. \tag{3.67}$$

In Eq. (3.67), l_t is a signed quantity $(-v_t \leq l_t \leq v_t)$ so the right-hand side is *not* a polynomial in the dummy variable u. The wavefunctions obtained from this generating function may be written explicitly as

$$\langle \rho_t \phi_t | v_t l_t \rangle = \frac{(-1)^{(3v_t + l_t)/2}}{\sqrt{\pi}} \left(\frac{\left[\frac{1}{2}(v_t - l_t)\right]!}{\left[\frac{1}{2}(v_t + l_t)\right]!}\right)^{1/2} \rho_t^{(l_t + 1/2)} e^{-\rho_t^2/2} L^{l_t}_{\frac{1}{2}(v_t - l_t)}(\rho_t^2) e^{i l_t \phi_t}, \tag{3.68}$$

where $L_n^{\alpha}(x)$ represents the associated Laguerre polynomial. Note that Eq. (3.68) differs from the form of the wavefunction given in most textbooks by a factor of $\rho_t^{1/2}$. This factor is included to normalize the wavefunctions with respect to integration over polar coordinates,

$$\iint \mathrm{d}\rho_t \mathrm{d}\phi_t \langle v_t' l_t' | \rho_t \phi_t \rangle \langle \rho_t \phi_t | v_t l_t \rangle = \delta_{v_t', v_t} \delta_{l_t', l_t}. \tag{3.69}$$

To obtain a generating function for the Franck-Condon overlap integrals of doubly-degenerate bending modes in the linear ground state of acetylene, we may substitute the left-hand side of Eq. (3.67) for the appropriate normal mode dimensions in the second exponential of Eq. (3.60). In treating the *gerade* modes, Watson makes use of the Euler angle constraint $\phi_4 = 0$ and makes the substitution $u_4 = \exp(i\psi_4)$, which simplifies the resulting integral. The factor of $\exp(i\phi_4^u)$ is treated as part of the rotational wavefunction.

In the full-dimensional treatment of FC factors for the Ã—X̃ acetylene transition, however, there are *two* doubly degenerate bending modes that must be treated, ν_4'' and ν_5''. If we were to use a generating function for the ν_5'' wavefunctions of the type presented in Eq. (3.67), we would have to integrate over ϕ_5 and the exponential term in the integral would no longer be separable into a product of one-dimensional Gaussian integrals. Therefore, in order to simplify the integral in the current work, we choose to represent ν_5'' in the (v_x, v_y) basis and to use generating functions of the type presented in Eq. (3.52). We leave ν_4'' in the (v, l) basis to take advantage of the simplifications afforded by the Euler angle constraint on ϕ_4. Finally, we include an extra factor of ρ_4'' to capture the linear dependence on ρ_4'' of the transition dipole moment, as in Eq. (3.6). The resulting generating function is

$$\begin{aligned} G = (\det \mathbf{D})^{1/2} \int \mathbf{dq}''\ \pi^{-5/4} \exp\left(-\frac{1}{2}\tilde{\mathcal{Q}}''\mathcal{Q}'' + \sqrt{2}\tilde{\mathcal{T}}\mathcal{Q}'' - \frac{1}{2}\tilde{\mathcal{T}}\mathcal{T}\right) \\ \times \pi^{-1/2}(\rho_4'')^{3/2} \exp\left(-\frac{1}{2}(\rho_4'')^2 + \frac{2}{\sqrt{2}}\rho_4'' t_4 \cos\psi_4 - \frac{1}{2}t_4^2\right) \\ \times \pi^{-3/2} \exp\left(-\frac{1}{2}\tilde{\mathbf{q}}'\mathbf{q}' + \sqrt{2}\tilde{\mathbf{s}}\mathbf{q}' - \frac{1}{2}\tilde{\mathbf{s}}\mathbf{s}\right) \\ = \sum_{\mathbf{v}',\mathbf{v}'',l_4''} \frac{\langle \mathbf{v}' | \mathbf{v}'', l_4'' \rangle \prod\limits_{k',k''} s_{k'}^{v_{k'}'} t_{k''}^{v_{k''}''}}{(v_1'!v_2'!v_3'!v_4'!v_5'!v_6'!)^{1/2}(v_1''!v_2''!v_3''!v_{5x}''!v_{5y}''!)^{1/2}} \frac{\cos l_4''\psi_4}{\{2^{v_4''}[\frac{1}{2}(v_4''+l_4'')]![\frac{1}{2}(v_4''-l_4'')]!\}^{1/2}}, \end{aligned} \tag{3.70}$$

where

$$\begin{aligned} \mathbf{dq}'' &= \mathrm{d}q_1''\mathrm{d}q_2''\mathrm{d}q_3''\mathrm{d}\rho_4''\mathrm{d}q_{5x}''\mathrm{d}q_{5y}'', \\ \tilde{\mathcal{Q}}'' &= (q_1'', q_2'', q_3'', q_{5x}'', q_{5y}''), \\ \tilde{\mathcal{T}} &= (t_1, t_2, t_3, t_{5x}, t_{5y}), \end{aligned}$$

and $\tilde{\mathbf{q}}'$ and $\tilde{\mathbf{s}}'$ are (1×6) row vectors with one element for each excited-state normal mode. The limits of integration with respect to $\mathrm{d}\rho_4''$ are $(0, \infty)$, and all other limits of integration are $(-\infty, \infty)$. After substituting $\mathbf{q}' = \mathbf{D}\mathbf{q}'' + \boldsymbol{\delta}$ into Eq. (3.70), we obtain

$$\begin{aligned} G =& \pi^{-13/4}(\det \mathbf{D})^{1/2} \int \mathbf{dq}''(\rho_4'')^{3/2} \\ & \times \exp\left[-\tilde{\mathbf{q}}''\mathbf{A}\mathbf{q}'' + (-\tilde{\boldsymbol{\delta}}\mathbf{D} + \sqrt{2}\tilde{\mathbf{s}}\mathbf{D} + \sqrt{2}\tilde{\mathbf{T}})\mathbf{q}'' - \frac{1}{2}\tilde{\boldsymbol{\delta}}\boldsymbol{\delta} + \sqrt{2}\tilde{\mathbf{s}}\boldsymbol{\delta} - \frac{1}{2}\tilde{\mathbf{s}}\mathbf{s} - \frac{1}{2}\tilde{\mathbf{t}}\mathbf{t}\right], \end{aligned} \tag{3.71}$$

where

$$\tilde{\mathbf{q}}'' = (q_1'', q_2'', q_3'', \rho_4'', q_{5x}'', q_{5y}''), \tag{3.72}$$

$$\tilde{\mathbf{t}} = (t_1, t_2, t_3, t_4, t_{5x}, t_{5y}), \tag{3.73}$$

$$\tilde{\mathbf{T}} = (t_1, t_2, t_3, t_4 \cos\phi_4, t_{5x}, t_{5y}). \tag{3.74}$$

The integral in Eq. (3.71) differs from the one in Eq. (3.60) because it includes a factor of $(\rho_4'')^{3/2}$, and the limits of integration with respect to ρ_4'' are $(0, \infty)$. These considerations make it difficult to perform the change of variables as we did in Section 3.2.5. As mentioned in Section 3.2.1, the electronic transition dipole moment for the Ã—X̃ transition in acetylene vanishes at the linear configuration, so most of the overlap integral accumulates at configurations away from linearity ($\rho_4'' \neq 0$). Following Watson, we can use Laplace's approximation for the integral in Eq. (3.71), as follows. If $h(\mathbf{x})$ and $g(\mathbf{x})$ are real-valued functions and $g(\mathbf{x})$ has a single absolute maximum at $\mathbf{x_0}$ in the domain of integration, F, $g(\mathbf{x_0}) = \max[g(\mathbf{x})]$, then

$$\int_F \mathbf{dx}\, h(\mathbf{x}) \exp\left(Mg(\mathbf{x})\right) \approx \left(\frac{2\pi}{M}\right)^{\frac{n}{2}} \left(\frac{1}{|\det[\mathbf{H}_g(\mathbf{x_0})]|}\right)^{\frac{1}{2}} h(\mathbf{x_0}) \exp\left(Mg(\mathbf{x_0})\right), \tag{3.75}$$

where M is a real number, n is the length of the vector $\mathbf{x}$, and $\mathbf{H}_g(\mathbf{x_0})$ is the Hessian matrix of second derivatives of $g(\mathbf{x})$, evaluated at $\mathbf{x_0}$. Equation (3.75) is valid in the limit $M \to \infty$ and is an exact solution for the Gaussian case where $h(\mathbf{x})$ is constant, $g(\mathbf{x})$ is quadratic with negative second partial derivatives, and the limits of integration are $(-\infty, \infty)$ for all variables. Laplace's approximation is a good strategy for the integral in Eq. (3.71) because it would provide the exact solution if it were not for the $(\rho_4'')^{3/2}$ factor and the limits of integration with respect to ρ_4'', so in a sense it is an approximation only for a single coordinate. Furthermore, because the Franck-Condon overlap is expected to accumulate mostly at bending geometries intermediate to the Ã- and X̃-state equilibria, we expect this approximation to be valid with respect to the ρ_4'' coordinate.

We apply Eq. (3.75) to the integral in Eq. (3.71), letting $h(\mathbf{x}) = (\rho_4'')^{3/2}$, $M = 1$, and $g(\mathbf{x})$ equal the argument of the exponential in Eq. (3.71). We first find the value of $\mathbf{q}''$ that maximizes g. We note that since $\mathbf{A}$ is a symmetric matrix,

$$\frac{\partial}{\partial \mathbf{q}''}\,\tilde{\mathbf{q}}''\mathbf{A}\mathbf{q}'' = 2\mathbf{A}\mathbf{q}''. \tag{3.76}$$

We differentiate the exponential in (3.71) to obtain

$$\begin{aligned}\frac{\partial}{\partial \mathbf{q}''}\left[-\tilde{\mathbf{q}}''\mathbf{A}\mathbf{q}'' + (-\tilde{\boldsymbol{\delta}}\mathbf{D} + \sqrt{2}\tilde{\mathbf{s}}\mathbf{D} + \sqrt{2}\tilde{\mathbf{T}})\mathbf{q}'' - \frac{1}{2}\tilde{\boldsymbol{\delta}}\boldsymbol{\delta} + \sqrt{2}\tilde{\mathbf{s}}\boldsymbol{\delta} - \frac{1}{2}\tilde{\mathbf{s}}\mathbf{s} - \frac{1}{2}\tilde{\mathbf{t}}\mathbf{t}\right]\Bigg|_{\mathbf{q}_0''} &= 0 \\ -2\mathbf{A}\mathbf{q}_0'' - \tilde{\mathbf{D}}\boldsymbol{\delta} + \sqrt{2}\tilde{\mathbf{D}}\mathbf{s} + \sqrt{2}\mathbf{T} &= 0.\end{aligned} \tag{3.77}$$

Thus,

$$\mathbf{q}_0'' = \frac{1}{2}\mathbf{A}^{-1}\left(-\tilde{\mathbf{D}}\boldsymbol{\delta} + \sqrt{2}\tilde{\mathbf{D}}\mathbf{s} + \sqrt{2}\mathbf{T}\right). \tag{3.78}$$

The value of ρ_4'' at the maximum of the argument of the exponential is the fourth element of the vector equation (3.78),

$$(\rho_4'')_0 = [\mathbf{q}_0'']_4 = \left[\frac{1}{2}\mathbf{A}^{-1}\left(-\tilde{\mathbf{D}}\boldsymbol{\delta} + \sqrt{2}\tilde{\mathbf{D}}\mathbf{s} + \sqrt{2}\mathbf{T}\right)\right]_4. \tag{3.79}$$

We can now substitute Eq. (3.78) and Eq. (3.79) into Eq. (3.75), noting that $\mathbf{H}_g(\mathbf{q}_0'') =$

2**A**. After some algebra, we obtain

$$\begin{aligned} G = \pi^{-\frac{1}{4}}(\det \mathbf{X})^{-\frac{1}{2}}(\rho_4'')_0^{3/2} \exp\Bigg[& \frac{1}{2}\tilde{\mathbf{s}}(\mathbf{E} - \mathbf{B}^{-1})\mathbf{s} - \frac{1}{2}\tilde{\mathbf{t}}\mathbf{t} + \frac{1}{2}\tilde{\mathbf{T}}\mathbf{A}^{-1}\mathbf{T} + \tilde{\mathbf{s}}\mathbf{X}^{-1}\mathbf{T} \\ & + \frac{\sqrt{2}}{2}\tilde{\mathbf{s}}\mathbf{B}^{-1}\boldsymbol{\delta} - \frac{\sqrt{2}}{2}\tilde{\boldsymbol{\delta}}\mathbf{X}^{-1}\mathbf{T} - \frac{1}{4}\tilde{\boldsymbol{\delta}}\mathbf{B}^{-1}\boldsymbol{\delta}\Bigg] \\ = \sum_{\mathbf{v}',\mathbf{v}'',l_4''} & \frac{\langle \mathbf{v}'|\mathbf{v}'', l_4''\rangle \prod\limits_{k',k''}(s_{k'})^{v'_{k'}}(t_{k''})^{v''_{k''}}}{(v_1'!v_2'!v_3'!v_4'!v_5'!v_6'!)^{1/2}(v_1''!v_2''!v_3''!v_{5x}''!v_{5y}''!)^{1/2}} \frac{\cos l_4''\psi_4}{\{2^{v_4''}[\frac{1}{2}(v_4''+l_4'')]![\frac{1}{2}(v_4''-l_4'')]!\}^{1/2}}. \end{aligned} \tag{3.80}$$

This equation has the same form as that derived by Watson (Eq. 29 of Ref. 104), except for the definitions of $\mathbf{s}$, $\mathbf{t}$, and $\mathbf{T}$. Also, we have not included the factor of $(2 - \delta_{l_4'',0})$, which Watson uses to account for the degeneracy of states with $|l_4''| = \pm l_4''$. In the current work, we are interested applying our Franck-Condon calculation to cases in which states differing only in ± parity may be resolved or in which transitions to only one of the parity components is allowed.

Change of Basis for ν_5''

The generating function in Eq. (3.80) calculates overlap integrals for the cis-bending mode ν_5'' in the $|v_{5x}'', v_{5y}''\rangle$ basis, but for most spectroscopic applications, we wish to work in the $|v_5'', l_5''\rangle$ basis. A state in the $|v_5'', l_5''\rangle$ basis may be expressed as a linear combination of states in the $|v_{5x}'', v_{5y}''\rangle$ basis with $v_{5x}'' + v_{5y}'' = v_5''$,

$$|\{\boldsymbol{\alpha''}\}, v_5'', l_5''\rangle = \sum_{i=0}^{v_5''} c_i |\{\boldsymbol{\alpha''}\}, v_{5x}'' = v_5 - i, v_{5y}'' = i\rangle \tag{3.81}$$

where $\{\boldsymbol{\alpha''}\}$ represents a given set of values for all other quantum numbers of the state. Therefore, the Franck-Condon overlap integral in the $|v_5'', l_5''\rangle$ basis may be expressed as a linear combination of Franck-Condon overlap integrals in the $|v_{5x}'', v_{5y}''\rangle$

basis with the same coefficients.

$$\langle \mathbf{v}' | \{\boldsymbol{\alpha}''\}, v_5'', l_5'' \rangle = \sum_{i=0}^{v_5''} c_i \langle \mathbf{v}' | \{\boldsymbol{\alpha}''\}, v_{5x}'' = v_5'' - i, v_{5y}'' = i \rangle \tag{3.82}$$

The coefficients c_i may be obtained by applying 2-dimensional harmonic oscillator raising and lowering operators found in many quantum mechanics textbooks, such as Ref. 121. Briefly, the coefficients may be obtained by expanding the operator equation

$$|v, l\rangle = \frac{1}{\sqrt{[(v+l)/2]![(v-l)/2]!}} \left(\hat{a}_x^\dagger + i\hat{a}_y^\dagger\right)^{(v+l)/2} \left(\hat{a}_x^\dagger - i\hat{a}_y^\dagger\right)^{(v-l)/2} |0, 0\rangle, \tag{3.83}$$

and evaluating terms on the right-hand side according to

$$\left(\hat{a}_x^\dagger\right)^{n_x} \left(\hat{a}_y^\dagger\right)^{n_y} |0, 0\rangle = \sqrt{n_x! n_y!}\ |n_x, n_y\rangle. \tag{3.84}$$

3.3 Calculation of Coordinate Transformation Parameters for the Ã—X̃ System of Acetylene

The normal mode frequencies and symmetries of the X̃ and Ã states are summarized in Tables 3.2 and 3.3. Parameters for the X̃-state equilibrium geometry and harmonic force field used in the evaluation of the coordinate transformation were taken from Halonen *et al.* ("Model II" of the paper).[123] In order to reproduce the results of

Table 3.2: Normal mode labels for X̃-state acetylene. The harmonic vibrational frequencies (taken from Ref. 84) were determined from experiment after deperturbing the anharmonic resonances.

Mode	Description	Symmetry	ω/cm^{-1}
ν_1''	symmetric stretch	σ_g^+	3397.12
ν_2''	CC stretch	σ_g^+	1981.80
ν_3''	antisymmetric stretch	σ_u^+	3316.86
ν_4''	trans bend	π_g	608.73
ν_5''	cis bend	π_u	729.08

Table 3.3: Normal mode labels for Ã-state acetylene. The harmonic vibrational frequencies (taken from Ref. 122) were determined from experiment after deperturbing the anharmonic resonances.

Mode	Description	Symmetry	ω/cm^{-1}
ν_1'	symmetric stretch	a_g	3052.1
ν_2'	CC stretch	a_g	1420.9
ν_3'	trans bend	a_g	1098.0
ν_4'	torsion	a_u	787.7
ν_5'	antisymmetric stretch	b_u	3032.4
ν_6'	cis bend	b_u	801.6

Watson, we first used the Ã-state geometry and harmonic force field from Tobiason *et al.*[124] Using these force fields, we obtained elements for the *gerade* block of $\mathbf{D}^{(\text{a-s})}$ and $\boldsymbol{\delta}^{(\text{a-s})}$ that agree with those obtained by Watson to within a phase factor of ± 1.[104] The phase factor of ± 1 reflects the fact that Watson uses a different phase convention for the columns of the $\mathbf{l}$ matrices. The choice of phase convention will not affect the magnitude of individual Franck-Condon factors between harmonic oscillator basis states, but may affect the relative signs of the overlap integrals. Therefore, if we wish to be able to calculate interference effects arising from admixture of harmonic oscillator basis states involved in the initial and final states of a given transition, we must ensure that the phase convention used to define the normal modes given by the columns of the $\mathbf{l}$ matrix is consistent with the phases used to determine the signs of the matrix elements between the basis states. In the current work, we have chosen the columns of $\mathbf{l}''$ to be consistent with the parameters of the X̃-state effective Hamiltonian reported by Herman and coworkers[79,81] and expanded by Jacobson and coworkers.[82,86,125]. The columns of $\mathbf{l}'$ are chosen to have positive overlap with the corresponding columns of $\mathbf{l}''$. We have chosen $\mathbf{l}''_{\mathbf{R}}$ and $\mathbf{l}'_{\mathbf{R}}$ so that positive displacement corresponds to right-handed rotation around the axes as defined in Figure 3-3.

Recent spectral analysis published since the Tobiason *et al.* force field[124] has uncovered new parameters relevant to the force field of the Ã-state of acetylene. Most notably, the fundamental frequencies ν_1' of $^{12}C_2H_2$ (Ref. 92) and ν_2' and ν_3' of $^{13}C_2H_2$ (Ref. 122) have been found and a complete set of $^{12}C_2H_2$ x_{ij} cross anharmonicities

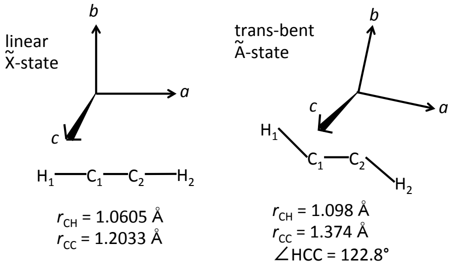

Figure 3-3: The labeling of the acetylene nuclei and the orientation of the principal inertial axis system used in the construction of **l** matrices. The *c*-axis points out of the page towards the viewer. The equilibrium geometries used in the calculation are also shown.

has now been determined.[88,92–94,126–128] Jiang *et al.* have recently reported an updated force field for the Ã-state that takes the large amount of new data into account.[122] We have used the updated force field from "Fit Method I" in Ref. 122 (Column 1 of Table 6 in the reference) in our determination of the coordinate transformations reported below.

The **l** matrices (Tables 3.4 and 3.5) were obtained by diagonalizing the **FG** matrix as described by Wilson, Decius and Cross,[111] and the $\mathbf{l_R}$ matrices are calculated from

$$(\mathbf{l_R})_{i\alpha,\beta} = \sum_{\gamma\delta} e_{\alpha\gamma\delta} m_i^{1/2} (\mathbf{r_e})_{i\delta} (\mathbf{I_e}^{-1/2})_{\gamma\beta}, \tag{3.85}$$

where the i subscript refers to the i^{th} nucleus, Greek letter subscripts refer to Cartesian directions, $e_{\alpha\gamma\delta}$ is the antisymmetric unit tensor, and $\mathbf{I_e}$ is the moment of inertia tensor evaluated at the equilibrium geometry. The equilibrium Eckart rotation matrix is then obtained by solving Eq. (3.19) at the equilibrium X̃-state geometry ($\mathbf{q}'' = \mathbf{0}$). That is,

$$\tilde{\mathbf{l}}'_{\mathbf{R}} \mathbf{\Lambda_e} \mathbf{m}^{1/2} \mathbf{r}''_{\mathbf{e}} = \mathbf{0}. \tag{3.86}$$

In order to illustrate the effects of axis-switching and curvilinear modes on the coordinate transformation, we first report the zeroth-order transformation (Table 3.6),

Table 3.4: Elements of the $\mathbf{l}''$ and $\mathbf{l}''_{\mathbf{R}}$ matrices for the $\tilde{\mathrm{X}}$ state of acetylene evaluated using the force field of Ref. 123.

	$\mathbf{l}''$						$\mathbf{l}''_{\mathbf{R}}$		
	q''_1	q''_2	q''_{4b}	q''_3	q''_{5b}	q''_{5c}	R''_a (q''_{4c})	R''_b	R''_c
a_{H_1}	−0.6420	−0.2964	0	−0.6791	0	0	0	0	0
b_{H_1}	0	0	0.5520	0	0.6792	0	0	0	−0.4419
c_{H_1}	0	0	0	0	0	0.6792	0.5520	0.4419	0
a_{C_1}	0.2964	−0.6420	0	0.1968	0	0	0	0	0
b_{C_1}	0	0	−0.4419	0	−0.1968	0	0	0	−0.5520
c_{C_1}	0	0	0	0	0	−0.1968	−0.4419	0.5520	0
a_{C_2}	−0.2964	0.6420	0	0.1968	0	0	0	0	0
b_{C_2}	0	0	0.4419	0	−0.1968	0	0	0	0.5520
c_{C_2}	0	0	0	0	0	−0.1968	0.4419	−0.5520	0
a_{H_2}	0.6420	0.2964	0	−0.6792	0	0	0	0	0
b_{H_2}	0	0	−0.5520	0	0.6792	0	0	0	0.4419
c_{H_2}	0	0	0	0	0	0.6792	−0.5520	−0.4419	0

obtained from

$$\boldsymbol{\delta}^{(0)} = (\boldsymbol{\gamma}')^{1/2}\left[\tilde{\mathbf{l}}'\mathbf{m}^{1/2}\mathbf{r}''_{\mathbf{e}} - \tilde{\mathbf{l}}'\mathbf{m}^{1/2}\mathbf{r}'_{\mathbf{e}}\right] \tag{3.87}$$

$$\mathbf{D}^{(0)} = (\boldsymbol{\gamma}')^{1/2}\tilde{\mathbf{l}}'\mathbf{l}''(\boldsymbol{\gamma}'')^{-1/2}. \tag{3.88}$$

Next, we report corrections to the zeroth-order transformation. The coordinate transformation with first-order correction for axis-switching effects is calculated from Eqs. (3.26–3.27), and the parameters are tabulated in Table 3.7. The geometry change results in an equilibrium Eckart rotation of −2.143° about the c-axis. The coordinate transformation in the basis of curvilinear normal mode coordinates is calculated from Eqs. (3.41–3.42), and the parameters are tabulated in Table 3.8.

Inspection of the parameters tabulated in Tables 3.6–3.8 reveals the relative magnitudes of the corrections to the zeroth-order coordinate transformation. Axis-switching has a relatively strong effect (∼10%) on the shift of origin for ν'_1, and a weaker effect on the Duschinsky rotation of in-plane vibrational modes. The first order correction term (the second term in Eq. 3.27) only affects the Duschinsky rotation in the totally symmetric a_g block of $\mathbf{D}$, because rotation about the c-axis has the same symmetry as a_g vibration, which leads to a first-order interaction between axis switching and a_g

Table 3.5: Elements of the $\mathbf{l}'$ and $\mathbf{l}'_{\mathbf{R}}$ matrices for the Ã state of acetylene evaluated using the force field of Jiang *et al.*[122]

	$\mathbf{l}'$						$\mathbf{l}'_{\mathbf{R}}$		
	q'_1	q'_2	q'_3	q'_5	q'_6	q'_4	R'_a	R'_b	R'_c
a_{H_1}	−0.4757	−0.1970	0.4539	−0.4804	0.4812	0	0	0	−0.1695
b_{H_1}	0.4811	0.0150	0.3787	0.4801	0.4804	0	0	0	−0.3535
c_{H_1}	0	0	0	0	0	0.6792	0.6036	0.3683	0
a_{C_1}	0.1630	−0.6750	−0.0836	0.1392	−0.1391	0	0	0	0.1035
b_{C_1}	−0.1251	−0.0720	−0.3789	−0.1391	−0.1392	0	0	0	−0.5792
c_{C_1}	0	0	0	0	0	−0.1968	−0.3683	0.6036	0
a_{C_2}	−0.1629	0.6751	0.0836	0.1392	−0.1391	0	0	0	−0.1034
b_{C_2}	0.1252	0.0721	0.3789	−0.1391	−0.1392	0	0	0	0.5793
c_{C_2}	0	0	0	0	0	−0.1968	0.3683	−0.6036	0
a_{H_2}	0.4758	0.1971	−0.4539	−0.4804	0.4812	0	0	0	0.1696
b_{H_2}	−0.4810	−0.0150	−0.3787	0.4801	0.4793	0	0	0	0.3535
c_{H_2}	0	0	0	0	0	0.6792	−0.6036	−0.3683	0

Table 3.6: Elements of the zeroth order Duschinsky matrix $\mathbf{D}^{(0)}$ and displacement vector $\boldsymbol{\delta}^{(0)}$ for the Ã—X̃ transition of acetylene calculated by Eqs. (3.87–3.88) from the $\mathbf{l}$ matrices from Tables 3.4 and 3.5 (using the force fields of Ref. 123 for the X̃ state and Ref. 122 for the Ã state.)

	$\mathbf{D}^{(0)}$						
	q''_1	q''_2	q''_{4b}	q''_3	q''_{5b}	q''_{5c}	$\boldsymbol{\delta}^{(0)}$
q'_1	0.8081	0.0415	1.5628	0	0	0	−4.3103
q'_2	−0.1303	0.8490	0.0857	0	0	0	−2.1803
q'_3	−0.3764	−0.1134	0.9754	0	0	0	−6.2585
q'_5	0	0	0	0.6672	1.424	0	0
q'_6	0	0	0	−0.3428	0.7324	0	0
q'_4	0	0	0	0	0	1.0275	0

vibration. The first order correction decreases the Duschinsky rotation between trans bend and symmetric stretch by about 5% and increases Duschinsky rotation between trans bend and C–C stretch by about 3%.

The use of curvilinear coordinates, on the other hand, appears to have a much more profound impact on the coordinate transformation. The rectilinear displacement vectors $\boldsymbol{\delta}^{(0)}$ and $\boldsymbol{\delta}^{(\text{a-s})}$ both exhibit a large displacement along the symmetric C—H stretch coordinate, q'_1, even though the equilibrium geometries of the Ã and X̃ states have nearly identical C—H bond lengths (Figure 3-3). The use of curvilinear coordinates removes displacement along $\bar{q}'_1$ almost entirely. The reason for the displacement

Table 3.7: Elements of the Duschinsky matrix $\mathbf{D}^{(\text{a-s})}$ and displacement vector $\boldsymbol{\delta}^{(\text{a-s})}$ for the Ã—X̃ transition of acetylene, with first-order corrections for axis switching, are calculated from equations Eqs. (3.26–3.27), evaluated using the $\mathbf{l}$ and $\mathbf{l}_{\mathbf{R}}$ matrices from Tables 3.4 and 3.5.

	$\mathbf{D}^{(\text{a-s})}$						
	q''_1	q''_2	q''_{4b}	q''_3	q''_{5b}	q''_{5c}	$\boldsymbol{\delta}^{(\text{a-s})}$
q'_1	0.7571	0.0718	1.4347	0	0	0	−3.931
q'_2	−0.1104	0.8396	0.1247	0	0	0	−2.257
q'_3	−0.3497	−0.1244	1.0154	0	0	0	−6.321
q'_5	0	0	0	0.6917	1.3700	0	0
q'_6	0	0	0	−0.3297	0.7593	0	0
q'_4	0	0	0	0	0	1.0275	0

Table 3.8: Elements of the Duschinsky matrix $\mathbf{D}^{(\text{c-l})}$ and displacement vector $\boldsymbol{\delta}^{(\text{c-l})}$ for the Ã—X̃ transition of acetylene, performed in the basis of harmonic wavefunctions of curvilinear normal mode coordinates, are calculated from equations Eqs. (3.41–3.42), evaluated using the $\mathbf{l}$ matrices from Tables 3.4 and 3.5.

	$\mathbf{D}^{(\text{c-l})}$						
	$\bar{q}''_1$	$\bar{q}''_2$	$\bar{q}''_{4b}$	$\bar{q}''_3$	$\bar{q}''_{5b}$	$\bar{q}''_{5c}$	$\boldsymbol{\delta}^{(\text{c-l})}$
$\bar{q}'_1$	0.9215	0.1805	0.0144	0	0	0	0.1021
$\bar{q}'_2$	−0.0916	0.8404	−0.0893	0	0	0	−0.9681
$\bar{q}'_3$	−0.0084	0.0431	1.3240	0	0	0	−7.400
$\bar{q}'_5$	0	0	0	0.9427	−0.0733	0	0
$\bar{q}'_6$	0	0	0	0.0176	1.0350	0	0
$\bar{q}'_4$	0	0	0	0	0	1.0275	0

in the rectilinear stretching coordinate is that the rectilinear bending coordinate q'_3 stretches the C—H bond. The result is that in order to arrive at the linear X̃-state equilibrium from the trans-bent Ã-state equilibrium it is necessary to straighten the molecule by a negative displacement in q'_3 and then contract the elongated C—H bond by a negative displacement in q'_1. The small value of $\delta_1^{(\text{c-l})}$ is consistent with the experimental observation that there is very little Franck-Condon activity in ν'_1. Furthermore, the rectilinear coordinate transformations (Tables 3.6–3.7) exhibit a large Duschinsky rotation between the bending and C—H stretch coordinates in both the a$_g$ block ($D_{1',4b''}$) and the b$_u$ block ($D_{5',5b''}$), whereas the use of the curvilinear harmonic basis decreases these off-diagonal elements of the Duschinsky matrix by almost two orders of magnitude.

3.4 Evaluation of Calculated FC intensities for the *gerade* modes

We first evaluate FC intensities for transitions involving only *gerade* vibrational modes. The results are compared with experiment and with the calculation by Watson.[104] Transitions involving *ungerade* modes will be considered in Chapter 4.

3.4.1 $v_3' \leftarrow 0$ Progession

The most prominent feature in the ground state $\tilde{\mathrm{A}} \leftarrow \tilde{\mathrm{X}}$ absorption spectrum is the strong Franck-Condon progression in ν_3'. Table 3.9 and Figure 3-4 provide a comparison between experimental absorption data and calculated relative intensities using both the Tobiason *et al.*[124] force field and the Jiang *et al.*[122] force field, and using the three types of coordinate transformation discussed in Section 3.3. The oscillator strengths in Table 3.9 were calculated according to

$$f = \frac{4\pi m_e c \nu_{0\text{-}0}}{3\hbar e^2} \left|\langle \Psi'_{\mathrm{el}} | \mu_c | \Psi''_{\mathrm{el}} \rangle\right|^2 \left|\langle \Psi'_{\mathrm{vib}} | q''_4 | \Psi''_{\mathrm{vib}} \rangle\right|^2 , \tag{3.89}$$

where $\nu_{0\text{-}0}$ is the transition frequency between the ground vibrational levels of the two electronic states (in wavenumber units), m_e and e are the electron mass and charge and c is the speed of light. The quantity $\langle \Psi'_{\mathrm{el}} | \mu_c | \Psi''_{\mathrm{el}} \rangle$ was estimated by taking the value of the *ab initio* electronic transition dipole moment (plotted in Figure 3-1) at the geometry $\mathbf{q_0''}$ (defined in Eq. 3.78) that maximizes the exponential factor in the vibrational overlap integral.

Inspection of the trends in Table 3.9 reveals that the calculations appear to underestimate the absolute magnitude of the vibrationless 0–0 transition by approximately three orders of magnitude. The Franck-Condon factor for the 0–0 transition is sensitively dependent on the displacement in equilibrium geometry between the two electronic states, and the equilibrium geometries are far from the geometry $\mathbf{q_0}$

Table 3.9: Observed oscillator strengths (f_{obs}) for the $v_3' \leftarrow 0$ progression of the $\tilde{\text{A}} \leftarrow \tilde{\text{X}}$ transition of acetylene and calculated vibrational intensity factors obtained using two different $\tilde{\text{A}}$-state force fields and three different types of coordinate transformation.

$\tilde{\text{A}}$-State FF:		Tobiason (Ref. 124)		Jiang (Ref. 122)					
Coord. trans.:		(a-s)^a		(0)^b		(a-s)^a		(c-l)^c	
v_3'	$f_{\text{obs}}{}^d$ $\times 10^8$	f_{calc} $\times 10^{12}$	$f_{\text{obs}}/f_{\text{calc}}$ $\times 10^3$	f_{calc} $\times 10^{12}$	$f_{\text{obs}}/f_{\text{calc}}$ $\times 10^3$	f_{calc} $\times 10^{12}$	$f_{\text{obs}}/f_{\text{calc}}$ $\times 10^3$	f_{calc} $\times 10^{12}$	$f_{\text{obs}}/f_{\text{calc}}$ $\times 10^3$
0		1.22		0.744		0.977		3.95	
1	4.2	19.9	2.11	10.9	3.86	14.0	3.01	49.4	0.849
2	36	158	2.28	77.6	4.64	97.9	3.68	321	1.12
3	145	819	1.77	360.	4.03	447	3.24	1430	1.01
4	510	3103	1.64	1220	4.18	1500	3.41	4930	1.03
5	1200	9170	1.31	3220	3.73	3910	3.07	13970	0.859
mean:			1.82		4.09		3.28		0.976
std. dev.:			21%		8.7%		8.3%		12%

---

[a] Calculated using the coordinate transformation in Eqs. (3.26–3.27).

[b] Calculated using the coordinate transformation in Eqs. (3.87–3.88).

[c] Calculated using the coordinate transformation in Eqs. (3.41–3.42).

[d] Values from Ref. 60. The measurement uncertainty is 15%.

that maximizes the exponential factor in the vibrational overlap integral. Using the curvilinear coordinate transformation in Table 3.8, we find that $\mathbf{q_0}$ is located at a displacement of $(\bar{q}_1'', \bar{q}_2'', \bar{q}_{4b}'') = (-0.18, 0.68, 3.17)$. Because the $\tilde{\text{A}}$—$\tilde{\text{X}}$ transition intensity accumulates at geometries involving large-amplitude displacement in the trans-bending coordinate, q_3', the failure of the calculation to match the experimentally observed oscillator strength is likely due to the fact that the large-amplitude q_3' displacement is not well described in the harmonic basis. The use of curvilinear normal mode coordinates mitigates the discrepancy, but only by a factor of ∼3–4. In Figure 3-5, the vibrational intensity factor for the 0–0 transition is plotted as a function of $\delta_{3'}^{\text{(c-l)}}$ with all other parameters held fixed to the values in Table 3.8. The intensity increases rapidly as the magnitude of $\delta_{3'}^{\text{(c-l)}}$ decreases. A change in $\delta_{3'}^{\text{(c-l)}}$ by ∼20% would give rise to a factor of $\sim 10^3$ increase in intensity. Including higher-order corrections for the anharmonicity in the trans-bending mode may help to bring the calculation into better agreement with experiment, but that is beyond the scope of the current work.

Although the absolute oscillator strength of the 0–0 transition is underestimated, the trend in the scaled vibrational intensities for the $v_3' \leftarrow 0$ progression (shown

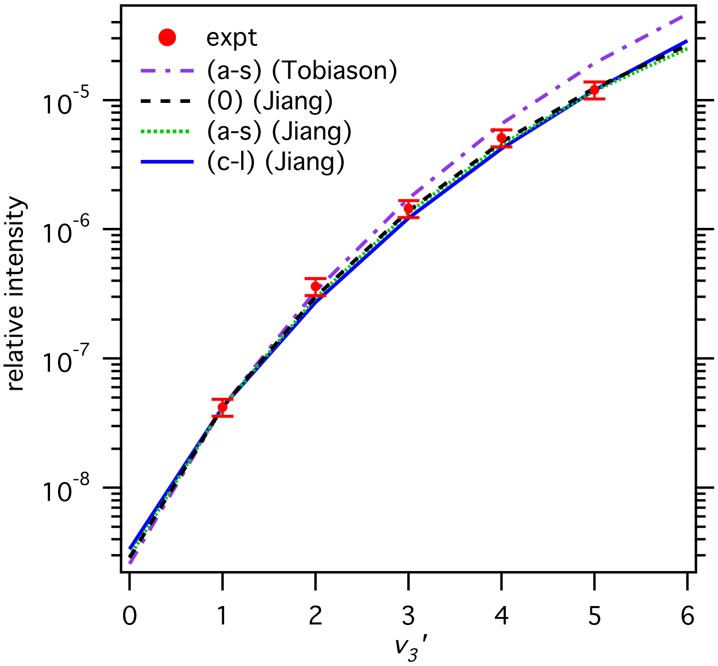

Figure 3-4: The experimentally observed oscillator strengths from Ref. 60 for the $v_3' \leftarrow 0$ progression for the $\tilde{\mathrm{A}} \leftarrow \tilde{\mathrm{X}}$ system of acetylene are plotted with the reported error of 15% (red markers). Calculated vibrational intensity factors are shown for comparison. The calculated values were obtained using the Tobiason *et al.*[124] force field with the axis-switching transformation in Table 3.7 (purple dash-dot curve); and the Jiang *et al.*[122] force field with the zero-order transformation of Table 3.6 (black dashed curve), the axis-switching transformation of Table 3.7 (green dotted curve), and the curvilinear transformation of Table 3.8. The calculations are scaled to match the experimental f_{obs} for $v_3' = 1$.

in Figure 3-4) is in good agreement with experiment. The Franck-Condon factors obtained using the Tobiason *et al.* force field match Watson's calculation, which used the same force field and coordinate transformation. These intensities increase slightly too rapidly with v_3'. The trend in intensities calculated with the Jiang *et al.* force field seems to provide excellent agreement with experiment, such that it is difficult to distinguish the traces on the scale plotted in Figure 3-4. Throughout the rest of this series of papers, we will use the more recent Jiang force field.

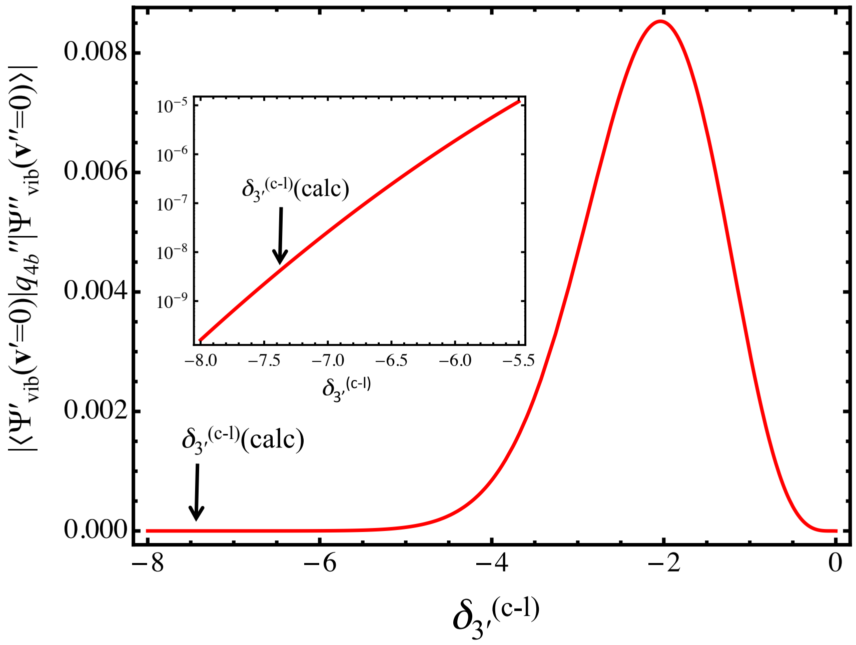

Figure 3-5: The magnitude of the vibrational intensity factor $|\langle\Psi'_{\mathrm{vib}}(\mathbf{v}'=0)|q''_{4b}|\Psi''_{\mathrm{vib}}(\mathbf{v}''=0)\rangle|^2$ for the vibrationless 0–0 transition is shown as a function of the displacement in the trans-bending mode $\delta_{3'}$ between the equilibrium geometries of the $\tilde{\mathrm{A}}$ and $\tilde{\mathrm{X}}$ states of acetylene. All other parameters of the coordinate transformation are held fixed to the values in Table 3.8. The arrow points to the calculated value of $\delta_{3'}^{\text{(c-l)}}$, and the inset displays a magnified region plotted on a logarithmic scale.

3.4.2 Emission from $\tilde{\mathrm{A}}(2^j3^k)$

Quantitative experimental intensity data is also available from dispersed fluorescence measurements in the dominant intensity Franck-Condon progressions ($2^j_m\mathrm{V}^k_n$), where V refers to quanta in the trans-bending mode v_3' or v_4''.[129] Trends in emission intensities from the $\tilde{\mathrm{A}}$-state origin, 3^2, 2^13^1, and 2^13^2 levels are shown in Figure 3-6, and the calculated intensities obtained from the coordinate transformations in Tables 3.6–3.8 are shown for comparison. The dispersed fluorescence spectra from Ref. 129 were recorded on a CCD (charge-coupled device) detector attached to a monachromator, and the relative intensities in each emission spectrum were calibrated by dispersing a halogen lamp to the same detector. Therefore, the relative intensities within each spectrum are well determined. However, due to variation and fluctuation in the intensity of the laser power used to excite each spectrum, the relative intensities between spectra from different Ã-state vibrational levels was not determined. As a result, the reported intensities in Ref. 129 are normalized relative to the strongest transition in each spectrum. For comparison, the calculated intensities shown in Figure 3-6 are normalized in the same way, by setting the strongest calculated vibronic intensity in each emission spectrum equal to one.

It is evident in Figure 3-6 that the effects of using curvilinear normal mode coordinates are much more profound than the effects of correcting for axis switching. In fact, the emission intensities obtained from the axis-switching coordinate transformation (Table 3.7) are so close in magnitude to those obtained from the zero-order coordinate transformation (Table 3.6) that it is difficult to tell the traces apart in some of the panels of the figure. The various calculations do a comparable job at reproducing the emission trends along v_2''. The zero-order transformation and the axis-switching transformation correctly locate the node in emission from $2^1 3^1$ and $2^1 3^2$ at $v_2'' = 2$, whereas the curvilinear transformation places the node at $v_2'' = 1$. All three calculations underestimate the intensity of the second lobe relative to the first (probably as a result of anharmonicity), but the curvilinear transformation performs slightly better at predicting the shape of the overall intensity envelope along ν_2'' progressions.

As one would expect, the curvilinear coordinate transformation notably improves the performance of the calculation at high quanta in the bending mode, ν_4''. The rectilinear calculations fail to reproduce the emission intensity into ν_4'' above ∼12 quanta of excitation. The reason for this is that the rectilinear coordinate transformations overestimate the Duschinsky rotation between q_1' and q_{4b}'' (see Tables 3.6 and 3.7) due to the bend-stretch coupling induced by the coordinate system (as illustrated in Figure 3-2). On the other hand, the curvilinear calculation produces near-quantitative results up to 22 quanta of bend excitation. This is a remarkable result, given that this amount of bending energy is almost enough to reach the acetylene↔vinylindene reaction barrier at ∼15,200 cm^{-1}. The experimentally observed Franck-Condon factors reported in Ref. 129 are based on a polyad fit model that takes into account fractionation of intensity within the pure-bending polyads with conserved quantum number $N_B = v_4'' + v_5''$. Therefore, most of the important resonance interactions are already taken into account by the experiment, and the observed intensities represent the vibrational intensity into the *zero-order* bright state, which has all of the excitation in the trans-bend. Because the pure-bending polyad quantum number is known to be approximately conserved up to at least 22 quanta of bend excitation,[85] it is therefore not too surprising that a harmonic calculation—performed in the correct basis—reproduces the experimentally observed intensity pattern.

3.5 Conclusions

There are obvious limitations to treating FC factors of the Ã—X̃ system of acetylene in the harmonic basis, and we do not expect complete quantitative agreement with experimental intensities. Because of the large displacement in equilibrium geometry between the two states, the harmonic calculation is unable to reproduce the observed oscillator strength for the vibrationless 0–0 transition. However, we have shown that a simple computational method can effectively reproduce qualitative trends in the spectrum.

We have shown how the methods developed by Watson[104,106,119] for calculating Franck-Condon factors for electronic transitions involving linear↔non-linear geometry changes may be generalized to full dimensionality. The methods outlined in this paper may also be applied to any linear↔non-linear transition, provided that most of the value of the integral does not accumulate at the linear geometry, where the $n_{\text{vib}} = 3N - 6$ treatment becomes invalid. One of the components of a degenerate bending mode may always be chosen to correlate with a-axis rotation in the non-linear state. The angular component of this mode may be constrained and its $\mathbf{l}$ vector may then be moved into $\mathbf{l_R}$. To simplify the integration of the generating function, the remaining degenerate bending modes may be treated in the Cartesian two-dimensional harmonic oscillator basis, and the resulting integral will have a form similar to Eq. (3.70). The basis set conversion to (v, l) quantum numbers that describe the two-

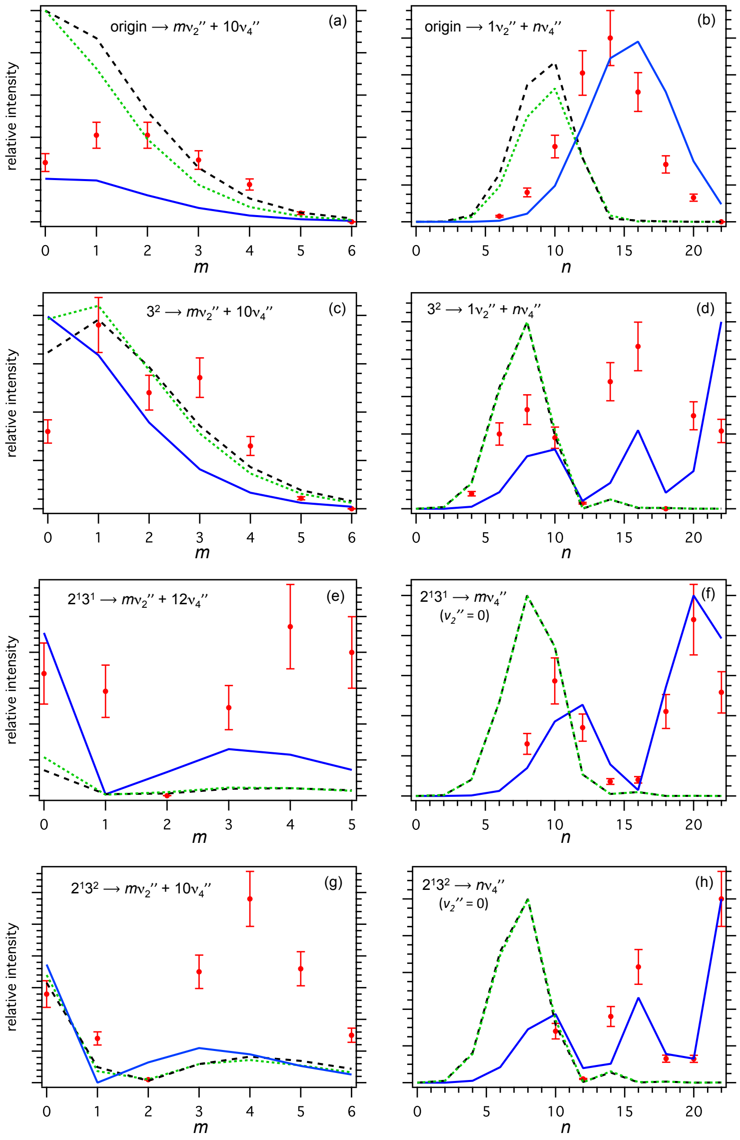

Figure 3-6: Relative emission intensities for a selection of $(2^j_m \mathrm{V}^k_n)$ vibrational transitions of the acetylene $\tilde{\mathrm{A}} \rightarrow \tilde{\mathrm{X}}$ transition. Emission is shown from the $\tilde{\mathrm{A}}$ origin (panels a and b); 3^2 (panels c and d); $2^1 3^1$ (panels e and f); and $2^1 3^2$ (panels g and h). The left column of panels displays progressions in v_2'' (v_4'' held constant), and the right column of panels displays progressions in v_4'' (v_2'' held constant). The choice of which progression to plot was based on the availability of the most complete set of experimental data for comparison. Experimental intensities from dispersed fluorescence measurements were taken from Ref. 129 and are displayed as points with 15% uncertainty. The calculated intensities shown are the sum of the squares of vibrational overlap intensities to $|l_4''| = 0$ and $|l_4''| = 2$, obtained using the zero-order coordinate transformation in Table 3.6 (dashed black curves), the axis-switching coordinate transformation in Table 3.7 (green dotted curves), and the curvilinear coordinate transformation in Table 3.8 (blue solid curves). The observed and calculated intensities in the emission spectrum from each $\tilde{\mathrm{A}}$-state vibrational level are normalized relative to the strongest vibronic transition in the spectrum.

dimensional harmonic oscillators in polar coordinates may be performed after the overlap integrals have been calculated.

Furthermore, in π-bonded systems it is very common to have large-amplitude bending displacements between the equilibrium geometries of different electronic states. The reason is that an electronic $\pi^* \leftarrow \pi$ excitation effectively changes the sp^n hybridization, which leads to a qualitative change in equilibrium bond angle. As a result, such electronic transitions are accompanied by long Franck-Condon progressions in modes involving the displaced bending coordinates. As demonstrated in this paper, simple methods for working in curvilinear normal mode coordinates are capable of producing notable improvement the intensity progressions at high quanta of bend excitation that occur in these cases.

Finally, our FC calculations have provided a test of the new force field for $\tilde{\mathrm{A}}$-state acetylene reported by Jiang.[122] The force field takes into account new data that was not previously available. The new force field appears to produce improved agreement with experiment along the dominant intensity FC progressions.

3.6 Acknowledgements

The author is grateful to Robert W. Field for providing guidance and mentorship on this work. The author would also like to thank James K. G. Watson, Joshua H. Baraban, P. Bryan Changala, and Jun Jiang for helpful discussions. This material is based on work supported by the U.S. Department of Energy, Office of Science, Chemical Sciences, Geosciences and Biosciences Division of the Basic Energy Sciences Office, under Award Number DE-FG0287ER13671.

Chapter 4

Full Dimensional Franck-Condon Factors for the Acetylene $\tilde{\mathbf{A}}\ {}^1\mathbf{A_u}$—$\tilde{\mathbf{X}}\ {}^1\mathbf{\Sigma_g^+}$ Transition. II. Vibrational Overlap Factors for Levels Involving Excitation in ***ungerade*** Modes

Abstract

A full dimensional Franck-Condon calculation has been applied to the $\tilde{\mathrm{A}}\ {}^1\mathrm{A}_u$—$\tilde{\mathrm{X}}\ {}^1\Sigma_g^+$ transition in acetylene in the harmonic normal mode basis. Details of the calculation are discussed in Chaper 3. To our knowledge, this is the first full-dimensional Franck-Condon calculation on a tetra-atomic molecule undergoing a linear-to-bent geometry change. In the current work, the vibrational intensity factors for levels involving excitation in *ungerade* vibrational modes are evaluated. Because the Franck-Condon integral accumulates away from the linear geometry, we have been able to treat the out-of-plane component of trans bend (ν_4'') in the linear $\tilde{\mathrm{X}}$ state in the rotational part of the problem, restoring the χ Euler angle and the a-axis Eckart conditions. A consequence of the Eckart conditions is that the out-of-plane component of ν_4'' *does not participate* in the vibrational overlap integral. This affects the structure of the coordinate transformation and the symmetry of the vibrational wavefunctions used in the overlap integral, and results in propensity rules involving the bending modes of the $\tilde{\mathrm{X}}$ state that were not previously understood. We explain the origin of some of the unexpected propensities observed in IR-UV laser-induced fluorescence

spectra, and we calculate emission intensities from bending levels of the Ã state into bending levels of the X̃ state, using normal bending mode and local bending mode basis sets. Our calculations also reveal Franck-Condon propensities for the Cartesian components of the cis bend (ν_5''), and we predict that the best Ã-state vibrational levels for populating X̃-state levels with large amplitude bending motion localized in a single C–H bond (the acetylene↔vinylidene isomerization coordinate) involve a high degree of excitation in ν_6' (cis-bend). Mode ν_4' (torsion) populates levels with large amplitude counter-rotational motion of the two hydrogen atoms.[a]

4.1 Introduction

The Ã ^{1}A$_u$(C$_{2h}$)—X̃ $^1\Sigma_g^+$(D$_{\infty h}$) transition in acetylene has received extensive attention[59–95] because it was the first molecular system in which a qualitative change in geometry and symmetry accompanying an electronic excitation was proven by spectroscopic methods.[59–61] Of particular interest to the chemical community are the acetylene↔vinylidene[85,130–133] and cis↔trans[95,107,127,134,135] isomerizations that take place on the X̃-state and Ã-state surfaces, respectively. Because so much detailed work has been done on these electronic states, acetylene is a prototype for studying the spectroscopic signatures of isomerizing systems and the vibrational dynamics that occur at chemically interesting regions of the potential surface. Considerable work has been done by the Field group and collaborators to find stimulated emission pumping (SEP) and dispersed fluorescence (DF) schemes for populating levels of the X̃ state relevant to the acetylene↔vinylidene isomerization. However, highly excited vibrational levels in the vicinity of reaction barriers are difficult to access because most of the amplitude of the vibrational wavefunction is at geometries far from equilibrium. This has motivated our calculation of full-dimensional Franck-Condon factors for the Ã—X̃ system.

The method used to calculate full-dimensional Franck-Condon factors is detailed in Chapter 3. This chapter is intended to be accessible to those who have not read Chapter 3, but readers should be aware of the following details of the calculation.

1. The vibrational overlap integrals are performed in the harmonic normal mode

---

[a] This chapter is reprinted with permission from G. B. Park, J. H. Baraban, and R. W. Field, *J. Chem. Phys.* **141**, 134305 (2014). Copyright 2014, AIP Publishing LLC.

basis, using a curvilinear coordinate transformation. There are quantitative discrepancies between the calculated and observed intensities. Most notably, the calculation underestimates the overall oscillator strength for the vibrationless 0–0 intensity by ∼3 orders of magnitude. The most likely explanation is that the large amplitude displacement along the trans-bend coordinate between the equilibrium geometries of the Ã and X̃ states is not well described by the harmonic treatment, which is expected to give quantitative results only at small amplitudes. As shown in Chapter 3, the 0–0 vibrational overlap depends sensitively on the displacement between the equilibrium geometries. In spite of this discrepancy, the qualitative trends in calculated FC factors are in agreement with the experimental observations, especially for progressions involving the trans-bending mode, and we believe that the calculations yield qualitatively accurate and meaningful trends, when normalized to the 0–0 intensity. It is likely that higher-order calculations that take into account vibrational anharmonicity will succeed at achieving better quantitative results, but these are beyond the scope of the current work.

2. The angular component of the doubly-degenerate trans bend (ν_4'') in the linear X̃ state has been treated as a rotation. The wavefunction used for this doubly degenerate mode has the form shown in Eq. (3.68). The angular factor $\exp(il_4\phi_4)$ is excluded from the vibrational integral and is treated instead in the rotational integral. This treatment is valid because most of the FC integral accumulates away from the linear geometry. As shown in Section 3.2.3, the vibrational coordinates of the X̃ state satisfy rotational Eckart conditions for the a-axis, and the treatment is equivalent to constraining the vibrational coordinate q_4'' to lie in the plane of the equilibrium geometry of the trans-bent Ã state. An important consequence is that the out-of-plane component of ν_4'' *does not contribute* to vibrational overlap with the Ã state. This fact plays a major role in the vibrational propensities, discussed in Sections 4.4 and 4.5.

3. In Chapter 3, we found that a curvilinear formulation of the normal mode

> coordinate transformation provides better agreement with experiment than the coordinate transformation used by Watson[104], which involves rectilinear normal mode coordinates with a first-order correction for axis-switching effects. The improvement is most profound for the bending progressions in v_4''. We also found that the newer Ã-state force field parameters of Ref. 122 provide better agreement with experimental intensities than the parameters of Ref. 124. In the present chapter, we provide a brief comparison in Section 4.3.1 between the performance of the curvilinear coordinate transformation (Table 3.8) and the rectilinear transformation with corrections for axis-switching (Table 3.7). The subsequent calculations in Sections 4.3.2–4.5 use the curvilinear transformation exclusively.

In this work, we apply the methods described in Chapter 3 to calculate vibrational intensity factors for levels of the acetylene Ã–X̃ system that involve excitation in *ungerade* modes. In Section 4.3, we compare our results to experimentally-determined intensities from IR-UV double resonance pumped DF measurements.[86] In Section 4.4, we use our calculation to explain experimentally observed propensities in IR-UV pumped laser induced fluorescence experiments. Finally, in Section 4.5, we perform a normal to local mode basis transformation and apply our results to the problem of accessing large amplitude local-bending bright states relevant to the acetylene↔vinylidene isomerization.

4.2 Polyad structure and bending dynamics in the Ã—X̃ system

The acetylene↔vinylidene isomerization that occurs on the X̃-state surface and the cis↔trans isomerization that occurs on the Ã-state surface both involve primarily bending degrees of freedom. We will therefore provide some background on the properties of bending vibrations in acetylene, and how the bending modes relate to overall vibrational polyad structures. The frequencies, symmetries, and descriptions of the normal modes of the $\tilde{\mathrm{X}}$ and $\tilde{\mathrm{A}}$ states are summarized in Tables 3.2 and 3.3, respectively.

4.2.1 $\tilde{\mathrm{X}}$-state polyad structure

The vibrational Hamiltonian of the $\tilde{\mathrm{X}}$ state of acetylene is known to be approximately block diagonal in the polyad-forming quantum numbers

$$N_s = v_1'' + v_2'' + v_3'' \tag{4.1}$$

$$N_{\mathrm{res}} = 5v_1'' + 3v_2'' + 5v_3'' + v_4'' + v_5'' \tag{4.2}$$

$$l = l_4 + l_5, \tag{4.3}$$

up to energies of at least 15,000 cm^{-1}.[85] In this chapter, polyads of the $\tilde{\mathrm{X}}$ state will be identified by the shorthand notation $\{N_s, N_{\mathrm{res}}, l\}$, followed by a $\mathrm{D}_{\infty\mathrm{h}}$ vibrational symmetry label. The zero-order states that comprise each polyad are notated $(v_1, v_2, v_3, v_4^{l_4}, v_5^{l_5})$. These basis states have well-defined g/u symmetry and may be symmetrized to have well-defined $+/-$ total parity. The parity and g/u symmetry are conserved by the vibrational Hamiltonian, and are therefore also conserved within each polyad.

In the absence of excitation in the stretching modes, $N_s = 0$ and the bending modes $\nu_4''(\pi_g)$ and $\nu_5''(\pi_u)$ form pure bending polyads with conserved polyad numbers

$$N_B = N_{\mathrm{res}} = v_4'' + v_5'' \tag{4.4}$$

$$l = l_4 + l_5. \tag{4.5}$$

As we shall see in Section 4.5, the pure bending polyads may be described in the basis of normal modes, as above, or in the basis of local bending modes. At high quanta of bending excitation, the local modes become a better zero-order description of the vibrational eigenstates.[136] In the absence of axis-switching, the selection rule for l arises from the c-axis electronic transition moment for the $\tilde{\mathrm{A}}$—$\tilde{\mathrm{X}}$ system, which leads to $K' - l'' = \pm 1$ for the projection of angular momentum on the a-axis.

4.2.2 Bending modes of the $\tilde{\text{A}}$ state

The torsion $\nu_4'(\text{a}_u)$ and cis-bending $\nu_6'(\text{b}_u)$ modes of the $\tilde{\text{A}}$ state are near-degenerate and interact through strong Darling-Dennison[93,94] and Coriolis resonances.[89] In this chapter, we refer to polyads with $v_4' + v_6' = n$ as B^n. Modes ν_4' and ν_6' correlate with the out-of-plane and in-plane components, respectively, of the $\tilde{\text{X}}$-state cis-bend, ν_5''. This gives rise to a Franck-Condon propensity $v_5'' = v_4' + v_6'$ in the $\tilde{\text{A}}$—$\tilde{\text{X}}$ spectrum.

Because of the large displacement in the trans-bend coordinate between the $\tilde{\text{A}}$- and $\tilde{\text{X}}$-state equilibrium geometries, there is a strong Franck-Condon intensity progression in the trans-bending mode, $\nu_3'(\text{a}_g)$. The trans-bend is higher in frequency than ν_4' and ν_6' and does not interact strongly with the B^n polyads at low vibrational quanta. However, the cis-trans isomerization gives rise to very strong negative anharmonicity between modes ν_3' and ν_6' because the in-plane isomerization coordinate is a combination of q_3' and q_6'. Therefore, in combination levels $3^m B^n$, mode ν_3' effectively tunes ν_6' out of resonance with ν_4' and weakens the intrapolyad interactions.[94,107,126,127,134]

4.3 Dispersed Fluorescence from $\tilde{\text{A}}(3^m6^1)$

4.3.1 The $\tilde{\text{A}}(3^{m}6^1) \rightarrow \tilde{\text{X}}(0,v_2,0,v_4^{+1},1^{-1})\Sigma_u^+$ Progressions

In Figure 4-1, calculated emission intensities to the dominant progressions observed from $2\nu_3' + \nu_6'$ and $3\nu_3' + \nu_6'$ to $\tilde{\text{X}}(0,v_2,0,v_4^{+1},1^{-1})\Sigma_u^+$ are compared with experimental observations obtained from dispersed fluorescence (DF) measurements by Hoshina *et al.*[86] In the experiment, *ungerade* ($K'_{K_a',K_c'} = 1_{1,0}, e$) levels of the $\tilde{\text{A}}$ state were excited by a two-photon scheme, via the $\nu_3''(\sigma_u^+)$ intermediate state. The fluorescence was dispersed onto a CCD detector attached to a monochromator, and the relative intensities in each emission spectrum were calibrated by dispersing a halogen lamp onto the same detector. Only the relative FC intensities within each emission spectrum are reported—the relative intensities between different emission spectra are uncertain due to power variation and fluctuation in the lasers used to pump the excited state. Therefore, the experimental data and calculated intensities shown in Figure

4-1 are all consistently normalized to the strongest transition in the first lobe of the v_4'' progression.

The calculation places the maximum in the v_2'' progression at 0–1 quanta, whereas the observed maximum is at 2 quanta. In the v_4'' progressions, the calculated location of the first node is in good qualitative agreement with experiment. The calculation places the first node in fluorescence from $2\nu_3' + \nu_6'$ at $v_4'' = 13$ and the first node in fluorescence from $3\nu_3' + \nu_6'$ at $v_4'' = 11$, whereas in the experiment the nodes are observed at $v_4'' = 11$ and $v_4'' = 9$, respectively. This shift that occurs in the node position when the upper level is changed from $2\nu_3'+\nu_6'$ to $3\nu_3'+\nu_6'$ reflects a shift in the first node position along the trans-bend coordinate of the upper state wavefunction. The experimental DF spectra did not extend sufficiently high in energy to determine the locations of higher-lying nodes. As with dispersed fluorescence data from *gerade* levels of the Ã state (shown in Chapter 3), the curvilinear coordinate transformation does a better job at reproducing the observed intensity at high quanta in v_4''.

4.3.2 Multiple Zero-Order Bright States in Spectra from Ã-state 3^m6^1

Hoshina and coworkers[86] also report interference effects from multiple zero-order bright states in the DF spectra from the *ungerade* Ã-state levels 3^26^1 and 3^36^1. As mentioned in Section 4.2.1, the Franck-Condon propensity rule for the cis-bending mode ν_5'' is that the nominal zero-order bright states (ZOBSs) should conserve the quanta of $v_5'' = v_4' + v_6'$. Furthermore, because the Ã ← X̃ transition involves little change in the symmetric CH stretch frequencies, ν_1'' and ν_1', the antisymmetric stretch frequencies, ν_3'' and ν_5', *or* the equilibrium C—H bond length, there are additional FC propensity rules for $v_1'' = v_1'$ and $v_3'' = v_5'$ to be conserved.

Within each polyad with given values of $N_s = v_2''$ and N_{res}, defined in Eqs. (5.1–5.3), there is only one nominal zero-order state that is bright in each Σ_u^+ polyad: $(0, v_2'', 0, v_4''^{+1}, 1^{-1})\Sigma_u^+$, and there are two nominal zero-order bright states in each Δ_u polyad: $(0, v_2'', 0, v_4''^{+1}, 1^{+1})\Delta_u$ and $(0, v_2'', 0, v_4''^{+3}, 1^{-1})\Delta_u$. (Throughout this sec-

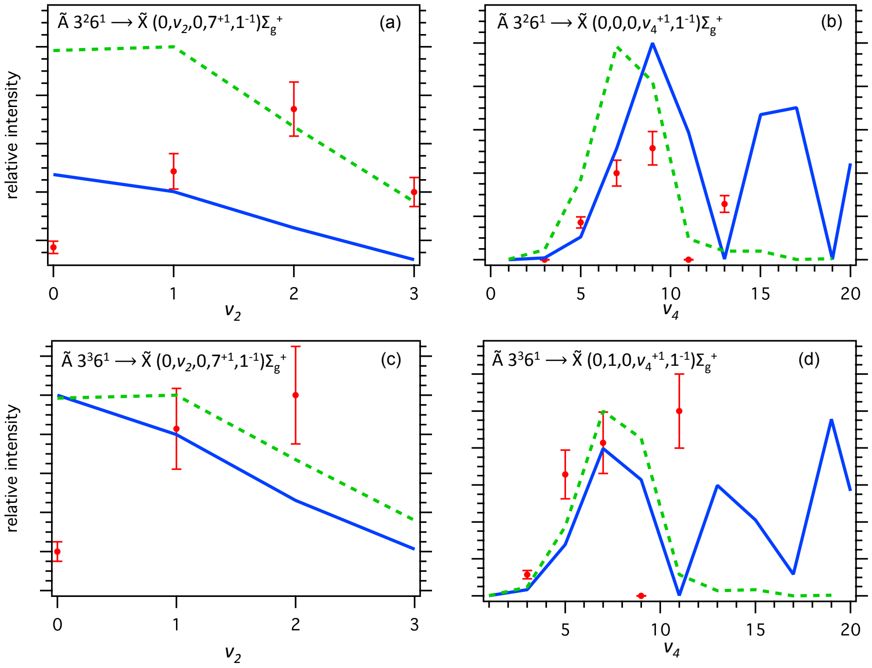

Figure 4-1: Relative emission intensities for $\tilde{\mathrm{A}}(3^m6^1)(\mathrm{b}_u)$ to zero-order bright states $\tilde{\mathrm{X}}(0, v_2, 0, v_4^{+1}, 1^{-1})\Sigma_u^+$ of acetylene. Emission is shown from $\tilde{\mathrm{A}}(3^26^1)$ (panels (a) and (b)) and $\tilde{\mathrm{A}}(3^36^1)$ (panels (c) and (d)). Panels (a) and (c) display progressions in v_2'' ($v_4'' = 7$ and $v_5'' = 1$), and panels (b) and (d) display progressions in v_4'' (v_2'' =0 or $1, v_5'' = 1$). Representative progressions were chosen based on the best availability of experimental data for comparison. Experimental intensities from IR-UV-DF measurements[86] are displayed as points with 15% uncertainty. The observed and calculated intensities from both emission spectra are normalized relative to the strongest transition in the first lobe of the v_4'' progression. The calculations were performed with a curvilinear coordinate transformation (solid blue curve) and a rectilinear coordinate transformation with first-order corrections for axis switching (dotted green curve).

tion, the zero-order Σ states are assumed to be symmetrized so that the total parity is +. i.e. $(0, v_2'', 0, v_4''^{+1}, 1^{-1})\Sigma_u^+$ is shorthand for the symmetric linear combination $(1/\sqrt{2})[(0, v_2'', 0, v_4''^{+1}, 1^{-1}) + (0, v_2'', 0, v_4''^{-1}, 1^{+1})]$.) For this nominally bright class of states, the number of quanta in ν_4'' is given by $v_4'' = N_{\mathrm{res}} - 3N_s - 1$.

However, the observed interference effects suggest that there is an *additional* class of zero-order bright state contributing to the intensity in the emission spectra. The authors of Ref. 86 find strong evidence that the interfering class of zero-order states are of the type $(0, \{v_2'' - 1\}, 1, \{v_4'' - 1\}^0, 0^0)\Sigma_u^+$ or $(0, \{v_2'' - 1\}, 1, \{v_4'' - 1\}^{+2}, 0^0)\Delta_u$, which is bright due to Duschinsky rotation between the b_u vibrational modes. To obtain this new class of ZOBS, we have exchanged $\nu_2'' + \nu_4'' + \nu_5''$ for ν_3''. Ref. 86, reports the ratio of emission intensities obtained by fitting the observed interference patterns to an effective Hamiltonian polyad model for the X̃ state.

Table 4.1 lists the calculated and experimentally determined intensity ratios for emission from 3^m6^1 levels of the Ã state into the nominally allowed zero-order Δ_u states with different combinations of $l_4 + l_5 = 2$: $(0, v_2'', 0, v_4''^{+1}, 1^{+1})\Delta_u$ and $(0, v_2'', 0, v_4''^{+3}, 1^{-1})\Delta_u$. The calculated and observed values are all on the same order of magnitude, ranging from ∼0.05–0.5. The calculation places slightly higher relative intensity into the $(0, v_2'', 0, v_4''^{+3}, 1^{-1})\Delta_u$ states than is observed. However, both the calculation and the experimental observations find that the ratio increases with increasing quanta in v_4''.

Table 4.1: The FC intensity ratio for emission from Ã 3^m6^1 into $(0, v_2, 0, v_4^{+3}, 1^{-1})\Delta_u$ and $(0, v_2, 0, v_4^{+1}, 1^{+1})\Delta_u$ levels of the X̃ state. The ratio is calculated from $\left|\langle 3^m6^1 | q_{4b}'' | (0, v_2, 0, v_4^{+3}, 1^{-1})\rangle : \langle 3^m6^1 | q_{4b}'' | (0, v_2, 0, v_4^{+1}, 1^{+1})\rangle\right|^2$. The uncertainty in the experimentally observed ratios is estimated to be ∼20%.

X̃-state polyad			Upper level:	3^26^1		3^36^1	
$\{N_\mathrm{s}, N_\mathrm{res}, l\}$	v_2''	v_4''	Ratio:	Calc.	Expt.[a]	Calc.	Expt.[a]
$\{0, 4, 2\}\Delta_u$	0	3		0.16		0.17	
$\{0, 6, 2\}\Delta_u$	0	5		0.36	0.13	0.38	0.28
$\{0, 8, 2\}\Delta_u$	0	7		0.52	0.18	0.56	0.31
$\{1, 7, 2\}\Delta_u$	1	3		0.16	0.058	0.17	0.10
$\{1, 9, 2\}\Delta_u$	1	5		0.36	0.090	0.38	0.18
$\{1, 11, 2\}\Delta_u$	1	7		0.52	0.12	0.56	0.30

Tables 4.2 and 4.3 list the calculated and experimentally determined intensity ratios for emission from 3^m6^1 levels of the Ã state into the nominally bright zero-order *ungerade* states, $(0, v_2, 0, v_4, 1)$, and into the FC propensity forbidden zero-order states, $(0, \{v_2 - 1\}, 1, \{v_4 - 1\}, 0)$ with $l = 2$ or 0. The calculated and observed intensity ratios are all on an order of magnitude ranging from $\sim 10^{-3}$ to 10^{-2}, and exhibit an increasing trend with increasing N_res. The qualitative agreement between experiment and calculation provides strong evidence that our calculations do a good job of reproducing the magnitudes of Duschinsky rotation effects, and that the model used

---

[a] Reference 86

by Hoshina et al.,[86] correctly identified which class of zero-order states is responsible for the interference effect. The calculated ratios are, on average, slightly smaller than the experimental ratios, indicating that the calculation may underestimate the degree of Duschinsky rotation of the b_u modes.

Table 4.2: The FC intensity ratio for emission from $\tilde{\mathrm{A}}$ 3^m6^1 into $(0,1,0,v_4^{+1},1^{+1})\Delta_u$ and $(0,0,1,\{v_4-1\}^{+2},0^0)\Delta_u$ levels of the $\tilde{\mathrm{X}}$ state. Intensity into the latter class of zero-order state arises from Duschinsky rotation between the b_u vibrational modes. The ratio is calculated from $\left|\langle 3^m6^1|q''_{4b}|(0,0,1,\{v_4-1\}^{+2},0^0)\rangle : \langle 3^m6^1|q''_{4b}|(0,1,0,v_4^{+1},1^{+1})\rangle\right|^2$. The uncertainty in the experimentally observed ratios is estimated to be ~20%.

$\tilde{\mathrm{X}}$-state polyad		Upper level:	3^26^1		3^36^1	
$\{N_\mathrm{s},N_\mathrm{res},l\}$	v''_4	Ratio ($\times10^3$):	Calc.	Expt.[a]	Calc.	Expt.[a]
$\{1,7,2\}\Delta_u$	3		0.38	1.0	0.47	7.6
$\{1,9,2\}\Delta_u$	5		1.0	3.1	1.3	3.1
$\{1,11,2\}\Delta_u$	7		2.0	3.0	2.7	6.5
$\{1,13,2\}\Delta_u$	9		3.5		6.5	

---

[a] Reference 86

Table 4.3: The FC intensity ratio for emission from $\tilde{\mathrm{A}}$ 3^m6^1 into $(0,1,0,v_4^{+1},1^{-1})\Sigma_u^+$ and $(0,0,1,\{v_4-1\}^0,0^0)\Sigma_u^+$ levels of the $\tilde{\mathrm{X}}$ state. Intensity into the latter class of zero-order state arises from Duschinsky rotation between the b_u vibrational modes. The ratio is calculated from $\left|\langle 3^m6^1|q''_{4b}|(0,0,1,\{v_4-1\}^0,0^0)\rangle : \langle 3^m6^1|q''_{4b}|(0,1,0,v_4^{+1},1^{-1})\rangle\right|^2$. The uncertainty in the experimentally observed ratios is estimated to be ~20%.

$\tilde{\mathrm{X}}$-state polyad		Upper level:	3^26^1		3^36^1	
$\{N_\mathrm{s},N_\mathrm{res},l\}$	v''_4	Ratio ($\times10^3$):	Calc.	Expt.[a]	Calc.	Expt.[a]
$\{1,5,0\}\Sigma_u^+$	1		0.87		1.0	
$\{1,7,0\}\Sigma_u^+$	3		1.3	8.5	1.5	0.80
$\{1,9,0\}\Sigma_u^+$	5		1.9	2.0	2.4	2.3
$\{1,11,0\}\Sigma_u^+$	7		2.9	9.0	3.9	11.
$\{1,13,0\}\Sigma_u^+$	9		4.5	19.	8.1	

---

[a] Reference 86

The calculated intensity ratios reported in Tables 4.2 and 4.3 were obtained using the curvilinear coordinate transformation described in Chapter 3. (See Table 3.8.) In this transformation, the Duschinsky rotation is described by the relationship $\bar{q}'_6 = 1.03\bar{q}''_{5b} + 0.0176\bar{q}''_3$, or a rotation of ~2% between the b_u vibrational modes. We note that the Duschinsky rotation matrix elements obtained from the rectilinear coordinate transformation (Tables 3.6 and 3.7) are larger by an order of magnitude (∼40% rotation). Intensity calculations based on the rectilinear coordinate transformations overestimate the observed intensity ratios in Tables 4.2 and 4.3 *by two orders of magnitude*. This provides further evidence that the curvilinear formulation provides a more physically realistic description of the normal coordinate transformation for the Ã—X̃ transition in acetylene than the rectilinear formulation used by Watson.[104]

4.4 Propensities in IR-UV fluorescence

Merer and coworkers[93] note that the relative strengths of transitions to Ã-state $K' = 0$ levels with a_u and b_u vibrational symmetry depend on which X̃-state π_u intermediate level is used in the double resonance scheme. In their paper, they use the $\nu_3'' + \nu_4''$ intermediate and they note that transitions to b_u levels of the Ã-state are much more intense in the fluorescence spectrum than transitions to a_u levels. The authors mention that in experiments on other polyads via the $\nu_1'' + \nu_5''$ (π_u) intermediate, a_u levels are dominant in intensity. However, they remark that it was unclear to them why this dramatic difference in intensity patterns should occur.

Calculated Franck-Condon factors for transitions between each of these two π_u intermediate levels and members of the lowest-lying *ungerade* B^n polyads of the Ã state are shown in Table 4.4. The intensities arising from each Cartesian component of ν_5'' (out-of-plane ν_{5x}'' versus in-plane ν_{5y}'') are shown separately. For transitions out of ν_4'', the Franck-Condon calculation only grants transition intensity from the in-plane component ν_{4y}'' because the a-axis Eckart constraint $\phi_4 = 0$ requires that the out-of-plane component ν_{4x}'' must transform like an a-axis rotation in C_{2h}. The ν_{4x}'' degree of freedom is included in the $\tilde{\mathbf{l}}_{\mathbf{R}}''$ matrix for rotations rather than the $\tilde{\mathbf{l}}''$ matrix for vibrations, and the Eckart conditions ensure that it does *not* contribute to vibrational overlap intensity.

This Eckart constraint explains the physical origin of the trend in intensities observed in Ref. 93 for double-resonance spectra obtained via the $\nu_3'' + \nu_4''$ (π_u) interme-

Table 4.4: Calculated Franck-Condon factors for transitions between zero-order members of the *ungerade* $\tilde{\text{A}}$-state B^n polyads and the π_u levels of the $\tilde{\text{X}}$-state used as pump states in IR-UV double resonance experiments. The values are given relative to the vibrationless 0–0 intensity.[93]

π_u intermediate:		$v_1'' + v_{5x}''$	$v_1'' + v_{5y}''$	$v_3'' + v_{4y}''$
	$\text{D}_{\infty\text{h}}$:	$\sigma_g^+ \otimes \pi_u$	$\sigma_g^+ \otimes \pi_u$	$\sigma_u^+ \otimes \pi_g$
	$\text{C}_{2\text{h}}$:	$\text{a}_g \otimes \text{a}_u$	$\text{a}_g \otimes \text{b}_u$	$\text{b}_u \otimes \text{a}_g$
B^1	4^1 (a_u)	0.0683	0	0
	6^1 (b_u)	0	0.0680	0.0280
B^3	4^3 (a_u)	7.54×10^{-5}	0	0
	$4^2 6^1$ (b_u)	0	2.50×10^{-5}	1.03×10^{-5}
	$4^1 6^2$ (a_u)	3.85×10^{-5}	0	0
	6^3 (b_u)	0	1.15×10^{-4}	4.74×10^{-5}

diate. When using the $\nu_3'' + \nu_4''$ intermediate level, all intensity must come from the in-plane component, ν_{4y}'', which has a_g symmetry in $\text{C}_{2\text{h}}$. Therefore, by symmetry, non-zero vibrational overlap may only occur between $\nu_3'' + \nu_4''$ and states of b_u vibrational symmetry. We should note that in the actual spectrum transition intensity from $\nu_3'' + \nu_4''$ into a_u levels will be non-zero due primarily to Coriolis interactions in the B^n polyads that are not treated here.

On the other hand, $\nu_1'' + \nu_5''$ grants Franck-Condon access to both a_u and b_u vibrational levels. Access to a_u levels comes solely from the out-of-plane component, $\nu_1'' + \nu_{5x}''$, and access to b_u levels comes solely from the in-plane-component, $\nu_1'' + \nu_{5y}''$. In the B^1 polyad, the harmonic calculation predicts approximately equal intensity into the $\nu_4'(\text{a}_u)$ and $\nu_6'(\text{b}_u)$ levels. Because the harmonic frequencies of the zero-order members of the B^1 polyad are very nearly degenerate and the equilibrium displacement along *ungerade* normal mode coordinates is zero, we would not expect our harmonic intensity calculation to favor one plane of cis-bend motion over the other, so this result is not surprising. The very small intensity advantage of ν_4' over ν_6' comes from the isolation of the out-of-plane (a_u) block of the Duschinsky matrix. That is, ν_6' loses some of its intensity due to Duschinsky rotation in the b_u modes, whereas ν_4' is the only mode with a_u symmetry, so it does not experience any Duschinsky rotation. As mentioned in Section 4.3.2, the fact that the calculation underestimates the ratios reported in Tables 4.2 and 4.3 indicates that the calculation may underestimate the degree of b_u Duschinsky rotation, so that it overestimates the intensity from $\nu_1'' + \nu_5''$ into ν_6'. However, this effect is probably not large enough to explain the strongly observed propensities, and other anharmonic factors are probably at play.

There are two reasons why the $\nu_6'(\mathrm{b}_u)$ level within each B^1 polyad is likely to undergo more severe anharmonic interactions with other levels than the $\nu_4'(\mathrm{a}_u)$ level. First, the total density of b_u levels is higher than the density of a_u levels (because ν_5' also has b_u character). Second, anharmonic overlap is more likely between zero-order basis states that encode motion in the same plane. Other than $\nu_6'(\mathrm{b}_u)$, there are four other in-plane vibrational modes, but there are no out-of-plane vibrational modes other than ν_4'. These anharmonic interactions will weaken the propensity for $v_{5y}'' = v_6'$, and might cause a_u levels to dominate in transitions from $\nu_1'' + \nu_5''$. Propensities for transitions from the $\nu_3'' + \nu_4''$ intermediate will not be affected by such anharmonic considerations, because the transition from $\nu_3'' + \nu_4''$ to all a_u levels are equally forbidden by the Eckart conditions.

The calculation does not in general find a strong preference for a_u levels over b_u levels in transitions to higher-lying B^n polyads. However, transitions from $\nu_1'' + \nu_5''$ to higher *ungerade* B^n polyads with $n \geq 3$ are very weak because they are forbidden by the Franck-Condon propensity $v_5'' = v_4' + v_6'$. The calculations in Table 4.4 indicate that Franck-Condon access to B^3 is weaker than the FC access to B^1 by three orders of magnitude. Therefore, as mentioned in Ref. 93, the higher-lying *ungerade* B^n polyads observed in the spectra from the $\nu_1'' + \nu_5''$ intermediate probably borrow much of their intensity from anharmonic interactions with nearby $2^m3^n\mathrm{B}^1$ levels that are strongly allowed by the Franck-Condon propensities. Because anharmonic interactions preserve vibrational symmetry, a_u levels of higher-lying B^n polyads will borrow intensity from the $2^m3^n4^1$ (a_u) member of the nearby B^1 polyad and b_u levels will borrow intensity from the $2^m3^n6^1$ (b_u) member. If we assume that our calculation has overestimated the intensity from $\nu_1'' + \nu_5''$ to ν_6', then that will be sufficient to to explain the general observation that a_u levels dominate in transitions from $\nu_1'' + \nu_5''$. For higher-lying *ungerade* B^n polyads, the effect is largely via intensity borrowing from $2^m3^n4^1$ levels.

4.5 Emission from levels of *gerade* B^n polyads to bending levels of the $\tilde{\mathrm{X}}$ state

Extensive work by the Field lab and collaborators has focussed on the approach to the acetylene $\rightleftharpoons$ vinylidene isomerization on the S_0 surface.[85] This has attracted interest to local bending modes of S_0, because the local bending motion lies along the reaction coordinate for the isomerization. Local bending in S_0 acetylene—where the bending motion is localized to a single CCH bond angle—is achieved through a one-to-one linear combination of modes ν_4'' and ν_5''. As discussed in Section 4.2.1, these modes form pure bending polyads with conserved polyad numbers $N_B = v_4''+v_5''$ and $l = l_4+l_5$. At low bending energies, the pure-bending polyad eigenstates are best described in the basis of trans-bend and cis-bend normal modes. The trans bend is lower in frequency than the cis bend, so levels with the most trans-bend character lie at the low energy extreme of the polyad and levels with the most cis-bend character lie at the high energy extreme of the polyad. Because the anharmonicities x_{44} and x_{55} have opposite signs, the trans and cis basis states converge as N_B increases. This causes strong Darling-Dennison interactions to turn on at $N_B \geq 12$, and new classes of motion emerge as a result. The pure-bending polyad structure rearranges itself so that the eigenstates are better described in the local mode basis. Jacobson *et al.*[136] have shown that for $l = 0$, large amplitude local bend levels fall to the low energy extreme of the polyad, and counter-rotating levels rise to the high energy extreme of the polyad. Tyng and Kellman have analyzed this normal mode bifurcation by semiclassical methods[137], and they have released an excellent collection of animations that illustrate the classical motions that result.[138]

One of the most challenging experimental obstacles in observing zero-order large amplitude local bending states—which are a 1:1 admixture of cis- and trans-bending modes—is that FC propensities make it difficult to achieve bending excitation with a high degree of cis-bending character. One of the driving goals of the extensive characterization of the acetylene Ã state has been to determine which "perfect pluck" vibrational levels will fluoresce to vinylidene-like local bending levels of the X̃ state. This problem has generated interest in members of the Ã-state B^n polyads because the ν_4' and ν_6' modes from which the polyads are composed correlate to the out-of-plane and in-plane components, respectively, of the X̃-state cis bend, ν_5''. The Franck-Condon propensity $v_5'' = v_4' + v_6'$ make the B^n polyads promising as candidates for intermediates in SEP or DF schemes for accessing ν_5'' character and reaching highly-excited local bending states of S_0.

However, the "perfect pluck" problem is not so simple as merely populating a zero-order bright state of S_0 with equal ν_4'' and ν_5'' character. In the high-lying pure bend polyads, there are many states that comprise the zero-order local mode product basis. Only a few of these states will contain the correctly-phased linear combination of zero-order *normal mode* product basis states to give rise to large-amplitude bending motion along the isomerization coordinate. The goal of this section is to understand the best strategy for reaching these zero-order levels.

4.5.1 Fluorescence intensities and phases for transitions into X̃-state pure bending polyads in the normal mode basis

A full table of calculated vibrational overlap integrals that connect zero-order members of the Ã-state *gerade* B^n polyads ($n = 0, 2, 4$) with members of X̃-state *gerade* pure-bending polyads ($N_B \leq 10$) in the harmonic normal mode basis may be found in Appendix A. There are a few important trends. First, overall brightness increases dramatically as N_B increases, primarily due to the strong FC progression in v_4''. At low N_B, as the number of quanta in B^n of the upper level increases, the overall fluorescence intensity into a given pure bending polyad of the X̃ state decreases. However, this trend begins to reverse at high quanta of excitation in the X̃-state pure-bending polyads. The propensity rule $v_5'' = v_4' + v_6'$ is fairly well obeyed within each ground state pure-bending polyad. From each B^n polyad, the vibrational overlap magnitude is strongly peaked at $\tilde{\mathrm{X}}$-state levels $v_5'' = n$. The propensity rule is slightly relaxed for ν_6' relative to ν_4' as a result of the fact that ν_4' is the only out-of-plane mode, and overlaps very efficiently with ν_{5c}''. (The out-of-plane component of ν_4'' does not participate in the Franck-Condon intensities due to the Eckart constraint, so overlap between totally symmetric overtones of ν_4' and ν_{4c}'' do not contribute to vibrational intensities.) On the other hand, ν_6' may mix into ν_3'' in the coordinate transformation via Duschinsky rotation, and even quanta of ν_6' will have a small amount of overlap with totally symmetric combinations of in-plane modes of the $\tilde{\mathrm{X}}$ state (such as even quanta of ν_{4b}''). As a result, the distribution of overlap from 6^n levels within each pure bending polyad of the $\tilde{\mathrm{X}}$ state is less sharply peaked at $v_5'' = n$ than is the case for 4^n levels.

Table 4.5 lists a small subset of the vibrational overlap integrals printed in the supplementary materials, relevant to the emission from zero-order members of the $\tilde{\mathrm{A}}$-state B^4 polyad to zero-order members of the $\tilde{\mathrm{X}}$-state $N_B = 8$ pure bending polyad. Despite the fact that overlap from 6^n levels is less sharply peaked, the intensity distribution from 6^n closely resembles the distribution from 4^n. However, within pure bending polyads of the $\tilde{\mathrm{X}}$ state, the *phases* of the overlap integrals with the various members of each B^n polyad *do not* resemble one another. The physical origin of this phenomenon comes from the fact that 4^n and 6^n place intensity into different Cartesian components of the ν_5'' 2-dimensional harmonic oscillator. In the following discussion, we use y to label the in-plane components and x to label the out-of-plane components. The 6^n level will overlap predominantly with $|v_{5x}'', v_{5y}''\rangle = |0, n\rangle$, whereas 4^n will overlap predominantly with $|n, 0\rangle$. As a result of the Eckart constraint, all intensity from $\tilde{\mathrm{A}} \to \tilde{\mathrm{X}}$ emission goes into the in-plane component of ν_4''. Therefore, in the product basis of Cartesian 2-dimensional harmonic oscillators, emission from $4^m 6^n$ will fluoresce predominantly to

$$\begin{aligned} 4^m 6^n \to |v_{4x}'', v_{4y}''\rangle |v_{5x}'', v_{5y}''\rangle &= |0, v_{4y}''\rangle |m, n\rangle \\ v_{4y}'' &= N_B - (n+m). \end{aligned} \tag{4.6}$$

Table 4.5: Calculated vibrational overlap integrals connecting zero-order members of the Ã-state *gerade* B^4 polyad with members of X̃-state $N_B = 8$ *gerade* pure-bending polyad in the harmonic normal mode basis.

X̃-state zero-order level			Ã-state B^4 polyad member				
N_B	l	$[v_4^{l_4}, v_5^{l_5}]$	6^4	$4^1 6^3$	$4^2 6^2$	$4^3 6^1$	4^4
8	0	$[8^0, 0^0]$	3.04×10^{-1}		2.01×10^{-1}		1.99×10^{-1}
		$[6^{+2}, 2^{-2}]$	3.98×10^{0}	$3.99i \times 10^{0}$	-3.18×10^{-1}	$3.22i \times 10^{0}$	-3.23×10^{0}
		$[6^0, 2^0]$	7.00×10^{0}		5.18×10^{0}		5.67×10^{0}
		$[4^{+4}, 4^{-4}]$	2.67×10^{0}	$5.35i \times 10^{0}$	-6.56×10^{0}	$-5.37i \times 10^{0}$	2.69×10^{0}
		$[4^{+2}, 4^{-2}]$	1.71×10^{1}	$1.71i \times 10^{1}$	-1.41×10^{-3}	$1.72i \times 10^{1}$	-1.72×10^{1}
		$[4^0, 4^0]$	2.92×10^{1}		2.39×10^{1}		2.94×10^{1}
		$[2^{+2}, 6^{-2}]$	-2.44×10^{-1}	$-2.25i \times 10^{-1}$	-9.49×10^{-3}	$-2.10i \times 10^{-1}$	1.91×10^{-1}
		$[2^0, 6^0]$	-5.73×10^{-1}		-4.29×10^{-1}		-4.77×10^{-1}
		$[0^0, 8^0]$	4.38×10^{-3}		3.00×10^{-3}		3.02×10^{-3}
	2	$[8^{+2}, 0^0]$	-2.61×10^{-1}		-1.72×10^{-1}		-1.70×10^{-1}
		$[6^{+4}, 2^{-2}]$	-1.97×10^{0}	$-1.97i \times 10^{0}$	1.57×10^{-1}	$-1.60i \times 10^{0}$	1.60×10^{0}
		$[6^{+2}, 2^0]$	-5.63×10^{0}		-4.16×10^{0}		-4.57×10^{0}
		$[6^0, 2^{+2}]$	-4.95×10^{0}	$4.96i \times 10^{0}$	3.95×10^{-1}	$4.01i \times 10^{0}$	4.01×10^{0}
		$[4^{+4}, 4^{-2}]$	-5.32×10^{0}	$-5.33i \times 10^{0}$	4.39×10^{-4}	$-5.35i \times 10^{0}$	5.36×10^{0}
		$[4^{+2}, 4^0]$	-2.09×10^{1}		-1.71×10^{1}		-2.11×10^{1}
		$[4^0, 4^{+2}]$	-2.38×10^{1}	$2.39i \times 10^{1}$	1.97×10^{-3}	$2.40i \times 10^{1}$	2.40×10^{1}
		$[4^{-2}, 4^{+4}]$	-8.57×10^{0}	$1.72i \times 10^{1}$	2.11×10^{1}	$-1.72i \times 10^{1}$	-8.64×10^{0}
		$[2^{+2}, 6^0]$	3.09×10^{-1}		2.31×10^{-1}		2.57×10^{-1}
		$[2^0, 6^{+2}]$	4.53×10^{-1}	$-4.18i \times 10^{-1}$	1.76×10^{-2}	$-3.91i \times 10^{-1}$	-3.55×10^{-1}
		$[2^{-2}, 6^{+4}]$	1.10×10^{-1}	$-1.97i \times 10^{-1}$	-2.11×10^{-1}	$1.48i \times 10^{-1}$	6.19×10^{-2}
		$[0, 8^{+2}]$	-3.44×10^{-3}	$2.93i \times 10^{-3}$	-2.38×10^{-4}	$2.55i \times 10^{-3}$	2.10×10^{-3}

The Cartesian product basis states in Eq. (4.6) are converted to the polar $|v_4^{l_4}, v_5^{l_5}\rangle$ basis by standard ladder operator methods.[121] Matrix elements are obtained from the relationship

$$
\begin{aligned}
|v_4^{l_4}, v_5^{l_5}\rangle = & \left[\left(\frac{v_4 + l_4}{2}\right)! \left(\frac{v_4 - l_4}{2}\right)! \left(\frac{v_5 + l_5}{2}\right)! \left(\frac{v_5 - l_5}{2}\right)!\right]^{-1/2} \\
& \times \left(\hat{a}_{4x}^{\dagger} + i\hat{a}_{4y}^{\dagger}\right)^{(v_4+l_4)/2} \left(\hat{a}_{4x}^{\dagger} - i\hat{a}_{4y}^{\dagger}\right)^{(v_4-l_4)/2} \\
& \times \left(\hat{a}_{5x}^{\dagger} + i\hat{a}_{5y}^{\dagger}\right)^{(v_5+l_5)/2} \left(\hat{a}_{5x}^{\dagger} - i\hat{a}_{5y}^{\dagger}\right)^{(v_5-l_5)/2} |0,0\rangle|0,0\rangle.
\end{aligned}
\tag{4.7}
$$

The terms in the expansion of Eq. (5.9) are evaluated according to

$$
(\hat{a}_{4x}^{\dagger})^{v_{4x}} (\hat{a}_{4y}^{\dagger})^{v_{4y}} (\hat{a}_{5x}^{\dagger})^{v_{5x}} (\hat{a}_{5y}^{\dagger})^{v_{5y}} |0,0\rangle|0,0\rangle = (v_{4x}! v_{4y}! v_{5x}! v_{5y}!)^{1/2} |v_{4x}, v_{4y}\rangle|v_{5x}, v_{5y}\rangle.
\tag{4.8}
$$

The dominant contribution to the overlap integrals in the polar $|v_4^{l_4}, v_5^{l_5}\rangle$ basis will be proportional to the matrix elements for the basis transformation of Eq. (4.6). Let us ignore for a moment the constant prefactors and look only at the phases of the matrix elements, which arise from factors of $\pm i$ that multiply the in-plane ladder operators in Eq. (5.9). The general formula for the phase of the $\langle v_4^{l_4}, v_5^{l_5}|v_{4x}, v_{4y}\rangle|v_{4x}, v_{4y}\rangle$ matrix element is complicated. However, the expression is simple if we consider the matrix elements for the dominant overlap with the extreme members of the B^n polyad: $|0, v_{4y}\rangle|n, 0\rangle$ and $|0, v_{4y}\rangle|0, n\rangle$ for emission from 4^n and 6^n, respectively. For these cases, we obtain

$$\langle v_4^{l_4}, v_5^{l_5}|0, v_{4y}\rangle|n, 0\rangle \propto i^{(2v_4-l_4)} = i^{(2N_B-2v_5-l+l_5)} \tag{4.9}$$

$$\langle v_4^{l_4}, v_5^{l_5}|0, v_{4y}\rangle|0, n\rangle \propto i^{(2v_4+2v_5-l_4-l_5)} = i^{(2N_B-l)}. \tag{4.10}$$

The matrix element in Eq. (4.9) for purely out-of-plane cis-bend excitation does not depend directly on v_5 or l_5 because the out-of-plane ladder operator $\hat{a}_{5x}^{\dagger}$ carries a phase of (+1). However, purely in-plane cis-bend excitation contributes a phase of $i^{2v_5-l_5}$ to Eq. (4.10), and as a result, the phase factor for the purely in-plane cis bend is a function of only N_B and l. That is, within a given pure bending polyad of the $\tilde{\mathrm{X}}$ state, the predominant zero-order states that receive their brightness from the extreme 6^n member of the B^n polyad will all have the same phase. In the *gerade* pure bending polyads of the $\tilde{\mathrm{X}}$ state, N_B and l are both even, so the phase factor will be +1 for $l = 0, 4, ...$ and -1 for $l = 2, 6, ...$ We expect overlap integrals from the extreme 4^n member of the B^n polyad to differ in phase by a factor of $i^{2v_5-l_5}$. We will return to this result in Section 4.5.2 when we discuss the fluorescence intensities in the local mode basis.

The b$_g$ members of the B^n polyads (with odd quanta of ν_4' and ν_6') have a different overlap pattern, which may be explained by symmetry considerations. Because b$_g$ and a$_g$ levels have vibrational wavefunctions with opposite total parity, the vibrational overlap integrals listed in Table 4.5 and in the supplementary materials from b$_g$ levels are $\pi/2$ out-of-phase with those from a$_g$ levels. However, because a- and b-axis Coriolis interactions between a$_g$ and b$_g$ vibrational levels must preserve total parity, they couple rovibrational levels with opposite rotational parity, and the matrix elements for the Coriolis interactions are purely imaginary.[93] As we have noted, only the in-plane a_g component of ν_4'' contributes to the FC overlap integral because the out-of-plane b_g component correlates with a rotation. Therefore, the vibrational symmetry of pure-bending S_0 levels in the overlap integral is determined by the contribution of ν_5''. The *gerade* overtones of ν_5'' have symmetry Σ_g^+ (for $l_5 = 0$), Δ_g (for $l_5 = 2$), Γ_g (for $l_5 = 4$), etc. In C_{2h}, Σ_g^+ correlates with A_g, whereas Δ_g and all higher-order *gerade* representations correlate with $A_g + B_g$. A consequence is that b_g members of the *gerade* B^n polyads may *only* fluoresce to states with $l_5 \neq 0$. For $l_4 + l_5 = 0$ levels of the $\tilde{X}$ state, B_g correlates with Σ_g^-, so fluorescence from a_g and b_g upper levels will reach $l = 0$ lower levels that differ in vibronic parity.

The different phases that are obtained for the vibrational overlap integrals in Table 4.5 lead to qualitatively different intensity patterns in the emission spectra from $\tilde{A}$-state B^n polyads to $\tilde{X}$-state bending polyads. This is because each zero-order bright state within the bending polyads of $\tilde{X}$ is fractionated into multiple different eigenstates by intrapolyad interactions.[80] Because the $v_5'' = v_4' + v_6'$ propensity rule will lead to brightness in more than one zero-order state of each pure bending polyad (of the type $|v_4^{l_4}, v_5^{l_5}\rangle = |(N_B - n)^{l_4}, n^{l_5}\rangle$ with different combinations of $l_4 + l_5 = l$), the intensity emitted into each eigenstate of the $\tilde{X}$-state pure bending polyads will result from constructive and destructive interferences between the contributions of various zero-order states that are bright in the spectrum, and the phases of the Franck-Condon overlap integrals will contribute in an important way. In our calculation, we have chosen the phases of the $\tilde{X}$-state normal modes to be consistent with the parameters of the $\tilde{X}$-state effective Hamiltonian reported by Herman and coworkers[79,81] and expanded by Jacobson and coworkers.[82,86,125].

The effective Hamiltonian parameters from Ref. 82 were used to calculate the fractionation of the zero-order states and simulate the emission spectra from zero-order members of the low-lying $\tilde{A}$-state B^n polyads (Figure 4-2). A few trends are visible in the simulated spectra. First, the overall intensity envelope increases dramatically with excitation in the $\tilde{X}$-state bending polyad, due to the favorable Franck-Condon contribution of ν_4''. Overall intensity decreases with increasing quanta of B^n. Below $N_B = 12$, the eigenstates of the polyad are well described in the normal mode basis. In this regime, increasing the number of quanta of B^n in the upper level shifts the emission intensity envelope within each $\tilde{\mathrm{X}}$-state bending polyad to higher frequency, because the nominal zero-order bright states obtained from the $v_5'' = v_4' + v_6'$ propensity rule contain more cis-bend character.

As N_B increases, there is an increase in the fractionation due to the Darling Dennison resonance K_{4466}, which leads to emergence of local mode eigenstates at $N_B \geq 12$. The different members of each B^n polyad start to give rise to qualitatively different interference patterns in the emission spectra. Above $N_B = 12$, $\tilde{\mathrm{A}}$-state levels with the most ν_6' character emit to the low-frequency end of the polyad where the eigenstates have the most large amplitude local bend character and levels with the most ν_4' character emit to the high-frequency end of the polyad where the eigenstates have the most counter-rotational character. Emission from the $\tilde{\mathrm{A}}$-state origin to the pure trans-bend bright state is fractionated among eigenstates in the center of the polyad, because in this regime the trans-bend is no longer a good basis function for describing of the motion encoded by the eigenstates.

4.5.2 Transformation of $\tilde{\mathrm{X}}$-state intrapolyad pure bend intensities to the local mode basis

Access to the local bending zero-order states of $\tilde{\mathrm{X}}$ may be calculated explicitly by performing a change of basis from the normal mode to the local mode basis. We will use the local mode definitions outlined by Jacobson and coworkers,[136] and the basis transformation described therein. Briefly, we label the CCH local bending modes A and B, and we define the local mode coordinates as linear combinations of the normal

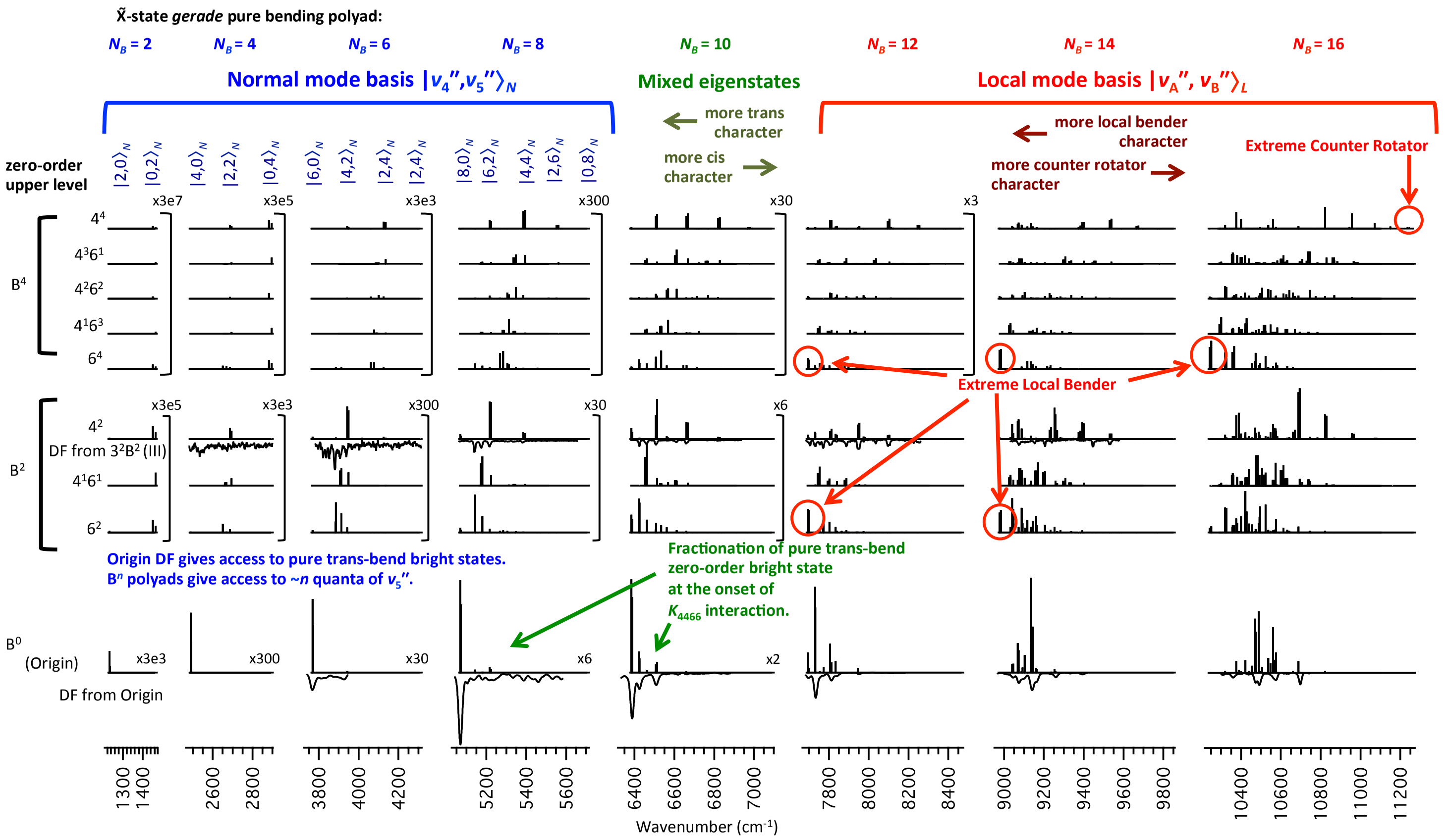

Figure 4-2: Calculated emission intensities from zero-order members of low-lying B^n polyads of S_1 acetylene to pure bending polyads of S_0. The calculation takes into account interactions that occur within S_0 pure bending polyads, but ignores intrapolyad interactions in B^n. Vertical magnification (if any) is indicated to the right of each segment. The dispersed fluorescence spectrum from the highest-energy member of the $3^2\mathrm{B}^2$ polyad and the $\tilde{\mathrm{A}}$-state origin are shown for comparison. Some features in the DF spectrum from $3^2\mathrm{B}^2$ (III) such as the peaks at 5140 and 5180 cm^{-1} may be explained through intrapolyad Darling-Dennison and a-axis Coriolis interactions within the $3^2\mathrm{B}^2$ polyad. At $N_B \geq 12$, the opposing anharmonicities of ν_4'' and ν_5'' cause strong Darling-Dennison interaction within the $\tilde{\mathrm{X}}$-state bending polyads, leading to the emergence of new classes of motion. Eigenstates with extreme local bender character are intense in emission from upper levels with ν_6' character and eigenstates with extreme counter-rotational character are intense in emission spectra from upper levels with ν_4' character.

mode coordinates:

$$q_{Ax} = \frac{1}{\sqrt{2}}(q_{4x} + q_{5x}), \tag{4.11}$$

$$q_{Ay} = \frac{1}{\sqrt{2}}(q_{4y} + q_{5y}), \tag{4.12}$$

$$q_{Bx} = \frac{1}{\sqrt{2}}(-q_{4x} + q_{5x}), \tag{4.13}$$

$$q_{By} = \frac{1}{\sqrt{2}}(-q_{4y} + q_{5y}). \tag{4.14}$$

Because the bending amplitudes of ν_4'' and ν_5'' are well matched, this definition gives local bending modes that are almost (but not completely) localized in a single CCH bond angle. (The dimensionless normal coordinates used in this work are scaled by the square root of the frequency, so the bending amplitudes will differ by a factor of $\sqrt{\nu_4''/\nu_5''}$, or approximately 8%.) From this definition, it is possible to derive local mode ladder operators:

$$\hat{a}_{Ad} = \frac{1}{\sqrt{2}}(\hat{a}_{4d} + \hat{a}_{5d}), \tag{4.15}$$

$$\hat{a}_{Ag} = \frac{1}{\sqrt{2}}(\hat{a}_{4g} + \hat{a}_{5g}), \tag{4.16}$$

$$\hat{a}_{Bd} = \frac{1}{\sqrt{2}}(\hat{a}_{4d} - \hat{a}_{5d}), \tag{4.17}$$

$$\hat{a}_{Bg} = \frac{1}{\sqrt{2}}(\hat{a}_{4g} - \hat{a}_{5g}), \tag{4.18}$$

so that local mode basis states may be generated according to

$$\left(\hat{a}_{Ad}^{\dagger}\right)^{n_{Ad}} \left(\hat{a}_{Ag}^{\dagger}\right)^{n_{Ag}} \left(\hat{a}_{Bd}^{\dagger}\right)^{n_{Bd}} \left(\hat{a}_{Bg}^{\dagger}\right)^{n_{Bg}} |0^0, 0^0\rangle = \sqrt{n_{Ad}! n_{Ag}! n_{Bd}! n_{Bg}!}\ |n_A^{l_A}, n_B^{l_B}\rangle_L, \tag{4.19}$$

where

$$n_{Ad} = (n_A + l_A)/2 \tag{4.20}$$

$$n_{Ag} = (n_A - l_A)/2 \tag{4.21}$$

$$n_{Bd} = (n_B + l_B)/2 \tag{4.22}$$

$$n_{Bg} = (n_B - l_B)/2, \tag{4.23}$$

and the subscript L denotes that the state labels are in the local mode basis. A transformation from normal to local mode basis may be obtained by substituting Eqs. (4.15–4.18) into Eq. (4.19). However, the local mode basis states obtained in this manner will not be properly symmetrized with respect to either g/u inversion symmetry or total $+/-$ parity.

In the normal mode basis, the zero-order states have well-defined g/u symmetry, which is determined by the number of quanta of $\nu_5''(\pi_u)$. Normal mode basis states with well-defined $+/-$ symmetry are obtained by taking the linear combination

$$|n_4^{l_4}, n_5^{l_5}\rangle_N^{\pm} = \frac{1}{\sqrt{2}}\left(|n_4^{l_4}, n_5^{l_5}\rangle_N \pm |n_4^{-l_4}, n_5^{-l_5}\rangle_N\right). \tag{4.24}$$

We will use the N subscript to denote that the quantum numbers are in the normal mode basis. Local mode basis states may be symmetrized with respect to total $+/-$ parity in a similar manner,

$$|n_A^{l_A}, n_B^{l_B}\rangle_L^{\pm} = \frac{1}{\sqrt{2}}\left(|n_A^{l_A}, n_B^{l_B}\rangle_L \pm |n_A^{-l_A}, n_B^{-l_B}\rangle_L\right), \tag{4.25}$$

but states generated using Eq. (4.25) will still lack well-defined g/u symmetry. Symmetrization with respect to molecular-frame inversion may be obtained by interchanging the quantum numbers for the two local modes,

$$|n_A^{l_A}, n_B^{l_B}\rangle_L^{g/u} = \frac{1}{\sqrt{2}}\left(|n_A^{l_A}, n_B^{l_B}\rangle_L \pm |n_B^{l_B}, n_A^{l_A}\rangle_L\right), \tag{4.26}$$

where the $+$ combination corresponds to g symmetry and the $-$ combination corresponds to u symmetry. Both Eqs. (4.25) and (4.26) must be applied to achieve proper symmetrization, and the resulting symmetrized state will be a linear combination of up to four local mode basis states.

The normal to local mode basis transformation was applied to members of the pure bending polyads of the $\tilde{\mathrm{X}}$ state in order to calculate the Franck-Condon access to local bending zero-order states. Within a polyad with $v_4'' + v_5'' = N_B$ and $l = 0$, the zero-order state undergoing the purest local bending motion will be $|{N_B}^0, 0^0\rangle_L$ (hereafter referred to as the "extreme local bender"), and the zero-order state undergoing the purest counter-rotational motion will be $|(N_B/2)^{N_B/2}, (N_B/2)^{-N_B/2}\rangle_L$ (hereafter referred to as the "extreme counter rotator").

Figures 4-3 and 4-4 show the emission intensity for transitions from the zero-order a_g members of $\tilde{\mathrm{A}}$-state B^n polyads into the extreme local bender and the extreme counter rotator, respectively, of each pure bending polyad of the $\tilde{\mathrm{X}}$ state, up to $N_B = 20$. Figure 4-3 also shows the total overall intensity into each pure bending polyad.

Some interesting trends are apparent in the figures. As n increases, the B^n polyads shift the overall FC envelope of the pure-bending polyads to higher energy (see column 1 of Figure 4-3), primarily because higher quanta in B^n provide Franck-Condon access to higher quanta of ν_5''. There appears to be a slight overall decrease in the amplitude of the FC envelope with increasing quanta of B^n, but for pure bending polyads of the $\tilde{\mathrm{X}}$ state with the highest values of N_B, the total FC intensity *increases* with excitation in B^n.

Within an $\tilde{\mathrm{X}}$-state pure bending polyad, the fraction of the bright state that corresponds to the extreme counter rotator (shown in the second column of Figure 4-3) depends only weakly on the identity of the $\tilde{\mathrm{A}}$-state B^n polyad, but depends very sensitively on the number of quanta in ν_4'. As the number of quanta in ν_4' increases, access to the extreme counter rotator shifts to higher-lying polyads of the $\tilde{\mathrm{X}}$ state, and the maximum counter rotational character is found in the polyad with approximately $N_B = 2v_4'$. On the other hand, the fraction of the bright state that corresponds to the extreme local bender (shown in the first column of Figure 4-4) depends very

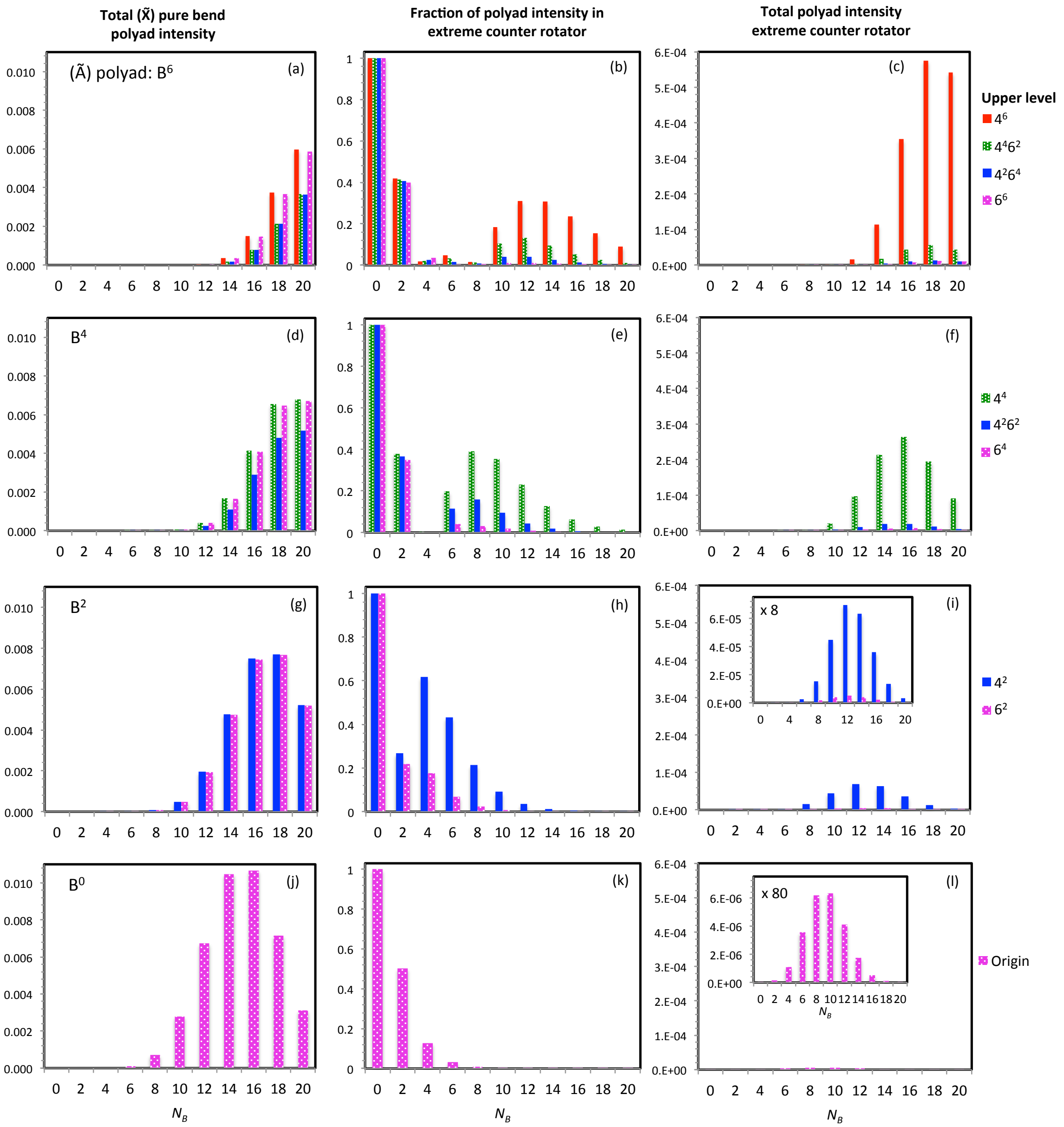

Figure 4-3: Calculated vibrational intensity for emission from a$_g$ members of B^n polyads of Ã-state acetylene to pure bending polyads of the X̃ state with Σ_g^+ symmetry, illustrating access to the extreme counter rotator of each polyad. The first column gives the total overall intensity from each upper level to the X̃ state bending polyads. Column 2 gives the fraction of the total intensity in the extreme counter rotator zero-order state, $(|N_B/2^{N_B/2}, N_B/2^{-N_B/2}\rangle_L^{g+})$. Column 3 gives the total vibrational intensity in the extreme counter rotator zero-order state. For emission to a given X̃ state bending polyad, the quanta in ν_6' of the upper level increase from left to right, and the upper state levels are colored and textured according to the legend at the right.

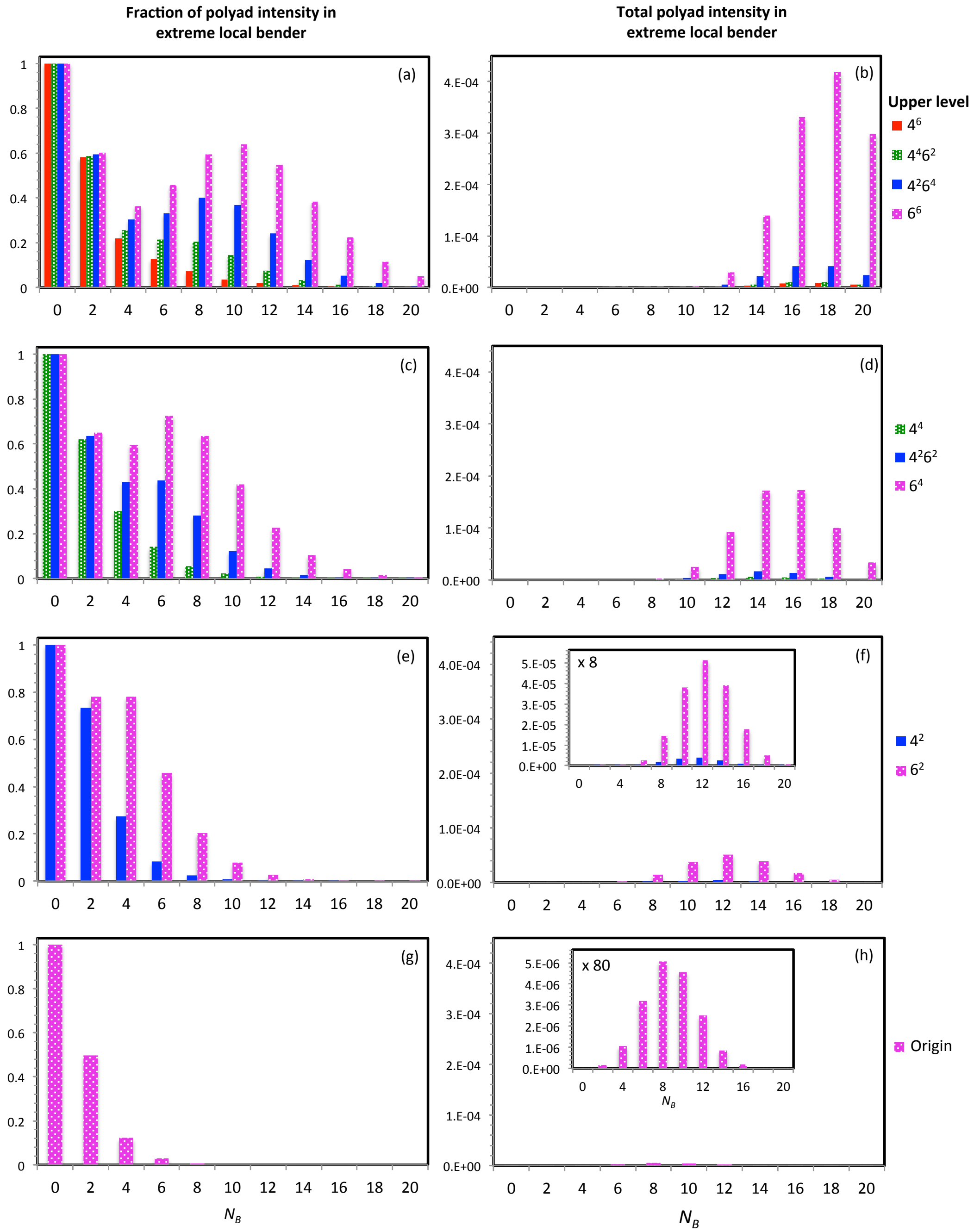

Figure 4-4: Calculated vibrational intensity for emission from a_g members of B^n polyads of $\tilde{\mathrm{A}}$-state acetylene to the extreme local bender zero-order state, $(|N_B^0, 0^0\rangle_L^{g+})$, of each Σ_g^+ pure bending polyad of the $\tilde{\mathrm{X}}$ state. The panels on the left side give the fraction of the total polyad intensity in the extreme local bender, and the panels on the right side give the total vibrational intensity in the extreme local bender. For emission to a given $\tilde{\mathrm{X}}$ state bending polyad, the quanta in ν_6' of the upper level increase from left to right, and the upper state levels are colored and textured according to the legend at the right.

sensitively on the number of quanta in ν_6', and the maximum local bender character is found in the polyad with approximately $N_B = 2v_6'$.

This result is consistent with the FC propensity $v_5'' = v_4' + v_6'$ and with the fact that the pure local mode basis states require an equal combination of cis- and trans-bend character. When $N_B = 2n$, ν_4'' and ν_5'' will contribute equally to the character of the nominally-allowed zero-order bright states. The plurality of extreme counter rotational character obtained in bright states reached from ν_4' overtones and extreme local bender character obtained in bright states reached from ν_6' overtones increases with N_B. For example, although the extreme local bender character of the $N_B = 10$ polyad in the bright state accessed from 4^6 is only 64%, the rest of the intensity is fractionated among ten other zero-order states, and the state with the next-highest intensity ($|8^{+2}, 2^{-2}\rangle_L^{g+}$) carries only 14% of the brightness. This is why we see in Figure 4-2 that although emission from the Ã-state origin becomes increasingly fractionated at high N_B, the fractionation of the emission from the zero-order B^n levels may actually *decrease* slightly because the bright states that are accessed from these levels more closely resemble the character of the eigenstates, which are better described in the local mode basis.

The extreme local bender is obtained from the vibrationless ground state via the ladder operator expression

$$\begin{aligned}|N_B^0, 0^0\rangle_L^{g+} &= \frac{1}{\sqrt{2}}\left[|N_B^0, 0^0\rangle_L + |0^0, N_B^0\rangle_L\right] \\ &= \frac{1}{\sqrt{2}}\left[(\hat{a}_{Ad}^\dagger)^{\frac{N_B}{2}}(\hat{a}_{Ag}^\dagger)^{\frac{N_B}{2}} + (\hat{a}_{Bd}^\dagger)^{\frac{N_B}{2}}(\hat{a}_{Bg}^\dagger)^{\frac{N_B}{2}}\right]|0^0 0^0\rangle \\ &= \frac{1}{2\sqrt{2}}\left[(\hat{a}_{4d}^\dagger + \hat{a}_{5d}^\dagger)^{\frac{N_B}{2}}(\hat{a}_{4g}^\dagger + \hat{a}_{5g}^\dagger)^{\frac{N_B}{2}} + (\hat{a}_{4d}^\dagger - \hat{a}_{5d}^\dagger)^{\frac{N_B}{2}}(\hat{a}_{4g}^\dagger - \hat{a}_{5g}^\dagger)^{\frac{N_B}{2}}\right]|0^0 0^0\rangle. \end{aligned} \tag{4.27}$$

For integer $N_B/2$, the negative terms in Eq. 4.27 cancel so that all of the matrix elements for the transformation from the normal $|v_4^{l_4}, v_5^{l_5}\rangle_N$ basis to the extreme local bend, $|N_B^0, 0^0\rangle_L$, have the same constant phase factor of +1. On the other hand, the extreme counter rotator is obtained from

$$
\begin{aligned}
\left|\left(\tfrac{N_B}{2}\right)^{\frac{+N_B}{2}},\left(\tfrac{N_B}{2}\right)^{\frac{-N_B}{2}}\right\rangle_L^{g+} &= \tfrac{1}{\sqrt{2}}\left[\left|\left(\tfrac{N_B}{2}\right)^{\frac{+N_B}{2}},\left(\tfrac{N_B}{2}\right)^{\frac{-N_B}{2}}\right\rangle_L + \left|\left(\tfrac{N_B}{2}\right)^{\frac{-N_B}{2}},\left(\tfrac{N_B}{2}\right)^{\frac{+N_B}{2}}\right\rangle_L\right] \\
&= \tfrac{1}{\sqrt{2}}\left[(\hat{a}^{\dagger}_{Ad})^{\frac{N_B}{2}}(\hat{a}^{\dagger}_{Bg})^{\frac{N_B}{2}} + (\hat{a}^{\dagger}_{Ag})^{\frac{N_B}{2}}(\hat{a}^{\dagger}_{Bd})^{\frac{N_B}{2}}\right]|0^00^0\rangle \\
&= \tfrac{1}{2}\Big[(\hat{a}^{\dagger}_{4d}+\hat{a}^{\dagger}_{5d})^{\frac{N_B}{2}}(\hat{a}^{\dagger}_{4g}-\hat{a}^{\dagger}_{5g})^{\frac{N_B}{2}} \\
&\qquad + (\hat{a}^{\dagger}_{4g}+\hat{a}^{\dagger}_{5g})^{\frac{N_B}{2}}(\hat{a}^{\dagger}_{4d}-\hat{a}^{\dagger}_{5d})^{\frac{N_B}{2}}\Big]|0^00^0\rangle
\end{aligned}
\tag{4.28}
$$

Matrix elements from Eq. 4.28 carry a phase of $(-1)^{(v_5''+l_5)/2}$ for integer $N_B/2$. We have shown that the matrix element of the extreme local bender have the same relative phase as the bright state $|v_{4x},v_{4y}\rangle|v_{5x},v_{5y}\rangle = |0,v_{4y}\rangle|n,0\rangle$ that is reached from 6^n (all phases are $+1$). The relative phases of the extreme counter rotator are not identical to the phases of the bright state $|0,v_{4y}\rangle|n,0\rangle$ reached from 4^n, but there is a favorable amount of overlap, as evidenced in Figure 4-3.

In fact, from the relationship

$$\hat{a}^{\dagger}_{4d} = \frac{1}{\sqrt{2}}\left(\hat{a}^{\dagger}_{4x}+i\hat{a}^{\dagger}_{4y}\right) \tag{4.29}$$

$$\hat{a}^{\dagger}_{5d} = \frac{1}{\sqrt{2}}\left(\hat{a}^{\dagger}_{5x}+i\hat{a}^{\dagger}_{5y}\right) \tag{4.30}$$

$$\hat{a}^{\dagger}_{4g} = \frac{1}{\sqrt{2}}\left(\hat{a}^{\dagger}_{4x}-i\hat{a}^{\dagger}_{4y}\right) \tag{4.31}$$

$$\hat{a}^{\dagger}_{5g} = \frac{1}{\sqrt{2}}\left(\hat{a}^{\dagger}_{5x}-i\hat{a}^{\dagger}_{5y}\right), \tag{4.32}$$

we find the transformation from the Cartesian components of the normal mode basis to the extreme local bender,

$$
\begin{aligned}
|N_B^0,0^0\rangle_L^{g+} = \frac{1}{4}\Bigg\{&\left[\left(\hat{a}^{\dagger}_{4x}+\hat{a}^{\dagger}_{5x}\right)^2+\left(\hat{a}^{\dagger}_{4y}+\hat{a}^{\dagger}_{5y}\right)^2\right]^{N_B/2} \\
&+\left[\left(\hat{a}^{\dagger}_{4x}-\hat{a}^{\dagger}_{5x}\right)^2+\left(\hat{a}^{\dagger}_{4y}-\hat{a}^{\dagger}_{5y}\right)^2\right]^{N_B/2}\Bigg\}|0^00^0\rangle
\end{aligned}
\tag{4.33}
$$

and the corresponding transformation to the extreme counter rotator,

$$
\begin{aligned}
&|(N_B/2)^{+N_B/2},(N_B/2)^{-N_B/2}\rangle_L^{g+} \\
&\quad = \frac{1}{4}\Bigg\{\Big[(\hat{a}_{4x}^\dagger+\hat{a}_{5x}^\dagger)+i(\hat{a}_{4y}^\dagger+\hat{a}_{5y}^\dagger)\Big]^{N_B/2}\Big[(\hat{a}_{4x}^\dagger-\hat{a}_{5x}^\dagger)-i(\hat{a}_{4y}^\dagger-\hat{a}_{5y}^\dagger)\Big]^{N_B/2} \\
&\qquad +\Big[(\hat{a}_{4x}^\dagger+\hat{a}_{5x}^\dagger)-i(\hat{a}_{4y}^\dagger+\hat{a}_{5y}^\dagger)\Big]^{N_B/2}\Big[(\hat{a}_{4x}^\dagger-\hat{a}_{5x}^\dagger)+i(\hat{a}_{4y}^\dagger-\hat{a}_{5y}^\dagger)\Big]^{N_B/2}\Bigg\}|0^0 0^0\rangle.
\end{aligned}
\tag{4.34}
$$

Inspection of Eq. (4.33) reveals that cross terms among the in-plane components will provide good overlap between the extreme local bender and the $|v_{4x}, v_{4y}\rangle|v_{5x}, v_{5y}\rangle = |0, v_{4y}\rangle|0, n\rangle$ bright state reached from 6^n, whereas inspection of Eq. (4.34) reveals that cross terms of $\hat{a}_{4y}$ with $\hat{a}_{5x}$ will provide good overlap between the extreme counter rotator and the $|0, v_{4y}\rangle|n, 0\rangle$ bright state reached from 4^n.

When viewed from a semi-classical perspective, this result is intuitive and unsurprising. When the trans-bent Ã-state acetylene molecule is displaced along the in-plane cis bend (q_6'), it reaches a half-linear geometry, which is exactly the classical turning point of the extreme local bending vibration in the X̃ state. By putting the correct number of quanta into ν_6', it should be possible to achieve good overlap with the extreme local bend. We can expect the overlap to reach its maximum when the number of quanta in ν_6' are sufficient to reach the half-linear geometry at the classical turning point of the Ã-state vibration.

On the other hand, the extreme counter rotator has no amplitude at the linear geometry, but equal-and-opposite quanta of angular momentum in the two local bends. The classical analog of the motion along this mode involves circular motion of the two hydrogen atoms, in opposite directions. This is very similar to torsional motion in trans-bent Ã-state acetylene. At very high overtones of ν_4' (which have not been experimentally observed), we would expect the torsion to overcome the barrier to cis-trans isomerization, and the classical motion of the above barrier torsion will be very similar to that of the X̃-state extreme counter rotator.

It may be possible to enhance the brightness of FC intensity into large amplitude extreme local benders by adding quanta of the trans bend, ν_3'. Quanta of trans-bend dramatically increase the overall intensity of the Ã—X̃ transition because of the large-amplitude displacement between the two equilibria along the trans-bending coordinate. Furthermore, $\nu_3' + \nu_6'$ samples the cis↔trans isomerization on the S_1 surface, and the half-linear transition state geometries for the S_1 cis↔trans isomerization and the S_0 acetylene↔vinylidene isomerization are believed to be similar.[107,139] Thus if we follow the isomerization coordinate on the S_1 surface, it will give access to large amplitude local bending levels that sample the transition state geometry for the isomerization on the S_0 surface. Moreover, the cis↔trans isomerization causes ν_3' to have a large x_{36} cross-anharmonicity with ν_6' that decouples ν_6' from the B^n polyads.[94,107,126,127,134] As a result, ν_3' not only enhances FC intensity to large amplitude local bend ZOBSs, but it should also give rise to 3^m6^n perfect pluck levels that are relatively unsullied by intrapolyad interactions with levels of ν_4' character, which have been ignored in the present calculation. Chapter 5 discusses the effects of Ã-state anharmonic interactions on the emission intensities.

4.6 Conclusions

Our FC calculation for the Ã—X̃ system of acetylene is done in the harmonic basis, so we do not expect quantitative agreement, especially at high vibrational energies where anharmonic effects become important. However, we have shown that a simple computational method can reproduce qualitative trends in the spectrum and correctly explain observed interference effects. The calculation provides physical explanations for initially puzzling observations, while also uncovering new insights into Franck-Condon propensity rules that will hopefully guide ongoing areas of research. Our results suggest that the search for "local-bender pluck" eigenstates of S_1 acetylene that will grant the best access to local benders in S_0 should focus on states with many quanta in ν_6'. Adding quanta of ν_3' is also likely to improve the FC intensity.

The application of a-axis Eckart constraints to the full-dimensional vibrational overlap integral in the Ã—X̃ system of acetylene removes the out-of-plane component of the trans bend from the vibrational overlap integral. This affects the structure of the coordinate transformation and the symmetry properties of the wavefunctions that participate in the integral, but the consequences have been neglected by previous investigators. Furthermore, because of the generality of the method developed in Paper I for polyatomic linear-bent transitions—provided that the FC integral does not accumulate near the linear geometry—we predict that analogous consequences should appear in the Franck-Condon propensities of other linear-bent systems. In general, application of the *a*-axis Eckart constraint for the linear molecule (restoring the χ Euler angle) will remove one of the degrees of freedom from the bending vibrations of the linear molecule, and this degree of freedom will not contribute to the Franck-Condon integral away from linear geometry. The effect of the Eckart constraint on the vibrational degrees of freedom will depend on the structure of the molecule in the linear and non-linear states, but it will always lead to FC propensity rules involving the bending modes of the linear molecule.

Our calculations suggest that the FC intensity for emission into the ν_5'' cis bend is also best viewed in the Cartesian in-plane vs. out-of-plane basis rather than the polar basis (with v, l quantum numbers), because the properties of the trans-bent $\tilde{\mathrm{A}}$-state give rise to a simple propensity rule for each Cartesian component of ν_5'' (Eq. (4.6)). The propensity rules in Eq. (4.6) are more specific than the $v_5'' = v_4' + v_6'$ propensity rule, and may be used to predict the exact zero-order bright state composition in any basis. To our knowledge, the FC propensities into the Cartesian components of ν_5'' have not been discussed by previous authors.

4.7 Acknowledgements

GBP would like to thank P. Bryan Changala, and Jun Jiang for valuable discussions. We would like to thank Professor Kaoru Yamanouchi and Dr. Richard Duan for sharing their raw dispersed fluorescence data. This material is based upon work supported by the U.S. Department of Energy, Office of Science, Chemical Sciences Geosciences and Biosciences Division of the Basic Energy Sciences Office, under Award Number DE-FG0287ER13671.

Chapter 5

A simplified Cartesian basis model for intrapolyad emission intensities in the bent-to-linear electronic transition of acetylene

Abstract

The acetylene emission spectrum from the *trans*-bent electronically excited $\tilde{\mathrm{A}}$ state to the linear ground electronic $\tilde{\mathrm{X}}$ state has attracted considerable attention because it grants Franck-Condon access to local bending vibrational levels of the $\tilde{\mathrm{X}}$ state with large-amplitude motion along the acetylene $\rightleftharpoons$ vinylidene isomerization coordinate. For emission from the ground vibrational level of the $\tilde{\mathrm{A}}$ state, there is a simplifying set of Franck-Condon propensity rules that gives rise to *only one* zero-order bright state per conserved vibrational polyad of the $\tilde{\mathrm{X}}$ state. Unfortunately, when the upper level involves excitation in the highly admixed *ungerade* bending modes, ν_4' and ν_6', the simplifying Franck-Condon propensity rule breaks down—as long as the usual polar basis (with v and l quantum numbers) is used to describe the degenerate bending vibrations of the $\tilde{\mathrm{X}}$ state—and the intrapolyad intensities result from complicated interference patterns between many zero-order bright states. In this article, we show that, when the degenerate bending levels are instead treated in the Cartesian two-dimensional harmonic oscillator basis (with v_x and v_y quantum numbers), the propensity for *only one* zero-order bright state (in the Cartesian basis) is *restored*, and the intrapolyad intensities are simple to model, as long as corrections are made for anharmonic interactions. As a result of *trans* $\rightleftharpoons$ *cis* isomerization in the $\tilde{\mathrm{A}}$ state, intrapolyad emission patterns from overtones of ν_4' and ν_6' evolve as quanta of *trans* bend (ν_3') are

added, so the emission intensities are not only relevant to the ground-state acetylene $\rightleftharpoons$ vinylidene isomerization—they are also a direct reporter of isomerization in the electronically-excited state.[a]

5.1 Introduction

The bending dynamics of acetylene in both its ground ($\tilde{\mathrm{X}}\ ^1\Sigma_g^+$) and first singlet excited ($\tilde{\mathrm{A}}\ ^1\mathrm{A}_u$) electronic states have attracted considerable spectroscopic and theoretical attention. Acetylene has a linear equilibrium geometry in the $\tilde{\mathrm{X}}$ state but becomes *trans*-bent upon excitation to the $\tilde{\mathrm{A}}$ electronic state. Although acetylene was the first molecule for which a qualitative change in geometry and symmetry accompanying an electronic excitation was proven by spectroscopic methods,[59–61] similar large-amplitude displacements along bending coordinates are known to be quite common in the electronic spectroscopy of π-bonded molecules. Qualitative changes in bond angles and geometries are expected to result whenever an electronic $\pi^* \leftarrow \pi$ excitation changes the effective bond order and the accompanying sp^n hybridization.

Because acetylene is the prototype molecule for CC triple bond systems, its dynamics are of broad interest to the chemical community. Significant work has been done to characterize the acetylene $\rightleftharpoons$ vinylidene and *trans* $\rightleftharpoons$ *cis* isomerization reactions that occur on the $\tilde{\mathrm{X}}$ and $\tilde{\mathrm{A}}$ electronic surfaces, respectively. Both of these reactions primarily involve bending vibrations. Because the $\tilde{\mathrm{A}}$–$\tilde{\mathrm{X}}$ transition involves a large change in equilibrium bond angles, the electronic transition grants Franck-Condon (FC) access to high overtones of the bending vibrations on both electronic surfaces, which has allowed extensive characterization of large-amplitude bending dynamics relevant to chemical isomerization.[85,94] Investigators have used a variety of spectroscopic schemes to observe these levels, including laser-induced fluorescence (LIF),[89,90,93–95,122,126] dispersed fluorescence (DF),[80,86,125,135] and stimulated emission pumping (SEP).[109,140]

---

[a] At the time of the submission of this thesis, the contents of this chapter have been accepted for publication (DOI: 10.1021/jp5113608). The material is reproduced with permission from *The Journal of Physical Chemistry A*, in press. Unpublished work copyright 2015 American Chemical Society.

One phenomenon of particular interest is the emergence of vibrational eigenstates on the $\tilde{\mathrm{X}}$ electronic surface that have large-amplitude local bending character (i.e., with the bending amplitude localized in a single CCH bend), because this vibrational motion lies approximately along the acetylene $\rightleftharpoons$ vinylidene minimum-energy isomerization path.[136,137] Excited bending levels of the $\tilde{\mathrm{A}}$ state might provide Franck-Condon access (via DF or SEP) to isomerization-relevant levels of the $\tilde{\mathrm{X}}$ state, because the half-linear transition state geometry of the *trans* $\rightleftharpoons$ *cis* isomerization in the $\tilde{\mathrm{A}}$ state[107] is believed to resemble the acetylene $\rightleftharpoons$ vinylidene transition state geometry.[131,139,141] This has motivated a recent full-dimensional calculation of Franck-Condon factors in the harmonic normal mode basis.[142,143] The results of the harmonic calculation indicate that $\tilde{\mathrm{A}}$-state levels with high quanta of torsion (ν_4') and *cis*-bend (ν_6') excitation provide good FC overlap with large-amplitude counter-rotational and local bending zero-order bright states, respectively, of the $\tilde{\mathrm{X}}$ state. However, the results of Refs. 142,143 provide only qualitative—not quantitative—agreement with experiment, largely because the treatment fails to account for anharmonic interactions that occur in the $\tilde{\mathrm{A}}$ state.

In this article, we correct for interactions among bending levels of the $\tilde{\mathrm{A}}$ state and obtain near-quantitative agreement with the patterns observed in DF and SEP spectra. Furthermore, we demonstrate that, within sets of pure bending polyads of the $\tilde{\mathrm{X}}$ state with conserved total number of bending quanta, $v_4'' + v_5''$, the emission intensity patterns are correctly explained by a simple Franck-Condon propensity rule in the Cartesian basis for the degenerate two-dimensional harmonic oscillator (2DHO) bending wavefunctions of the linear $\tilde{\mathrm{X}}$ state. These propensities are analogous to those that are naturally applied in the case of nonlinear symmetric-to-asymmetric top transitions.

5.2 Polyad structure and bending dynamics in the $\tilde{\text{A}}$—$\tilde{\text{X}}$ system

Descriptions and frequencies of the acetylene $\tilde{\text{X}}$-state normal modes are given in Table 3.2. The vibrational Hamiltonian of the $\tilde{\text{X}}$ state of acetylene is approximately block diagonal in the polyad-forming quantum numbers, $\{N_{\text{s}}, N_{\text{res}}, l\}$,

$$N_s = v_1'' + v_2'' + v_3'' \tag{5.1}$$

$$N_{\text{res}} = 5v_1'' + 3v_2'' + 5v_3'' + v_4'' + v_5'' \tag{5.2}$$

$$l = l_4 + l_5, \tag{5.3}$$

up to energies of at least 15,000 cm^{-1}.[79–82,84,85,125] In other words, zero-order vibrational levels with the same polyad quantum numbers may interact with one another, but do not interact with levels belonging to other polyads. The N_s quantum number conserves the total quanta of stretching excitation, and the l quantum number conserves the total quanta of vibrational angular momentum from the bending modes. The N_{res} quantum number is approximately proportional to the vibrational energy and arises from near-integer ratios between the mode frequencies that lead to resonances. In addition to the polyad numbers, $\{N_{\text{s}}, N_{\text{res}}, l\}$, the vibrational levels also have well-defined g/u symmetry and can be symmetrized to have well-defined $+/-$ total parity. The parity and g/u symmetry are conserved by the vibrational Hamiltonian, and are therefore also conserved within each polyad. In this paper, we will use the term "polyad set" to mean the set of polyads with given values of $\{N_s, N_{res}\}$, which may differ in l, g/u symmetry, and $+/-$ total parity. In the absence of excitation in the stretching modes, $N_s = 0$ and the bending modes $\nu_4''(\pi_g)$ and $\nu_5''(\pi_u)$ form *pure bending* polyads with conserved polyad numbers

$$N_B = N_{\text{res}} = v_4'' + v_5'' \tag{5.4}$$

$$l = l_4 + l_5. \tag{5.5}$$

At high quanta of bending excitation ($N_B \geq 12$), the ν_4'' and ν_5'' normal modes become strongly mixed through intrapolyad Darling-Dennison interactions, and local bending quantum numbers provide a better zero-order description of the vibrational eigenstates.[136,137]

Descriptions and frequencies of the Ã-state normal modes are given in Table 3.3. A global rovibrational effective Hamiltonian fit has not been attempted for the Ã state, but a polyad model has been used for the near-degenerate torsion $\nu_4'(\mathrm{a}_u)$ and *cis*-bending $\nu_6'(\mathrm{b}_u)$ modes, which interact through Darling-Dennison resonances and *a*- and *b*-axis Coriolis interactions. In this article, we refer to polyads with $v_4' + v_6' = n$ as B^n.

5.3 Franck-Condon propensity rules in the Cartesian basis

The ν_6' (*cis*-bend) and ν_4' (torsion) vibrational modes that comprise the Ã-state B^n polyads correlate to the in-plane and out-of-plane components of the ν_5'' (*cis*-bend) vibration in the X̃ state. Because the frequencies of ν_6' and ν_4' are nearly degenerate and are close to the ν_5'' frequency and because there is no displacement along the *ungerade cis*-bend vibrational mode between the equilibrium geometries of the X̃ and Ã states, there is a Franck-Condon propensity for quanta in these modes to be conserved in the Ã–X̃ transition. That is, there is a vibrational propensity for transitions between levels with $v_5'' = v_4' + v_6'$ to be strongly allowed, but for transitions between vibrational levels with $v_5'' \neq v_4' + v_6'$ to be much weaker. This propensity is well established,[80,85,144] and similar arguments that stem from the near-equal CH bond lengths in the X̃ and Ã states lead to FC propensities conserving the quanta of symmetric and antisymmetric CH stretch, $v_1'' = v_1'$ and $v_3'' = v_5'$, respectively. This leads to a simplifying golden rule that has long guided our understanding of the emission spectrum of acetylene: emission from Ã-state levels *with no excitation in the* B^n *polyads* will lead to *only one* zero-order bright state within each X̃-state polyad. That is, an Ã-state vibrational level with vibrational quantum numbers $(v_1', v_2', v_3', v_4' = 0, v_5', v_6' = 0)$ will have a strong propensity to fluoresce to the zero-order bright state within each X̃-state polyad (with given values of $\{N_s, N_{\text{res}}, l\}$) with quantum numbers

$$\begin{aligned} v_1'' &= v_1', \quad v_2'' = N_s - v_1' - v_5', \\ v_3'' &= v_5', \quad v_4'' = N_{\text{res}} - 5v_1' - 3v_2' - 5v_3', \\ l_4 &= l, \qquad v_5'' = l_5 = 0. \end{aligned} \tag{5.6}$$

Intrapolyad interactions described by the global effective Hamiltonian will fractionate the single zero-order bright state (5.6) between the eigenstates of the polyad in a manner that is well understood.[84,86]

On the other hand, in emission experiments from Ã-state vibrational levels with excitation in the B^n polyads, previous investigators—who used the conventional basis of polar $|v, l\rangle$ quantum numbers to label the degenerate linear molecule bending (2DHO) wavefunctions—observed *multiple* zero-order bright states within a given X̃-state polyad with different combinations of $l_4 + l_5 = l$.[86,145] The observed emission pattern within each X̃-state polyad results from interferences that arise when the multiple zero-order states are fractionated among the eigenstates of the polyad. The SEP and DF spectra in Figure 5-1 from the three $K' = 1$ members of the Ã-state 3^2B^2 polyad to the $N_B = 10$ pure bending polyad of the X̃ state illustrate this point. Each member of the 3^2B^2 polyad gives rise to a qualitatively different pattern of intensities that are distributed across the polyad set. Because many quanta of both v_4'' and v_5'' are required to form large-amplitude local bending levels relevant to the acetylene $\rightleftharpoons$ vinylidene isomerization, it is important to understand the emission intensities from B^n polyads. This was a large part of the motivation for our recent full-dimensional FC calculation.[142,143]

In complement to previous work, we show that—when the X̃-state bending modes ν_4'' and ν_5'' are viewed in the basis of *Cartesian* doubly degenerate 2DHOs with in-plane (y) and out-of-plane (x) bending quanta—there are additional, stricter, Franck-Condon propensities that require conservation of the number of in-plane vs. out-of-

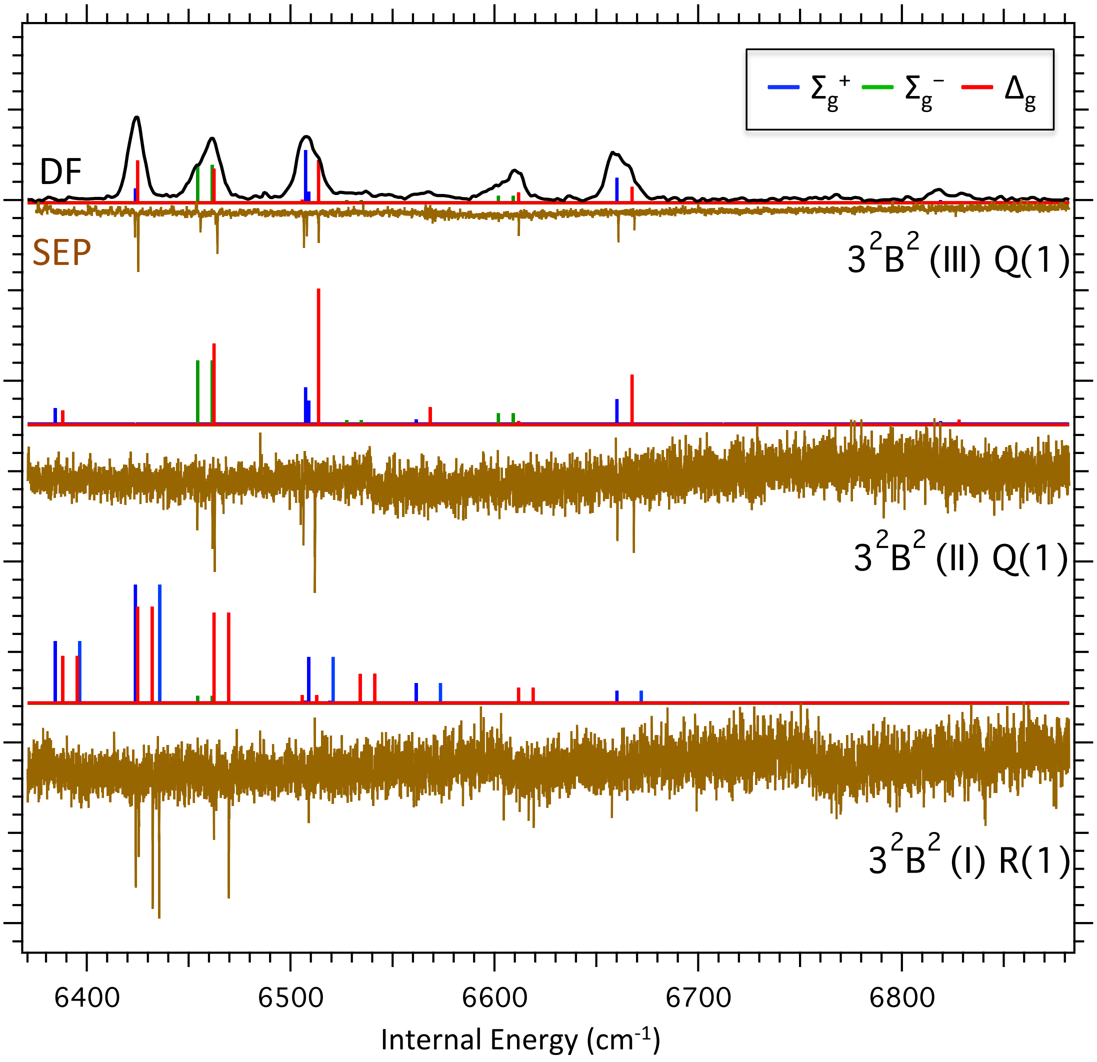

Figure 5-1: The SEP spectra from $J' = 1$ intermediate levels of the three different $K' = 1$ stacks of the 3^2B^2 polyad of the $\tilde{A}$ state (labeled with Roman numerals in order of increasing energy) into the $\{N_s, N_{\text{res}}\} = \{0, 10\}$ pure bending polyad set of the $\tilde{X}$ state are displayed as downward-directed peaks. The eigenstate compositions of the SEP intermediates are given in Table 5.2. The DF spectrum from 3^2B^2 $K' = 1$ Q(1) is shown for comparison at the top of the figure. Also shown as upward stick spectra are the polyad set intensities obtained from the Cartesian propensity model. The stick spectrum is colored according to the symmetry of the lower level (see legend).

plane *cis* bend quanta. That is, there is a strong propensity for

$$v''_{5x} = v'_4, \quad v''_{5y} = v'_6. \tag{5.7}$$

Also, because the out-of-plane component of ν''_4 correlates with a rotation in the *trans*-bent Ã-state, the Ã-state Eckart conditions prevent ν''_{4x} from participating in the *vibrational* FC overlap intensities. This leads to the additional Cartesian propensity, $v''_{4x} = 0$. This Eckart restriction is explained in detail in Ref. 142, and is based on considerations for linear-to-bent transitions that were first utilized by Kovner *et al.*[100] and later described in detail by Watson.[104,119] However, the work of Kovner and Watson was limited to systems where only one bending vibration was considered, so these authors did not explore the multidimensional bending dynamics encoded by bright states that arise from linear-to-bent transitions in polyatomic molecules.

The advantage of applying these stricter Cartesian-basis propensity rules is that in the new basis there is *only one* zero-order state within a given X̃-state polyad that is bright in emission from *any* zero-order level of the Ã state, including those with excitation in the members of the B^n polyads. Thus, when the bright state is viewed in the Cartesian basis, there is no interference. An Ã-state level with vibrational quantum numbers $(v'_1, v'_2, v'_3, v'_4, v'_5, v'_6)$ will have a propensity to fluoresce to the member of a given X̃-state polyad set with quantum numbers

$$\begin{aligned} v''_1 &= v'_1, \quad v''_2 = N_s - v'_1 - v'_5, \\ v''_3 &= v'_5, \quad v''_{4y} = N_{\mathrm{res}} - 5v'_1 - 3v'_2 - 5v'_3 - v'_4 - v'_6, \\ v''_{4x} &= 0, \quad v''_{5x} = v'_4, \quad v''_{5y} = v'_6. \end{aligned} \tag{5.8}$$

Bright states of the type given in Eq. (5.8) represent a well-defined linear combination of degenerate 2DHO states in the polar basis with quantum numbers $|v_4^{(l_4)}, v_5^{(l_5)}\rangle$, which is the basis in which the X̃-state global effective Hamiltonian is written.[84,86,87] The Cartesian-to-polar transformation (in the signed-l product basis of ν''_4 and ν''_5) is obtained by standard ladder operator methods,

$$\begin{aligned}|v_4^{l_4}, v_5^{l_5}\rangle &= [(n_{4d})!\,(n_{4g})!\,(n_{5d})!\,(n_{5g})!]^{-1/2} \\ &\times \left(\hat{a}_{4x}^\dagger + i\hat{a}_{4y}^\dagger\right)^{n_{4d}} \left(\hat{a}_{4x}^\dagger - i\hat{a}_{4y}^\dagger\right)^{n_{4g}} \\ &\times \left(\hat{a}_{5x}^\dagger + i\hat{a}_{5y}^\dagger\right)^{n_{5d}} \left(\hat{a}_{5x}^\dagger - i\hat{a}_{5y}^\dagger\right)^{n_{5g}} |0,0\rangle|0,0\rangle, \end{aligned} \tag{5.9}$$

where

$$\begin{aligned} n_{4d} &= \frac{1}{2}(v_4 + l_4), \quad n_{4g} = \frac{1}{2}(v_4 - l_4), \\ n_{5d} &= \frac{1}{2}(v_5 + l_5), \quad n_{5g} = \frac{1}{2}(v_5 - l_5). \end{aligned}$$

The terms in the expansion of Eq. (5.9) are evaluated according to

$$\begin{aligned} &(\hat{a}_{4x}^\dagger)^{v_{4x}} (\hat{a}_{4y}^\dagger)^{v_{4y}} (\hat{a}_{5x}^\dagger)^{v_{5x}} (\hat{a}_{5y}^\dagger)^{v_{5y}} |0,0\rangle|0,0\rangle \\ &\qquad = (v_{4x}! v_{4y}! v_{5x}! v_{5y}!)^{1/2}\, |v_{4x}, v_{4y}\rangle|v_{5x}, v_{5y}\rangle. \end{aligned} \tag{5.10}$$

The $|v_4^{(l_4)}, v_5^{(l_5)}\rangle$ basis functions must be symmetrized to form states of well-defined vibrational parity,

$$|v_4^{(l_4)}, v_5^{(l_5)}\rangle^{\pm} = \frac{1}{\sqrt{2}} \left(|v_4^{(l_4)}, v_5^{(l_5)}\rangle \pm |v_4^{(-l_4)}, v_5^{(-l_5)}\rangle\right). \tag{5.11}$$

Because of the $K' - l'' = \pm 1$ rotational selection rule for the *c*-type transition moment, only a handful of terms from Eq. (5.9) must be evaluated to obtain the desired transformation. The basis transformation coefficients have asymptotically limiting behavior as N_B increases. For example, in Figure 5-2, the Cartesian overlap coefficients are shown for emission from the a_g members of B^2 upper levels to the various classes of pure-bending bright states, as a function of N_B. Note that the overlaps from the in-plane 6^2 vibrational level and the out-of-plane 4^2 vibrational level are identical in magnitude, but have a *phase relationship* that gives rise to *qualitatively different* bending dynamics and spectral intensity patterns.[143] From the correlation table connecting $\mathrm{D}_{\infty\mathrm{h}}$ to $\mathrm{C}_{2\mathrm{h}}$, we find that in emission to $l = 0$ levels of the $\tilde{\mathrm{X}}$-state, the vibrational selection rules are $\mathrm{a}_g \rightarrow \sigma_g^+$, $\mathrm{b}_g \rightarrow \sigma_g^-$, $\mathrm{a}_u \rightarrow \sigma_u^-$, and

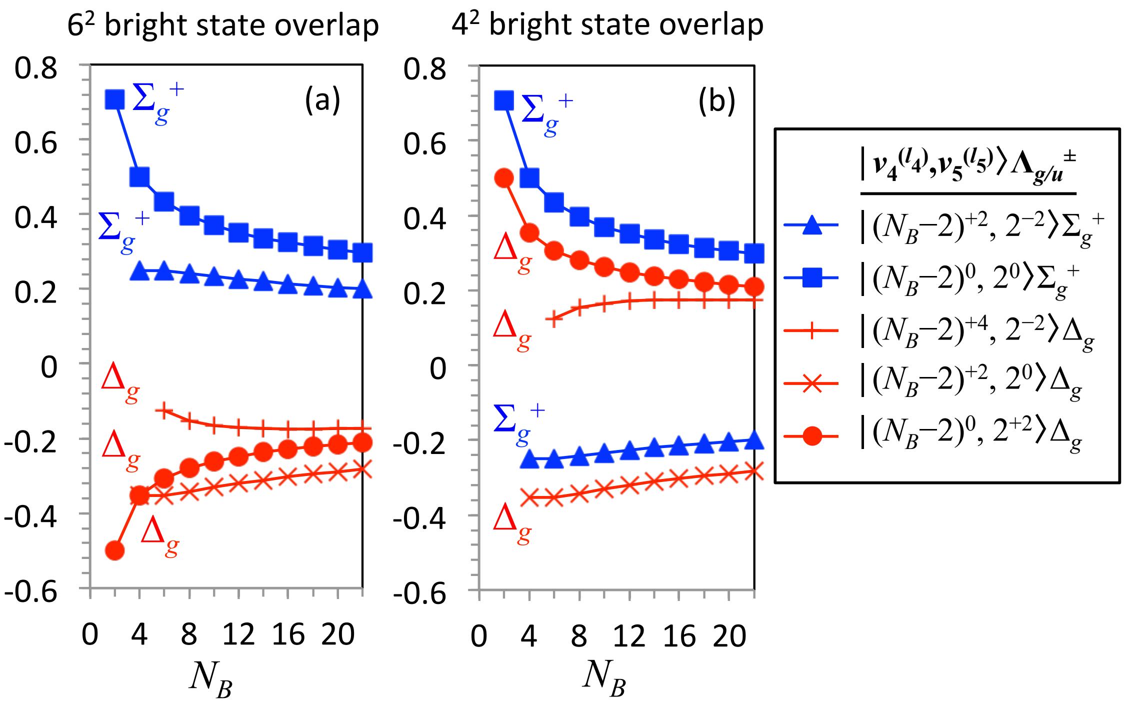

Figure 5-2: Overlap of the zero-order Cartesian bright states $|v''_{4x}, v''_{4y}\rangle |v''_{5x}, v''_{5y}\rangle = |0, N_B - 2\rangle |0, 2\rangle$ (panel a) and $|0, N_B - 2\rangle |2, 0\rangle$ (panel b)—which are accessed from 6^2 and 4^2, respectively—with the $l = 0, 2$ zero-order polar 2DHO basis states. The various classes of polar basis bright states are indicated in the legend. The magnitude of overlap does not depend on which Cartesian plane of ν''_5 is excited. However, the different pattern of phases obtained from either plane encodes a qualitatively different spectral interference pattern from 6^n vs. 4^n (as in Figure 5-1) and qualitatively different bending dynamics (see Figures 3 and 4 of Ref. 143).

$\mathrm{b}_u \rightarrow \sigma_u^+$.

5.4 Corrections for anharmonic interactions

In the current work, we use the $\tilde{\mathrm{X}}$-state global effective Hamiltonian parameters of Ref. 86 to obtain the fractionation of zero-order basis states obtained from Eq. (5.8) into the eigenstates on the $\tilde{\mathrm{X}}$ electronic surface. Although a global effective Hamiltonian fit has not been reported for the $\tilde{\mathrm{A}}$ state, considerable effort has been made to characterize the vibrational structure, and most of the B^n intrapolyad interactions are understood up to 5000 cm^{-1} above the $\tilde{\mathrm{A}}$-state origin.[89,90,93,94,126,146] The individual polyad fit models (using the complex matrix elements defined in Eq. 8 of Ref. 93) can be used to obtain the correctly phased linear combination of zero-order bright states given in Eq. (5.8). Tables 5.1 and 5.2 list the zero-order contributions to the specific eigenstates of the 3^2B^1, 3^3B^1, and 3^2B^2 polyads whose emission spectra are modeled in Section 5.5. In Section 5.5, the *b*-axis Coriolis interaction with the $K' = 0$ levels is neglected, because it is a small effect and any $K' = 0$ character that results will fluoresce to $\tilde{X}$-state polyads with $l = 1$.

Table 5.1: Eigenenergies (in cm^{-1}) and basis state coefficients for the nominally 3^n6^1 $J_{K_aK_c} = 1_{10}$ upper levels used to obtain the DF spectra reported in Ref. 86. The coefficients are obtained from the fit parameters for *a*- and *b*-axis Coriolis interactions given in Refs. 89 and 90.

zero-order vib. level	$J_{K_aK_c}$	$n = 2$ 44972.36	$n = 3$ 45941.07
3^n6^1	1_{10}	$-0.841i$	$-0.938i$
3^n4^1	1_{01}	0.036	0.027
	1_{11}	0.539	0.345

Table 5.2: Eigenenergies (in cm^{-1}) and basis state coefficients for the three $K' = 1$ levels of the 3^2B^2 used as the upper level for the SEP spectra in Figure 5-1. The levels are labeled with Roman numerals in order of increasing energy. The R(0) and Q(1) transitions used in the PUMP terminate on levels of opposite total rovibronic parity.

zero-order vib. level	$J_{K_aK_c}$	(I) R(0) 45728.12	(II) Q(1) 45728.20	(III) Q(1) 45812.77
$3^24^2(a_g)$	1_{01}		$0.054i$	0.035
	1_{11}		$0.63i$	0.74
	1_{10}	0.19		
$3^24^16^1(b_g)$	1_{01}	$0.021i$		
	1_{11}	$0.25i$		
	1_{10}		0.77	$-0.59i$
$3^26^2(a_g)$	1_{01}		$-0.0013i$	-0.016
	1_{11}		$0.078i$	-0.31
	1_{10}	0.95		

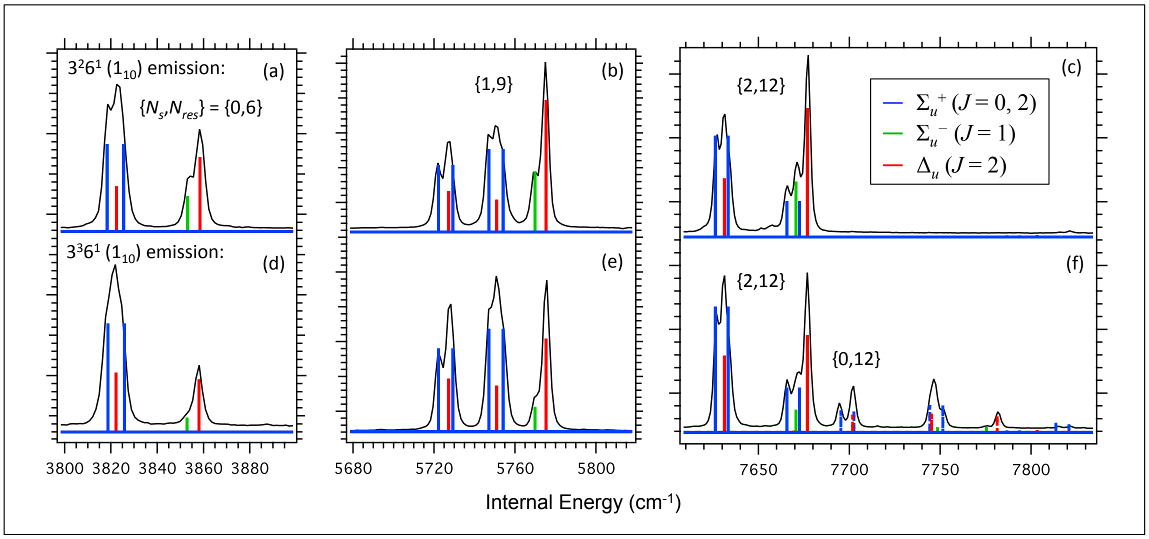

Figure 5-3: High-resolution DF spectra obtained from $J_{K_aK_c} = 1_{10}$ rotational levels of 3^26^1 and 3^36^1 into a representative collection of pure-bend and stretch-bend polyad sets. The DF spectra were previously reported in Ref. 86, and the eigenstate compositions of the upper levels are given in Table 5.1. Stick spectra show the relative intensities obtained from the Cartesian propensity model, colored according to the symmetry of the lower state. In panels (c) and (d), the modeled intensities into the polyad sets $\{N_s, N_{res}\} = \{2, 12\}$ and $\{0, 12\}$ are scaled by the relative Franck-Condon factors reported in Ref. 86.

5.5 Comparison of measured emission intensity patterns with the Cartesian bright state model

Figure 5-3 provides a comparison between the high-resolution DF spectra obtained from the $J_{K_aK_c} = 1_{10}$ rotational level of 3^26^1 and 3^36^1 (Ref. 86) and the Cartesian propensity model developed in Section 5.3. The zero-order members of the B^1 polyad are almost exactly degenerate, and the eigenstates are strongly mixed by *a*- and *b*-axis Coriolis interactions.[89] However, because modes ν_3' and ν_6' combine to form the reaction coordinate for the *trans* $\rightleftharpoons$ *cis* isomerization, there is a large negative x_{36} cross-anharmonicity that encodes the softening of the potential energy surface along the approach to the barrier.[94] In the combination polyads, 3^nB^1, the addition of mode ν_3' causes a much larger decrease in the effective ν_6' frequency than in the effective ν_4' frequency. As a result, the zero-order 3^n6^1 levels are detuned from resonance, and the mixing angle of zero-order 3^n4^1 into the nominally 3^n6^1 eigenstate decreases with increasing n (see Table 5.1).

The model captures several clear differences between the intrapolyad intensity patterns in Figure 5-3 that result from the evolution of the $3^n\mathrm{B}^1$ polyad structure. First, because the symmetry of $3^n4^1(\mathrm{a}_u)$ correlates to Σ_u^- and the symmetry of $3^n6^1(\mathrm{b}_u)$ correlates to Σ_u^+, the relative intensity of transitions to Σ_u^- levels is a direct measurement of the a_u character of the upper level. There is a $\sim$ 2-fold decrease in the relative intensity of Σ_u^- levels when the upper level is changed from 3^26^1 to 3^36^1, which is consistent with the decreased admixture of 3^n4^1 character from a-axis Coriolis effects in the upper level. Similar arguments are used by the authors of Ref. 94 to determine the a_g vs. b_g character of the members of $3^2\mathrm{B}^2$ from the appearance of Σ_g^- peaks in the SEP spectrum.

On the other hand, Δ_u correlates with $\mathrm{a}_u + \mathrm{b}_u$, so the intensities of transitions to Δ_u levels in Figure 5-3 arise from *interferences* between the zero-order a_u and b_u contributions to the upper eigenstate. For example, the intensities of the transitions to the Δ_u level at 3860 cm^{-1} in the pure-bend polyad set $\{N_s, N_{\mathrm{res}}\} = \{0, 6\}$ and at 5770 cm^{-1} in the stretch-bend polyad $\{1, 9\}$ arise from constructive interference with the admixed 3^n4^1 character. Thus, the relative intensity decreases with n.

The emission to $N_{\mathrm{res}} = 12$, shown in Figure 5-3 panels c and f, is qualitatively different because $v_4'' = 11$ is the location of the first node in the *trans*-bending progression from 3^26^1, so the set of pure bending polyads with $\{N_s, N_{\mathrm{res}}\} = \{0, 12\}$ do not appear in the spectrum from 3^26^1. On the other hand, the *trans*-bending progression from 3^36^1 has its first node in the *trans*-bending progression at $v_4'' = 9$, so both the $\{2, 12\}$ and $\{0, 12\}$ polyad sets appear in the spectrum. This shift in the node position reflects the shift in the first node of the upper state vibrational wavefunction along the *trans*-bend coordinate.

The DF spectrum to the $\{1, 11\}$ polyad set is shown in Figure 5-4 and is compared with both the results of the full Franck-Condon calculation, described in Refs. 142 and 143 (upward stick spectra), and the Cartesian propensity model described in Section 5.3 (downward stick spectra). The Cartesian propensity model does a fairly good job of reproducing the highly fractionated bright states, but the relative intensities at the weak, high-frequency end of the polyad are not reproduced by the model. For example, the model overestimates the intensity of the cluster at ~7080 cm^{-1} relative to the peaks at ~7220 cm^{-1}. When the full FC calculation is used, the relative intensities are in closer agreement with the observed spectrum. The cause for this is Duschinsky rotation among the b_u levels (ν_5' and ν_6', which correlate to ν_3'' and ν_5''—see Tables 3.2-3.3). In the full FC calculation, there is non-negligible intensity into the class of bright states $(v_1, v_2, v_3, v_4^{(l_4)}, v_5^{(l_5)}) = (0, 0, 1, 6^{(l)}, 0^0)$. This class of bright states involves an exchange of one quantum of ν_3'' for $\nu_2'' + \nu_4'' + \nu_5''$ and carries approximately 0.3% of the intensity away from the nominally bright states of the type $(0, 1, 0, 7^{(l_4)}, 1^{(l_5)})$, which is sufficient to cause noticeable disagreement with the model at the weak, high-frequency end of the polyad. In emission from $3^3 6^1$, the full FC calculation still places too much relative intensity in the cluster at ~7120 cm^{-1}. This is probably caused by additional anharmonic interactions between $3^3 6^1$ and nearby levels (most notably B^5(II) $K = 1$).[126] At present, these interactions are incompletely understood and are not taken into account in our model.

Figure 5-1 shows the SEP spectra (downward peaks) from the three $K' = 1$ rotational stacks of the 3^2B^2 polyad. Roman numerals are used to label the admixed energy levels from low to high. Also shown for comparison are the DF spectrum from 3^2B^2(III) and the relative intensity patterns obtained from the Cartesian propensity model. The SEP spectra are obtained at much higher resolution than the DF spectrum, but the DF spectrum has greater sensitivity. Furthermore, the DF spectrum has its intensity calibrated against the emission spectrum of a halogen lamp dispersed to the same detector, whereas the intensities in the SEP spectra are not corrected for fluctuations in laser power and laboratory conditions as the laser is scanned. Therefore, the relative intensities in the DF spectrum are quantitatively accurate to within better than 15%, whereas the relative intensities in the SEP spectra are only qualitative.

The intensity patterns in Figure 5-1 are reproduced remarkably well by the Cartesian propensity model. The zero-order $3^2 6^2$ state is detuned from polyad resonance by isomerization-induced x_{36} cross anharmonicity so that it is separated from the zero-

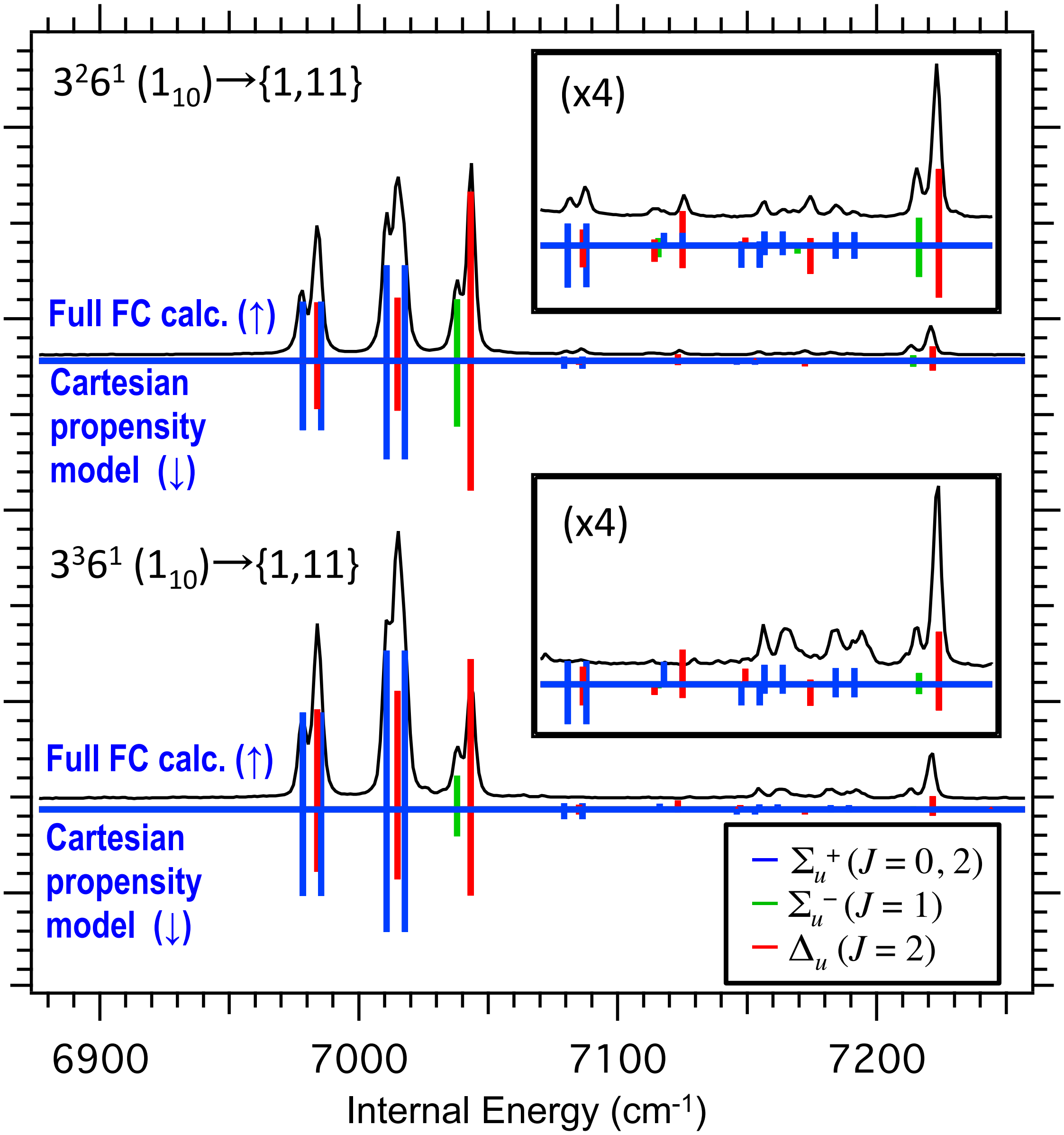

Figure 5-4: High-resolution DF spectra obtained from $J_{K_aK_c} = 1_{10}$ rotational levels of 3^26^1 and 3^36^1 into the $\{N_s, N_{\text{res}}\} = \{1, 11\}$ polyad set. The DF spectra have been previously reported in Ref. 86. For comparison, the relative intensities obtained from the Cartesian propensity model (downward stick spectra) and the Full Franck-Condon calculation described in Ref. 142 (upward stick spectra) are shown, colored according to the vibrational symmetry of the lower level (see legend). Duschinsky rotation of the b$_u$ modes leads to minor discrepancies between the observed spectrum and the Cartesian propensity model, which are reproduced by using the Full FC calculation. (See the text for further discussion.)

order $3^24^16^1$ level by 82.12 cm^{-1} and from the zero-order 3^24^2 level by 102.91 cm^{-1}. As a result, the 3^2B^2(I) $J_{K_aK_c} = 1_{10}$ level escapes most of the effect of a-axis Coriolis interaction with $3^24^16^1$ through the $2A\zeta^a_{46} = 23.559$ cm^{-1} matrix element, but it is not immune to Darling-Dennison interaction with 3^24^2 through the $K_{4466} = -66.502$ cm^{-1} matrix element (see Table 5.2).[94]

As a result of strong a-axis Coriolis interaction between 3^24^2(a$_g$) and $3^24^16^1$(b$_g$), the emission spectra from 3^2B^2(II) and 3^2B^2(III) both terminate on levels with Σ_g^+ and Σ_g^- symmetry with comparable relative intensity, even though 3^24^2(a$_g$) nominally fluoresces only to $l = 0$ levels of Σ_g^+ symmetry and $3^24^16^1$(b$_g$) fluoresces only to $l = 0$ levels of Σ_g^- symmetry. On the other hand, the emission spectrum from 3^2B^2(I) includes fluorescence only to $l = 0$ levels of Σ_g^+ symmetry, because 3^26^2 is detuned from a-axis Coriolis resonance with $3^24^16^1$. In the emission spectrum from 3^2B^2(III), the first cluster at ∼6380 cm^{-1} is absent due to destructive interference from $3^24^2 \leftrightarrow 3^26^2$ Darling-Dennison interaction. Unfortunately, the SEP spectrum obtained from 3^2B^2(I) has a poor signal-to-noise ratio due to the weakness of the PUMP transition, so the complementary constructive interference is not observed in the spectrum. Nevertheless, the six peaks in the 3^2B^2(I) SEP spectrum that are above the signal-to-noise floor are the six strongest transitions predicted by the Cartesian propensity model.

5.6 Analogy to nonlinear molecular systems

Our goal in the current work has been to model the emission spectrum of acetylene, but in this section, we briefly point out that our analysis is generally applicable to a wide range of molecular systems. In any electronic transition that involves a change of equilibrium geometry from a point group with degenerate representations to one without degenerate representations, each doubly-degenerate vibrational mode will correlate with two non-degenerate vibrational modes of different symmetry. Therefore, we expect similar effects not only in other linear-to-bent transitions but also in any other symmetric-to-asymmetric-top transitions, where the coordinate transformations for Franck-Condon integrals are most naturally performed using a Cartesian basis for the degenerate vibrations.

As a concrete example, consider the doubly degenerate mode ν''_{11} in the ground electronic state of allene $^1\mathrm{A}_1$ ($\mathrm{D}_{2\mathrm{d}}$), pictured in the bottom half of Figure 5-5. Because allene is a symmetric top in the $\mathrm{D}_{2\mathrm{d}}$ configuration, the choice of molecule-fixed x and y axes is arbitrary and any linear combination of the degenerate components can be used to represent the vibration. In Figure 5-5, we chose the x and y axes to lie in the planes defined by the H–C–H groups at either end of the molecule, which are oriented at 90° to one another. We have chosen the phases of the two components so that ν''_{11x} encodes motion in the xz plane and ν''_{11y} encodes motion in the yz plane. In either case, one of the H–C–H groups undergoes an out-of-plane rocking motion and the other H–C–H group undergoes an in-plane wagging motion. In the rotating allene molecule, the components of the degenerate e vibrational modes are split by first-order (and higher-order) a-axis Coriolis interactions into eigenstates with well-defined l quantum number.[147] Eigenstates of this type with $\pm l_{11}$ vibrational angular momentum quantum number will have wavefunctions that depend on the complex linear combination of Cartesian normal coordinates $q''_{11x} \pm i q''_{11y}$.

The first excited $^1\mathrm{B}_1$ electronic state of allene is stabilized by a large-amplitude torsion according to Walsh's rules, and theoretical calculations predict a planar geometry.[148] (The electronic symmetry correlates to $^1\mathrm{A}_g$ in $\mathrm{D}_{2\mathrm{h}}$.) The doubly-degenerate e vibrational modes are split into singly degenerate modes of b_2 and b_3 symmetry. The top half of Figure 5-5 shows the $\nu'_{14}(\mathrm{b}_{3u})$ and $\nu'_{15}(\mathrm{b}_{2u})$ modes that correlate with the y- and x-axis components of ν''_{11y} and ν''_{11x}, respectively. Although similar correlations exist for the other doubly degenerate modes of allene, we have chosen this mode as an example because it bears a striking resemblance to the acetylene case where out-of-plane torsion (ν'_4) and in-plane bending (ν'_6) modes in the excited electronic state correlate with the Cartesian components of the degenerate ground electronic state *cis* bend (ν''_5).

In analogy to acetylene, we expect the Franck-Condon factors to obey propensity rules in the basis of the *Cartesian* components of ν''_{11}. That is, we expect bright states that conserve quanta of $v''_{11y} = v'_{14}$ and $v''_{11x} = v'_{15}$ to have the strongest Franck-Condon factors. These zero-order Cartesian bright states will be fractionated by the effective Hamiltonian into eigenstates with well-defined vibrational angular momentum. Certainly, this is not a novel idea, because the natural approach to the coordinate transformation in the planar$\leftrightarrow$twisted allene problem is to use the point group of lower symmetry ($\mathrm{D_{2h}}$). The authors of Ref. 149 used *ab initio* calculations of the ground $^1\mathrm{A}_1$ and excited $^1\mathrm{A}_g$ electronic states to calculate a full-dimensional Duschinsky matrix for the transition. The results indicate that the q'_{14} and q'_{15} modes remain essentially unmixed with other normal coordinates, which supports our argument for Cartesian propensity rules. In Table 5 of Ref. 149, the relative orientations of the x and y axes for the ground state Cartesian-to-normal-mode transformation are not specified (and the choice is arbitrary for symmetric top molecules), but the normal coordinates will match those given in our Figure 5-5 if the axes are chosen to lie in the dihedral planes (rotated 45° about the z-axis relative to our axis choice in Figure 5-5).

There are numerous double-bonded systems that undergo torsional displacement upon electronic excitation and similar propensity arguments should hold. Such systems have received widespread attention because of interest in photoinduced *cis-trans* isomerization.[150] Propensities will exist for conserved quanta in Cartesian Franck-Condon zero-order bright states to be fractionated among the eigenstates by Coriolis forces and other interactions. Of course, the zero-order Franck-Condon bright states have a direct bearing on photoinduced isomerization dynamics.

5.7 Discussion and Conclusions

Although the $\tilde{\mathrm{A}} \rightarrow \tilde{\mathrm{X}}$ emission intensities in acetylene have attracted the attention of researchers for more than two decades, the origin of relative intensities within polyad sets with given $\{N_s, N_{\mathrm{res}}\}$ quantum numbers have not previously been fully understood. For example, the authors of Ref. 86 were forced to treat the interference pattern of Δ_u levels in the 3^n6^1 DF spectra by empirical fitting—it was not understood

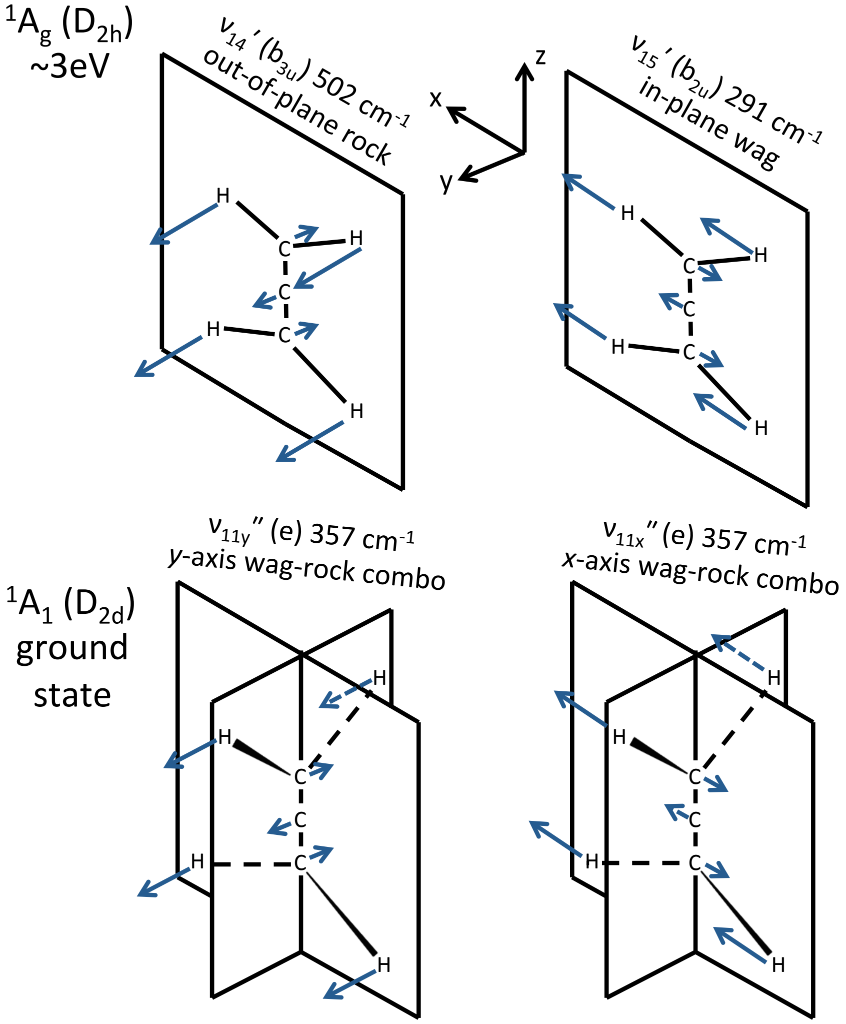

Figure 5-5: Allene has a twisted D_{2d} geometry in its $^1A_1$ ground state but $\pi^* \leftarrow \pi$ excitation leads to a planar D_{2h} ^1A_g state at an adiabatic (non-vertical) electronic excitation energy of $\sim$3 eV. The lower half of the figure depicts the two Cartesian components of the degenerate ν''_{11} (e) vibrational mode. These components correlate to the non-degenerate out-of-plane rock ν'_{14} and in-plane wag ν'_{15} of the excited state.

at the time how to predict the interferences, even though the eigenstate compositions of the upper levels[90] and the lower levels[86,87] were already known. So far, fluorescence patterns obtained from Ã-state levels with intensity in B^n polyads have always been discussed in terms of *more than one* bright state per polyad of the X̃ state, because the X̃-state effective Hamiltonian is written in terms of the polar 2DHO basis.[86] In the current work, we demonstrate that in the *Cartesian* basis of degenerate 2DHOs for the bending modes, this is *not* the case, and there is a propensity for *only one* bright state per X̃-state polyad, described in Eq. (5.8). In other words, we show that the most appropriate basis for writing the effective Hamiltonian of the linear X̃ state (the polar basis) is *not the same* as the "best" basis for describing the zero-order bright states that are observed in emission from the Ã state. These are better described in the Cartesian basis because of the way in which the bent Ã state "chooses" an x, y axis frame for Franck-Condon integral. However, the two basis sets are connected by a straightforward ladder operator transformation that enables us to greatly simplify our interpretation of the intensity patterns.

Our treatment of the linear-to-bent acetylene transition is analogous to the most natural treatment for nonlinear symmetric-to-asymmetric top transitions, where the x and y components of degenerate symmetric top vibrations are chosen to correlate to the components of the lower-symmetry modes along the well-defined x and y asymmetric top axes. However, linear-to-bent transitions have led to confusion in the literature because the number of vibrational degrees of freedom changes from $3N-5$ to $3N-6$, so the correlation of the bending modes is not straightforward. We believe that our treatment should be quite general for linear polyatomic molecules undergoing transitions to bent geometries. One Cartesian bending mode component will correlate to the a-axis rotation in the bent molecule. Due to Eckart constraints, this component will not contribute to the vibrational FC overlap. Franck-Condon propensities in the other bending modes should be viewed in the basis of in-plane vs. out-of-plane Cartesian components of the planes chosen by the nonlinear equilibrium configuration.

Furthermore, the relative intensities *between* the different polyads that comprise a polyad set with given $\{N_s, N_{\text{res}}\}$ quantum numbers (but differing in l, g/u symmetry, and $+/-$ total parity) are also correctly described by the Cartesian propensity model. Of course, in predict the relative intensities between polyad sets differing in N_s and N_{res}, one must also know the Franck-Condon progressions in the FC-active modes, ν_2'' and ν_4''. A full FC treatment is also necessary to correct for the effects of Duschinsky rotation or for interferences caused by Ã-state interactions that are off-diagonal in the approximately conserved B^n polyads. The effects of Duschinsky rotation are minor and will not affect emission intensities into pure bending polyads because each of the Ã-state bending modes (ν_3', ν_4', and ν_6') belong to different symmetry blocks, so Duschinsky rotation only causes stretch↔stretch or stretch↔bend interactions, and *not* bend↔bend interactions. However, in the absence of a global rovibrational Ã-state effective Hamiltonian, *extrapolyad* interactions remain a challenge.

The success of our Cartesian propensity model relies on our knowledge of the B^n intrapolyad interactions in the Ã state. Not only does the model provide an additional physical test of our description of intrapolyad interactions in the upper levels—it should also provide us with a means of observing directly the evolution of the bending dynamics of Ã-state acetylene in the vicinity of the *trans* ⇌ *cis* isomerization. For example, Figure 4 of Ref. 134 depicts the evolution of the 3^nB^4 polyad wavefunctions as quanta of ν_3' are added. Intrapolyad Darling-Dennison resonance causes the wavefunctions of B^4 to resemble degenerate 2DHO wavefunctions with well-defined l quantum number. However, as quanta in ν_3' are added, the isomerization causes the bending character to evolve in a manner that ought to be directly observable in the emission patterns from these levels. Previous work has made qualitative use of intensity distributions in overview DF spectra to characterize levels of Ã-state acetylene.[135,151] However, as shown in the current work, the full emission spectrum is not necessary—the high-resolution emission pattern from the upper level in question to a single X̃-state polyad set provides the quantitative information necessary for a complete characterization of the bending dynamics of the upper level.

Finally, the Cartesian propensity model provides an additional tool for understanding the vibrational dynamics in the X̃ state that are encoded by the intrapolyad fractionation patterns that are observed in the spectrum, since it is straightforward to transform from a Cartesian zero-order bright state to a spectral interference pattern. As shown in Ref. 143, it is also straightforward to transform to the basis of local bending modes relevant to the acetylene $\rightleftharpoons$ vinylidene isomerization. Indeed, the quest to find $\tilde{\mathrm{A}}$-state levels that grant access to local bending levels along the acetylene-vinylidene isomerization path was a major motivating factor for the work described here.

5.8 Acknowledgements

We are indebted to Prof. Kaoru Yamanouchi and Dr. Richard Duan for sharing their raw DF data with us. G. B. P. thanks P. Bryan Changala for stimulating discussions. This material is based upon work supported by the U.S. Department of Energy, Office of Science, Chemical Sciences Geosciences and Biosciences Division of the Basic Energy Sciences Office, under Award Number DE-FG0287ER13671.

Chapter 6

Millimeter-wave optical double resonance schemes for rapid assignment of perturbed spectra, with applications to the $\tilde{\mathrm{C}}\ ^1\mathrm{B}_2$ state of SO_2

Abstract

Millimeter-wave detected, millimeter-wave optical double resonance spectroscopy (mmODR) is a powerful tool for the analysis of dense, complicated regions in the optical spectra of small molecules. The availability of chirped-pulse Fourier-transform millimeter-wave spectrometers opens up new schemes for double resonance experiments, based on broadband detection of free induction decay. We demonstrate a multiplexed population labeling scheme for rapid acquisition of double resonance spectra, probing multiple rotational transitions simultaneously. We also demonstrate a millimeter-wave implementation of the coherence-converted population transfer scheme for background-free mmODR, which provides a ∼10-fold sensitivity improvement over the population labeling scheme. We analyze perturbations in the $(v_1, v_2, v_3) = (1, 3, 2)$ level of the $\tilde{\mathrm{C}}$ state of SO_2, and we rotationally assign a b_2 vibrational level that borrows intensity via a *c*-axis Coriolis interaction. We also demonstrate the effectiveness of our multiplexed mmODR scheme for rapid acquisition and assignment of three predissociated vibrational levels of the $\tilde{\mathrm{C}}$ state of SO_2 between 46800 and 47650 cm^{-1}.

6.1 Introduction

The $\tilde{\mathrm{C}}$ ($^1\mathrm{B}_2$) state of SO_2 has attracted considerable attention from spectroscopists, dynamicists, and theorists. The origin at $\nu_{0-0} = 42,573.45$ cm^{-1} is close in energy to the onset of dissociation into ground state $\mathrm{SO}(^3\Sigma^-)$ + $\mathrm{O}(^3\mathrm{P})$ at ∼45,725 cm^{-1}.[152] Thus, the $\tilde{\mathrm{C}}$ state plays an important role in the photodissociation of SO_2 in the earth's atmosphere. However, there is evidence for more than one dissociation mechanism, including vibronic coupling to the dissociation continuum of the ground $\tilde{\mathrm{X}}$ electronic state,[153–155] intersystem crossing to one or more dissociative triplet states,[152,156–158] and a singlet mechanism due to avoided crossing with the dissociative 3 $^1\mathrm{A}'$ state.[159,160] It is likely that all three mechanisms contribute, and that the relative contribution depends on the energy.[161,162]

The $\tilde{\mathrm{C}}$ state potential energy surface (PES) has an unusual structure around equilibrium. There is a double-minimum potential in the q_3 antisymmetric stretch coordinate with a barrier of ∼141 cm^{-1} at the $\mathrm{C}_{2\mathrm{v}}$ geometry.[163] The global minimum of the PES is doubly-degenerate and has a C_s equilibrium geometry with non-equivalent SO bond lengths of ∼1.491 and 1.639 Å.[163] There is considerable indirect evidence for staggering in the $(v'_1, v'_2, v'_3) = (0, 0, v'_3)$ progression that reflects the presence of the barrier,[163–165] but direct observation of b_2 vibrational levels (with odd quanta of v'_3) has not previously been made because transitions to b_2 vibrational levels of the $\tilde{\mathrm{C}}$ state are forbidden from the vibrationless level of the $\tilde{\mathrm{X}}$ $^1\mathrm{A}_1$ ground electronic state. (Throughout this chapter, we will use the notation (v_1, v_2, v_3) to refer to the vibrational quantum numbers.) There have been observations of dispersed fluorescence from $\tilde{\mathrm{C}}$-state levels around 47,620–50,570 cm^{-1} of excitation, terminating on $\tilde{\mathrm{X}}$-state levels of b_2 vibrational symmetry,[159,166] which indicates $\mathrm{a}_1/\mathrm{b}_2$ vibrational admixture at 5000–8000 cm^{-1} of vibrational excitation in the $\tilde{\mathrm{C}}$-state. Brand *et al.*[166] have attributed the admixture to rotation-vibration interaction via *c*-axis Coriolis matrix elements, but Ray *et al.*[159] have argued that the admixture is due to vibronic interaction with the dissociative 3 $^1\mathrm{A}'$ state. Here, we report the first direct observation and rotational assignment of a b_2 vibrational level of the $\tilde{\mathrm{C}}$ state, which borrows intensity via c-axis Coriolis interaction, and we provide a note of caution about interpreting the interaction mechanism in the absence of rotational assigments.

Above the dissociation threshold, the laser-induced fluorescence (LIF) intensities from the $\tilde{\mathrm{C}}$ state fall off rapidly, although the Franck-Condon absorption intensity envelope continues to increase.[154] The $(v_1', v_2', v_3') = (1, 3, 2)$ vibrational level, located $\sim$100 cm^{-1} below the dissociation threshold, is the strongest band in the LIF spectrum of SO$_2$. However, due to perturbations in the rotational structure, only a handful of rotational levels were assigned in the jet-cooled LIF spectra of Yamanouchi *et al.*[43] In the current work, we use this perturbed region to demonstrate the effectiveness of various millimeter-wave optical double resonance (mmODR) schemes, and we report a rotational analysis of the region surrounding the perturbed band.

The use of free induction decay (FID)-detected, mmODR schemes greatly simplifies the analysis of perturbed band structures. When monitoring millimeter-wave transitions of the ground state, mmODR information can be used for unambiguous identification of the lower level involved in the optical transition, because a double resonance signal indicates that the millimeter-wave transition and the optical transition share a common level. The broadband Fourier-transform capabilities of our chirped-pulse millimeter wave spectrometer,[51] based on the Pate design,[32,34] allow us to perform multiplexed mmODR, where more than one millimeter-wave transition is monitored simultaneously, and we demonstrate the effectiveness of multiplexed mmODR schemes for rapid acquisition and rotational assignment of three predissociated levels of the $\tilde{\mathrm{C}}$ state of SO$_2$ between 46800 and 47650 cm^{-1}. We have also made a millimeter-wave implementation of the background free coherence-converted population transfer (CCPT) technique.[167–169] We find that CCPT provides an excellent improvement in signal-to-noise over traditional population labeling schemes, and is a promising alternative to polarization-based background-free double-resonance methods.[44] However, there are challenges to implementing the technique in our current experimental configuration, where the coherent experiment must be completed in a time window that is short compared to the millimeter-wave Doppler lifetime of < 2 μs. In Section 7.3, we discuss the advantages of various double-resonance schemes.

6.2 Experimental details

6.2.1 Millimeter-wave optical double resonance configuration

The mmODR spectra were obtained in a vaccuum chamber equipped with a chirped-pulse millimeter-wave (CPmmW) spectrometer. The CPmmW spectrometer is described in Ref. 51, so we will omit the details here. The UV radiation was generated by a pulsed dye laser (Lambda Physik FL3002E), operating with Coumarin 440 dye, pumped by the 355 nm third harmonic of an Nd:YAG laser (Spectra-Physics DCR-3). The dye laser output was frequency-doubled in a β-barium borate crystal. A small portion of the fundamental was passed through a heated $^{130}\mathrm{Te}_2$ vapor cell for frequency calibration. An intracavity etalon reduced the spectral width to 0.04 cm^{-1}. An unskimmed molecular jet of neat SO_2 was expanded through a pulsed valve (General Valve, Series 9, $d = 1$ mm) at a backing pressure of 2 atm.

The geometry used for the double resonance experiment is shown schematically in Figure 6-1. The millimeter-wave beam was focused by a matched set of 20 cm diameter polytetrafluoroethylene (PTFE) lenses ($f \approx 30$ cm). The UV laser beam was expanded to match the millimeter-wave beam waist, which had a diffraction-limited diameter of approximately 2.5 cm. The laser beam was propagated counter to the molecular jet, and the millimeter waves were propagated at a 90° angle. The E-field of the focused millimeter-wave beam was $\sim$42 V/m and the UV power was $\sim$300 μJ/pulse. Both the UV laser and the millimeter waves were vertically polarized.

6.2.2 Available schemes for millimeter-wave optical double resonance

Microwave detected, microwave optical double resonance (MODR) was first demonstrated by Nakajima *et al.*[42] The authors of Ref. 42 pointed out two possible timing schemes for MODR experiments in which microwave free induction decay (FID) is detected (See Figure 6-2). In the following discussion, we will use a simplified version of the optical Bloch picture in the rotating frame, assuming that the driving

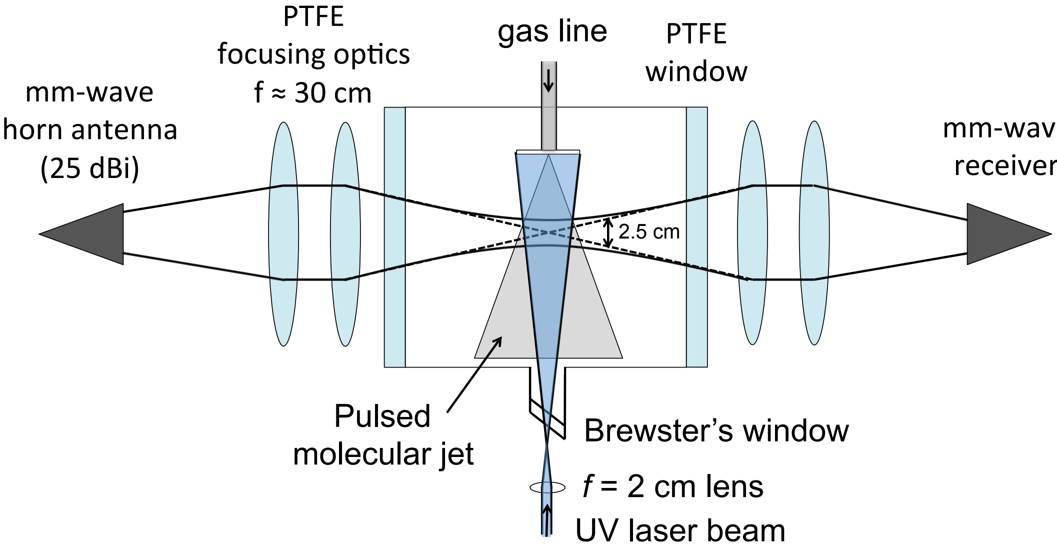

Figure 6-1: Schematic drawing of the experimental configuration used for the mmODR experiments. Our primary geometric consideration was to optimize the spatial overlap of the molecular, optical, and millimeter wave beams in the interaction region, since any portion of the molecular jet that overlaps with the millimeter waves, but *not* the optical pulse will contribute to background signal, but not to double-resonance signal. Thus we focus the millimeter wave beam to its diffraction limit, and we expand the optical beam to match.

pulse is on resonance, and ignoring dephasing effects. With these assumptions, the driving vector, $\mathbf{\Omega}$, lies along the x-axis with magnitude equal to the Rabi frequency, $|\mathbf{\Omega}| = \mu_{ab}\mathcal{E}/\hbar$. The dynamics of the Bloch vector, $\mathbf{\Theta}$, due to the microwave radiation are given by $\mathrm{d}\mathbf{\Theta}/\mathrm{d}t = \mathbf{\Omega} \times \mathbf{\Theta}$ so that the Bloch vector lies in the y, z plane. The z component is proportional to the population difference of the two level system and the y component is proportional to the coherent polarization. As pointed out by Neill *et al.*,[169] the Bloch sphere picture is not a completely accurate description of rotational transitions because there are multiple degenerate M_J subcomponents with different transition moments, but it a useful model for qualitative discussion of double-resonance schemes.

In Case 1 (top panel of Figure 6-2), the optical excitation comes before the microwave pulse. In this double-resonance case, the optical pulse depletes either (1) the lower level of the microwave transition or (2) the upper level of the microwave transition, which leads, respectively, to (1) a decrease in population difference between the levels of the microwave transition and a decrease in microwave signal, or (2) an increase in population difference between the levels of the microwave transition and an increase in the microwave signal. Thus, Case 1 is a population-labeling scheme, in which the sign of the double resonance signal corresponds to whether the optical transition is connected to the upper or lower level of the microwave transition.

In Case 2 (middle panel of Figure 6-2), the optical excitation comes after the microwave pulse. In this double resonance scheme, the optical photon has no effect on the initial population difference between the levels of the microwave transition. Instead, the optical pulse removes population of coherently-radiating molecules regardless of whether the resonance is with the upper or lower level of the microwave transition. In Case 2, the double resonance signal is always negative. Note that in in this case the effect of the optical pulse contributes both a z (population) and y (coherence) component to the Bloch vector. We see that this is the case from density matrix considerations. If a and b are the coefficients of the upper and lower states in the microwave transition, respectively, then an optical resonance with the upper level will lead to a decrease in the magnitude of $|a|$, leading to a decrease in the z-

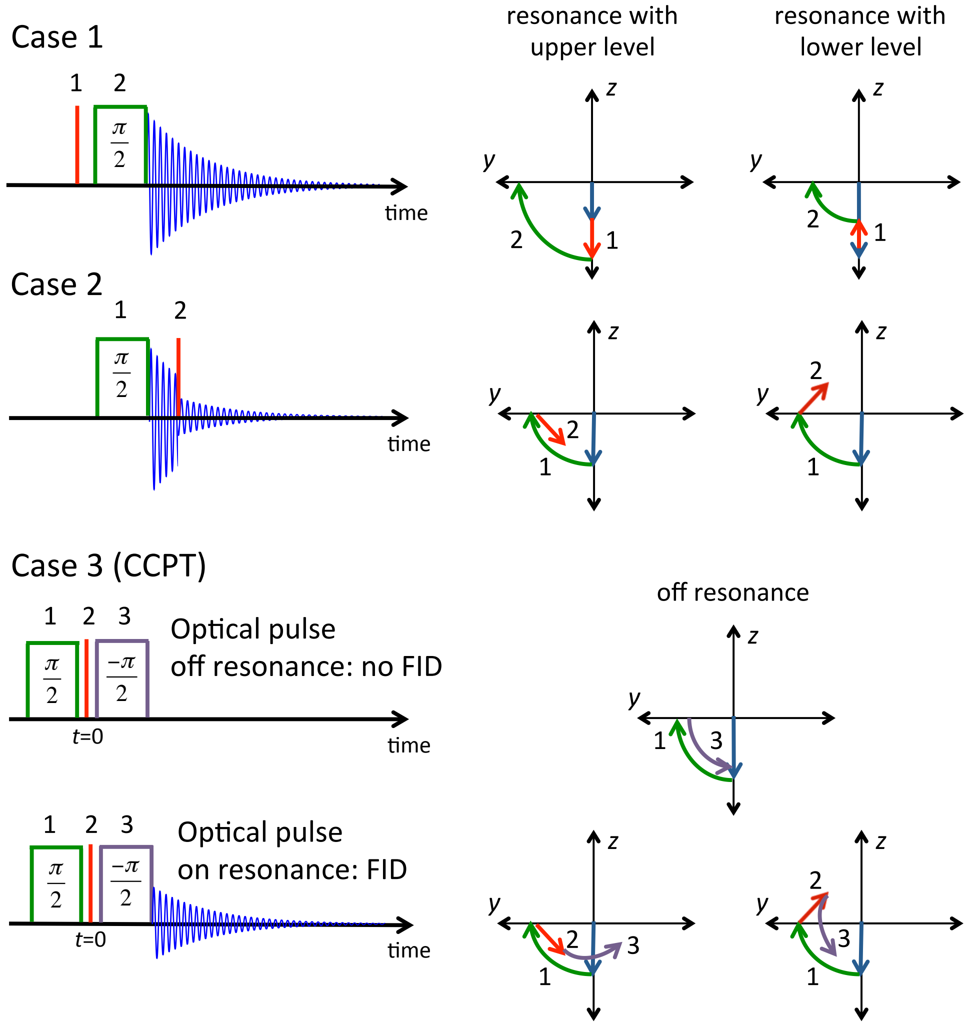

Figure 6-2: Schematic comparison of three FID-detected MODR schemes, reported in Refs. 42,167–169. The left-hand side of the figure shows the timing sequence. Microwave pulses are labeled "$\pi/2$" or "$-\pi/2$" to indicate the relative phase. The optical pulse is represented by a red line and the FID is represented by a blue decaying signal. The right-hand side of the figure shows a simplified schematic of the optical Bloch vector treatment for each FID-detected MODR case. The behavior of the Bloch vector is shown for an optical resonance with both the upper and lower levels of the microwave transitions. The z-axis represents the population difference $\rho^2_{aa} - \rho^2_{bb}$ between the levels involved in the microwave transition, and the y-axis is related to the coherence, $y = i(\rho_{ab} - \rho_{ba})$. For our schematic purposes, we ignore time evolution of the coherence, so we omit the x-axis ($x = \rho_{ab} + \rho_{ba}$).

component of the Bloch vector, $\rho_{aa}^2 - \rho_{bb}^2 = aa^* - bb^*$ *and* a decrease in the magnitude of the coherence, $|\rho_{ab}| = |ab^*|$. However, since the optical pulse comes later than the microwave pulse, the double resonance signal is only related to the depletion of the coherence.

The authors of Ref. 42 argue that in Case 1, a $> 50\%$ depletion of FID signal is not possible, but that in Case 2, a $> 50\%$ depletion can be obtained. However, we believe that the first clause of this argument—which would be true for most optical-optical double resonance experiments—is incorrect for *microwave detected* MODR. In a typical microwave experiment (even when run under jet-cooled conditions) $h\nu \ll kT$, so the initial population difference is typically on the order of a few percent or less. On the other hand, the upper level in the optical transition is negligibly populated, so a saturated optical absorption may deplete 50% of the *population* from one of the lower levels involved in the microwave transition. Since the FID signal is proportional to the initial population *difference* for the microwave transition, which is small, it is not only possible to deplete the FID signal by $> 50\%$ in Case 1—in our experience it is possible to remove enough population from the lower level of the microwave transition as to cause a population inversion between the lower levels, which will result in a 2nd derivative-type double resonance lineshape. For our purposes, we prefer Case 1 for strong double resonance signals because of the convenient population labeling. However, when the double-resonance signal is weak relative to pulse-to-pulse signal fluctuation, Case 2 provides an advantage because background signal fluctuations can largely be corrected by taking the ratio of FID intensity before and after the laser pulse.

A third type of MODR scheme known as Coherence-Converted Population Transfer (CCPT) was developed more recently by the research groups of B. H. Pate and his collaborators.[167–169] The technique is made possible by taking advantage of phase-coherent excitation and detection of the microwave FID. CCPT is a three-pulse sequence. The first "$\pi/2$" microwave pulse generates a coherence. A second "$-\pi/2$" microwave pulse with the same pulse area but *opposite* phase cancels the coherence.

An optical pulse interacts with the molecules at $t = 0$, *between* the two microwave pulses. The optical pulse removes population from one of the microwave levels. This will cause a z-axis component to be added to the Bloch vector (an accompanying loss of coherence will also occur). A positive z-axis component will be added if the laser is resonant with the lower level and a negative z-axis component will be added if the laser is resonant with the upper level. The result is that when the laser is resonant with one of the levels in the microwave transition, the $-\pi/2$ rotation of the Bloch vector by the second microwave pulse no longer cancels the coherence. Furthermore, the phase of the resulting FID is sensitive to whether the optical pulse was resonant with the upper or lower level of the microwave transition. Because the method is background free, there is a significant sensitivity advantage for Case 3, relative to Cases 1 and 2.

While CCPT is very effective for monitoring optical resonances connected to individual rotational lines excited by a single-frequency pulse, the technique is *incompatible* with chirped excitation schemes, where a broadband chirped pulse is used to multiplex the collection of double resonance information for a number of rotational transitions simultaneously. We believe there is some confusion about this point in the spectroscopy community, so we discuss it briefly. In order to null the FID using a "$\pi/2$" and "$-\pi/2$" pulse scheme, one must choose the correct relative phase of the "$-\pi/2$" pulse. The phase that will null the FID is the phase for which the magnitude Fourier transform of the two pulses, taken collectively, cancels at the resonance frequency, ω_0, because the net effect is that in the absence of optical double resonance the two pulse sequence transfers no power into the microwave transition. For the Fourier transform magnitude to be zero at ω_0, the real and imaginary components must both be zero. In other words, the ω_0 sine component of the two individual pulses must *collectively* create an even parity waveform and the ω_0 cosine component of the two individual pulses must collectively create an odd parity waveform. An example of such a pulse is shown in Figure 6-3b. The Fourier transform of this two-pulse sequence will be zero at the resonance frequency, but must contain a window function intensity pattern centered at the carrier frequency, which will re-generate the original waveform when the inverse Fourier transform is applied. If we were to add a contribution from

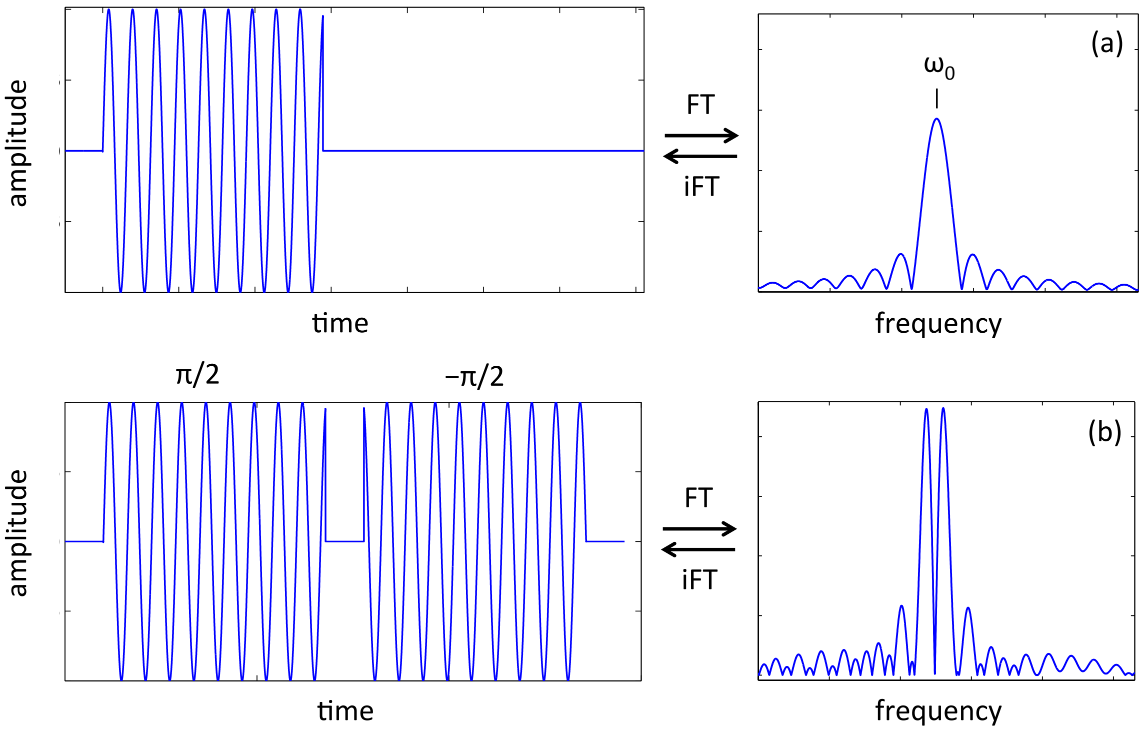

Figure 6-3: A windowed sine pulse has a frequency domain spectrum with power centered at the carrier frequency, ω_0, and an envelope determined by the window function (panel a). In CCPT, the "$\pi/2$" sine pulse is followed by a "$-\pi/2$" sine pulse. This combined waveform has even parity, but there is no cosine component at the ω_0 carrier frequency. The power spectrum must therefore be zero at ω_0, but will contain an envelope centered at the carrier frequency, whose shape is determined by the window function (panel b). The real and imaginary parts of the Fourier transform must regenerate the original time-doman waveform when the inverse Fourier transform is applied.

another frequency located arbitrarily nearby (at $\omega_0 + \delta\omega$), it would be impossible to cancel the Fourier transform magnitude at both frequencies simultaneously. The only windowed (non-infinite in duration) continuous time-domain function for which the *all* sine contributions and *all* cosine contributions vanish over a continuous range is the trivial solution $f(t) = 0$.

6.2.3 Implementation of millimeter-wave optical double resonance schemes

In our double resonance experiments, we have tried several different schemes. First, we have implemented a variant of Case 1 in which the millimeter-wave pulse probes multiple different ground state transitions simultaneously (upper panel of Figure 6-4). Double resonances with the various ground state transitions are easily resolved because the Fourier transform detection method distinguishes different frequency components of the FID. This scheme is multiplexed, so that as the laser is scanned, double resonances with multiple different ground-state rotational levels are observed simultaneously. This scheme was first considered by the B. H. Pate group at the University of Virginia,[170] but to our knowledge the scheme has not been discussed in the published literature, so we provide a brief description. In cases (such as the $\tilde{\mathrm{C}}$ state of SO_2) where the double-resonance signals are strong, but the LIF spectrum is difficult to assign due to perturbations and congestion, this scheme provides an incredible advantage, because the population labeling provides automatic rotational assignment of the LIF spectrum *in a single scan* of the laser through the band. In conventional non-multiplexed double resonance techniques, the laser must be scanned across the band many times, once for each ground state transition used in the double resonance scheme. Because our millimeter-wave spectrometer operates in the power-limited regime, we obtain the best signal when we drive each ground state microwave transition with a typically ~50–100 ns single-frequency rectangular pulse. The rectangular pulses are applied sequentially in the time domain so that the total time required to polarize five ground state microwave transitions (providing double-resonance information for up to ten rotational levels) is 250–500 ns.

We have also made a millimeter-wave implementation of the background-free CCPT technique, which significantly improved the sensitivity of our double-resonance experiment by at least an order of magnitude. Unlike the CCPT implementation described in Refs. 167–169 we do not employ a cavity, so our quality factor is unity ($Q = 1$) and we have access to a broad range of frequencies in each pulse. We therefore attempted a multiplexed implementation of CCPT using a series of single-frequency pulses, as shown in the bottom panel of Figure 6-4. This scheme works so long as the single frequency pulses are resolved and the window functions of each frequency component (Figure 6-3b) do not overlap. The phase of each "$-\pi/2$" frequency was tuned empirically to minimize the off-resonant FID. We found this multiplexed CCPT scheme to be challenging in our experimental configuration because the transverse Doppler dephasing time in our unskimmed jet is approximately 2 μs at 70 GHz. Because of its coherent nature, the *entire* CCPT experiment (including both sets of microwave pulses and the FID detection) must be carried out in a time that is short relative to 2 μs. When the amount of time between the "$\pi/2$" and "$-\pi/2$" pulses for a given frequency approaches the Doppler dephasing time, we observe a metamorphosis of the signal type from Case 3 to Case 1 (because the transition begins to lose memory of the first "$\pi/2$" pulse). Furthermore, because our spectrometer is power-limited by the current availability of broadband millimeter-wave amplifiers, we lose signal by using shorter excitation pulses.[51] Therefore, we prefer to use the multiplexed implementation of Case 1 when the double-resonance signals are strong because it provides rapid rotational assignment of the LIF spectrum (for many values of $J''_{K''_a K''_c}$) in a single scan of the laser. However, when greater sensitivity is desired, such as in our detection of levels that perturb the $\tilde{\mathrm{C}}(1,3,2)$ state of $\mathrm{SO_2}$, we prefer to use the non-multiplexed CCPT scheme (Case 3). Sample spectra obtained using the millimeter-wave CCPT implementation are shown in Figure 6-5. The sensitivity improvement over our Case 1 implementation is at least an order of magnitude although the acquisition time is longer because the laser must be scanned through the band once for each ground state microwave transition.

We briefly mention alternative schemes that may allow multiplexed implementation of background-free double resonance. One approach would be to change the experimental geometry so that the millimeter-waves propagate along the molecular beam axis. This can be accomplished using a rooftop reflector as described in Ref. 51. In this geometry, the Doppler dephasing time is an order of magnitude longer and it will be much easier to perform coherent experiments in less time than the

Doppler dephasing. There are experimental difficulties involved in overlapping the optical pulse in the rooftop reflector configuration, which we are currently working to resolve.

Another idea for multiplexed background-free mmODR is to use a polarization scheme such as the millimeter-wave detected, millimeter-wave optical polarization spectroscopy (mmOPS) used by Steeves *et al.*[44] In this scheme, the millimeter-wave source and receiver are cross polarized at 90° so that in the absence of double resonance, no signal reaches the detector. An optical pulse polarized at 45° to the millimeter-wave source and receiver alters the M_J'' distribution when it is brought into resonance with the one of the lower levels. This effectively rotates the polarization of the FID, allowing it to reach the detector. In the original implementation,[44] millimeter-wave power was detected non-coherently using a bolometer, but there is nothing that should prevent the technique being used for coherent multiplexed Fourier transform detection. Steeves *et al.* report a four-fold improvement in sensitivity in their bolometer-detected experiment. This is less than the sensitivity advantage of CCPT because CCPT is sensitive to the *total* population transfer (ignoring coherence losses) whereas mmOPS is only sensitive to the *relative* population transfer out of different M_J levels.

6.3 Results

6.3.1 Perturbations in the $\tilde{\mathrm{C}}$(1,3,2) level

The rotational structure of the $(v_1', v_2', v_3') = (1, 3, 2)$ vibrational level of the $\tilde{\mathrm{C}}$ state is severely perturbed. In the analysis of the high-resolution LIF spectrum, Yamanouchi *et al.*[43] assign only six term values, and they report an effective C constant that is greater than the effective B constant, presumably due to a pathological c-axis Coriolis perturbation. Assignment of the perturbed spectrum is further complicated by the fact that the B constant of SO_2 is small enough that many features in the LIF spectrum of the supersonic expansion at ∼10 K rotational temperature are not fully

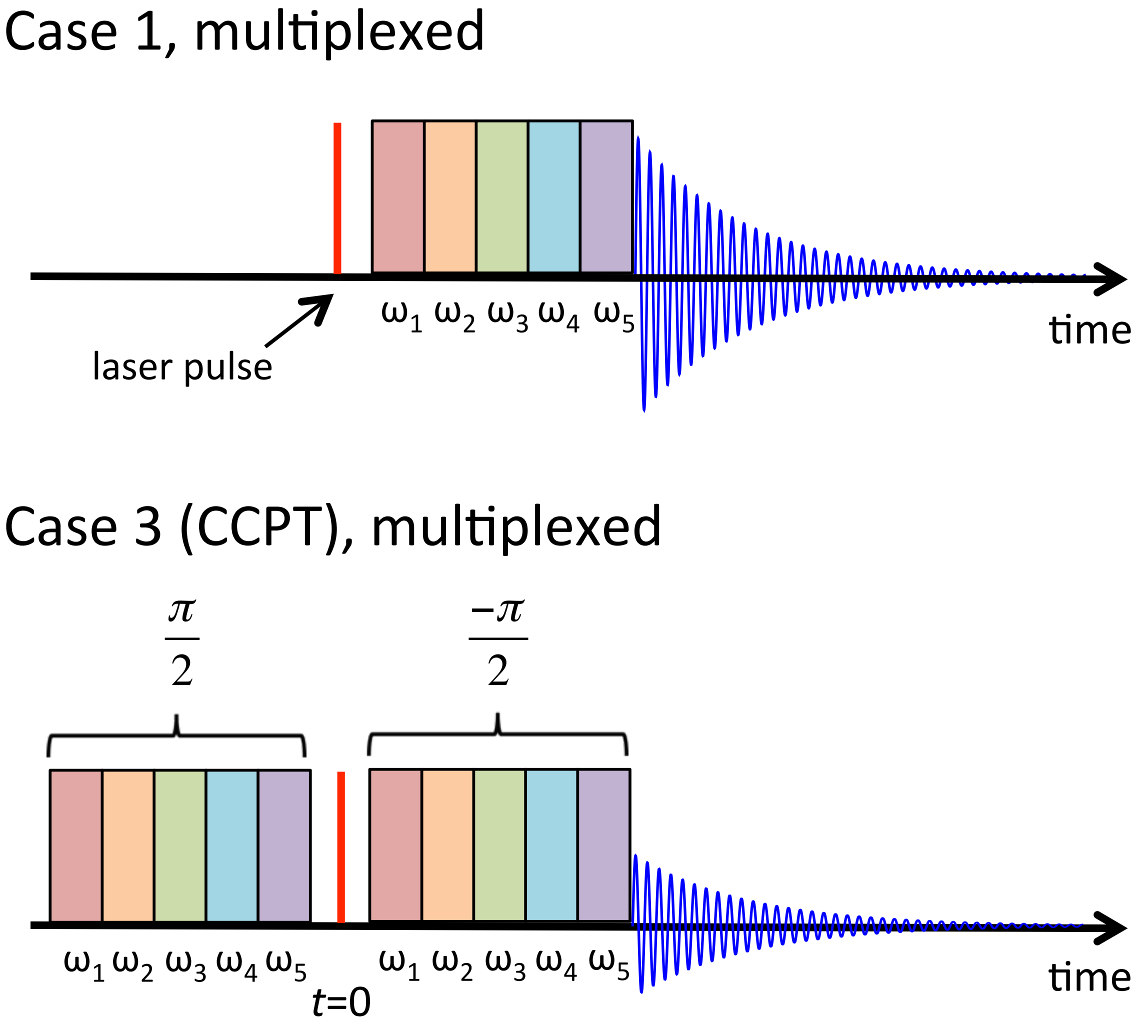

Figure 6-4: In the absence of a Fabry-Perot cavity, the FID-detected MODR schemes shown in Figure 6-2 may be multiplexed for the simultaneous acquisition of double-resonance information from many different microwave transitions. Schematic timing sequences are shown for multiplexed implementations of Case 1 and Case 3. Each excitation pulse contains a sequence of single-frequency rectangular pulses, which each polarize a different microwave transition. The double-resonance signal at each frequency is obtained from the Fourier transform of the FID.

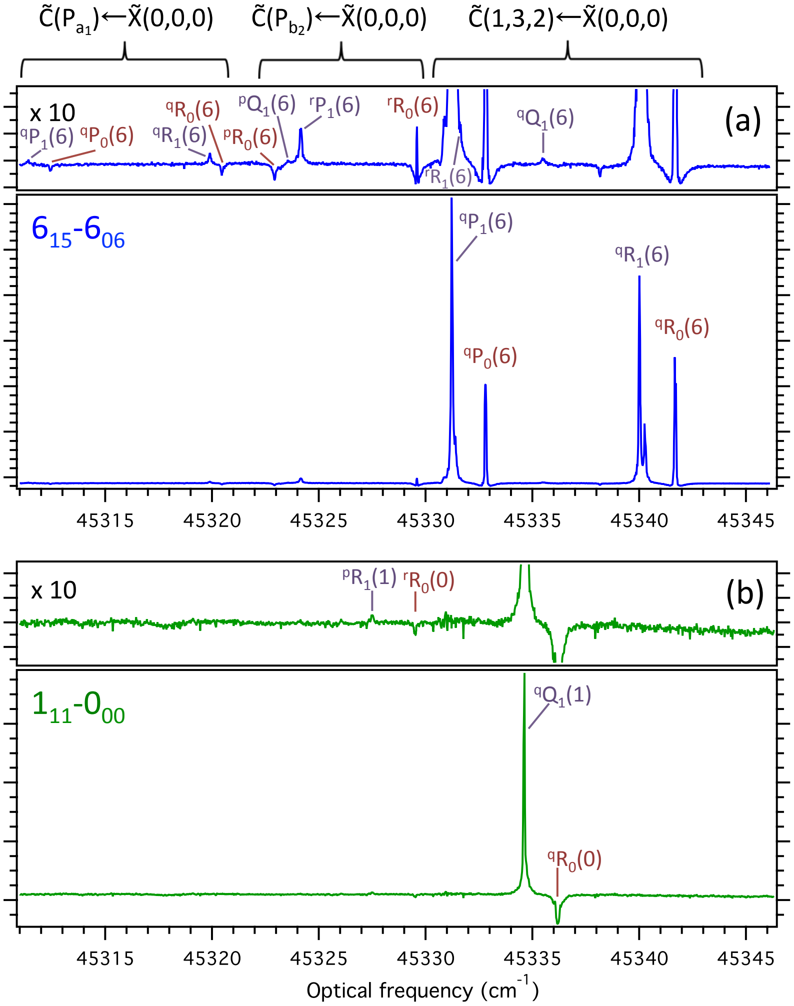

Figure 6-5: Sample mmODR spectra obtained using our millimeter-wave implementation of the CCPT scheme, showing the sensitivity of the technique. Panel (a) shows a double-resonance spectrum acquired using the $J''_{K''_a K''_c} = 6_{15}$–$6_{06}$ microwave transition and panel (b) shows a spectrum acquired using the 1_{11}–0_{00} microwave transition. The signal obtained for the bright $\tilde{\mathrm{C}}(1,3,2) \leftarrow \tilde{\mathrm{X}}(0,0,0)$ transition is very strong (roughly 100:1 signal:background noise). The insets show a 10× vertical magnification and transitions to perturbing levels are evident.

resolved.

We applied the multiplexed Case 1 mmODR scheme to the (1,3,2) level. From a single multiplexed mmODR scan, we are almost able to triple the number of assigned term values, due to the simultaneous rotational assignments afforded by the multiplexed technique. (See Table E.1 and Figure 6-6.) We followed up with more sensitive CCPT scans, probing a single ground-state rotational transition at a time. Figure 6-5 provides a sample of two CCPT spectra of the region surrounding the (1,3,2) level. Transitions to two perturbing vibrational levels are evident. The primary perturber, "$\mathrm{P_{b_2}}$," is a level of $\mathrm{b_2}$ vibrational symmetry that borrows intensity from $\tilde{\mathrm{C}}(1,3,2)$ via a c-axis Coriolis interaction. The Coriolis interaction lends much greater ($\sim$10×) intensity to the transitions from $J'' = 6$ (Fig. 6-5(a)) than to the transitions from $J'' = 0$ or 1 (Fig. 6-5(b))—the latter set of transitions is barely visible above the background noise. There is an additional set of weak transitions at the low-frequency end of Figure 6-5(a). This appears to be from a Franck-Condon weak transition to a level of $\mathrm{a_1}$ vibrational symmetry, which we call "$\mathrm{P_{a_1}}$," and which interacts with $\mathrm{P_{b_2}}$ via a c-axis Coriolis matrix element. The vibrational structure of the $\tilde{\mathrm{C}}$ state is perturbed by anharmonic interactions, including a large ϕ_{133} stretch-stretch Fermi term, and the level structure is not fully understood at $\sim$2000 $\mathrm{cm^{-1}}$ of vibrational excitation. Therefore, the vibrational levels in the region surrounding (1,3,2) are highly mixed in the harmonic basis and we have not attempted to make harmonic vibrational assignments to the perturbers.

Throughout this chapter, when labeling near prolate asymmetric top rotational transitions, we use a capital letter to denote the change in J and a lower case superscript to denote the change in K_a. The main and subscripted numbers in parentheses are J'' and K_a'' of the lower level, respectively. (For example, $^{\mathrm{q}}\mathrm{R}_1(6)$ means $K_a' = K_a'' = 1$ and $J' - 1 = J'' = 6$.) Due to oxygen atom nuclear spin statistics in $\mathrm{SO_2}$, only one value of K_c is allowed for a given set of other quantum numbers, so we omit the conventional K_c'' label. In our analysis of the spectra, we use the $\tilde{\mathrm{X}}$(0,0,0) ground state rotational term values from Ref. 171.

After performing a total of six CCPT scans probing different ground state rota-

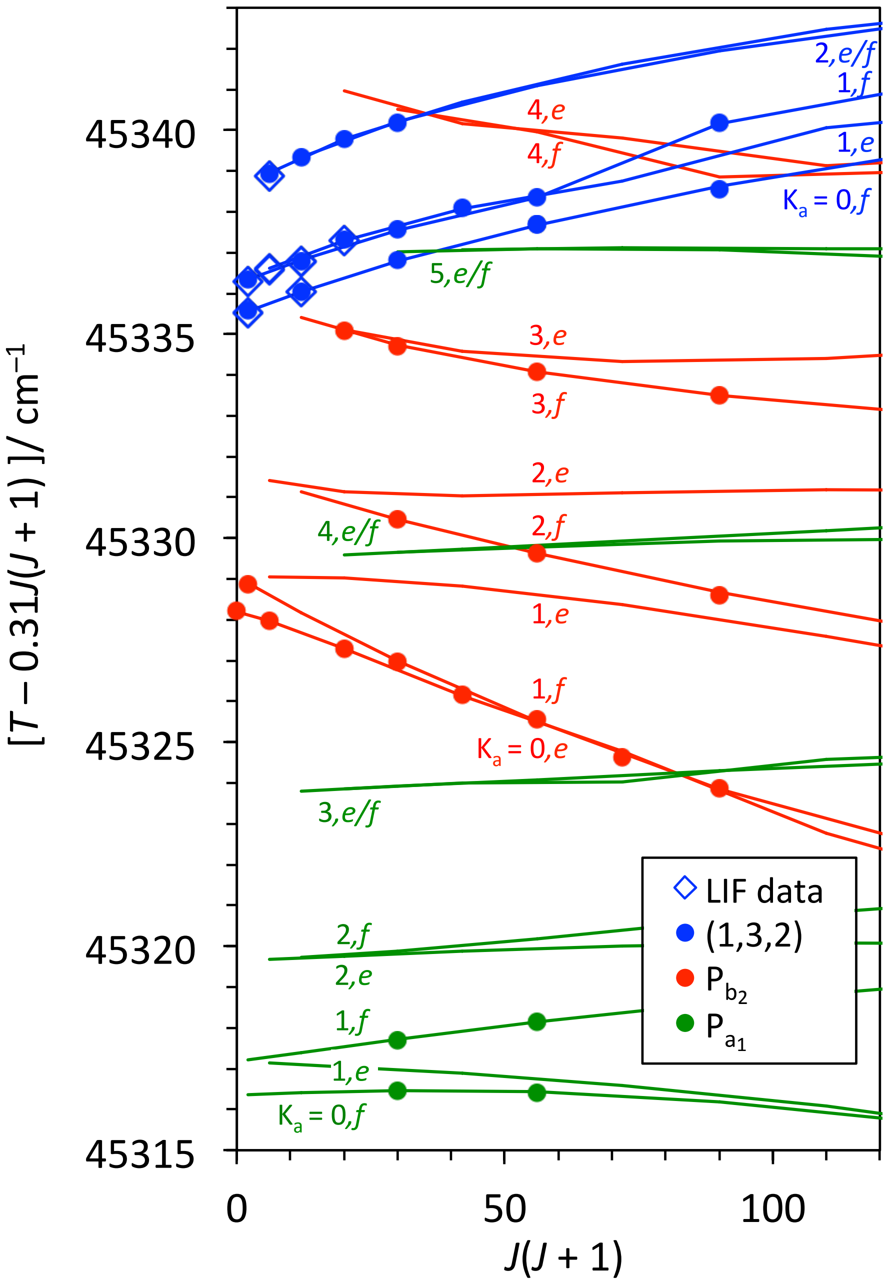

Figure 6-6: The observed low-J term energies near the (1,3,2) level, reduced by (0.31 cm^{-1}) $\times J(J+1)$, are plotted against $J(J+1)$. Curves through the data are from the fit given in Table E.1. Experimental data from the LIF spectrum of Ref. 43, corrected for the calibration offset (see text), are plotted as open diamonds and mmODR data from the current work are plotted as filled circles. The vibrational levels are colored according to the legend.

tional transitions, we were able to obtain 16 rotational term values belonging to $\mathrm{P}_{\mathrm{b}_2}$ and four rotational term values belonging to $\mathrm{P}_{\mathrm{a}_1}$. The term values are listed in Table E.1 and a reduced term value plot is shown in Figure 6-6. The data were fit to an asymmetric top Hamiltonian, including off-diagonal *c*-axis Coriolis matrix elements between levels of a_1 and b_2 vibrational symmetry. The matrix elements are given by

$$\langle V, J, k|\boldsymbol{H}|V, J, k\rangle = T_0(V) + \left[A - \frac{1}{2}(B+C)\right]k^2 + \frac{1}{2}(B+C)J(J+1), \quad (6.1)$$

$$\langle V, J, k \pm 2|\boldsymbol{H}|V, J, k\rangle = \frac{1}{4}(B-C)[J(J+1) - k(k\pm 1)]^{1/2} \times [J(J+1) - (k\pm 1)(k\pm 2)]^{1/2}, \quad (6.2)$$

$$\langle V', J, k \pm 1|\boldsymbol{H}|V, J, k\rangle = \mp t_1(V', V)[J(J+1) - k(k\pm 1)]^{1/2}. \quad (6.3)$$

Equations (6.1)–(6.2) give diagonal and off-diagonal elements of the rigid rotor Hamiltonian in the prolate symmetric top basis, and Eq. (7.5) gives the *c*-axis Coriolis matrix elements connecting levels of a_1 vibrational symmetry to levels of b_2 vibrational symmetry. V labels the vibrational state. The t_1 parameter depends on the vibrational levels, V and V', and replaces $C\zeta_{23}^{(c)}\Omega_{23}(v_2 v_3')^{1/2}$ or $C\zeta_{13}^{(c)}\Omega_{23}(v_1 v_3')^{1/2}$ in the harmonic expression for the $\zeta_{23}^{(c)}$- or $\zeta_{13}^{(c)}$-type matrix elements, respectively, where we have assumed $V = (v_1, v_2, v_3' - 1)$ and $V' = (v_1 - 1, v_2, v_3')$ or $(v_1, v_2 - 1, v_3')$. However, since the levels considered in the current work are highly anharmonic and the harmonic expansions of these levels are not well known, we treat the vibrational dependence of the matrix elements phenomenologically.

The best fit parameters for the (1,3,2), $\mathrm{P}_{\mathrm{b}_2}$, and $\mathrm{P}_{\mathrm{a}_1}$ levels are given in Table 6.1. The inertial defects in the rotational constants are all small, indicating that the most significant effects from Coriolis interactions on the rotational constants have probably been deperturbed. (The effective rotational constants reported in Ref. 43 have an inertial defect of -16.3 amu·Å^2.) However, there were significant correlations among the C constants and t_1 Coriolis parameter for the (1,3,2) and $\mathrm{P}_{\mathrm{b}_2}$ states, so these should be considered "effective" values and caution should be taken in extrapolating the fit to higher J. The average error of the fit was 0.028 cm^{-1}, which is on the order

Table 6.1: Fit parameters for the observed interacting levels (1,3,2), $\mathrm{P_{b_2}}$, and $\mathrm{P_{a_1}}$. All energies are in cm^{-1} units and the inertial defects (Δ) are listed in amu·Å^2 units. Reported statistical uncertainties are 2σ. There were three correlation coefficients greater than 0.9: between the C constants for the (1,3,2) and $\mathrm{P_{b_2}}$ states (-0.96), and between $t_1[(1,3,2)\text{-}\mathrm{P_{b_2}}]$ and the C constants for (1,3,2), (0.994), and $\mathrm{P_{b_2}}$, (-0.952). No other correlation coefficients were greater than 0.83. The average residual error of the fit was 0.028 cm^{-1}.

	(1,3,2)	$\mathrm{P_{b_2}}$	$\mathrm{P_{a_1}}$
T_0	45335.44(3)	45328.21(4)	45316.42(7)
T_{vib}	2761.99(3)	2754.76(4)	2742.98(7)
A	1.169(7)	1.140(10)	1.09(10)
B	0.3388(27)	0.341(3)	0.340(4)
C	0.280(21)	0.283(18)	0.298(5)
Δ (amu·Å^2)	-0.239	-0.279	-0.502
	$t_1[(1,3,2)\text{-}\mathrm{P_{b_2}}] = 0.43(4)$		
	$t_1[\mathrm{P_{b_2}}\text{-}\mathrm{P_{a_1}}] = 0.15(4)$		

of the calibration uncertainty of our pulsed dye laser.

The c-axis Coriolis interaction between (1,3,2) and $\mathrm{P_{b_2}}$ increases the effective C constant of (1,3,2) and decreases the effective C constant of $\mathrm{P_{b_2}}$. As a result, the e/f asymmetry splitting in $\mathrm{P_{b_2}}$ is pronounced, while the e/f splitting in (1,3,2) is very small—in fact, the splitting in the $K_a = 1$ stack of (1,3,2) is reversed at low J leading to a negative value for the apparent $(B - C)/2$ splitting parameter. There is a local perturbation in the $J_{K_aK_c} = 9_{18}$ level of (1,3,2) which appears to be caused by a narrowly avoided crossing between the $K_a = 1$ stack of (1,3,2) and the $K_a = 4$ stack of $\mathrm{P_{b_2}}$.

The frequencies reported in Ref. 43 for the (1,3,2) rotational levels appear to be offset from our measured frequencies by a constant value. Figure 6-7 shows the energy offset in the measured term energies for the rotational levels assigned in both the LIF spectrum of Ref. 43 and in our mmODR spectra. The spectra of Yamanouchi *et al.* were calibrated in a similar manner to our spectra, using a $\mathrm{Te_2}$ absorption spectrum as a frequency reference. However, our mmODR spectra were taken in short (~20 cm^{-1}) scans and each scan was calibrated individually, so that our calibration is local to the (1,3,2) region. We believe the calibration of Yamanouchi *et al.* may have been interpolated from a long scan of the LIF laser, so that the relative frequency steps are

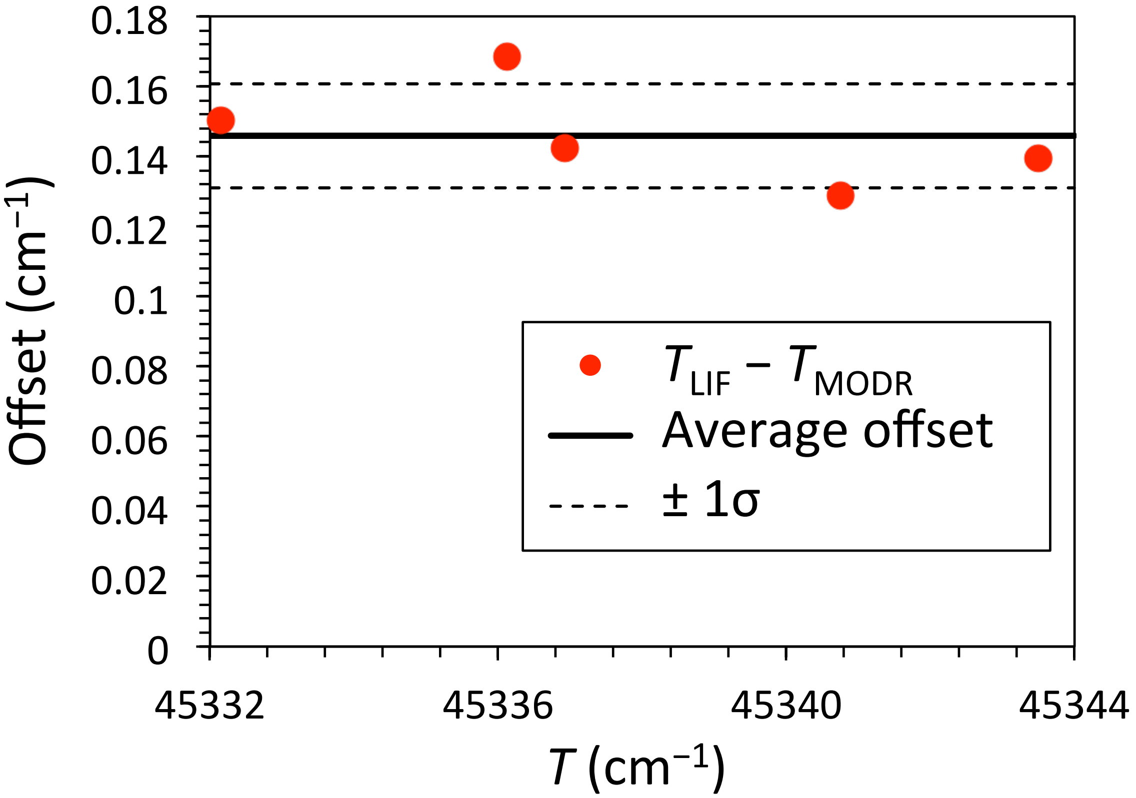

Figure 6-7: The difference in the term energies of $\tilde{\text{C}}(1,3,2)$ rotational levels reported in Ref. 43 (T_{LIF}) and in the current work (T_{MODR}) is plotted versus the term energy of levels determined in the current work. The average offset was 0.146 ± 0.0145 cm^{-1}. (The stated uncertainty in the offset is one standard deviation.)

accurate, but the overall local calibration has a small offset. The standard deviation of the measured offset, 0.0145 cm^{-1}, is approximately the calibration uncertainty of our laser. Therefore, for inclusion in our fitting and in our reduced term value plot (Fig. 6-6), we have subtracted a 0.146 cm^{-1} offset from the frequencies reported in Ref. 43. The offset affects the band origin reported in Ref. 43, but not the effective rotational constants.

There appears to be a splitting in the $J_{K_aK_c} = 7_{16}$ level of (1,3,2). Figure 6-8 shows the ^{q}P and ^{q}R transitions to the 7_{16} level, which have nearly identical structure. The most likely explanation is a local perturbation from a dark level, such as a triplet state or a highly vibrationally excited level of the $\tilde{\text{X}}$ state. In our fit, we have taken the center of gravity of the doublet as the transition frequency.

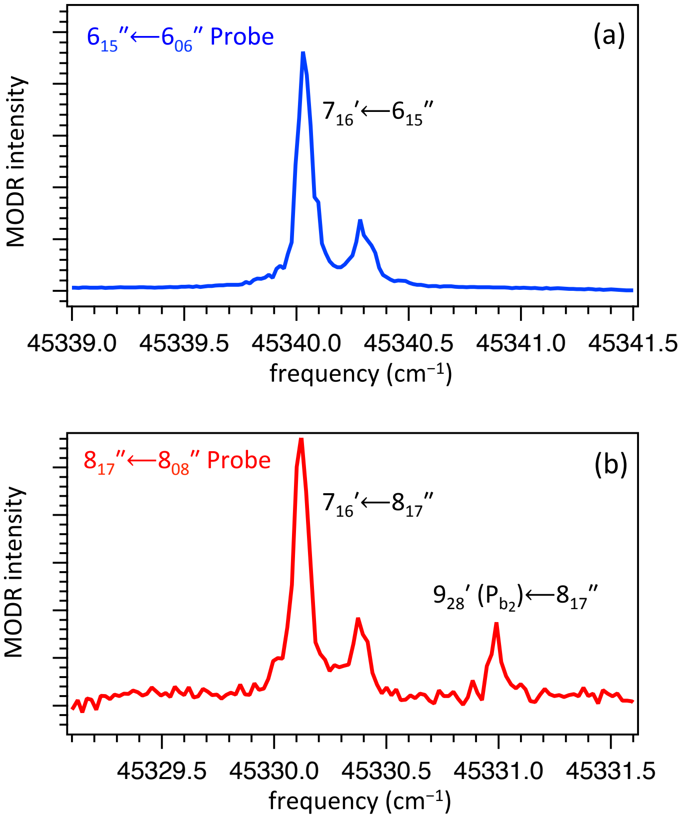

Figure 6-8: The ${}^{\mathrm{q}}\mathrm{R}_1(6)$ (panel a) and ${}^{\mathrm{q}}\mathrm{P}_1(8)$ (panel b) transition to the $J_{K_aK_c} = 7_{16}$ level of the $\tilde{\mathrm{C}}(1,3,2)$. The spectra were acquired using the CCPT scheme, probing the $6''_{15} \leftarrow 6''_{06}$ (panel a) and the $8''_{17} \leftarrow 8''_{08}$ (panel b) rotational transitions of the ground $\tilde{\mathrm{X}}(0,0,0)$ level. The nearly identical doublet structure observed in the R and P branches suggests that there is a local perturbation to the $7'_{16}$ level from an otherwise dark state that splits the line. The transition at the right-hand side of panel b is to the 9_{28} level of the $\mathrm{P_{b_2}}$ band.

6.3.2 The 46816 cm^{-1} level

The level at 46816 cm^{-1} is weak in both the LIF and absorption spectra.[43,154] We performed a Case 1 multiplexed mmODR scan on this band and found that the rotational structure is significantly perturbed. A reduced term value plot is shown in Fig. 6-9, and the effective rotational fitting parameters to Eqs. (6.1–6.2) are given in Table 6.2. Due to perturbations, the average error of the fit (0.296 cm^{-1}) was quite large. The depressed effective C constant and large positive inertial defect is suggestive of a c-axis Coriolis interaction with a nearby higher-lying level of $\mathrm{b_2}$ vibrational symmetry. There were a number of extra lines in the spectrum, probably from at

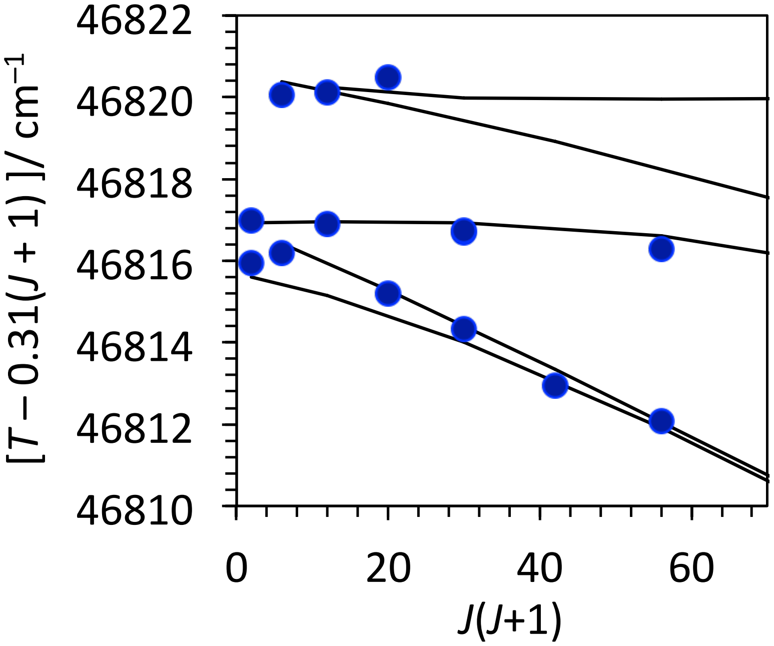

Figure 6-9: The observed low-J term energies for the perturbed 46816 cm^{-1} level, reduced by (0.31 cm^{-1}) × $J(J+1)$ are plotted against $J(J+1)$. Curves through the data are from the effective rotational fit given in Table 6.2.

least one perturbing vibrational level. However, because the signal-to-noise quality was poor, we did not have enough information to perform a fit to the perturbation.

6.3.3 The 47569 and 47616 cm^{-1} levels

Because the signal in the mmODR schemes used in the current work depends on the absorption strength of the laser transition rather than the fluorescence intensity, it is an advantageous technique for high-resolution spectroscopy of pre-dissociated levels. The fluorescence intensity from the $\tilde{\mathrm{C}}$ state of SO_2 falls off rapidly above the dissociation limit at ∼45,725 cm^{-1}, although the maximum of the Franck-Condon absorption envelope does not occur until ∼48,000 cm^{-1}.[154]

In order to demonstrate the effectiveness of the technique for rapid rotational assignment of pre-dissociated levels, we have acquired Case 1 multiplexed mmODR spectra of vibrational levels at 47569 and 47616 cm^{-1}, shown in Figs. 6-10 and 6-11. Both levels are labeled "(1,9,2)" by Okazaki *et al.*,[154] but we prefer to omit normal

Table 6.2: Effective rotational fit parameters for the observed vibrational levels at 46816, 47569, and 47616 cm^{-1}. All energies are in cm^{-1} units and the inertial defects (Δ) are listed in amu·Å^2 units. Reported statistical uncertainties are 2σ. $\langle\sigma\rangle$ indicates the average residual error in the fit.

T_0	46815.6(5)	47569.328(22)	47616.08(5)
T_{vib}	4242.2(5)	4995.878(22)	5042.63(5)
A	1.50(16)	1.166(7)	1.124(14)
B	0.36(4)	0.3344(11)	0.3272(24)
C	0.188(17)	0.2730(10)	0.2821(24)
Δ (amu·Å^2)	31.23	-3.109	-6.768
$\langle\sigma\rangle$	0.296	0.0176	0.0382

mode vibrational assignments for these high-lying levels since the $\tilde{\mathrm{C}}$ state is highly anharmonic and the vibrational levels are not well understood at these energies. The 47569 and 47616 cm^{-1} vibrational levels have fluorescence quantum yields of 0.0056 and 0.0026 and are weak in the LIF spectrum,[154] but the absorption cross sections of these levels from the $\tilde{\mathrm{X}}$(0,0,0) ground state are roughly 20 times that of the (1,3,2) level, so the transitions are strong in mmODR. Furthermore, the predissociation rate from these levels is 3.40×10^9 and $7.30{\times}10^9$ s^{-1},[154] so that the line broadening due to predissociation is on the same order of magnitude as the ∼1 GHz bandwidth of our pulsed dye laser and does not lead to significantly problematic broadening of rotational lines.

Reduced term value plots for the 47569 and 47616 cm^{-1} levels are shown in Fig. 6-12. Both levels were fit to the simple rigid rotor asymmetric top Hamiltonian given in Eqs. (6.1–6.2). The resulting rotational constants are shown in Table 6.2 and the fits are plotted in Fig. 6-12. The rotational structure of the 47569 cm^{-1} level exhibits no significant perturbations from the rigid rotor Hamiltonian, as evidenced by the 0.0176 cm^{-1} average fit error, which is smaller than the calibration uncertainty (∼0.02 cm^{-1}) of our dye laser. On the other hand, the rotational structure of the 47616 cm^{-1} level provides evidence of a small perturbation, as evidenced by the small value of $(B-C)/2$ and the fairly large average fit error of 0.0382 cm^{-1}. The perturbation might be from a c-axis Coriolis interaction with a lower-lying level of b$_2$ vibrational symmetry, but it is impossible to be certain without knowing a great deal more about the vibrational

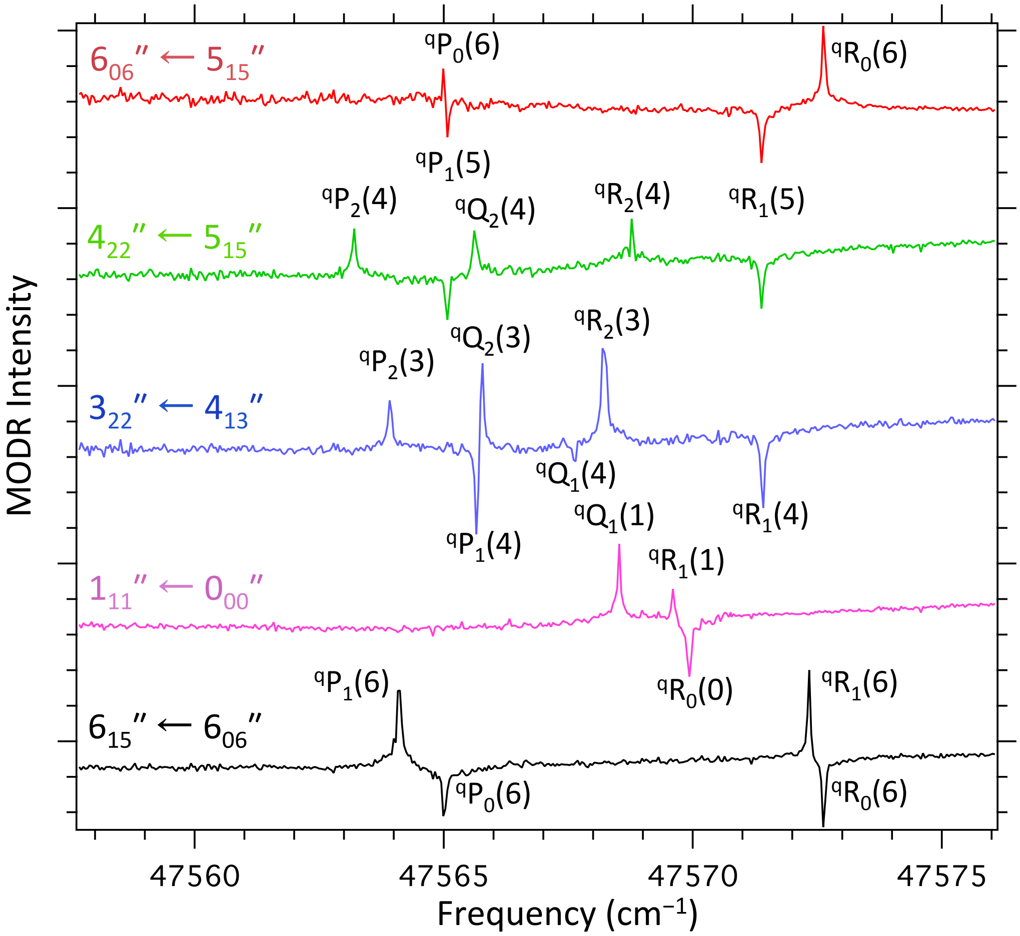

Figure 6-10: Case 1 multiplexed mmODR spectrum of the 47569 cm^{-1} vibrational level of the $\tilde{C}$ state of SO_2. Double resonance signals from five different rotational transitions of the $\tilde{X}(0,0,0)$ ground state (labeled on the left-hand side of the figure) were collected simultaneously in a single scan of the laser. Rotational assignments (shown in the figure) were straightforward due to the population labeling double resonance scheme. Downward and upward directed peaks in the mmODR spectrum represent transitions out of the lower and upper rotational level of the microwave probe, respectively.

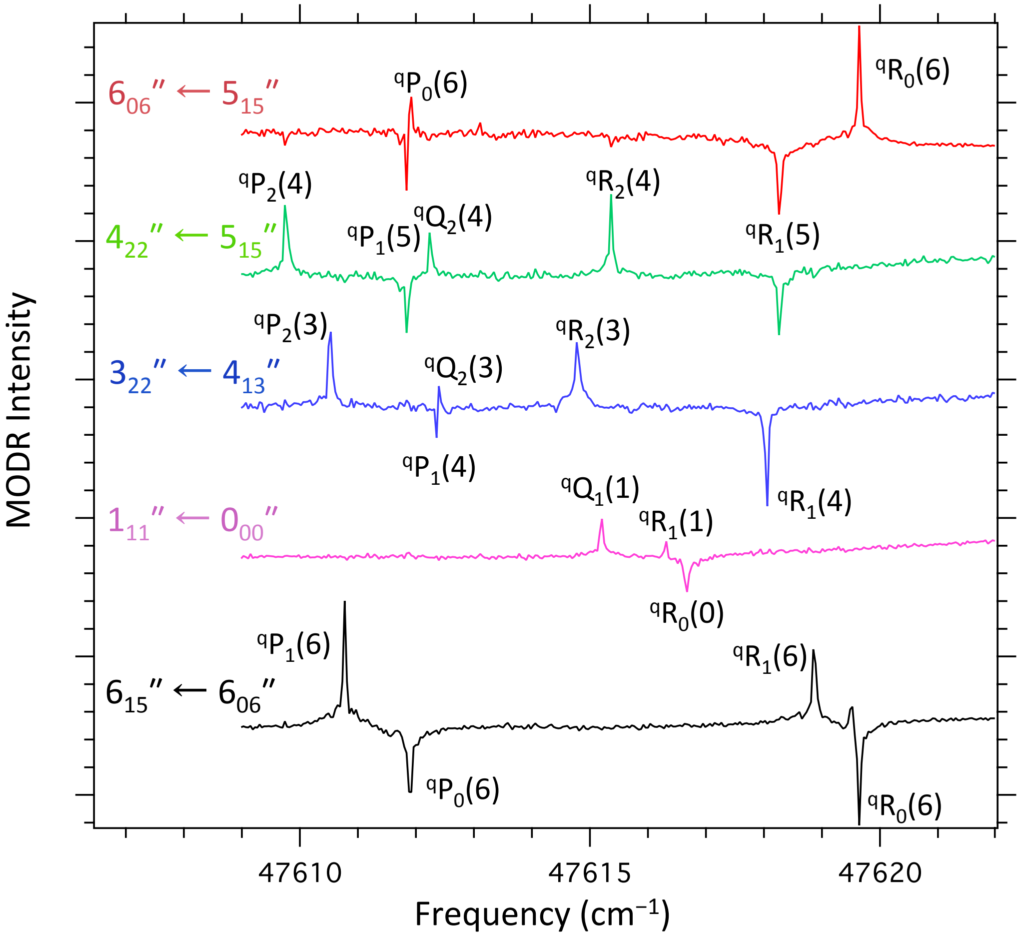

Figure 6-11: Case 1 multiplexed mmODR spectrum of the 47616 cm^{-1} vibrational level of the $\tilde{C}$ state of SO_2. Double resonance signals from five different rotational transitions of the $\tilde{X}(0,0,0)$ ground state (labeled on the left-hand side of the figure) were collected simultaneously in a single scan of the laser. Downward and upward directed peaks in the mmODR spectrum represent transitions out of the lower and upper rotational level of the microwave probe, respectively.

level structure in this energy region.

We briefly note the rapid rate of spectral acquisition and unambiguous rotational assignment afforded by the Case 1 multiplexed mmODR technique. Each of the sets of double resonance spectra shown in Figs. 6-10 and 6-11 were acquired simultaneously during a ∼15 minute scan of the pulsed dye laser. Furthermore, the rotational population labeling scheme automates the determination of upper state term energy and in the absence of pathological perturbations, rotational assignment is trivial. The most labor intensive step was frequency calibration via the $\mathrm{Te_2}$ reference spectrum.

6.4 Discussion

Because the vibrational level structure of the $\tilde{\mathrm{C}}$ state of $\mathrm{SO_2}$ is not yet completely understood in the energy regions investigated in the current work, our fitting parameters should be regarded as "effective." There are clearly perturbations in the levels at 46816 and 47616 cm^{-1} that have not been included in the fit. Furthermore, without a better understanding of the level structure, it is difficult to predict whether there are additional perturbers to the (1,3,2) band. If so, it is possible that effects from additional perturbations are folded into the effective constants that we report. If the $\mathrm{P_{a_1}}$ band were given the normal mode assignment (1,2,3), then, using $\zeta_{23}^{(c)} = 0.923$ and $C = 0.2654$ cm^{-1},[164] the naive harmonic prediction for the Coriolis interaction strength would be $t_1 = 0.734$ cm^{-1}, which is significantly greater than the 0.43 cm^{-1} interaction strength determined in our fit. The most likely reason for the discrepancy is that, as a result of anharmonicity, many zero-order harmonic basis states contribute to each eigenstate, and it is necessary to sum the harmonic contribution over the full expansion of each eigenstate. Another possibility is that the effects of other perturbations have been folded into the matrix element.

Our results from the $\tilde{\mathrm{C}}$(1,3,2) region also provide a note of caution to dynamicists investigating vibrational bands that are not fully understood. For example, Zhang *et al.*[172] have investigated collisional relaxation of highly vibrationally excited levels of the ground electronic state of $\mathrm{SO_2}$, which couple to the $\tilde{\mathrm{C}}$ state and cause quantum

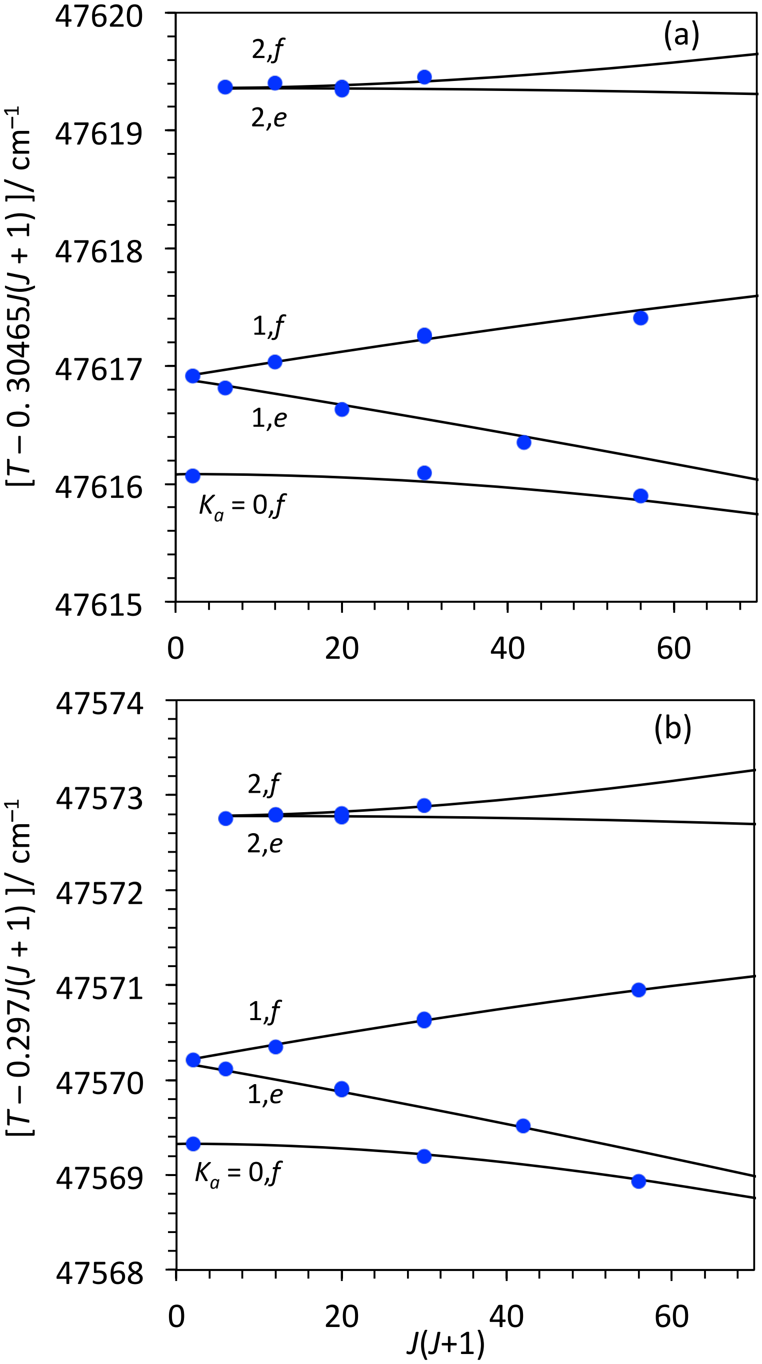

Figure 6-12: The observed low-J term energies for the 47616 cm^{-1} (panel a) and 47569 cm^{-1} (panel b) levels, reduced by (0.30465 cm^{-1}) $\times J(J+1)$ and (0.297 cm^{-1}) $\times J(J+1)$, respectively, are plotted against $J(J+1)$. Curves through the data are from the fit given in Table 6.2.

beats in the fluorescence decay. They use quantum beats in unassigned rotational lines of the "(1,3,2)" level, but our analysis shows that, for example, the line at 45329.6 cm^{-1} is actually most likely a transition to the $J_{K_aK_c} = 7_{17}$ level of the P_{b_2} band so that the nominal vibronic symmetry is A_1 rather than B_2. Although we do not believe the conclusions of Zhang *et al.* are incorrect, it can be dangerous to assume vibrational assignments in a perturbed and unanalyzed band.

Ray *et al.*[159] observe dispersed fluorescence from $\tilde{\text{C}}$-state levels between 49000–51000 cm^{-1} that terminates on $\tilde{\text{X}}$-state levels of b_2 vibrational symmetry, and they provide evidence for vibronic coupling of the $\tilde{\text{C}}$ state to the dissociative $4\,^1\text{A}'$ electronic state. These authors rule out Coriolis interactions as a source of coupling between levels of A_1 and B_2 vibronic symmetry because they observe strong fluorescence to b_2 levels in a rotationally cold spectrum. However, in the current work, we have observed *c*-axis Coriolis induced transitions to b_2 levels at $J' = 1$. Thus, although there is a strong evidence for vibronic coupling in the vicinity of the avoided crossing,[159,160,173] we do not believe it is possible to rule out Coriolis coupling mechanisms in the $\tilde{\text{C}}$ state of SO_2 on the grounds of low rotational temperature. The density of vibrational states at ~8000 cm^{-1} of vibrational excitation is $\sim 0.20/\text{cm}^{-1}$, or approximately one vibrational level per 5 cm^{-1}. Furthermore, at high vibrational energy, the density of b_2 levels approaches the density of a_1 levels (because both representations are singly degenerate.) As a result, it is statistically very likely that a given a_1 level in this energy region will be within < 10 cm^{-1} of the nearest b_2 level, and that there will be significant intensity borrowing through *c*-axis Coriolis matrix elements.

6.5 Conclusions and Future Work

We have discussed schemes for using the technology from our chirped-pulse millimeter wave spectrometer to improve the state-of-the-art for millimeter-wave optical double resonance spectroscopy. We have demonstrated the use of the multiplexed Case 1 mmODR scheme to obtain a full set of mmODR spectra, probing many ground state rotational levels simultaneously, in a single scan of the laser. The technique enables rapid spectral acquisition and assignment of congested regions. Our millimeter-wave implementation of the background-free CCPT scheme, originally developed by Twagirayezu and coworkers,[167–169] significantly increases the mmODR sensitivity and allows us to observe weak transitions to levels that perturb the $\tilde{\mathrm{C}}$(1,3,2) level of SO_2. Due to the relatively short Doppler-dephasing coherence time, we had difficulty implementing a multiplexed CCPT scheme. However, technology for high-power millimeter-wave amplifiers is rapidly advancing, and with higher available power, it will be possible to polarize the transitions faster relative to the coherence dephasing time.

To our knowledge, we also report the first high-resolution observation of a b_2 vibrational level of the $\tilde{\mathrm{C}}$ state of SO_2. We have recently acquired IR-UV double-resonance spectra of the low-lying b_2 levels, which will be reported in a future publication,[174] and we are using this data to improve our understanding of the PES and the vibrational dynamics of the $\tilde{\mathrm{C}}$ state.[175] Work is also ongoing to analyze the LIF spectrum of the $\tilde{\mathrm{C}}$(1,3,2) region fully, with the aid of our mmODR spectra.

6.6 Acknowledgments

G.B.P. is grateful for discussions with Brooks Pate, Justin Neill, Adam Steeves, and Kevin Lehmann. This material is based upon work supported by the U.S. Department of Energy, Office of Science, Chemical Sciences Geosciences and Biosciences Division of the Basic Energy Sciences Office, under Award Number DE-FG0287ER13671. We also acknowledge funding from the Camille and Henry Dreyfus Foundation Postdoctoral Program in Environmental Chemistry, and we thank support from NASA Exobiology (NNX10AR85G to S.O.)

Chapter 7

Direct observation of the low-lying b_2 symmetry vibrational levels of the $\tilde{C}$ $^1B_2$ state of SO_2 by IR-UV double resonance: Characterization of the asymmetry staggering and the origin of unequal bond lengths

Abstract

The $\tilde{C}$ state of SO_2 has an unusual double-minimum potential in the antisymmetric stretch q_3' coordinate so that the equilibrium SO bond lengths are non-equivalent and there is a slight barrier at the C_{2v} geometry. This double-minimum gives rise to a staggering in the ν_3' progression. However, no direct observation has previously been made of the low-lying levels with odd quanta of ν_3', which have b_2 vibrational symmetry, because the selection rules forbid one-photon transitions to these levels from the ground level of the $\tilde{X}$ state. We have used a two-photon IR-UV double resonance scheme to make direct observations of the b_2 vibrational levels below 1600 cm^{-1} of vibrational excitation in the $\tilde{C}$ state, which allows precise determination of the ν_3' level staggering and direct characterization of the asymmetry in the potential energy surface near equilibrium. We have also deperturbed the *c*-axis Coriolis interactions and report the vibrational dependence of the rotational constants. Our results are

consistent with a vibronic mechanism for the double-minimum, which involves coupling to the $2^1\mathrm{A}_1$ level. The degree of staggering in the ν_3' levels increases with quanta of bending excitation, which is consistent with the approach of the $\tilde{\mathrm{C}}$ state to a conical intersection with the $2^1\mathrm{A}_1$ at a bond angle of ∼145°.

7.1 Introduction

The $\tilde{\mathrm{C}}\ ^1\mathrm{B}_2$ state of SO_2, with origin at $v_{00} = 42,573.45\ \mathrm{cm}^{-1}$, has been the subject of extensive research. Early investigations by Duchesne and Rosen[176] assigned the $\tilde{\mathrm{C}} \leftarrow \tilde{\mathrm{X}}$ band system to two overlapping electronic transitions, labeled α_1 and α_2, but subsequent work by Jones and Coon[177] and by Brand and coworkers[163,164] provided evidence that the band system was due to a single electronic transition with unusual vibrational structure. Most notably, the antisymmetric stretching mode ν_3 of the $\tilde{\mathrm{C}}$ state has an uncharacteristically low fundamental vibrational frequency ($\sim$212 cm^{-1}), and displays an unusually large degree of anharmonicity. Further work by Brand and coworkers[163,164] and Hallin and Merer[165] provided evidence that the $\tilde{\mathrm{C}}$ state has a double minimum potential in q_3, with two equivalent minimum-energy configurations that exhibit unequal bond lengths.

Considerable evidence—including band origin isotope shifts, inertial defects, and centrifugal distortion constants—has been reported for staggering in the $(v_1', v_2', v_3') = (0, 0, v_3')$ progression and for an anomalously low ν_3 fundamental, including band origin isotope shifts, inertial defects, and centrifugal distortion constants.[164] (Throughout this work, we will use the notation (v_1, v_2, v_3) for the vibrational quantum numbers.) Transitions to vibrational levels of the $\tilde{\mathrm{C}}$ state with odd quanta of ν_3 (b_2 vibrational character) are nominally forbidden from the ground vibrational level of the $\tilde{\mathrm{X}}$ state, so direct observation of the staggering of low-lying levels with even vs. odd quanta of v_3' has not previously been reported. The locations of some of the dark b_2 vibrational levels have been inferred by fitting the strong *c*-axis Coriolis perturbations between the b_2 levels and the bright a_1 vibrational levels.[43,163–165] Ivanco made an assignment of the ν_3' fundamental in low-resolution hot laser-induced fluorescence spectra, but our work shows his assignment to be incorrect.[178]

Mulliken suggested that an unsymmetrical distortion of the S–O bond lengths might minimize antibonding in $\tilde{\mathrm{C}}$-state $\mathrm{SO_2}$,[179] but Innes argued that the asymmetry in the potential is likely the result of vibronic interaction with a higher lying $^1\mathrm{A}_1$ state.[180] We believe it likely that Innes's explanation is correct, but his analysis is primarily qualitative and relies quantitatively on an incorrect assignment by Ivanco. References 158,181 report *ab initio* calculations for the $\tilde{\mathrm{C}}$ state that reproduce the observed double-minimum potential energy surface. A full-dimensional *ab initio* surface for the $\tilde{\mathrm{C}}$ state is reported in Ref. 182. The features of this surface agree qualitatively with experiment, but it must be scaled empirically in order to reproduce the experimentally observed vibrational level structure. To our knowledge, no authors have made theoretical calculations of the q_3-mediated vibronic coupling between the $\tilde{\mathrm{C}}$ (1 $^1\mathrm{B}_2$) level and the higher-lying 3 $^1\mathrm{A}'$ level in the diabatic basis.

Recently, we analyzed the *c*-axis Coriolis perturbation in the $\tilde{\mathrm{C}}(1,3,2)$ band, and we made rotationally-resolved observations the nominally dark perturbing level that borrows intensity from the Coriolis interaction.[183] To our knowledge, this was the first direct high-resolution measurement on a b_2 vibrational level in the $\tilde{\mathrm{C}}$ state. However, the this level is $\sim$2756 cm^{-1} above the $\tilde{\mathrm{C}}$-state origin, so it gives us very little ability to characterize the asymmetry near the bottom of the well.

In the current work, we have recorded high resolution spectra of the low-lying b_2 levels of the $\tilde{\mathrm{C}}$ state below $\sim$1600 cm^{-1} of vibrational excitation. We have used a two-photon IR-UV double-resonance fluorescence spectroscopy via the $\tilde{\mathrm{X}}(1,0,1)$ intermediate to gain spectroscopic access to the one-photon-dark b_2 levels. We analyze the level structure in terms of a vibronic interaction model, and we compare our measurements with available theoretical results.

7.2 Selection rules

The $\tilde{\mathrm{C}}$ state of $\mathrm{SO_2}$ exhibits a small barrier at the $\mathrm{C_{2v}}$ geometry along the q_3' antisymmetric stretch coordinate. Thus the equilibrium geometry is doubly-degenerate and has $\mathrm{C_s}$ symmetry. Despite this fact, it is convenient to treat the molecule in

C_{2v} symmetry, in keeping with previous investigators. The barrier at C_{2v} is small and is an even function of q_3, so there are no terms in the vibrational Hamiltonian that break the vibrational symmetries in the representations of C_{2v}. Therefore, in the absence of rovibrational Coriolis interactions, the low-lying levels of the $\tilde{C}$ state conserve a_1 (even quanta of v_3) and b_2 (odd quanta of v_3) vibrational symmetry.

It is of course also possible for vibronic interactions to cause vibrational dependence of the transition dipole moment (Herzberg-Teller coupling) that would destroy the vibrational selection rules in the $\tilde{C} \leftrightarrow \tilde{X}$ transition. This effect has been reported in dispersed fluorescence experiments from highly-excited predissociated vibrational levels of the $\tilde{C}$-state between 210–205 cm^{-1}, from which the dispersed fluorescence includes transitions to both a_1 and b_2 vibrational levels of the ground electronic state.[159,160,166,173] Brand *et al.*[166] propose that the most likely mechanism is *c*-axis Coriolis interaction, but Ray *et al.*[159] argue that the cold rotational temperature of their supersonic expansion rules out Coriolis interactions. In the current work, we observe nominally forbidden transitions that borrow intensity via Coriolis interactions at rotational quantum numbers as low as $J = 2$, so we do not believe that it is possible to rule out Coriolis interactions without first understanding the level structure. However, in the 210–205 nm region, theory predicts an avoided crossing of the $\tilde{C}$ state with the repulsive $3\ ^1A'$ state.[158,161,182] Therefore, although the relative contributions of rotation-vibration and vibration-electronic interactions to the a_1/b_2 admixture at each energy are unknown, it does seem likely that vibronic interactions make an important contribution in this region. However, in the low-lying non-predissociated region below 2000 cm^{-1} of vibrational excitation, there is no evidence for vibronically allowed transition intensity. In the absence of rovibrational Coriolis interactions, the spectrum in this region obeys strict vibrational selection rules $a_1' \leftrightarrow a_1''$ and $b_2' \leftrightarrow b_2''$.

The $\tilde{C}(^1B_2) \leftarrow \tilde{X}(^1A_1)$ transition has an *a*-axis electronic transition dipole moment, and obeys *a*-type rotational selection rules. However, as a consequence of oxygen atom nuclear spin statistics, only half of the rovibronic levels exist. The total wavefunction must be even with respect to interchange of the spin-zero oxygen nuclei. Since the equivalent rotation for the (12) nuclear exchange operation

Table 7.1: The character table for the C_{2v} molecular group. The symmetries of the vibrational and rotational parts of the wavefunction are given on the right side of the table in the I^r representation. The molecular frame axes are specified using principal inertial axis labels.

$\mathbf{C_{2v}(M)}$:	E	(12)	E^*	$(12)^*$			
$\mathbf{C_{2v}}$:	E	C_{2b}	σ_{bc}	σ_{ab}			
Equiv. rot:	E	C_{2b}	C_{2a}	C_{2a}		ψ_{vib}	K_aK_c
A_1	1	1	1	1 :	T_b	ν_1, ν_2	*ee*
A_2	1	1	−1	−1 :	J_b		*oo*
B_1	1	−1	1	−1 :	T_c, J_a		*eo*
B_2	1	−1	−1	1 :	T_a, J_c	ν_3	*oe*

is C_{2b}, the total rotation-vibration-electronic wavefunction must therefore be A_1 or A_2. In the I^r representation of the rotational wavefunctions, even (e) and odd (o) values of K_aK_c correspond to the C_{2v} molecular group representations as follows: ee $\leftrightarrow$ a_1, oo $\leftrightarrow$ a_2, eo $\leftrightarrow$ b_1, and oe $\leftrightarrow$ b_2. As a result, levels with A_1 or A_2 vibration-electronic character may only have ee or oo rotational wavefunctions and levels with B_1 or B_2 vibration-electronic character may only have eo or oe rotational wavefunctions. The consequence is that in the absorption spectrum from the ground state, the combination of vibrational selection rule and *a*-type rotational selection rule leads to $a_1(eo)' \leftarrow a_1(ee)''$ or $a_1(oe)' \leftarrow a_1(oo)''$ transitions, whereas in IR-UV experiments using a b_2 IR intermediate, the transitions are of the type $b_2(ee)' \leftarrow b_2(eo)''$ or $b_2(oo)' \leftarrow b_2(oe)''$. Table 7.1 summarizes the symmetries of the rotational and vibrational wavefunctions of SO_2 in the C_{2v} molecular group.

7.3 Experimental

7.3.1 Strategies for observing the b_2 levels

Before our successful IR-UV double resonance experiments, we attempted other schemes for observing the ν_3' fundamental of the $\tilde{C}$ state, including hot band pumping, using a vibrationally hot (but rotationally cold) expansion from a heated nozzle. This approach proved to be challenging, because, although the antisymmetric stretching mode ν_3 has the *lowest* fundamental vibrational frequency in the $\tilde{\text{C}}$ state (212 cm^{-1}), it has the *highest* fundamental vibrational frequency in the $\tilde{\text{X}}$ state (1362 cm^{-1}). The maximum population in the $\tilde{\text{X}}(0,0,1)$ does not occur until a vibrational temperature of ∼1200 K is reached, at which temperature the population in $\tilde{\text{X}}(0,0,1)$ is only 5%. It is even more unfortunate that the much stronger $\tilde{\text{C}}(0,0,0) \leftarrow \tilde{\text{X}}(1,0,0)$ hot band lies within 2 cm^{-1} of the desired $\tilde{\text{C}}(0,0,1) \leftarrow \tilde{\text{X}}(0,0,1)$. Thus, it was challenging to identify hot band transitions to the $\tilde{\text{C}}(0,0,1)$ level.

We first attempted to observe IR-UV signal using the $\tilde{\text{X}}(0,0,3)$ intermediate because the $\tilde{\text{X}}(0,0,3) \leftarrow \tilde{\text{X}}(0,0,0)$ transition at 4054 cm^{-1} was readily accessible to our difference frequency IR laser. However, this transition was too weak to use in the double resonance scheme. We finally had success using the much stronger $\tilde{\text{X}}(1,0,1) \leftarrow \tilde{\text{X}}(0,0,0)$ IR transition at 2500 cm^{-1}, which required us to work at the extreme low-frequency end of our difference frequency generation capabilities.

7.3.2 Experimental details

The experimental apparatus for the IR-UV measurements has been described previously,[126] so we will give only a brief summary of our apparatus, but we will expand on details unique to the SO_2 experiment. The IR was obtained by difference frequency generation in a $LiNbO_3$ crystal pumped by an injection-seeded Nd:YAG laser (Spectra-Physics PRO-270) at 1064 nm and a tunable dye laser (Lambda Physik FL2002) operating at 840 nm (LDS 821 dye), which was pumped by the 2nd harmonic 532 nm output of the same Nd:YAG laser to obtain ∼400 μJ/pulse of IR power at 2500 cm^{-1}. To ensure resonance of the IR frequency with transitions in the $\tilde{\text{X}}(1,0,1)$ band, a photoacoustic cell with 15 torr of neat SO_2 at room temperature was monitored.

The grating-limited IR spectral width of 0.1 cm^{-1} was insufficiently narrow to ensure that only a single rotational eigenstate was selected as the IR-UV intermediate, so our double resonance spectra contain features from intermediate levels populated via several nearby IR transitions. We used the relatively sparse R branch of the $\tilde{\text{X}}(1,0,1) \leftarrow \tilde{\text{X}}(0,0,0)$ transition to minimize "extra" intermediate levels, but in the

Table 7.2: Because the IR laser had a bandwidth of ∼0.1 cm^{-1}, it was possible to observe double resonance simultaneously from lower levels with a range of K_a. The a-type IR transitions within the bandwidth of the nominal IR pump were typically such that we could populate levels with K_a = 1-3 simultaneously. In the P, Q, R notation used to label rovibrational transitions, the subscript and superscript refer to the initial value of K_a and the change in K_a, respectively. K_c is omitted because it is constrained by the nuclear spin statistics.

Nominal IR Pump	Transitions within the IR bandwidth (frequencies/cm^{-1})			
P(2)	${}^{q}P_0(2)(2498.59)$	${}^{q}P_1(2)(2498.52)$		
R(1)		${}^{q}R_1(1)(2501.06)$		
R(2)	${}^{q}R_0(2)(2501.75)$	${}^{q}R_0(2)(2501.81)$	${}^{q}R_0(2)(2501.69)$	
R(3)		${}^{q}R_1(3)(2502.25)$	${}^{q}R_2(3)(2502.30)$	${}^{q}R_3(3)(2502.22)$
R(4)	${}^{q}R_0(4)(2502.96)$	${}^{q}R_1(4)(2503.08)$	${}^{q}R_2(4)(2502.93)$	${}^{q}R_3(4)(2502.83)$
R(5)		${}^{q}R_1(5)(2503.41)$	${}^{q}R_2(5)(2503.51)$	${}^{q}R_3(5)(2503.44)$
R(6)	${}^{q}R_0(6)(2504.12)$	${}^{q}R_1(6)(2504.32)$	${}^{q}R_2(6)(2504.17)$	${}^{q}R_3(6)(2504.04)$
R(7)		${}^{q}R_1(7)(2504.54)$	${}^{q}R_2(7)(2504.70)$	${}^{q}R_3(7)(2504.64)$

a-type IR transition typically more than one K_a sub-branch was populated. We used this to our advantage to collect double resonance spectra from the various K_a sub-branches simultaneously. For each J, the IR laser was typically broad enough to excite transitions with K_a =0-3. Because the IR spectrum is well understood, it was straightforward to predict the identity and intensity of the various K_a levels and any other spurious levels populated by nearby IR transitions. Table 7.2 provides an overview of the transitions that were excited in our typical IR pump schemes.

To generate the UV photon, the 355 nm third harmonic of the same Nd:YAG used in the IR generation pumped a second dye laser (Lambda Physik FL3002E) to produce laser radiation over the range 480–497 nm (Coumarin 480 or 503). This output was frequency doubled with a β-barium borate crystal and a small portion of the fundamental was passed through a heated $^{130}Te_2$ vapor absorption cell for frequency calibration. An intracavity etalon reduced the spectral width to 0.04 cm^{-1}, and after frequency doubling, the UV power was approximately 100–200 μJ/pulse. The IR and UV beams were counter-propagated through a molecular beam chamber. As a single Nd:YAG laser generated both pulses, their relative arrival times at the chamber could be controlled only through the addition of a delay line in the UV beam path. The length of the delay line was such that the UV pulse arrived 15 ns after the IR pulse.

The IR and UV pulses interacted with an unskimmed supersonic jet of 0.1% SO_2 in He, expanded through a General Valve (Series 9, $d = 1.0$ mm). The jet was backed by a pressure of 1 atm, and the chamber operated at $\sim 1\times 10^{-5}$ torr average pressure while under gas load. The IR and UV radiation interacted with the jet at a distance of 2 cm from the nozzle. A Hamamatsu R375 photomultiplier tube collected the laser-induced fluorescence at an angle mutually perpendicular to the laser path and molecular beam, using $f/1.2$ collection optics and a UG-11 filter to block laser scatter. The IR and UV lasers were sent through a set of baffles, described in Ref. 126, to minimize scattered light onto the detector. The photomultiplier tube signal was split and one line was input to a 30 dB voltage amplifier (Femto DHPVA-200) to increase the dynamic range of detection. The fluorescence decay was recorded on an oscilloscope and had a lifetime of typically 40 ns. For each ~ 0.018 cm^{-1} frequency resolution element, the fluorescence signal was averaged for 20 laser shots. The fluorescence spectrum was obtained by integrating the first 30 ns of fluorescence decay.

7.4 Rotational structure and Coriolis interactions

Because the ω_3 frequency is depressed in the $\tilde{\mathrm{C}}$ state it is brought into near resonance with ω_2, which results in a strong c-axis Coriolis interaction between ν_2 and ν_3. Particularly at low vibrational excitation, the effective ν_3 frequency is very low due to the double-minimum potential, which results in closely spaced sets of levels with conserved quanta of $\nu_2 + \nu_3$ that are coupled via c-axis Coriolis interactions that mix levels of a_1 and b_2 vibrational character. In the harmonic approximation, the form of the resulting matrix element in the signed k basis is

$$\begin{aligned}\langle v_1, v_2 - 1, v_3 + 1, J, k \pm 1|\boldsymbol{H}|v_1, v_2, v_3, J, k\rangle = \\ \mp C\zeta_{23}^{(c)}\Omega_{23}[J(J+1) - k(k \pm 1)]^{1/2}[v_2(v_3 + 1)]^{1/2}, \quad (7.1)\end{aligned}$$

where $\Omega_{kl} = 1/2[(\omega_k/\omega_l)^{1/2} + (\omega_l/\omega_k)^{1/2}]$. c-axis Coriolis interactions between ν_1 and ν_3 are also possible:

$$\langle v_1 - 1, v_2, v_3 + 1, J, k \pm 1|\boldsymbol{H}|v_1, v_2, v_3, J, k\rangle = \mp C\zeta_{13}^{(c)}\Omega_{13}[J(J+1) - k(k \pm 1)]^{1/2}[v_2(v_3+1)]^{1/2}, \quad (7.2)$$

and the sum rule $|\zeta_{23}^{(c)}|^2 + |\zeta_{13}^{(c)}|^2 = 1$ applies.[164] However, this latter interaction is relatively unimportant because the energy denominator for the interaction is large. The matrix elements (7.1)–(7.2) are added to the rigid rotor Hamiltonian matrix elements in the same basis,

$$\langle v_1, v_2, v_3, J, k|\boldsymbol{H}|v_1, v_2, v_3, J, k\rangle = T_0(v_1, v_2, v_3) + \left[A - \frac{1}{2}(B+C)\right]k^2 + \frac{1}{2}(B+C)J(J+1), \quad (7.3)$$

$$\langle v_1, v_2, v_3, J, k \pm 2|\boldsymbol{H}|v_1, v_2, v_3, J, k\rangle = \frac{1}{4}(B-C)[J(J+1) - k(k \pm 1)]^{1/2} \times [J(J+1) - (k \pm 1)(k \pm 2)]^{1/2}, \quad (7.4)$$

and the resulting matrix is diagonalized to obtain the rovibrational energies. Because the $\tilde{\mathrm{C}}$ state is highly anharmonic, we do not attempt to describe the interactions in terms of a global $\zeta_{23}^{(c)}$ parameter. Instead, we assign each set of levels an effective interaction strength $t_1^{(2)}$, which replaces $C\zeta_{23}^{(c)}\Omega_{23}[v_2(v_3+1)]^{1/2}$ in Eq. (7.1) to give matrix elements of the form

$$\langle v_1, v_2 - 1, v_3 + 1, J, k \pm 1|\boldsymbol{H}|v_1, v_2, v_3, J, k\rangle = \mp t_1^{(2)}[J(J+1) - k(k \pm 1)]^{1/2}. \quad (7.5)$$

Following the notation of Ref. 165, we use $t_m^{(n)}$ for the rotationally independent prefactor of the vibration-rotation matrix element, where m gives the power of the rotational operator(s), J_α, and n gives the combined power of the vibrational momentum and position operators, p_k and q_k, in the matrix element.

Table 7.3 lists the effective rotational constants obtained from a fit to each vibrational level individually, ignoring Coriolis interactions. As noted by Hallin[165] and Yamanouchi *et al.*,[43] many of the levels are rotationally perturbed, as evidenced by the wide range of C rotational constants, large magnitudes of inertial defect, and average fit errors much larger than the frequency calibration uncertainty ($\sim$0.02 cm^{-1}).

7.4.1 The (0,0,1) level

The IR-UV spectrum to the $\nu_3' = 1$ level is shown in Figure 7-1. The rotational structure of the ν_3 fundamental band of the $\tilde{\mathrm{C}}$ state does not appear to be significantly perturbed. The inertial defect of 0.8644 amu·Å^2 is similar to that of the zero-point level (0.361 amu·Å^2) and the average error obtained in fitting the rotational structure (0.016 cm^{-1}) is less than the laser calibration uncertainty, so we conclude that for the J and K_a values observed in our jet cooled spectra, there are no significant Coriolis interactions. The nominally allowed interaction via Eq. (7.5) is with the (0,1,0) level, which is 165 cm^{-1} higher in energy, so we do not expect any significant interactions at low rotational quanta via the $t_1^{(2)} \approx 0.3$ cm^{-1} c-axis Coriolis matrix element.

We note that the estimate of the ν_3' fundamental made by Hoy and Brand[163] (212 cm^{-1}) is in remarkably good agreement with our observation (212.575 cm^{-1}). The quantitative accuracy of their prediction appears to be the result of a fortuitous cancellation between the x_{23} cross-anharmonicity (neglected in Ref. 163) and the error in the inferred location (via perturbations in the $\tilde{\mathrm{C}}$(0,0,2) level) of the $\tilde{\mathrm{C}}$(0,1,1) level, which was too high by $\sim$10 cm^{-1}. The incorrect value of 228 cm^{-1} for the ν_3' fundamental reported by Ivanco[178] appears to have been obtained from a misassigned feature in his hot-band fluorescence spectrum.

7.4.2 The (0,1,1) and (0,0,2) levels

Hallin noted a large inertial defect and a large average error in his fit to the effective rotational constants of $\tilde{\mathrm{C}}(0,0,2)$ (see Table 7.3) and surmised that the perturbed rotational structure was the result of Coriolis interactions with $\tilde{\mathrm{C}}(0,1,1)$, which had

Table 7.3: Effective rotational constants and origins for the vibrational levels of the $\tilde{\mathrm{C}}$ state of SO_2 below ~1600 cm^{-1} of vibrational excitation, obtained by fitting the rotational structure of each band separately. All energies are in cm^{-1} units and the inertial defects (Δ) are listed in amu·$\mathrm{Å}^2$ units.

(v_1', v_2', v_3')	T	T_{vib}	A	B	C	Δ	Ave error
(0,0,0)[a]	42573.450(4)	0	1.15050(9)	0.34751(5)	0.26537(4)	0.361	0.008
(0,0,1)	42786.025(6)	212.575(6)	1.1479(16)	0.3444(4)	0.2614(4)	0.8644	0.016
(0,1,0)[a]	42950.933(4)	377.483(4)	1.17052(6)	0.34589(4)	0.26576(4)	0.292	0.010
(0,0,2)[a]	43134.672(7)	561.222(4)	1.14509(19)	0.34227(11)	0.24572(11)	4.632	0.041
(0,1,1)	43155.635(8)	582.184(8)	1.1722(8)	0.3443(5)	0.2743(7)	−1.876	0.016
(0,2,0)[a]	43324.992(4)	751.542(4)	1.19140(12)	0.34429(4)	0.26565(3)	0.344	0.013
(0,0,3)	43464.382(6)	890.932(6)	1.1424(13)	0.3407(5)	0.2498(4)	3.242	0.015
(0,1,2)[a]	43505.31(10)	931.87(1)	1.152(14)	0.336(4)	0.242(4)	4.85	0.11
(0,2,1)	43522.564(10)	949.114(10)	1.1908(20)	0.3430(7)	0.2906(6)	−5.29	0.036
(1,0,0)[a]	43533.51(12)	960.06(12)	1.149(9)	0.346(15)	0.266(16)	−0.107	0.17
(0,3,0)[b]	43695.48(3)	1122.03(3)	1.209(12)	0.3419(24)	0.2650(21)	0.37	
(0,0,4)[b]	43818.90(5)	1245.45(9)	1.113(17)	0.345(2)	0.2008(18)	20.01	0.031
(1,0,1)	43834.762(7)	1261.311(7)	1.1462(12)	0.3420(3)	0.2558(2)	1.917	0.0126
(0,1,3)	43825.81(5)	1252.36(5)	1.209(19)	0.349(3)	0.2926(20)	−4.631	0.094
(0,2,2)[b]	43873.42(2)	1299.97(2)	1.188(13)	0.3453(18)	0.2069(23)	18.47	0.017
(0,3,1)	43886.705(21)	1313.255(21)	1.222(4)	0.3452(17)	0.3188(14)	−9.77	0.034
(0,0,5)	44169.266(17)	1595.816(21)	1.129(4)	0.3411(13)	0.2128(10)	14.85	0.052
(0,1,4)[b]	44177.70(2)	1604.25(2)	1.1596(147)	0.3535(16)	0.1795(11)	31.70	
(1,0,2)[b]	44227.12(1)	1653.67(1)	1.1410(66)	0.3408(13)	0.2709(7)	−2.37	

---

[a] Ref. 165

[b] Ref. 43

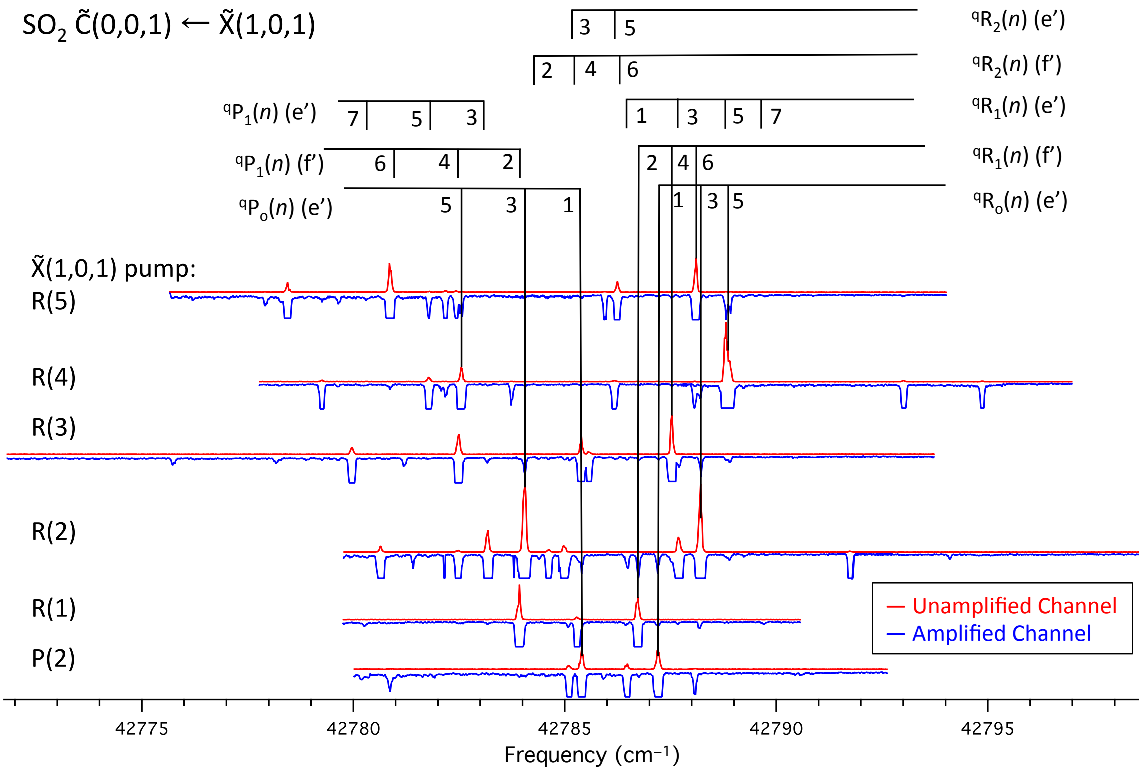

Figure 7-1: Spectra of the $\tilde{\mathrm{C}}(0,0,1) \leftarrow \tilde{\mathrm{X}}(1,0,1)$ transition, observed by IR-UV double resonance. The energy of the $\tilde{\mathrm{X}}(1,0,1)$ origin (2499.87 cm^{-1}) has been added to the frequency axis. The unamplified signal channel is shown with upward peaks (red) and the amplified signal channel is shown with downward peaks (blue). The main ^{q}P and ^{q}R branches are labeled. For simplicity of presentation, the weaker ^{q}Q branches and $\Delta K_a = 2$ transitions are not labeled. The IR pump transition used in each trace is shown on the left-hand side. There were typically several K_a levels populated at each IR pump transition frequency (see Table 7.2).

not been directly observed at that time.[165] He performed a fit to the (0,0,2) rotational structure to obtain the term energy of (0,1,1) and its $t_1^{(2)}$ matrix element for c-axis Coriolis interaction with (0,0,2). (See Table 7.4.)

We have reanalyzed the interaction using Hallin's data and our direct observations on (0,1,1). Because Hallin's spectrum was recorded at dry ice temperature ($T = 195$ K), while our spectrum was recorded in a supersonic jet expansion ($T_{rot} \approx 10$ K), the data set for (0,0,2) extends significantly higher in J and K_a than does our data set for (0,1,1). As a result, our attempts to fit to both the centrifugal distortion constants and the Coriolis matrix element simultaneously led to large correlations between the parameters. Therefore, we constrained the centrifugal distortion constants of both levels to reasonable values. We use the values obtained by Hallin for the $\tilde{\mathrm{C}}(0,0,0)$ level. Even with this constraint in place, significant correlation (> 0.99) remained between the C constants and the $t_1^{(2)}$ matrix element. We therefore used the inertial defects to set a constraint on the C rotational constants.

The inertial defect, $\Delta = I_c - I_a - I_b$, in a planar molecule may be expressed as a sum of Coriolis, vibrational, centrifugal distortion, and electronic contributions:

$$\Delta = \Delta_{\mathrm{Cor}} + \Delta_{\mathrm{vib}} + \Delta_{\mathrm{CD}} + \Delta_{\mathrm{elec}}. \tag{7.6}$$

Harmonic expressions for the last three terms of Eq. (7.6) were derived by Oka and Morino for triatomic C_{2v} molecules.[184] Hoy and Brand discussed the inertial defects in the $\tilde{\mathrm{C}}$ state of SO_2.[163] They derive modified expressions for the inertial defects that treat modes ν_1 and ν_2 harmonically, but include an anharmonic expansion in ν_3. We follow the treatment in Ref. 163 to estimate the contribution of the last three terms in Eq. (7.6).

We expect the electronic contribution to be negligible, so we ignore it. The contribution from centrifugal distortion is obtained from

$$\Delta_{\mathrm{CD}} = -\tau_{abab}^{(i)} \left(\frac{3I_c}{4C} + \frac{I_b}{2B} + \frac{I_a}{2A} \right), \tag{7.7}$$

where I_α is a diagonal component of the moment of inertia tensor, and A, B, and

C are the rotational constants. The quantity $\tau_{abab}^{(i)}$ is given by a modified expression for the quartic centrifugal distortion constant of the vibrational eigenlevel $|i\rangle$ that corrects for quartic anharmonicity in ν_3:

$$\tau_{abab}^{(i)} = 2\tau_{abab}\omega_3 \sum_f \frac{|\langle i|q_3|f\rangle|^2}{E_f - E_i} \tag{7.8}$$

$$\tau_{abab} = -16ABC/\omega_3^2. \tag{7.9}$$

In Eq. (7.8), the summation is over all zero-order vibrational states, $|f\rangle$, and the expansion of $|i\rangle$ is determined from our updated force field, which will be reported in a future work.[175]

We obtain the vibrational contribution to the inertial defect from

$$\begin{aligned}\Delta_{\text{vib}} = -\frac{3h}{16\pi^2 c}\Bigg\{&\left[\frac{(a_1^{cc})^2}{I_c} - \frac{(a_1^{bb})^2}{I_b} - \frac{(a_1^{aa})^2}{I_a}\right]\left(\frac{v_1+\frac{1}{2}}{\omega_1}\right)\\ &+\left[\frac{(a_2^{cc})^2}{I_c} - \frac{(a_2^{bb})^2}{I_b} - \frac{(a_2^{aa})^2}{I_a}\right]\left(\frac{v_2+\frac{1}{2}}{\omega_2}\right) - \frac{4}{\omega_3}\langle i|q_3^2|i\rangle\Bigg\},\end{aligned} \tag{7.10}$$

where $a_k^{\alpha\beta} = (\partial I_{\alpha\beta}/\partial q_k)_0$ are the derivatives of the moment of inertia tensor matrix elements with respect to the normal coordinates, evaluated at the (C_{2v}) equilibrium reference geometry. Again, we obtain the expansion of the eigenstates $|i\rangle$ used in Eq. (7.10) from our updated force field.[175]

Equation (7.10) accounts for vibrational dependence of the rotational constants that arises from harmonic vibrational motion along q_1 and q_2 and anharmonic motion along q_3, but it does not account for the Δ_{Cor} contribution to the inertial defect by level-specific c-axis Coriolis interactions that perturb the C rotational constants of the interacting levels. Hallin assumed that Δ_{Cor} was the primary contribution to Eq. (7.6), so in his fit he constrained the C rotational constants with the requirement $\Delta = 0$ in order to alleviate correlation in his fit between the Coriolis interaction matrix elements and the rotational constants. However, the expected values of Δ_{vib} for the (0,0,2) and (0,1,1) levels are 0.8675 and 0.7186 amu·Å^2, respectively, which are comparable in magnitude to the contribution of Δ_{Cor} (approximately 3.76 and

-2.59 amu·Å^2, respectively). Therefore, we obtain smaller fitting error and better determination of fit parameters when we instead constrain the C rotational constants with the requirement $\Delta = \Delta_{\text{vib}} + \Delta_{\text{CD}}$. That is, we constrain the fit so that our deperturbed rotational constants retain the expected contribution of centrifugal distortion and vibration to the inertial defect, but we remove the contribution from Coriolis interactions.

We ignore effects from the interaction of (0,1,1) with (0,2,0) because the energy denominator is large ($\sim$170 cm^{-1}) and is not expected to make a significant contribution to the low rotational energy levels that we observe. The resulting fit, given in Table 7.4, has no correlations greater than 0.81. The observed origin of $(0, 1, 1)$ is approximately 10 cm^{-1} lower than the fit value obtained by Hallin. Furthermore, our observed A rotational constant is significantly larger than that observed by Hallin. The A constants we obtain for (0,1,1) and (0,0,2) are in better agreement with physical expectations, because we expect the A constant to increase when one quantum of stretching excitation is exchanged for one quantum of bending excitation.

7.4.3 The (0,0,3), (0,1,2), (0,2,1), and (1,0,0) levels

A reduced term value plot for the $\tilde{\text{C}}$(0,0,3), (0,1,2), (0,2,1), and (1,0,0) levels is shown in Figure 7-2. The (0,0,3), (0,1,2), (0,2,1), and (0,3,0) levels comprise the next highest set of states that nominally interact via $\zeta_{23}^{(c)}$ interactions. The first three of these states are within < 50 cm^{-1} of their neighbors, but (0,3,0) is higher in energy by $\sim$170 cm^{-1}, and interactions with (0,3,0) are insignificant at low rotational temperatures. Hallin observed the (0,1,2) and (1,0,0) levels and deduced the term value and rotational constants for (0,2,1) by deperturbing the Coriolis interactions.[165] Hallin used a model that included not only the $\zeta_{23}^{(c)}$ interaction between (0,1,2) and (0,2,1), but also a higher-order $\zeta_{1/223}^{(c)}$ interaction between (0,2,1) and (1,0,0) and a non-rotationally dependent $t_0^{(4)}$ interaction between (0,1,2) and (1,0,0).

Because our jet cooled spectra do not extend as high in J and K_a as Hallin's dry ice temperature spectra, we have constrained the centrifugal distortion constants to reasonable values (Table 7.5), obtained from Hallin's fit. Our initial fit did not

Table 7.4: Fit parameters for the interacting levels (0,1,1) and (0,0,2) of the $\tilde{\text{C}}$ state obtained from the current work are compared to the fit parameters of Ref. 165. All energies are in cm^{-1} units and the inertial defects (Δ) are listed in amu·Å^2 units. Reported statistical uncertainties are 2σ and do not reflect any uncertainty in the model.

	This work		Ref. 165	
	(0,1,1)	(0,0,2)	(0,1,1)	(0,0,2)
T_0	43155.630(11)	43134.649(10)	43166.747(46)	43134.674(2)
T_{vib}	582.180(11)	561.199(10)	593.297(46)	561.224(2)
A	1.1720(25)	1.1461(4)	1.12941(62)	1.144971(77)
B	0.3408(7)	0.3432(4)	0.34651(13)	0.343338(19)
C	0.2605^a	0.2612^a	0.26516^a	0.264133^a
Δ	0.8675	0.7186	0	0
$10^{-7}\Delta_J$	4.98^a	4.98^a	4.98^a	4.98^a
$10^{-7}\Delta_{JK}$	129.2^a	129.2^a	129.2^a	81.6(27)
$10^{-7}\Delta_K$	73.8^a	73.8^a	73.8^a	192.2(51)
$10^{-7}\delta_J$	1.6^a	1.6^a	1.6^a	1.6^a
$10^{-7}\delta_K$	84^a	84^a	84^a	90.1(15)
$t_1^{(2)}$	0.289(5)		0.40183(13)	
σ	0.022		0.010	

---

[a] Constrained. See text.

converge to a reasonable set of rotational constants, so we again imposed a constraint on the inertial defect, setting the C constants of (0,0,3), (0,1,2), and (0,2,1) such that $\Delta = \Delta_{\text{vib}} + \Delta_{\text{CD}}$ obtained from Eqs. (7.7) and (7.10). With this constraint, we obtain a reasonable fit to the set of interacting levels. We attempted to fit the higher order $t_1^{(4)}$ ($\zeta_{1/223}^{(c)}$) c-axis Coriolis interaction between the (1,0,0) and (0,2,1) levels and the rotationally independent $t_0^{(4)}$ interaction between (0,1,2) and (1,0,0) level reported by Hallin, but our data do not give a statistically significant determination of these values, so we omit these interactions. Although (1,0,0) exhibits a negative inertial defect (-0.107 amu·Å^2) in its effective rotational constants (Table 7.3), which could be indicative of a Coriolis interaction with a lower-lying level, our data do not give a statistically significant determination of the interaction, probably because the weak fourth-order coupling is significant only at high J, and our jet-cooled IR-UV measurements on (0,2,1) do not extend higher than $J = 7$. When we fit the rotational constants of (1,0,0) only including rotational levels with $J < 10$, we obtain a positive intertial defect of 0.09 amu·Å^2, which is consistent with the argument that higher-order interactions that cause the negative inertial defect are most significant at high J. The results of our fit are compared to Hallin's fit in Table 7.5.

We find Hallin's determination of the (0,2,1) origin to be impressively accurate (within $\sim$2 cm^{-1}), considering that no transitions to (0,2,1) had been observed at the time. However, our results indicate that the Coriolis interaction of (0,1,2) with (0,0,3) makes an important contribution to the rotational structure and cannot be neglected. We believe that the $t_1^{(4)}$ and the $t_0^{(4)}$ matrix elements reported by Hallin effectively absorb some of the effects of interaction with (0,0,3), which is neglected in Hallin's analysis. One notable difference between the two sets of fit parameters in Table 7.5 is that our value of the $\zeta_{23}^{(c)}$ matrix element between (0,1,2) and (0,2,1) is significantly larger than Hallin's. Because the (0,1,2) level is sandwiched between (0,0,3) and (0,2,1) the c-axis Coriolis interactions with these two levels have an opposing effect on the effective C rotational constant of (0,1,2). Thus, it is not surprising that the inclusion of (0,0,3) in our fit allows the $t_1^{(2)}$ interaction between (0,1,2) and (0,2,1) to be stronger. Based on harmonic scaling arguments (Eq. 7.5), we believe our matrix

Table 7.5: Fit parameters for the interacting levels between 890–960 cm^{-1} obtained in the current work are compared to the fit parameters of Ref. 165. In the current work, we did not include higher order interactions with the (1,0,0) level, but we did include interactions with the (0,0,3) level. All energies are in cm^{-1} units and the inertial defects (Δ) are listed in amu·Å^2 units. Reported statistical uncertainties are 2σ and do not reflect any uncertainty in the model.

	This work			Ref. 165		
	(0,0,3)	(0,1,2)	(0,2,1)	(0,1,2)	(0,2,1)	(1,0,0)
T_0	43464.40(2)	43505.371(16)	43522.561(21)	43505.429(19)	43520.41(23)	43533.451(14)
T_{vib}	890.95(2)	931.921(16)	949.111(21)	931.979(19)	946.96(23)	960.001(14)
A	1.143(4)	1.1506(8)	1.1917(38)	1.15721(66)	1.2113(70)	1.14757(35)
B	0.3416(12)	0.3333(6)	0.3446(13)	0.3308(19)	0.34244(146)	0.34514(11)
C	0.2601^a	0.2547^a	0.2626^a	0.25864^a	0.26697^a	0.26534^a
Δ (amu·Å^2)	0.7222	0.9551	1.1223	0	0	0
$10^{-7}\Delta_J$	4.98^b	5.4^c	6.0^d	5.4^c	6.0^d	4.98^f
$10^{-7}\Delta_{JK}$	81.6^b	95^e	109.3^d	95(88)	109.3^d	66(7)
$10^{-7}\Delta_K$	192.2^b	207.5^c	175.7^d	207.5^c	175.7^d	64(20)
$10^{-7}\delta_J$	1.6^b	7.0^c	14.2^d	7.0^c	14.2^d	1.60^f
$10^{-7}\delta_K$	90.1^b	53.0^c	97.0^d	53.0^c	97.0^d	84.0^f
	$t_1^{(2)}$[(0,0,3)-(0,1,2)] = 0.353(19)			$t_1^{(2)}$[(0,1,2)-(0,2,1)] = 0.2537(17)		
	$t_1^{(2)}$[(0,1,2)-(0,2,1)] = 0.335(9)			$t_1^{(4)}$[(0,2,1)-(1,0,0)] = −0.0659(16)		
				$t_0^{(4)}$[(0,1,2)-(1,0,0)] = 1.24(9)		
	$\sigma = 0.037$			$\sigma = 0.034$		

---

[a] Constrained. See text.

[b] Constrained to the value for (0,0,2) determined in Ref. 165.

[c] Constrained to the value for $(0,1,0) + [(0,0,2) - (0,0,0)]$ determined in Ref. 165.

[d] Constrained to the value for $(0,2,0) + \frac{1}{2}[(0,0,2) - (0,0,0)]$ determined in Ref. 165.

[e] Constrained to the fit value determined in Ref. 165

[f] Constrained to the value for (0,0,0) determined in Ref. 165.

elements are more physically reasonable than Hallin's, because they show the expected increasing trend with increasing quantum numbers, whereas Hallin's reported matrix element for the (0,1,2)-(0,2,1) interaction is *smaller* than his reported matrix element for (0,2,0)-(0,1,1). Hallin mentions that the ratio between his matrix elements agrees with the expected ratio of $\sqrt{2}$, but he appears to have gotten the scaling backwards by accident (i.e. his reported ratio is actually the reciprocal of the expected harmonic scaling). The disagreement in the origins of (0,1,2) and (1,0,0) between our fit and Hallin's arises from the fact that Hallin includes a non-rotationally dependent $t_0^{(4)}$ interaction between these levels.

7.4.4 The (0,0,4), (0,1,3), (1,0,1), (0,2,2), and (0,3,1) levels

The a_1 levels (0,0,4) and (0,2,2) were observed in the one-photon LIF spectrum recorded by Yamanouchi *et al.*[43] We have observed the nearby b_2 levels (0,1,3), (1,0,1), and (0,3,1) via IR-UV double resonance. The reduced term value plots of the levels in this region are shown in Figures 7-3 and 7-4. The origins of the (0,1,3) and (0,0,4) levels are only ~7 cm^{-1} apart and these levels interact strongly via the *c*-axis Coriolis matrix element. As a result, we observe nominally forbidden lines from (0,0,4) in our IR-UV double resonance spectra. In particular, there is a pathological near-degeneracy between the $K_a > 3$ sub-branches of (0,0,4) with the $K_a - 1$ sub-branches of (0,3,1). The $K_a = 3$ sub-branch of (0,0,4) interacts with both $K_a = 0$ and $K_a = 2$ of (0,3,1). The $K_a = 4$ sub-branch of (0,0,4) interacts with $K_a = 3$ levels of (0,3,1) at low J, but is pushed down in energy toward an avoided crossing with $K_a = 1$ levels of (0,3,1) at $J \approx 10$. Our fit predicts that the $K_a = 5$ sub-branch of (0,0,4) overtakes the $K_a = 4$ sub-branch of (0,3,1) so that above $K_a = 5$, the energy ordering is reversed and the $K_a = 5$ sub-branch of (0,0,4) is pushed *up* in energy by the Coriolis interaction. Most of our rotational assignments on (0,0,4) were not reported in the one-photon LIF study,[43] presumably because *c*-axis Coriolis perturbations made rotational assignment of the congested LIF spectrum challenging. We have included data from both the one-photon and two-photon spectra in our fit.

The (1,0,1) level is only 10 cm^{-1} higher than (0,1,3), but its rotational structure

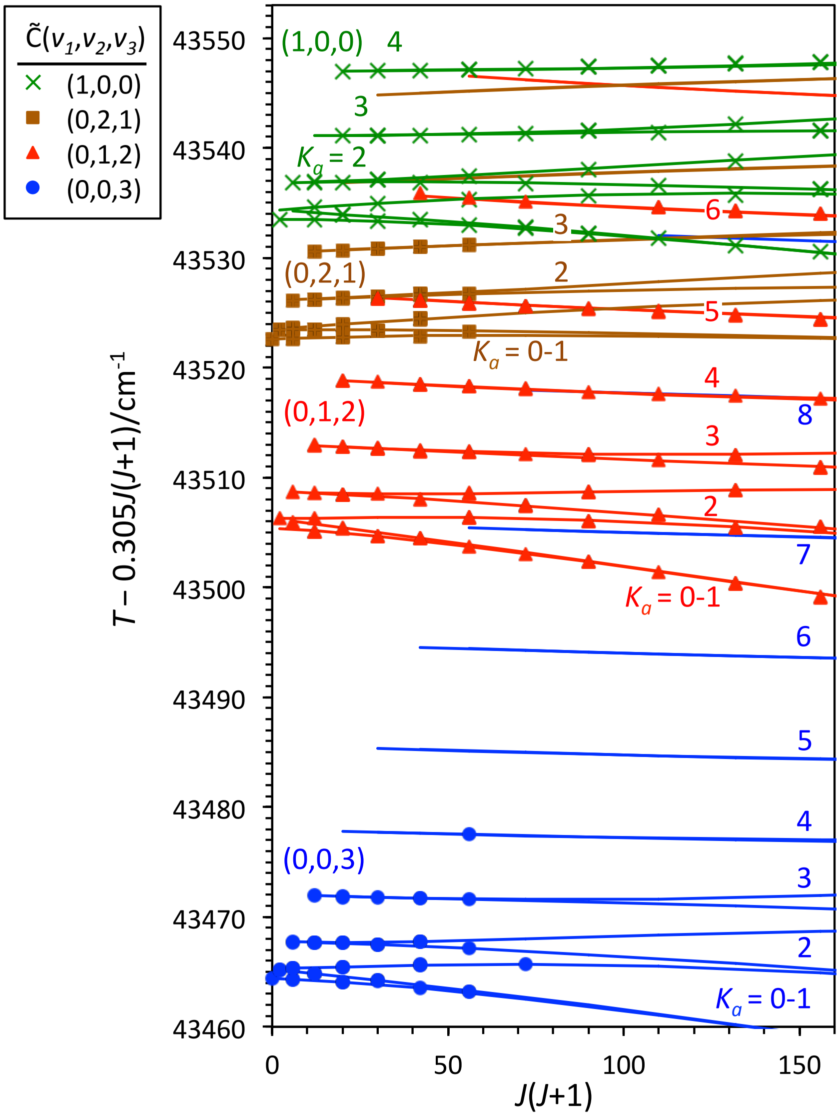

Figure 7-2: The observed low-J term energies around 43,500 cm^{-1}, reduced by (0.305 cm^{-1}) $\times J(J+1)$, are plotted against $J(J+1)$. Curves through the data are from the fit given in the left side of Table 7.5. Experimental data from the (0,0,3) and (0,2,1) levels are obtained in the current work. Data from the (0,1,2) and (1,0,0) levels is taken from Ref. 165.

Table 7.6: Fit parameters for the observed interacting levels with $v_2 + v_3 = 4$. All energies are in cm^{-1} units and the inertial defects (Δ) are listed in amu·Å^2 units. Reported statistical uncertainties are 2σ.

	(0,0,4)	(0,1,3)	(0,2,2)	(0,3,1)
T_0	43818.918(10)	43825.754(13)	43873.434(14)	43886.690(11)
T_{vib}	1245.468(10)	1252.304(13)	1299.984(14)	1313.240(11)
A	1.1393(15)	1.1673(29)	1.186(9)	1.2147(25)
B	0.3398(4)	0.3403(6)	0.3369(10)	0.3391(8)
C	0.2589^a	0.2594^a	0.2575^a	0.2605^a
Δ (amu·Å^2)	0.7	1.0	1.2	1.1
	$t_1^{(2)}$[(0,0,4)-(0,1,3)] = 0.3469(13)			
	$t_1^{(2)}$[(0,1,3)-(0,2,2)] = 0.449(10)			
	$t_1^{(2)}$[(0,2,2)-(0,3,1)] = 0.476(4)			
	$\sigma = 0.020$			

---

[a] Constrained.

is not significantly perturbed at low J and K_a, as evidenced by the small error and moderate inertial defect in the effective rotational constant fit reported in Table 7.3. We expect any Coriolis interaction between (1,0,1) and (0,0,4) to arise primarily as a result of Fermi admixture of (1,0,1) with (0,1,3) which would then couple (1,0,1) to (0,0,4) via ζ_{23}^c, but we do not have sufficient high J data to observe this higher-order interaction. Therefore, we neglect rotationally-dependent interactions with (1,0,1) in our fit. We do, however, find that it is necessary to include all three ζ_{23}^c interactions between (0,0,4), (0,1,3), (0,2,2), and (0,3,1). The highest level in this series of 1:1 v_2/v_3 exchange would be (0,4,0), which was not observed by Yamanouchi due to weak Franck-Condon factors, but it is expected to lie at around 44071 cm^{-1}, almost 200 cm^{-1} higher than (0,1,3). We therefore do not expect significant Coriolis interactions with (0,4,0) at low J.

The results of our fit to the rotational constants and c-axis Coriolis matrix elements for (0,0,4), (0,1,3), (0,2,2), and (0,3,1) are shown in Table 7.6. The C constants and the Coriolis matrix elements were highly correlated (0.999). Therefore, we constrained the C constants in the manner described in Section 7.4.2. With this constraint in place, there were no correlations larger than 0.77 in magnitude.

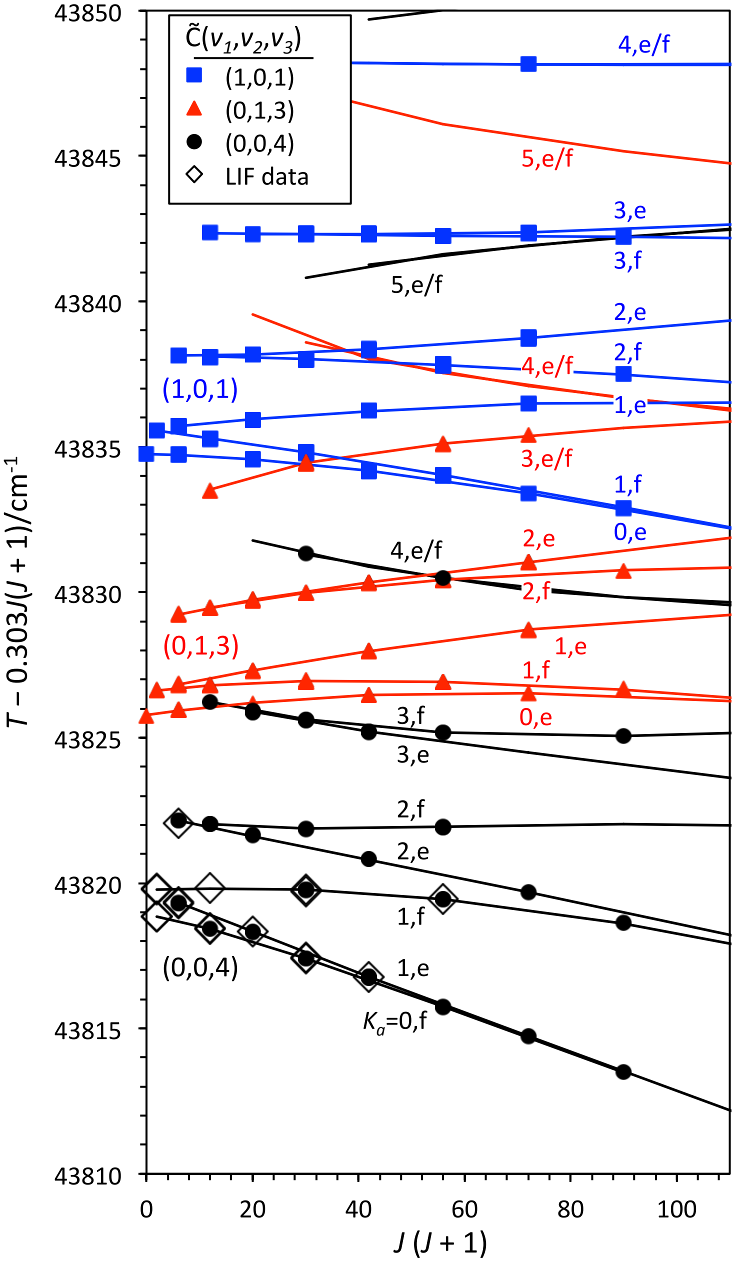

Figure 7-3: The observed low-J term energies around 43,830 cm^{-1}, reduced by (0.303 cm^{-1}) $\times$ $J(J+1)$, are plotted against $J(J+1)$. Curves through the data are from the fit given in Table 7.6 and from the (1,0,1) rotational constants given in Table 7.3. For the (0,0,4) level, experimental data is included from both the one-photon LIF spectrum of Ref. 43 (open diamonds) and from our current double-resonance work (filled circles), where we observe transitions that borrow intensity via c-axis Coriolis interactions.

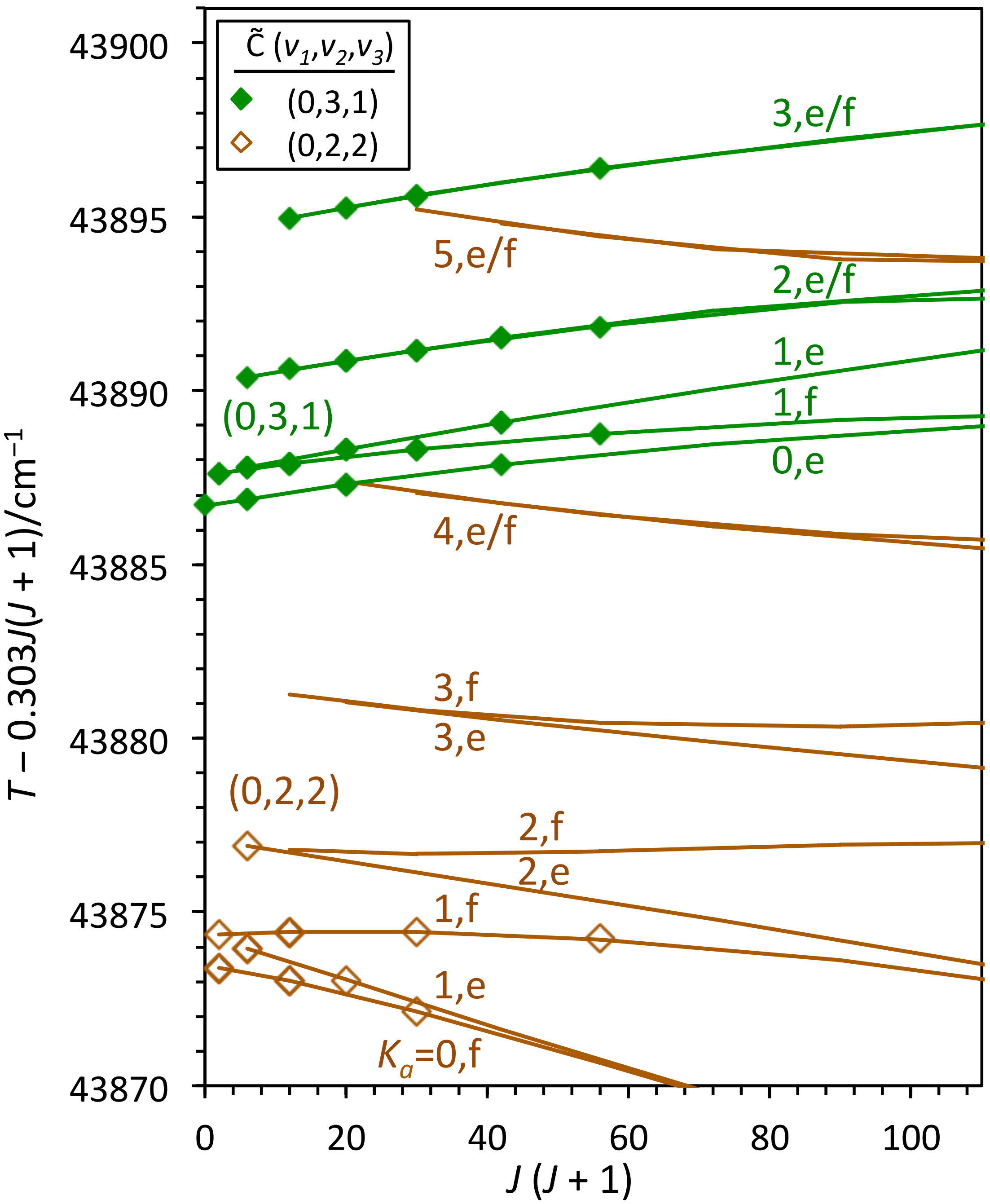

Figure 7-4: The observed low-J term energies around 43,885 cm^{-1}, reduced by (0.303 cm^{-1}) × $J(J+1)$, are plotted against $J(J+1)$. Curves through the data are from the fit given in Table 7.6. Experimental data for the (0,2,2) level is taken from Ref. 43.

7.4.5 The (0,0,5) level

A reduced term value plot of the observed (0,0,5) rotational levels is shown in Figure 7-5. The (0,0,5) level has a strong *c*-axis Coriolis interaction with (0,1,4). The (0,1,4) rotational levels reported by Yamanouchi *et al.*[43] are also shown in Figure. We attempted a fit to the rotational constants and Coriolis matrix element between (0,0,5) and (0,1,4). Although we were able to fit the data to within ~0.025 cm^{-1}, the fitting parameters we obtained were unreasonable for several reasons. Both (0,0,5) and (0,1,4) exhibited unreasonably small C constants (0.238 and 0.161 cm^{-1}, respectively) and large positive inertial defects (6.40 and 41.8 amu·Å^2, respectively). Furthermore, the $t_1^{(2)}$ matrix element that we obtained (0.20 cm^{-1}) was much smaller than expected. Placing a constraint on the inertial defects led to divergence of the fit. It was therefore necessary to include (0,2,3) and its *c*-axis Coriolis interaction with (0,1,4). We did not record the spectrum of this level, because it fell just outside of the range that we observed. However, we are able to predict that the (0,2,3) origin lies at 1610 cm^{-1} using our force field[175] and we predicted a reasonable set of rotational constants for (0,2,3) by adding the rotational constants of (0,1,3) and (0,2,0) and subtracting those of (0,1,0). We constrained the origin and rotational constants of (0,2,3) but floated the Coriolis matrix element with (0,1,4). We also constrained the C constants of (0,0,5) and (0,1,4) to yield the expected inertial defects, as described in Section 7.4.2.

The parameters obtained from our fit are listed in Table 7.7 and the fit is shown in Figure 7-5. Despite the relatively strong Coriolis interactions, we did not observe any a_1 levels via intensity borrowing in our IR-UV spectra. Our fit parameters predict severe interactions between the $K_a = 4$ sub-branch of (0,1,4) and the $K_a = 3$ sub-branch of (0,2,3), due to a near degeneracy. However, since the (0,2,3) level has not been observed directly, there is some uncertainty as to the severity of the interaction, since a small shift of the (0,2,3) origin would lead to a significantly different pattern.

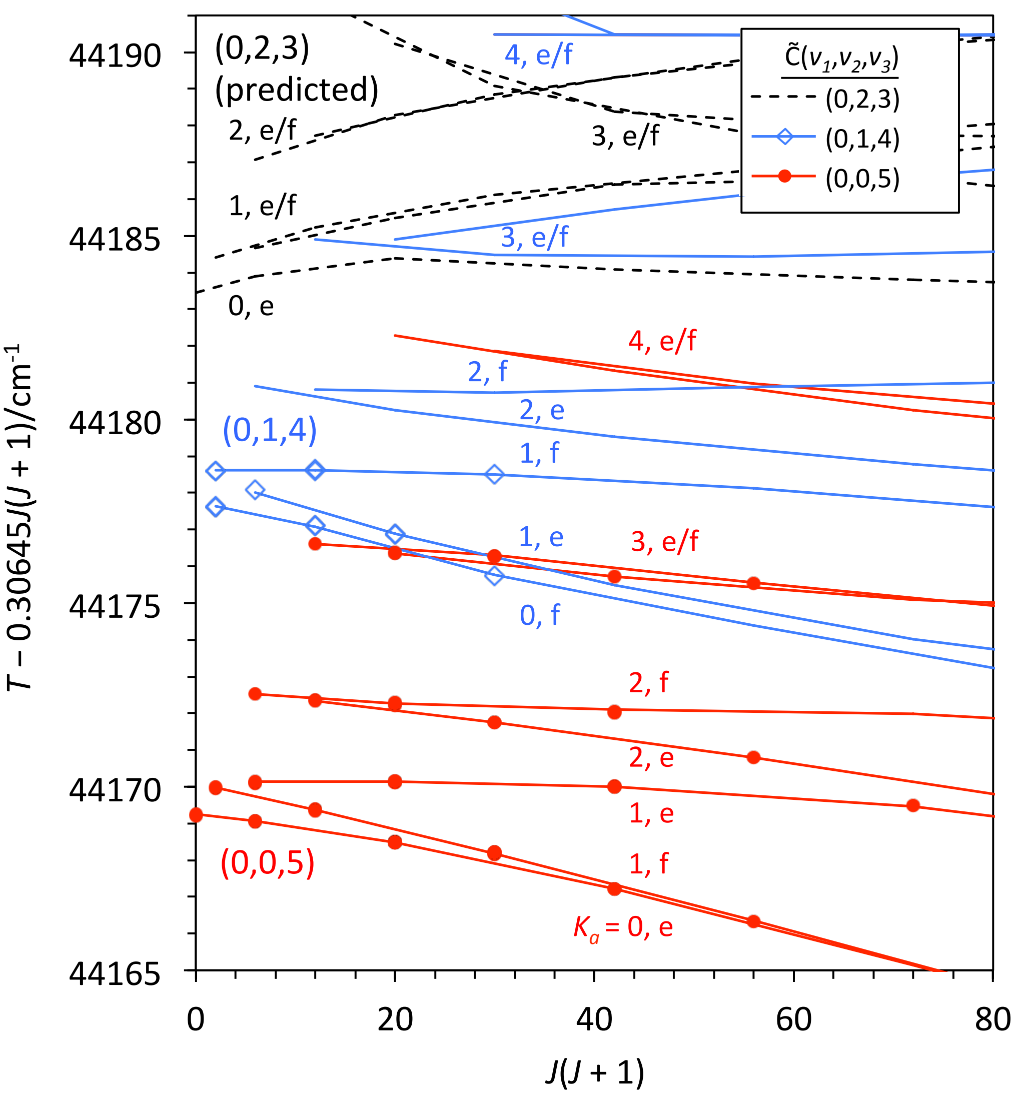

Figure 7-5: The observed low-J term energies around 44,180 cm^{-1}, reduced by (0.30645 cm^{-1}) $\times$ $J(J+1)$, are plotted against $J(J+1)$. Curves through the data are from the fit given in Table 7.7. Experimental data for the (0,1,4) level is taken from Ref. 43. The interacting (0,2,3) level has not been directly observed, but its predicted energy from the fit is shown with dotted curves.

Table 7.7: Fit parameters for the observed interacting levels (0,0,5), (0,1,4), and (0,2,3). The (0,2,3) level has not been observed, but its origin and rotational constants are predicted and the *c*-axis Coriolis matrix element is determined from a fit to the perturbed rotational structure of the observed levels. All energies are in cm^{-1} units and the inertial defects (Δ) are listed in amu·Å^2 units. Reported statistical uncertainties are 2σ.

	(0,0,5)	(0,1,4)	(0,2,3)
T_0	44169.247(14)	44177.737(26)	44183.45[a]
T_{vib}	1595.797(10)	1604.287(26)	1610[a]
A	1.1406(31)	1.1607(29)	1.18818[a]
B	0.3384(5)	0.3378(28)	0.3387[a]
C	0.2582[a]	0.2581[a]	0.25929[a]
Δ (amu·Å^2)	0.7	0.9	1.055
	$t_1^{(2)}$[(0,0,5)-(0,1,4)] = 0.302(4)		
	$t_1^{(2)}$[(0,1,4)-(0,2,3)] = 0.472(8)		
	$\sigma = 0.021$		

---

[a] Constrained.

7.4.6 Summary of rotational parameters derived in this work

Tables 7.8 and 7.9 provide a summary of the deperturbed vibrational origins and rotational constants obtained from the current work for the low-lying vibrational levels of the $\tilde{\mathrm{C}}$ state of SO$_2$. In cases where the C constant was constrained via the inertial defects, we estimate the uncertainty in the C constant to be twice the uncertainty in the B constant. The dependence of the deperturbed rotational constants on vibrational quanta in each normal mode is plotted in Figure 7-6. Members of the $(v_1, 0, 0)$

Table 7.8: Term values, rotational constants, and inertial defects (Δ) for low-lying b$_2$ levels of the $\tilde{\mathrm{C}}$ state of SO$_2$ below ∼1600 cm^{-1} of vibrational excitation. All energies are in cm^{-1} units and inertial defects are in amu·Å^2 units.

(v_1', v_2', v_3')	T	T_{vib}	A	B	C	Δ
(0,0,1)	42786.025(6)	212.575(6)	1.1479(16)	0.3444(4)	0.2614(4)	0.8644
(0,1,1)	43155.630(11)	582.180(11)	1.1720(25)	0.3408(7)	0.2605(14)	0.8675
(0,0,3)	43464.40(2)	890.95(2)	1.143(4)	0.3416(12)	0.2601(24)	0.7222
(0,2,1)	43522.561(21)	949.111(21)	1.1917(38)	0.3446(13)	0.2626(26)	1.1223
(0,1,3)	43825.754(13)	1252.304(13)	1.1673(29)	0.3403(6)	0.2594(12)	1.0
(1,0,1)	43834.761(7)	1261.311(7)	1.1462(12)	0.3420(3)	0.2558(10)	1.917
(0,3,1)	43885.690(11)	1313.240(11)	1.2147(25)	0.3391(8)	0.2605(16)	1.1
(0,0,5)	44169.247(10)	1595.797(10)	1.1406(31)	0.3384(5)	0.2582(10)	0.7

Table 7.9: Term values, rotational constants, and inertial defects for low-lying a_1 levels of the $\tilde{\mathrm{C}}$ state of SO_2 below ∼1600 cm^{-1} of vibrational excitation. All energies are in cm^{-1} units and inertial defects are in amu·$Å^2$ units.

(v_1', v_2', v_3')	T	T_{vib}	A	B	C	Δ
(0,0,0)[a]	42573.450(4)	0	1.15050(9)	0.34751(5)	0.26537(4)	0.361
(0,1,0)[a]	42950.933(4)	377.483(4)	1.17052(6)	0.34589(4)	0.26576(4)	0.292
(0,0,2)[b]	43134.649(10)	561.199(10)	1.1461(4)	0.3432(4)	0.2612(8)	0.7186
(0,2,0)[a]	43324.992(4)	751.542(4)	1.19140(12)	0.34429(4)	0.26565(3)	0.344
(0,1,2)[b]	43505.371(16)	931.921(16)	1.1506(8)	0.3333(6)	0.2547(12)	0.9551
(1,0,0)[a]	43533.451(14)	960.001(14)	1.14757(35)	0.34514(11)	0.26534(22)	0
(0,3,0)[c]	43695.48(3)	1122.03(3)	1.209(12)	0.3419(24)	0.2650(21)	0.37
(0,0,4)[d]	43818.918(10)	1245.468(10)	1.1393(15)	0.3398(4)	0.2589(8)	0.7
(0,2,2)[d]	43873.434(14)	1299.984(14)	1.186(9)	0.3369(10)	0.2575(20)	1.2
(0,1,4)[d]	44177.737(26)	1604.287(26)	1.1607(29)	0.3378(28)	0.2581(56)	0.9

---

[a] Ref. 165

[b] Deperturbed rotational constants obtained from a combined fit to data from Ref. 165 and data from interacting b_2 levels observed in the current work.

[c] Ref. 43

[d] Deperturbed rotational constants obtained from a combined fit to data from Ref. 43 and data from interacting b_2 levels observed in the current work.

and $(0, v_2, 0)$ progressions are relatively unperturbed by Coriolis interactions. Therefore, with the exception of (1,0,0), for which we use Hallin's constants,[165] the data in the first two columns of Figure 7-6 are taken from the effective rotational constants in Table 7.3. However, we note that the C constants for the $(v_1, 0, 0)$ progression seem to be somewhat perturbed, probably mostly due to higher-order interactions for which we have not corrected. Most of the data points in the third column of Figure 7-6 for the $(0, 0, v_3)$ progression were obtained after deperturbation of a manifold of $\zeta_{23}^{(c)}$-type Coriolis interactions, described above. We note that the *effective* (non-deperturbed) A, B, and C rotational constants shown in Table 7.3 deviate strongly from a linear trend in the $(0, 0, v_3)$ progression. The fact that our deperturbed A, B, and C constants all follow a fairly regular trend with the $(0, 0, v_1)$ vibrational progression provides support for the reasonableness of our fitting procedure.

The data shown in Figure 7-6 were fit in a weighted linear regression to determine the $\alpha_k^{A,B,C}$ constants, reported in Table 7.10. These constants are related to both the molecular structure and to the cubic force field parameters, so accurate determination of the α_3 values is germane to the characterization of the double-minimum potential.

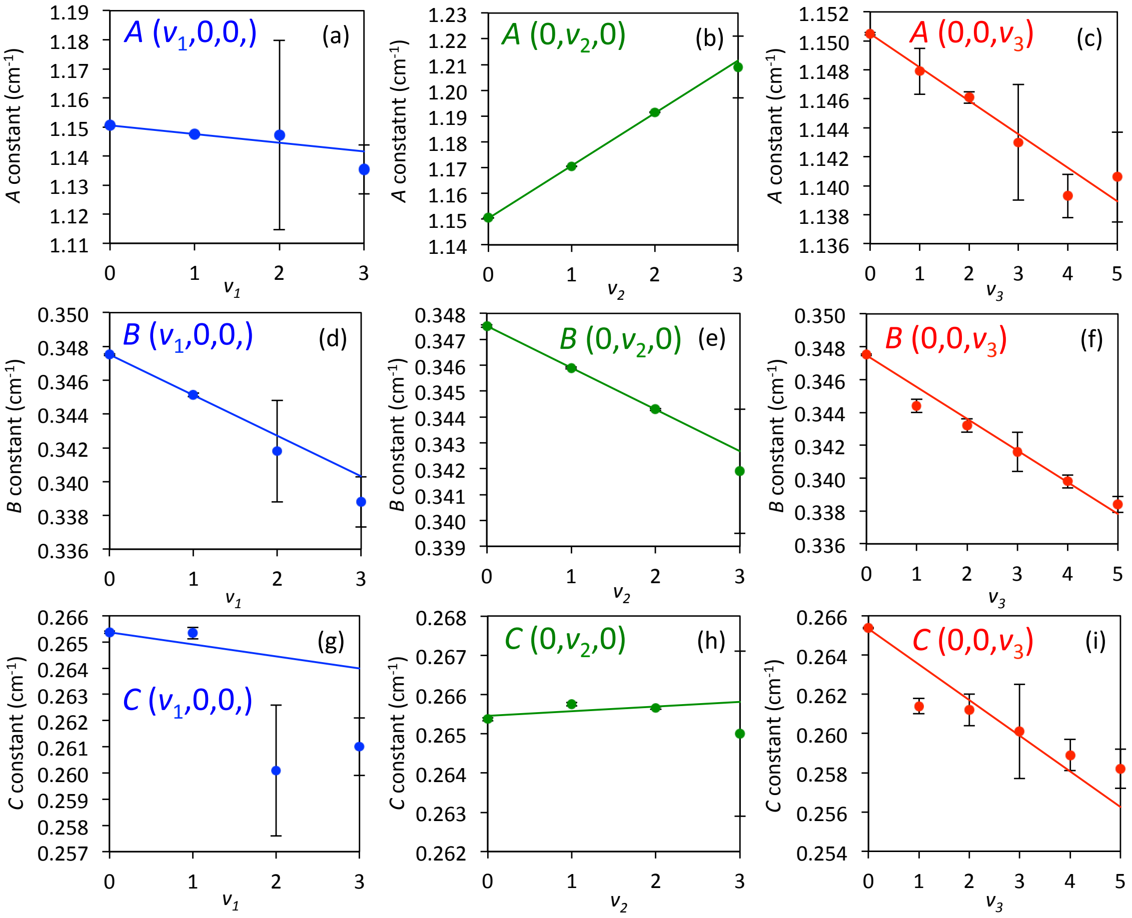

Figure 7-6: The dependence of the deperturbed rotational constants on the vibrational quantum number is plotted for progressions in each normal mode of the $\tilde{\mathrm{C}}$ state of SO_2. Error bars represent the statistical 2σ standard deviation obtained by fitting the rotational structure, and the weighted linear least-squares fit is shown for each progression. The derived α constants are given in Table 7.10.

Table 7.10: The dependence of the rotational constants on quanta of vibrational excitation for the $\tilde{\mathrm{C}}$ state of SO_2, $\alpha_k^X = -(\partial X/\partial v_k)_0$, where $X = A$, B, or C and k labels the modes. Values are listed in cm^{-1} units and numbers in parentheses represent two times the standard error obtained from a weighted fit to the data shown in Figure 7-6.

k	$\alpha_k^A \times 10^3$	$\alpha_k^B \times 10^3$	$\alpha_k^C \times 10^3$
1	3.0(4)	2.40(9)	
2	−20.3(5)	1.609(17)	−0.12(18)
3	2.31(26)	1.93(22)	1.8(7)

Due to the perturbed nature of the C constants for the $(v_1, 0, 0)$ progression, we do not report a value for α_1^C. The deperturbed C constant reported by Hallin for the (1,0,0) level is nearly identical to the C constant for the (0,0,0) level, even though we expect the C constant to decrease as symmetric stretching quanta are added. We take this as evidence that the deperturbed constants obtained by Hallin may be uncertain due to his fit model, in which he constrained the inertial defect to zero.

As expected, the remaining α values for the stretching vibrations are all positive (the rotational constants decrease as quanta of stretching vibration are added). For the progression in the bending vibration, the α_2^A constant is negative, indicating that the bending vibration experiences a softer potential at the wide bond angle turning point than at the narrow bond angle turning point (because the A constant increases as the geometry approaches linearity). The α_2^B constant is positive because the straightening vibration displaces the oxygen nuclei away from the b-axis, but does not move the sulphur nucleus away from the b-axis. The α_2^C constant is approximately zero since the straightening vibration moves the oxygen nuclei away from the c-axis but moves the sulphur nucleus toward the c-axis and the effects cancel.

Table 7.11 provides a summary of the c-axis Coriolis matrix elements obtained from our fits to the experimental data. For comparison, the predicted matrix elements from our harmonic force field are also listed. Although the experimentally-determined constants scale approximately as the harmonic prediction, the experimental numbers are all smaller than the harmonic prediction by ∼20–50%. This discrepancy is not surprising in light of the *anharmonic* nature of the $\tilde{\mathrm{C}}$ state of SO_2. In the $\tilde{\mathrm{C}}$ state,

Table 7.11: Experimentally determined *c*-axis Coriolis matrix elements (in cm^{-1} units) between pairs of interacting levels are compared with the harmonic prediction obtained using the parameters $C = 0.26537$ cm^{-1}, $\omega_2 = 390$ cm^{-1}, $\omega_3 = 650$ cm^{-1}, and $\zeta_{23}^{(c)} = 0.92$.

Interacting levels	$t_1^{(2)}$ Expt.	$C\zeta_{23}^{(c)}\Omega_{23}[v_2(v_3+1)]^{1/2}$ Harmonic
(0,1,1)-(0,0,2)	0.289(5)	0.3566
(0,0,3)-(0,1,2)	0.353(19)	0.4367
(0,2,1)-(0,1,2)	0.335(9)	0.5043
(0,1,3)-(0,0,4)	0.3469(13)	0.5043
(0,1,3)-(0,2,2)	0.449(10)	0.6176
(0,3,1)-(0,2,2)	0.476(4)	0.6176
(0,0,5)-(0,1,4)	0.302(4)	0.5638
(0,2,3)-(0,1,4)	0.472(8)	0.7132

ν_2 is relatively harmonic, but modes ν_1 and ν_3 are strongly coupled by both Fermi ($K_{1/33}$) and Darling-Dennison ($K_{11/33}$) interactions. Therefore, in the case of $\zeta_{23}^{(c)}$-type interactions among levels with no excitation in ν_1, we expect anharmonic effects to *decrease* the effective $\zeta_{23}^{(c)}$ strength. When there is no excitation in ν_1, Fermi (or Darling-Dennison) resonances cause coupling to levels with one (or two) quanta of ν_1 and $v_3 - 2$ quanta of ν_3. Because the interacting level has fewer quanta in ν_3, it will have a smaller $\zeta_{23}^{(c)}$ constant and the anharmonic interaction will cause a decrease in the effective $\zeta_{23}^{(c)}$. Ongoing work is being done to model the anharmonic Coriolis interactions.[175]

7.5 Vibrational level structure

The observed vibrational origins up to 1600 cm^{-1} above the $\tilde{\text{C}}$ state origin are shown in Figure 7-7. Levels with a single quantum of ν_3 are significantly depressed in frequency, but the degree of staggering decreases with increasing v_3, indicating a low barrier at the $\text{C}_{2\text{v}}$ geometry. We can define a parameter to characterize the degree of ν_3 staggering as a function of the other vibrational quanta, v_1 and v_2:

$$\Delta\omega_s(v_1, v_2) = \frac{T(v_1, v_2, 0) + T(v_1, v_2, 2)}{2} - T(v_1, v_2, 1). \tag{7.11}$$

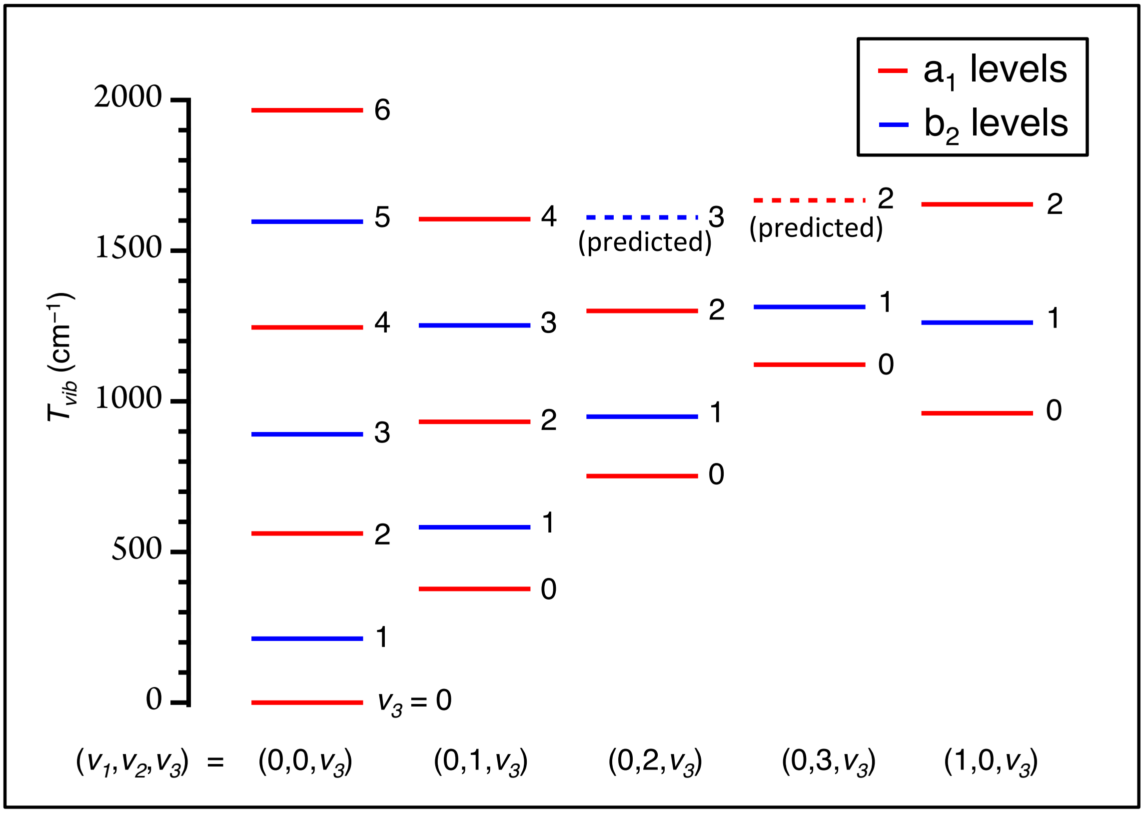

Figure 7-7: The low-lying vibrational level structure of the $\tilde{\text{C}}$ state of SO_2 is shown, arranged as progressions in ν_3.

Equation 7.11 gives the energy by which the *expected* harmonic energy of $(v_1, v_2, 1)$—which would be halfway between $(v_1, v_2, 0)$ and $(v_1, v_2, 2)$—is higher than the *observed* energy of $(v_1, v_2, 1)$, see inset of Figure 7-8. A larger value of $\Delta\omega_s$ indicates an increased amount of staggering and a higher effective barrier height. The value of $\Delta\omega_s$ is plotted as a function of v_1 and v_2 in Figure 7-8. The value of $\Delta\omega_s$ increases with v_2 but decreases with v_1. The increase in $\Delta\omega_s$ with v_2 is consistent with a vibronic coupling model for the double-well potential, in which the asymmetry results from q_3-mediated interaction between the diabatic 1^1B_2 ($\tilde{\text{C}}$) state and the 2^1A_1 state.

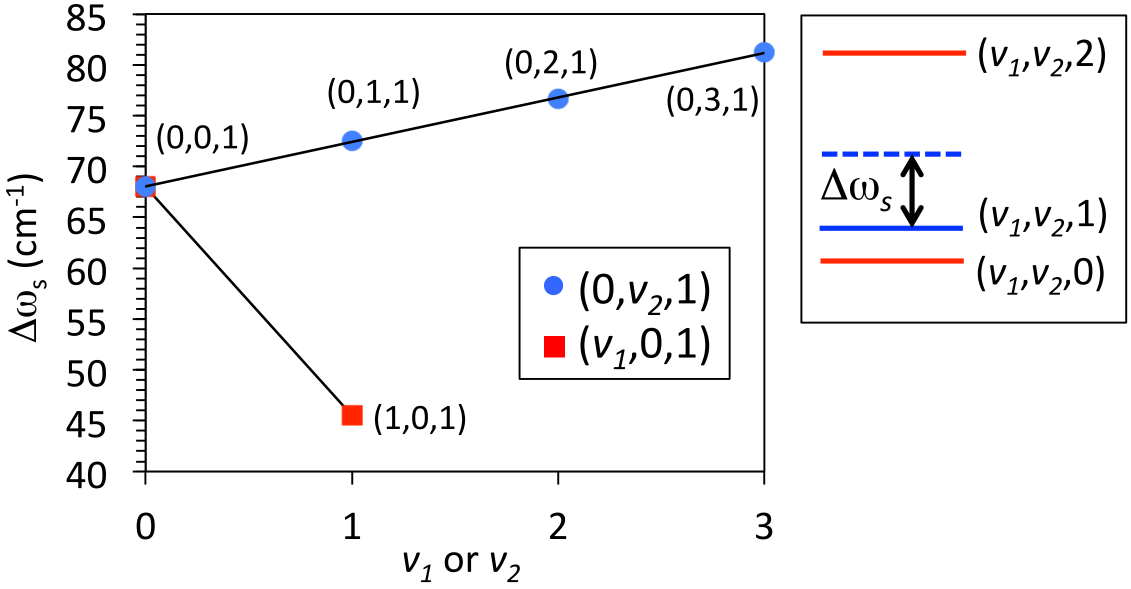

Figure 7-8: The staggering parameter, $\Delta\omega_s$, defined in Eq. (7.11), is plotted as a function of v_2 and v_3. The parameter, shown schematically in the right panel of the figure, is related to the effective barrier height at the C_{2v} geometry. It increases linearly with v_2 as the $\tilde{C}$-state PES approaches a conical intersection with the 2^1A_1 potential at a bending angle of ∼145°, which is consistent with a vibronic model for the double-well potential.

7.6 Discussion

7.6.1 Interaction of the $\tilde{\mathrm{C}}$ state with $2^1\mathrm{A}_1$

The avoided crossing between the $1^1\mathrm{B}_2$ ($\tilde{\mathrm{C}}$) and $2^1\mathrm{A}_1$ states has been extensively investigated at $\mathrm{C_s}$ geometries along the $\mathrm{SO_2}(\tilde{\mathrm{C}}) \rightarrow \mathrm{SO} + \mathrm{O}$ photodissociation pathway.[158–162,173,182] The $\tilde{\mathrm{C}}$ state correlates diabatically to the excited singlet $\mathrm{SO}(^1\Delta) + \mathrm{O}(^1\mathrm{D})$ photodissociation products. However, the $2^3\mathrm{A}'$ and $3^1\mathrm{A}'$ (which is $2^1\mathrm{A}_1$ in $\mathrm{C_{2v}}$) states both appear to correlate to the ground state triplet $\mathrm{SO}(^3\Sigma^-) + \mathrm{O}(^3\mathrm{P})$ product channel at geometries along the dissociation path. There is evidence for coupling to both the triplet and singlet dissociative states,[157,162] and both mechanisms probably contribute at different energies to the photodissociation of $\tilde{\mathrm{C}}$ state $\mathrm{SO_2}$ to triplet products. However, to our our knowledge, a full dimensional PES for the interacting $1^1\mathrm{B}_2$ ($\tilde{\mathrm{C}}$) and $2^1\mathrm{A}_1$ states has not been calculated, and in particular the interaction in the vicinity of the $\tilde{\mathrm{C}}$-state equilibrium has not received a thorough theoretical investigation, despite the suggestion by Innes that the double-well potential of the $\tilde{\mathrm{C}}$ state could arise from coupling to a *bound* state of $^1\mathrm{A}_1$ symmetry.[180] (Vibronic coupling to a repulsive diabat would *not* yield a double-well potential surface.)

Although the discussion in Refs. 158,161 is mostly focussed on the dissociative region of the PES, there is evidence in the calculations that the $2^1\mathrm{A}_1$ state is bound at the $\mathrm{C_{2v}}$ geometry and becomes dissociative (into the ground state product channel) as a result of interaction with the repulsive $3^1\mathrm{A}_1$ state. See, for example Figure 6 of Ref. 161, which indicates that $2^1\mathrm{A}_1$ probably correlates diabatically to the singlet $\mathrm{SO}(^1\Delta) + \mathrm{O}(^1\mathrm{D})$ dissociation channel before interacting with $3^1\mathrm{A}_1$ ($4^1\mathrm{A}'$ in $\mathrm{C_s}$). This was noted by Ray *et al.*[159], who calculated oscillator strengths for vertical electronic excitation from the ground state to the $1^1\mathrm{B}_2$ ($\tilde{\mathrm{C}}$), $2^1\mathrm{A}_1$, and $3^1\mathrm{A}_1$ states (See Table I of Ref. 159.) The calculated result was $f = 0.1336$ for the $1^1\mathrm{B}_2$ ($\tilde{\mathrm{C}}$) state; $f = 0.0290$ for the $2^1\mathrm{A}_1$ state; and $f = 0.1625$ for the $3^1\mathrm{A}_1$ state, where f is the oscillator strength. Therefore, the $3^1\mathrm{A}_1$ state is expected to have a comparable oscillator strength to the $\tilde{\mathrm{C}}$ state, but the oscillator strength to the $2^1\mathrm{A}_1$ state is expected to be smaller by almost an order of magnitude. This result would explain why q_3-mediated vibronic interaction of the $\tilde{\mathrm{C}}$ state with $2^1\mathrm{A}_1$ near equilibrium geometry could be strong enough to result in a double-minimum potential, but does not lend one-photon vibronically allowed intensity into b_2 vibrational levels, because the oscillator strength of the $2^1\mathrm{A}_1$ state is weak. On the other hand, along the dissociation coordinate, $3^1\mathrm{A}'$ correlates diabatically to the $3^1\mathrm{A}_1$ ($4^1\mathrm{A}'$ in $\mathrm{C_s}$) state, which has a much larger oscillator strength. As noted by Ray *et al.*,[159] this is probably the reason why dispersed fluorescence experiments from energies near the avoided crossing give rise to intensity into *both* a_1 and b_2 vibrational levels.

To our knowledge, no theoretical work has been done to determine the equilibrium structure of the $2^1\mathrm{A}_1$ state at bound geometries. Nevertheless, it appears that q_3-mediated vibronic interaction with the $2^1\mathrm{A}_1$ state may be responsible for *both* the double well potential of the $\tilde{\mathrm{C}}$ state near equilibrium *and* the avoided crossing that causes the $\tilde{\mathrm{C}}$-state to dissociate adiabatically to the ground state product channel. Thus, this is a case where a detailed understanding of the PES near equilibrium is highly relevant to dissociation processes that take place far from equilibrium since both are influenced by vibronic coupling to the same higher-lying electronic state.

7.6.2 Evidence for increased effective barrier height along the approach to conical intersection

The $1^1\mathrm{B}_2$ ($\tilde{\mathrm{C}}$) and $2^1\mathrm{A}_1$ states have different symmetries in $\mathrm{C_{2v}}$, but they both correlate to $^1\mathrm{A}'$ in $\mathrm{C_s}$ geometries. Therefore, although the crossing is avoided at $\mathrm{C_s}$ geometries, the levels may cross in $\mathrm{C_{2v}}$ geometries, resulting in a seam of conical intersection. Theoretical investigations[161,182] have reported the lowest seam of intersection to occur at bond angles between 145–150° in $\mathrm{C_{2v}}$ for bond lengths near the equilibrium value. This is a much wider bond angle than the $\sim$119° equilibrium bond angle of the $\tilde{\mathrm{C}}$ state. If the double-minimum potential of the $\tilde{\mathrm{C}}$ state were *caused* by q_3-mediated vibronic interactions with $2^1\mathrm{A}_1$ around the $\mathrm{C_{2v}}$ equilibrium, we would expect the effect to become very strong at geometries near the conical intersection, since the energy denominator for the interaction vanishes at the conical intersection.

As quanta of v_2 are added, we expect the vibrational wavefunction to have increased amplitude at wider bond angles, as evidenced by the large negative value of the α_2^A rotation-vibration constant (i.e. the effective A constant increases as quanta of v_2 are added—see Table 7.10 and Figure 7-6b.) Therefore, it is highly likely that the increase in $\Delta\omega_s$ as a function of v_2 (Figure 7-8) is a direct consequence of the approach to the seam of conical intersection.

To illustrate this point, we construct a toy one-dimensional model for the vibronic interaction between the bound $1^1\mathrm{B}_2$ and $2^1\mathrm{A}_1$ states and the higher-lying repulsive $3^1\mathrm{A}_1$ ($4^1\mathrm{A}'$) state. In the diabatic basis, the toy Hamiltonian is

$$\mathbf{H} = \begin{pmatrix} M_1 & V_{12} & 0 \\ V_{12} & M_2 & V_{23} \\ 0 & V_{23} & M_3 \end{pmatrix}, \tag{7.12}$$

where the matrix elements have the form

$$\begin{aligned} V_{12} &= \alpha_{12} q_3, & V_{23} &= \alpha_{23}, \\ M_1 &= \frac{1}{2}\omega_3 q_3^2, & M_2 &= \frac{1}{2}\omega_3' q_3^2 + \Delta_1, \\ M_3 &= (\Delta_2 - D_0)\exp\left(-|q_3/l|\right) + D_0. \end{aligned}$$

We assume that the V_{12} interaction is vibronic in nature since it couples states of different electronic symmetry in $\mathrm{C_{2v}}$ ($^1\mathrm{A}_1$ to $^1\mathrm{B}_2$), but the V_{23} interaction is assumed to be vibrationally independent since it couples states of the same ($^1\mathrm{A}_1$) electronic symmetry. The one-dimensional diabats and adiabats of the toy model are plotted in Figure 7-9 for three different values of Δ_1, which gives the energy difference between the bound $1^1\mathrm{B}_2$ and $2^1\mathrm{A}_1$ states. If a conical intersection between these levels exists at bond angles of ~145°, we expect Δ_1 to decrease as the bond angle increases from the $\tilde{\mathrm{C}}$ state equilibrium bond angle (Fig 7-9a) until it reaches zero at the conical intersection (Fig 7-9c). As Δ_1 decreases, the energy denominator for the vibronic interaction between the two bound levels decreases near equilibrium and the resulting effective barrier height at $\mathrm{C_{2v}}$ increases.

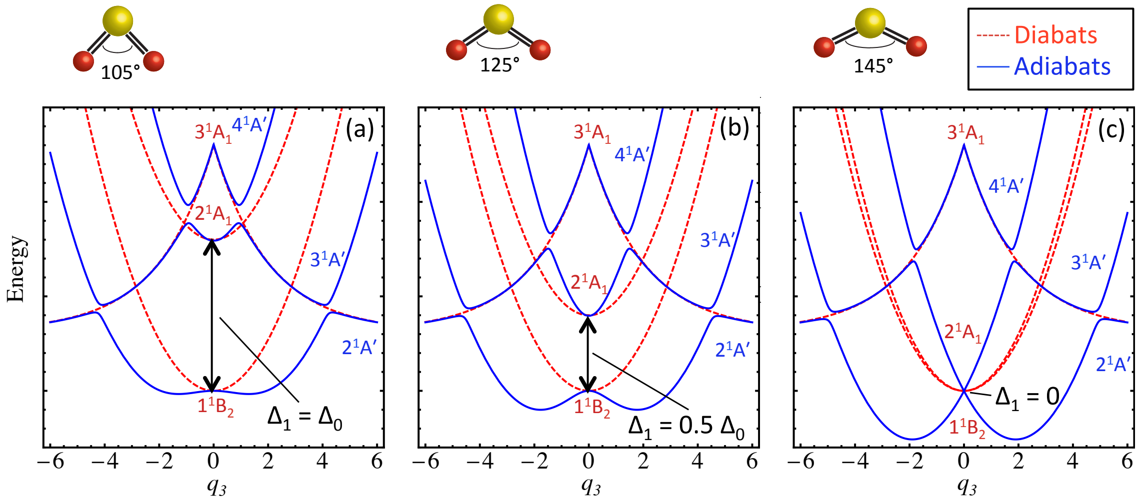

Figure 7-9: A toy one-dimensional model for the q_3-mediated vibronic interaction between the 1^1B_2 ($\tilde{C}$) state and the 2^1A_1 state is illustrated. The model is calculated from the Hamiltonian in Eq. (7.12) and is shown schematically as a function of Δ_1, which gives the separation between the two bound diabatic states. Interaction with the dissociative $4^1A'$ state is also included. The two bound potential energy surfaces cross via a conical intersection that occurs at a bond angle of ∼145°, but the crossing is avoided at C_s geometries. Therefore, as the bond angle increases, the energy denominator for the vibronic interaction decreases and the effective barrier in the $\tilde{C}$-state adiabatic potential energy surface increases, consistent with the observations shown in Figure 7-8.

Our results support the proposed vibronic coupling mechanism with the 2^1A_1 state and also provide predictions against which to test theoretical investigations which are currently underway. To our knowledge, calculation of a full dimensional PES for the interacting 1^1B_2 ($\tilde{C}$) and 2^1A_1 states has not been performed, and the location of the conical intersection as a function of q_1 has not been investigated. However, our results suggest that at the $\tilde{C}$ state equilibrium bond angle, the conical intersection occurs at *shorter* than the effective C_{2v} equilibrium bond distance of 1.576 Å, since the value of $\Delta\omega_s$ appears to *decrease* with v_1. That is, as the effective bond lengths are increased, the strength of the vibronic interaction decreases, probably because the energy denominator for the vibronic interaction increases, suggesting that the conical intersection occurs at shorter SO bond lengths.

7.7 Conclusions

We have observed the low-lying b_2 vibrational levels of the $\tilde{C}\ ^1B_2$ state of SO_2 via high-resolution two-photon IR-UV double resonance spectroscopy. For the low J rotational levels observed in the supersonic jet expansion, all rotational structure can be fit using an asymmetric top Hamiltonian that incorporates perturbations from c-axis ζ_{23} Coriolis interactions. After deperturbing the Coriolis interactions, the effective vibrational dependence of the rotational constants (α values) are determined. However, because there is a large degree of vibrational anharmonicity, we report effective Coriolis interaction matrix elements for each pair of interacting levels, and we compare the results with the harmonic scaling prediction. Ongoing work is being done to perform an internal force field determination of the potential energy surface for the $\tilde{C}$ state around equilibrium.[175]

Our observations are consistent with a vibronic coupling model for the asymmetric bonding structure, first proposed by Innes,[180], in which the $\tilde{C}$ state undergoes a q_3-mediated interaction with the (diabatically) bound 2^1A_1 state. The oscillator strength of the $2^1A_1 \leftarrow \tilde{X}\ 1^1A_1$ transition is believed to be relatively weak near the equilibrium C_{2v} geometry, which is consistent with the fact that no vibronically-allowed one-photon transitions to low-lying b_2 vibrational levels of the $\tilde{C}$ state have been observed. As noted in Ref. 159, vibronically allowed transitions that violate the vibrational selection rules are plausible at higher energies near the avoided crossing of the $\tilde{C}$-state with 2^1A_1 in the dissociative region, because 2^1A_1 probably borrows oscillator strength from an avoided crossing with the dissociative 3^1A_1 state. Furthermore, our results suggest an increase in the effective barrier height of the $\tilde{C}$ state PES at the C_{2v} geometry, as the bond angle is increased. This is consistent with theoretical predictions of a conical intersection of the $\tilde{C}$ state with the 2^1A_1 state at C_{2v} geometries with bond angles of around 145°. A collaboration is underway with John Stanton at the University of Texas to make *ab initio* calculations of the vibronic coupling around the equilibrium geometry of the $\tilde{C}$ state.

7.8 Acknowledgments

I would like to thank Jun Jiang for his collaboration on this project. Carrie Womack, Catherine Saladrigas, and Peter Richter also contributed to the work. I would like to Anthony Merer and John Stanton for valuable discussions. This material is based upon work supported by the U.S. Department of Energy, Office of Science, Chemical Sciences Geosciences and Biosciences Division of the Basic Energy Sciences Office, under Award Number DE-FG0287ER13671.

Appendix A

Tabulation of calculated vibrational overlap integrals from ***gerade*** B^n polyads of the $\tilde{\mathrm{A}}$ state to pure bending polyad levels of the $\tilde{\mathrm{X}}$ state of acetylene

Table A.1 lists the vibrational overlap integrals from *gerade* B^n polyads of the $\tilde{\mathrm{A}}$ state ($n = 0$–4) to pure bending polyad levels of the $\tilde{\mathrm{X}}$ state ($N_B = 0$–10) in the harmonic normal mode basis.

Table A.1: Calculated vibrational overlap integrals connecting zero-order members of the Ã-state *gerade* B^n polyads with members of X̃-state *gerade* pure-bending polyads in the harmonic normal mode basis.

X̃-state bending levels			Ã-state B^n polyads								
		ZOBS	B^0	B^2			B^4				
N_B	l	$[v_4^{l_4}, v_5^{l_5}]$	Origin	6^2	$4^1 6^1$	4^2	6^4	$4^1 6^3$	$4^2 6^2$	$4^3 6^1$	4^4
0	0	$[0^0, 0^0]$	1	2.37×10^{-2}		1.92×10^{-2}	6.91×10^{-4}		4.56×10^{-4}		4.51×10^{-4}
2	0	$[2^0, 0^0]$	9.09×10^{0}	2.16×10^{-1}		1.74×10^{-1}	6.28×10^{-3}		4.14×10^{-3}		4.10×10^{-3}
		$[0^0, 2^0]$	-3.16×10^{-2}	7.03×10^{-1}		7.06×10^{-1}	4.09×10^{-2}		3.03×10^{-2}		3.32×10^{-2}
	2	$[2^{+2}, 0^0]$	-4.90×10^{0}	-1.16×10^{-1}		-9.40×10^{-2}	-3.38×10^{-3}		-2.23×10^{-3}		-2.21×10^{-3}
		$[0^0, 2^{+2}]$	3.20×10^{-3}	-4.98×10^{-1}	$7.05i \times 10^{-1}$	5.00×10^{-1}	-2.90×10^{-2}	$2.90i \times 10^{-2}$	2.31×10^{-3}	$2.34i \times 10^{-2}$	2.35×10^{-2}
4	0	$[4^0, 0^0]$	4.82×10^{1}	1.15×10^{0}		9.25×10^{-1}	3.33×10^{-2}		2.20×10^{-2}		2.17×10^{-2}
		$[2^{+2}, 2^{-2}]$	-1.57×10^{-2}	2.44×10^{0}	$3.46i \times 10^{0}$	-2.45×10^{0}	1.42×10^{-1}	$1.42i \times 10^{-1}$	-1.13×10^{-2}	$1.15i \times 10^{-1}$	-1.15×10^{-1}
		$[2^0, 2^0]$	-2.88×10^{-1}	6.39×10^{0}		6.42×10^{0}	3.72×10^{-1}		2.75×10^{-1}		3.02×10^{-1}
		$[0^0, 4^0]$	1.01×10^{-3}	-4.77×10^{-2}		-4.15×10^{-2}	6.05×10^{-1}		4.96×10^{-1}		6.10×10^{-1}
	2	$[4^{+2}, 0^0]$	-3.46×10^{1}	-8.21×10^{-1}		-6.63×10^{-1}	-2.39×10^{-2}		-1.58×10^{-2}		-1.56×10^{-2}
		$[2^{+2}, 2^0]$	1.55×10^{-1}	-3.45×10^{0}		-3.46×10^{0}	-2.01×10^{-1}		-1.48×10^{-1}		-1.63×10^{-1}
		$[2^0, 2^{+2}]$	2.90×10^{-2}	-4.53×10^{0}	$6.41i \times 10^{0}$	4.54×10^{0}	-2.63×10^{-1}	$2.64i \times 10^{-1}$	2.10×10^{-2}	$2.13i \times 10^{-1}$	2.13×10^{-1}
		$[0^0, 4^{+2}]$	-1.75×10^{-4}	3.12×10^{-2}	$-3.87i \times 10^{-2}$	-2.35×10^{-2}	-4.94×10^{-1}	$4.95i \times 10^{-1}$	4.08×10^{-5}	$4.97i \times 10^{-1}$	4.98×10^{-1}
6	0	$[6^0, 0^0]$	1.71×10^{2}	4.06×10^{0}		3.28×10^{0}	1.18×10^{-1}		7.79×10^{-2}		7.71×10^{-2}
		$[4^{+2}, 2^{-2}]$	-1.10×10^{-1}	1.72×10^{1}	$2.44i \times 10^{1}$	-1.73×10^{1}	1.00×10^{0}	$1.00i \times 10^{0}$	-8.00×10^{-2}	$8.11i \times 10^{-1}$	-8.12×10^{-1}
		$[4^0, 2^0]$	-1.53×10^{0}	3.39×10^{1}		3.41×10^{1}	1.97×10^{0}		1.46×10^{0}		1.60×10^{0}
		$[2^{+2}, 4^{-2}]$	8.58×10^{-4}	-1.53×10^{-1}	$-1.89i \times 10^{-1}$	1.15×10^{-1}	2.42×10^{0}	$2.43i \times 10^{0}$	-2.00×10^{-4}	$2.44i \times 10^{0}$	-2.44×10^{0}
		$[2^0, 4^0]$	9.20×10^{-3}	-4.34×10^{-1}		-3.77×10^{-1}	5.50×10^{0}		4.51×10^{0}		5.54×10^{0}
		$[0^0, 6^0]$	-3.27×10^{-5}	2.44×10^{-3}		1.84×10^{-3}	-6.30×10^{-2}		-4.72×10^{-2}		-5.24×10^{-2}
	2	$[6^2, 0^0]$	-1.38×10^{2}	-3.27×10^{0}		-2.64×10^{0}	-9.50×10^{-2}		-6.27×10^{-2}		-6.20×10^{-2}
		$[4^{+4}, 2^{-2}]$	3.44×10^{-2}	-5.36×10^{0}	$-7.59i \times 10^{0}$	5.38×10^{1}	-3.12×10^{-1}	$-3.12i \times 10^{-1}$	2.49×10^{-2}	$-2.52i \times 10^{-1}$	2.53×10^{-1}
		$[4^{+2}, 2^0]$	1.09×10^{0}	-2.43×10^{1}		-2.44×10^{1}	-1.42×10^{0}		-1.05×10^{0}		-1.15×10^{0}
		$[4^0, 2^{+2}]$	1.54×10^{-1}	-2.40×10^{1}	$3.40i \times 10^{1}$	2.41×10^{1}	-1.40×10^{0}	$1.40i \times 10^{0}$	1.12×10^{-1}	$1.13i \times 10^{0}$	1.13×10^{0}
		$[2^{+2}, 4^0]$	-4.96×10^{-3}	2.34×10^{-1}		2.03×10^{-1}	-2.96×10^{0}		-2.43×10^{0}		-2.99×10^{0}
		$[2^0, 4^{+2}]$	-1.59×10^{-3}	2.84×10^{-1}	$-3.51i \times 10^{-1}$	-2.13×10^{-1}	-4.49×10^{0}	$4.50i \times 10^{0}$	3.71×10^{-4}	$4.52i \times 10^{0}$	4.53×10^{0}
		$[2^{-2}, 4^{+4}]$	-6.12×10^{-5}	1.91×10^{-2}	$-2.70i \times 10^{-2}$	-1.92×10^{-2}	-1.21×10^{0}	$2.43i \times 10^{0}$	2.99×10^{0}	$-2.44i \times 10^{0}$	-1.22×10^{0}
		$[0^0, 6^{+2}]$	7.88×10^{-6}	-1.59×10^{-3}	$1.74i \times 10^{-3}$	8.95×10^{-4}	4.98×10^{-2}	$-4.60i \times 10^{-2}$	1.94×10^{-3}	$-4.30i \times 10^{-2}$	-3.91×10^{-2}
8	0	$[8^0, 0^0]$	4.41×10^{2}	1.05×10^{1}		8.45×10^{0}	3.04×10^{-1}		2.01×10^{-1}		1.99×10^{-1}
		$[6^{+2}, 2^{-2}]$	-4.39×10^{-1}	6.85×10^{1}	$9.70i \times 10^{1}$	-6.87×10^{1}	3.98×10^{0}	$3.99i \times 10^{0}$	-3.18×10^{-1}	$3.22i \times 10^{0}$	-3.23×10^{0}
		$[6^0, 2^0]$	-5.41×10^{0}	1.20×10^{2}		1.21×10^{2}	7.00×10^{0}		5.18×10^{0}		5.67×10^{0}
		$[4^{+4}, 4^{-4}]$	1.35×10^{-4}	-4.20×10^{-2}	$-5.94i \times 10^{-2}$	4.21×10^{-2}	2.67×10^{0}	$5.35i \times 10^{0}$	-6.56×10^{0}	$-5.37i \times 10^{0}$	2.69×10^{0}
		$[4^{+2}, 4^{-2}]$	6.06×10^{-3}	-1.08×10^{0}	$-1.34i \times 10^{0}$	8.12×10^{-1}	1.71×10^{1}	$1.71i \times 10^{1}$	-1.41×10^{-3}	$1.72i \times 10^{1}$	-1.72×10^{1}
		$[4^0, 4^0]$	4.88×10^{-2}	-2.30×10^{0}		-2.00×10^{0}	2.92×10^{1}		2.39×10^{1}		2.94×10^{1}
		$[2^{+2}, 6^{-2}]$	-3.86×10^{-5}	7.78×10^{-3}	$8.52i \times 10^{-3}$	-4.38×10^{-3}	-2.44×10^{-1}	$-2.25i \times 10^{-1}$	-9.49×10^{-3}	$-2.10i \times 10^{-1}$	1.91×10^{-1}
		$[2^0, 6^0]$	-2.97×10^{-4}	2.22×10^{-2}		1.67×10^{-2}	-5.73×10^{-1}		-4.29×10^{-1}		-4.77×10^{-1}
		$[0^0, 8^0]$	1.06×10^{-6}	-1.11×10^{-4}		-7.30×10^{-5}	4.38×10^{-3}		3.00×10^{-3}		3.02×10^{-3}

$\tilde{\mathrm{X}}$-state bending levels			$\tilde{\mathrm{A}}$-state B^n polyads								
		ZOBS	B^0	B^2			B^4				
N_B	l	$[v_4^{l_4}, v_5^{l_5}]$	Origin	6^2	$4^1 6^1$	4^2	6^4	$4^1 6^3$	$4^2 6^2$	$4^3 6^1$	4^4
8	2	$[8^{+2}, 0^0]$	-3.78×10^2	-8.96×10^0		-7.24×10^0	-2.61×10^{-1}		-1.72×10^{-1}		-1.70×10^{-1}
		$[6^{+4}, 2^{-2}]$	2.17×10^{-1}	-3.39×10^1	$-4.80i \times 10^1$	3.40×10^1	-1.97×10^0	-1.97×10^0	1.57×10^{-1}	$-1.60i \times 10^0$	1.60×10^0
		$[6^{+2}, 2^0]$	4.35×10^0	-9.68×10^1		-9.71×10^1	-5.63×10^0		-4.16×10^0		-4.57×10^0
		$[6^0, 2^{+2}]$	5.46×10^{-1}	-8.51×10^1	$1.21i \times 10^2$	8.54×10^1	-4.95×10^0	$4.96i \times 10^0$	3.95×10^{-1}	$4.01i \times 10^0$	4.01×10^0
		$[4^{+4}, 4^{-2}]$	-1.89×10^{-3}	3.36×10^{-1}	$4.16i \times 10^{-1}$	-2.53×10^{-1}	-5.32×10^0	$-5.33i \times 10^0$	4.39×10^{-4}	$-5.35i \times 10^0$	5.36×10^0
		$[4^{+2}, 4^0]$	-3.50×10^{-2}	1.65×10^0		1.44×10^0	-2.09×10^1		-1.71×10^1		-2.11×10^1
		$[4^0, 4^{+2}]$	-8.45×10^{-3}	1.50×10^0	$-1.87i \times 10^0$	-1.13×10^0	-2.38×10^1	$2.39i \times 10^1$	1.97×10^{-3}	$2.40i \times 10^1$	2.40×10^1
		$[4^{-2}, 4^{+4}]$	-4.32×10^{-4}	1.35×10^{-1}	$-1.91i \times 10^{-1}$	-1.35×10^{-1}	-8.57×10^0	$1.72i \times 10^1$	2.11×10^1	$-1.72i \times 10^1$	-8.64×10^0
		$[2^{+2}, 6^0]$	1.60×10^{-4}	-1.19×10^{-2}		-9.02×10^{-3}	3.09×10^{-1}		2.31×10^{-1}		2.57×10^{-1}
		$[2^0, 6^{+2}]$	7.16×10^{-5}	-1.44×10^{-2}	$1.58i \times 10^{-2}$	8.13×10^{-3}	4.53×10^{-1}	$-4.18i \times 10^{-1}$	1.76×10^{-2}	$-3.91i \times 10^{-1}$	-3.55×10^{-1}
		$[2^{-2}, 6^{+4}]$	4.33×10^{-6}	-1.45×10^{-3}	$1.91i \times 10^{-3}$	1.26×10^{-3}	1.10×10^{-1}	$-1.97i \times 10^{-1}$	-2.11×10^{-1}	$1.48i \times 10^{-1}$	6.19×10^{-2}
		$[0, 8^{+2}]$	-3.25×10^{-7}	7.37×10^{-5}	$-7.18i \times 10^{-5}$	-3.08×10^{-5}	-3.44×10^{-3}	$2.93i \times 10^{-3}$	-2.38×10^{-4}	$2.55i \times 10^{-3}$	2.10×10^{-3}
10	0	$[10^0, 0^0]$	8.68×10^2	2.06×10^1		1.67×10^1	6.00×10^{-1}		3.96×10^{-1}		3.91×10^{-1}
		$[8^{+2}, 2^{-2}]$	-1.21×10^0	1.88×10^2	$2.66i \times 10^2$	-1.89×10^2	1.09×10^1	$1.10i \times 10^1$	-8.73×10^{-1}	$8.85i \times 10^0$	-8.86×10^0
		$[8^0, 2^0]$	-1.39×10^1	3.10×10^2		3.11×10^2	1.80×10^1		1.33×10^1		1.46×10^1
		$[6^{+4}, 4^{-4}]$	8.51×10^{-4}	-2.65×10^{-1}	$-3.76i \times 10^{-1}$	2.66×10^{-1}	1.69×10^1	$3.38i \times 10^1$	-4.15×10^1	$-3.39i \times 10^1$	1.70×10^1
		$[6^{+2}, 4^{-2}]$	2.41×10^{-2}	-4.29×10^0	$-5.32i \times 10^0$	3.23×10^0	6.80×10^1	$6.81i \times 10^1$	-5.61×10^{-3}	$6.48i \times 10^1$	-6.85×10^1
		$[6^0, 4^0]$	1.73×10^{-1}	-8.16×10^0		-7.10×10^0	1.03×10^2		8.47×10^1		1.04×10^2
		$[4^{+4}, 6^{-4}]$	-9.53×10^{-6}	3.18×10^{-3}	$4.21i \times 10^{-3}$	-2.77×10^{-3}	-2.43×10^{-1}	$-4.32i \times 10^{-1}$	4.64×10^{-1}	$3.26i \times 10^{-1}$	-1.36×10^{-1}
		$[4^{+2}, 6^{-2}]$	-2.72×10^{-4}	5.49×10^{-2}	$6.02i \times 10^{-2}$	-3.09×10^{-2}	-1.72×10^0	$-1.59i \times 10^0$	-6.70×10^{-2}	$-1.49i \times 10^0$	1.35×10^0
		$[4^0, 6^0]$	-1.58×10^{-3}	1.18×10^{-1}		8.88×10^{-2}	-3.04×10^0		-2.27×10^0		-2.53×10^0
		$[2^{+2}, 8^{-2}]$	1.59×10^{-6}	-3.61×10^{-4}	$-3.52i \times 10^{-4}$	1.51×10^{-4}	1.68×10^{-2}	$1.44i \times 10^{-2}$	1.17×10^{-3}	$1.25i \times 10^{-2}$	-1.03×10^{-2}
		$[2^0, 8^0]$	9.68×10^{-6}	-1.01×10^{-3}		-6.64×10^{-4}	3.98×10^{-2}		2.73×10^{-2}		2.74×10^{-2}
		$[0^0, 10^0]$	-3.50×10^{-8}	4.77×10^{-6}		2.73×10^{-6}	-2.54×10^{-4}		-1.60×10^{-4}		-1.45×10^{-4}
	2	$[10^{+2}, 0^0]$	-7.74×10^2	-1.84×10^1		-1.48×10^1	-5.34×10^{-1}		-3.52×10^{-1}		-3.49×10^{-1}
		$[8^{+4}, 2^{-2}]$	7.42×10^{-1}	-1.16×10^2	$-1.64i \times 10^2$	1.16×10^2	-6.72×10^0	$-6.73i \times 10^0$	5.37×10^{-1}	$-5.44i \times 10^0$	5.45×10^0
		$[8^{+2}, 2^0]$	1.19×10^1	-2.66×10^2		-2.67×10^2	-1.55×10^1		-1.14×10^1		-1.25×10^1
		$[8^0, 2^{+2}]$	1.41×10^0	-2.19×10^2	$3.11i \times 10^2$	2.20×10^2	-1.28×10^1	$1.28i \times 10^1$	1.02×10^0	$1.03i \times 10^1$	1.03×10^1
		$[6^{+6}, 4^{-4}]$	-2.03×10^{-4}	6.34×10^{-2}	$8.98i \times 10^{-2}$	-6.36×10^{-2}	-4.03×10^0	$-8.07i \times 10^0$	9.91×10^0	$8.11i \times 10^0$	-4.06×10^0
		$[6^{+4}, 4^{-2}]$	-1.19×10^{-2}	2.12×10^0	$2.63i \times 10^0$	-1.60×10^0	-3.36×10^1	$-3.37i \times 10^1$	2.78×10^{-3}	$-3.38i \times 10^1$	3.39×10^1
		$[6^{+2}, 4^0]$	-1.39×10^{-1}	6.57×10^0		5.71×10^0	-8.32×10^1		-6.82×10^1		-8.38×10^1
		$[6^0, 4^{+2}]$	-2.99×10^{-2}	5.33×10^0	$-6.61i \times 10^0$	-4.01×10^0	-8.45×10^1	$8.46i \times 10^1$	6.98×10^{-3}	$8.50i \times 10^1$	8.52×10^1
		$[6^{-2}, 4^{+4}]$	-1.72×10^{-3}	5.36×10^{-1}	$-7.59i \times 10^{-1}$	-5.38×10^{-1}	-3.41×10^1	$6.83i \times 10^1$	8.38×10^1	$-6.86i \times 10^1$	-3.44×10^1
		$[4^{+4}, 6^{-2}]$	8.48×10^{-5}	-1.71×10^{-2}	$-1.87i \times 10^{-2}$	9.63×10^{-3}	5.37×10^{-1}	$4.95i \times 10^1$	2.09×10^{-2}	$4.63i \times 10^{-1}$	-4.21×10^{-1}
		$[4^{+2}, 6^0]$	1.13×10^{-3}	-8.43×10^{-2}		-6.37×10^{-2}	2.18×10^0		1.63×10^0		1.81×10^0
		$[4^0, 6^{+2}]$	3.80×10^{-4}	-7.67×10^{-2}	$8.39i \times 10^{-2}$	4.32×10^{-2}	2.40×10^0	$-2.22i \times 10^0$	9.35×10^{-2}	$-2.07i \times 10^0$	-1.88×10^0
		$[4^{-2}, 6^{+4}]$	3.06×10^{-5}	-1.02×10^{-2}	$1.35i \times 10^{-2}$	8.89×10^{-3}	7.79×10^{-1}	$-1.39i \times 10^0$	-1.49×10^0	$1.05i \times 10^0$	4.37×10^{-1}
		$[4^{-4}, 6^{+6}]$	5.55×10^{-7}	-2.60×10^{-4}	$3.68i \times 10^{-4}$	2.60×10^{-4}	3.30×10^{-2}	$-6.62i \times 10^{-2}$	-8.12×10^{-2}	$6.64i \times 10^{-2}$	3.33×10^{-2}
		$[2^{+2}, 8^0]$	-5.22×10^{-6}	5.45×10^{-4}		3.58×10^{-4}	-2.15×10^{-2}		-1.47×10^{-2}		-1.48×10^{-2}
		$[2^0, 8^{+2}]$	-2.96×10^{-6}	6.70×10^{-4}	$-6.53i \times 10^{-4}$	-2.80×10^{-4}	-3.12×10^{-2}	$2.66i \times 10^{-1}$	-2.16×10^{-3}	$2.32i \times 10^{-2}$	1.90×10^{-2}
		$[2^{-2}, 8^{+4}]$	-2.38×10^{-7}	8.51×10^{-5}	$-1.05i \times 10^{-4}$	-6.42×10^{-5}	-7.59×10^{-3}	$1.22i \times 10^{-1}$	1.16×10^{-2}	$-6.87i \times 10^{-3}$	-2.23×10^{-3}
		$[0^0, 10^{+2}]$	1.28×10^{-8}	-3.23×10^{-6}	$2.83i \times 10^{-6}$	9.95×10^{-7}	2.00×10^{-4}	$-1.58i \times 10^{-2}$	1.85×10^{-5}	$-1.28i \times 10^{-4}$	-9.47×10^{-5}

Appendix B

Response of a two-level system to a slowly varying excitation pulse

Consider the free induction decay response of a two-level system after dipole interaction with a pulse of plane-polarized electromagnetic radiation. The Hamiltonian is

$$H = H_0 + V(t), \tag{B.1}$$

where

$$H_0 = \begin{pmatrix} E_a & 0 \\ 0 & E_b \end{pmatrix}, \quad V(t) = -2\mu\mathcal{E}\cos(\omega t).$$

We define the resonant frequency

$$\omega_0 = \frac{E_b - E_a}{\hbar}, \tag{B.2}$$

and the detuning frequency

$$\Delta\omega = \omega_0 - \omega. \tag{B.3}$$

B.0.1 Time dependence of the coherence

We consider the time dependence of the system in the density matrix formalism. The density matrix propagates according to the Liouville-Von Neumann equation,

$$i\hbar\frac{\partial\rho}{\partial t} = [H,\rho]\,. \tag{B.4}$$

We solve (B.4) in the interaction representation, where ρ_I, μ_I, and $V_I(t)$ are defined as

$$\rho_I = e^{iH_0t/\hbar}\rho e^{-iH_0t/\hbar} \tag{B.5}$$

$$\mu_I = e^{iH_0t/\hbar}\mu e^{-iH_0t/\hbar} \tag{B.6}$$

$$V_I(t) = e^{iH_0t/\hbar}V(t)e^{-iH_0t/\hbar} = -2\mu_I\mathcal{E}\cos{(\omega t)}. \tag{B.7}$$

We differentiate (B.5), using the fact that H_0 commutes with itself, to obtain the Liouville-Von Neumann equation written in the interaction picture,

$$\begin{aligned} i\hbar\frac{\partial\rho_I}{\partial t} &= [V_I(t),\rho_I] \\ &= -2\mathcal{E}\cos{(\omega t)}[\mu_I,\rho_I]. \end{aligned} \tag{B.8}$$

The interaction picture dipole moment operator μ_I has the form

$$\begin{aligned} \mu_I &= e^{iH_0t/\hbar}\mu e^{-iH_0t/\hbar} \\ &= \begin{pmatrix} e^{iE_at/\hbar} & 0 \\ 0 & e^{iE_bt/\hbar} \end{pmatrix} \begin{pmatrix} 0 & \mu_{ab} \\ \mu_{ba} & 0 \end{pmatrix} \begin{pmatrix} e^{-iE_at/\hbar} & 0 \\ 0 & e^{-iE_bt/\hbar} \end{pmatrix} \\ &= \begin{pmatrix} 0 & \mu_{ab}e^{-i\omega_0 t} \\ \mu_{ba}e^{i\omega_0 t} & 0 \end{pmatrix}. \end{aligned} \tag{B.9}$$

We have used the fact that the diagonal dipole moment elements of the two states, μ_{aa} and μ_{bb}, average to zero over the macroscopic sample and may be ignored. Therefore, the matrix elements of (B.8) are (after discarding rapidly varying terms)

$$i\hbar\left\langle a\left|\frac{\partial\rho_I}{\partial t}\right|a\right\rangle = -\mathcal{E}\mu_{ab}\rho_{I,ba}e^{-i\Delta\omega t} + \mathcal{E}\mu_{ba}\rho_{I,ab}e^{i\Delta\omega t} \tag{B.10}$$

$$i\hbar\left\langle b\left|\frac{\partial\rho_I}{\partial t}\right|b\right\rangle = -\mathcal{E}\mu_{ba}\rho_{I,ab}e^{i\Delta\omega t} + \mathcal{E}\mu_{ab}\rho_{I,ba}e^{-i\Delta\omega t} \tag{B.11}$$

$$i\hbar\left\langle a\left|\frac{\partial\rho_I}{\partial t}\right|b\right\rangle = \mathcal{E}\mu_{ab}(\rho_{aa} - \rho_{bb})e^{-i\Delta\omega t}. \tag{B.12}$$

B.0.2 Time dependence of the macroscopic polarization

We have worked out the time dependence of the system, so we can turn our attention to the polarization of the system, which is given by

$$\begin{aligned} P &= N\langle\mu\rangle \\ &= N\mathrm{Tr}(\mu\rho) = N\mathrm{Tr}(\mu_I\rho_I) \\ &= N\mathrm{Tr}\left[\begin{pmatrix} 0 & \mu_{ab}e^{-i\omega_0 t} \\ \mu_{ba}e^{i\omega_0 t} & 0 \end{pmatrix}\begin{pmatrix} \rho_{aa} & \rho_{I,ab} \\ \rho_{I,ba} & \rho_{bb} \end{pmatrix}\right] \\ &= N\big(\mu_{ab}\rho_{I,ba}e^{-i\omega_0 t} + \mu_{ba}\rho_{I,ab}e^{i\omega_0 t}\big). \end{aligned} \tag{B.13}$$

The second line is valid because of the invariance of trace under a unitary transformation. It is convenient to know the polarization in the rotating frame of the applied electromagnetic field. That is, we seek an equation for the polarization that is of the form

$$P = (P_r + iP_i)e^{i\omega t} + (P_r - iP_i)e^{-i\omega t}. \tag{B.14}$$

By manipulation of (B.13), we find

$$P_r + iP_i = N\mu_{ba}\rho_{I,ab}e^{i\Delta\omega t} \tag{B.15a}$$

$$P_r - iP_i = N\mu_{ab}\rho_{I,ba}e^{-i\Delta\omega t}. \tag{B.15b}$$

We are now ready to examine the time dependence of P,

$$\begin{aligned}\frac{\partial}{\partial t}\left(P_r + iP_i\right) &= N\mu_{ba}\frac{\partial\rho_{I,ab}}{\partial t}e^{i\Delta\omega t} + (i\Delta\omega)N\mu_{ba}\rho_{I,ab}e^{i\Delta\omega t} \\ i\hbar\frac{\partial}{\partial t}\left(P_r + iP_i\right) &= \mathcal{E}\left|\mu_{ab}\right|^2 N(\rho_{aa} - \rho_{bb}) - (P_r + iP_i)\hbar\Delta\omega \\ &= \mathcal{E}\left|\mu_{ab}\right|^2 \Delta N - (P_r + iP_i)\hbar\Delta\omega. \qquad \text{(B.16)}\end{aligned}$$

In the second line, we have substituted (B.12) for $\partial\rho_{I,ab}/\partial t$ and we have substituted (B.15a) for $\rho_{I,ab}$. In the third line, we have used the fact that the diagonal elements of the density matrix give populations, so $N(\rho_{aa} - \rho_{bb}) = N_a - N_b = \Delta N$ is the difference in number density. We can obtain a third equation for $\partial\Delta N/\partial t$ by taking the difference of equations (B.10) and (B.11),

$$\begin{aligned}i\hbar\frac{\partial}{\partial t}\Delta N &= 2N\mathcal{E}\left(\mu_{ab}\rho_{I,ba}e^{-i\Delta\omega t} + \mu_{ba}\rho_{I,ab}e^{i\Delta\omega t}\right) \\ \frac{\partial}{\partial t}\Delta N &= \frac{4\mathcal{E}}{\hbar}P_i. \qquad \text{(B.17)}\end{aligned}$$

In the second line, (B.15a) and (B.15b) have been substituted for $\rho_{I,ba}$ and $\rho_{I,ab}$ and convenient cancelation of P_r occurs.

We can separate the real and imaginary parts of (B.16) to obtain a set of master equations which can be integrated to obtain the polarization response of a two-level system to electromagnetic radiation,

$$\frac{\partial P_r}{\partial t} + \Delta\omega P_i = 0 \qquad \text{(B.18)}$$

$$\frac{\partial P_i}{\partial t} - \Delta\omega P_r + \frac{|\mu_{ab}|^2\mathcal{E}\Delta N}{\hbar} = 0 \qquad \text{(B.19)}$$

$$\frac{\partial}{\partial t}\Delta N - \frac{4\mathcal{E}}{\hbar}P_i = 0. \qquad \text{(B.20)}$$

These master equations agree with the ones derived by McGurk, Schmalz, and Flygare,[36,57] except that we have left out the phenomenological damping terms that give rise to the T_1 and T_2 decay mechanisms.

Appendix C

Electric field intensity of a free induction decay excited by a chirped pulse

The signal in a chirped-pulse spectrometer is proportional to the electric field radiated by the molecular polarization, which may be obtained by solving the inhomogeneous wave equation,

$$\frac{\partial^2 E}{\partial z^2} = \frac{1}{c^2}\frac{\partial^2 E}{\partial t^2} + \frac{4\pi}{c^2}\frac{\partial^2 P}{\partial t^2}, \tag{C.1}$$

where z is the propagation direction. As shown by McGurk *et al.*,[36,57] if we assume slowly varying envelope functions for the oscillating electric field and polarization,

$$E = 2\left[\mathcal{E}_i \cos(\omega t - kz) + \mathcal{E}_r \sin(\omega t - kz)\right] \tag{C.2}$$

$$P = 2\left[P_r \cos(\omega t - kz) - P_i \sin(\omega t - kz)\right], \tag{C.3}$$

and we assume $l/cT_2 \ll 1$, where l is the length of the sample, then the wave equation may be simplified to give the amplitude of the electric field radiated by the molecular sample,

$$\begin{aligned} E_{\mathrm{FID}} &= \frac{2\pi\omega l}{c} P \\ &= \frac{4\pi^{3/2} l \omega_0 |\mu_{ab}|^2 \mathcal{E} \Delta N_0}{\hbar c \alpha^{1/2}}. \end{aligned} \tag{C.4}$$

As we would expect from absorptivity arguments, the signal is proportional to the length of the sample and the number density, but *not* the area of the irradiated sample. Of course, if the emission from a large irradiated area (A) were focussed onto a smaller detector as is sometimes done in millimeter-wave experiments, the intensity would increase according to $I \propto 1/A$, so the E-field magnitude would increase as $E \propto 1/A^{1/2}$. However, as long as the experiment is in the unsaturated linear fast passage regime ($\mu_{ab}\mathcal{E}/\hbar \ll \alpha$), there will be no net advantage to expanding the microwave/millimeter wave beam to irradiate a larger area of sample. The factor of $A^{1/2}$ gained in focusing the emission onto the detector will be lost when the excitation beam is expanded because the polarization in Eq. (C.4) is also proportional to the electric field of the excitation beam. On the other hand, if there is enough power available to saturate the experiment, the signal can be increased (by $A^{1/2}$) by expanding the microwave beam to irradiate a larger area of sample and focussing the emitted FID onto the detector.

Appendix D

Signal scaling for a thermally equilibrated molecular sample excited by a chirped excitation pulse

For a sample at thermal equilibrium, the quantity ΔN_0 is given by

$$\begin{aligned}\Delta N_0 &= N_b - N_a \\ &= N\left(\frac{N_a}{N}\right)\left(1-\frac{N_b}{N_a}\right) \\ &= \frac{g_a N e^{-E_a/kT}}{Q}\left(1-e^{-\hbar\omega_0/kT}\right),\end{aligned}$$

where Q is the partition function, g_a is the degeneracy of the lower state, and the populations N_a and N_b are assumed to be independent of time in the low power limit. For most rotational spectroscopy experiments, $\hbar\omega_0 \ll kT$, and

$$\left(1-e^{-\hbar\omega_0/kT}\right) \approx \frac{\hbar\omega_0}{kT}.$$

Thus,

$$\Delta N_0 \approx \left(\frac{\hbar\omega_0}{kT}\right)\frac{g_a N e^{-E_a/kT}}{Q}. \tag{D.1}$$

We substitute (D.1) into (C.4) to obtain

$$E_{\mathrm{FID}} = \frac{4\pi^{3/2} l \omega_0^2 |\mu_{ab}|^2 \mathcal{E}}{c\alpha^{1/2}} \left(\frac{g_a N e^{-E_a/kT}}{kTQ} \right), \tag{D.2}$$

which gives the scaling of the signal intensity as a function of temperature.

Appendix E

Term values assigned from the mmODR spectra of Chapter 6

Table E.1 provides a list of term values of assigned rotational levels for the $\tilde{\mathrm{C}}$ state of SO_2 from the mmODR spectra reported in Chapter 6.

Table E.1: Rotational term values (T/cm^{-1}) of the SO_2 $\tilde{C}$-state levels reported in Chapter 6.

$J'_{K'_aK'_c}$	T	$J'_{K'_aK'_c}$	T	$J'_{K'_aK'_c}$	T	$J'_{K'_aK'_c}$	T	$J'_{K'_aK'_c}$	T
Vib. level: $\mathrm{P_{a_1}}$									
$K'_a = 0, f$		$K'_a = 1, f$							
5_{05}	45325.76	5_{14}	45327.76						
7_{07}	45333.78	7_{16}	45335.50						
Vib. level: $\mathrm{P_{b_2}}$									
$K'_a = 1, f$		$K'_a = 2, f$		$K'_a = 3, f$		$K'_a = 0, e$		$K'_a = 3, e$	
1_{11}	45329.51					0_{00}	45328.22	1_{10}	
5_{15}	45336.26	5_{24}	45339.76	5_{33}	45343.06	2_{02}	45329.83	3_{12}	
7_{17}	45342.91	7_{26}	45346.98	7_{35}	45344.01	4_{04}	45333.50	4_{31}	45341.29
9_{19}	45351.77	9_{28}	45356.51	9_{37}	45351.44	6_{06}	45339.18	7_{16}	
						8_{08}	45346.96	9_{18}	
$(v_1, v_2, v_3) = (1, 3, 2)$									
$K'_a = 0, f$		$K'_a = 1, f$		$K'_a = 2, f$		$K'_a = 1, e$		$K'_a = 2, e$	
1_{01}	45336.21	1_{10}	45336.94			2_{12}	45338.46[a]	2_{21}	45340.79
3_{03}	45339.75	3_{12}	45340.52	3_{21}	45343.05	4_{14}	45343.52	4_{23}	45345.98
5_{05}	45346.11	5_{14}	45346.86			6_{16}	45351.12		
7_{07}	45355.05	7_{16}	45355.71					8_{27}	45363.97
9_{09}	45366.46	9_{18}	45368.09						
Vib. level: 46816									
$K'_a = 0, f$		$K'_a = 1, f$		$K'_a = 2, f$		$K'_a = 1, e$		$K'_a = 2, e$	
1_{01}	46816.55	1_{10}	46817.59			2_{12}	46818.05	2_{21}	46821.92
		3_{12}	46820.62	3_{21}	46823.83	4_{14}	46821.39	4_{23}	46826.68
5_{05}	46823.63	5_{14}	46826.02			6_{16}	46815.07		
7_{07}	46829.44	7_{16}	46833.66						
Vib. level: 47569									
$K'_a = 0, f$		$K'_a = 1, f$		$K'_a = 2, f$		$K'_a = 1, e$		$K'_a = 2, e$	
1_{01}	47569.94	1_{10}	47570.82			2_{12}	47571.94	2_{21}	47574.57
		3_{12}	47573.99	3_{21}	47576.44	4_{14}	47575.97	4_{23}	47578.86
5_{05}	47578.31	5_{14}	47579.75	5_{23}	47582.00	6_{16}	47582.27		
7_{07}	47585.93	7_{16}	47587.95						
Vib. level: 47616									
$K'_a = 0, f$		$K'_a = 1, f$		$K'_a = 2, f$		$K'_a = 1, e$		$K'_a = 2, e$	
1_{01}	47616.67	1_{10}	47617.53			2_{12}	47618.64	2_{21}	47621.20
		3_{12}	47620.69	3_{21}	47623.01	4_{14}	47622.73	4_{23}	47625.45
5_{05}	47625.23	5_{14}	47626.40	5_{23}	47628.59	6_{16}	47629.15		
7_{07}	47632.96	7_{16}	47634.47						

---

[a] From Ref. 43, with correction for calibration offset.

Appendix F

Term values of the $\tilde{\mathrm{C}}$ state of SO_2 observed by IR-UV double resonance

Table F.1 summarizes the rotational term values for low-lying vibrational levels of the $\tilde{\mathrm{C}}$ state of SO_2, observed by IR-UV double resonance experiments described in Chapter 7.

Table F.1: Rotational term values (T/cm^{-1}) of the $\tilde{\mathrm{C}}$-state levels observed in by IR-UV double resonance. For brevity, the first two digits are printed only in the first table entry for each vibrational level, and are understood to be appended to the remaining entries.

$J'_{K'_aK'_c}$	T	$J'_{K'_aK'_c}$	T	$J'_{K'_aK'_c}$	T	$J'_{K'_aK'_c}$	T	$J'_{K'_aK'_c}$	T	$J'_{K'_aK'_c}$	T	$J'_{K'_aK'_c}$	T	$J'_{K'_aK'_c}$	T
								(0,0,1)							
$K'_a=0,e$		$K'_a=1,e$		$K'_a=2,e$		$K'_a=3,e$		$K'_a=1,f$		$K'_a=2,f$		$K'_a=3,f$		$K'_a=4,f$	
0_{00}	42786.03							1_{11}	787.44						
2_{02}	787.84	2_{11}	788.80	2_{20}	791.23			3_{13}	790.25	3_{22}	793.05	3_{31}	797.27		
4_{04}	791.99	4_{13}	793.32	4_{22}	795.56	4_{31}	799.72	5_{15}	795.28	5_{24}	798.48	5_{33}	802.74		
6_{06}	798.36	6_{15}	800.35	6_{24}	802.46	6_{33}	806.42	7_{17}	802.53	7_{26}	806.28	7_{35}	810.71	7_{44}	816.54
		8_{17}	809.77												
								(0,1,1)							
$K'_a=0,e$		$K'_a=1,e$		$K'_a=2,e$		$K'_a=3,e$		$K'_a=1,f$		$K'_a=2,f$		$K'_a=3,f$			
0_{00}	43155.61							1_{11}	157.05						
2_{02}	157.49	2_{11}	158.46	2_{20}	160.93			3_{13}	160.00	3_{22}	162.81	3_{31}	167.12		
4_{04}	161.74	4_{13}	163.02	4_{22}	165.32	4_{31}	169.59	5_{15}	165.21	5_{24}	168.33	5_{33}	172.68		
6_{06}	168.32	6_{15}	170.12	6_{24}	172.25	6_{33}	176.40	7_{17}	172.74	7_{26}		7_{35}	180.74		
								(0,0,3)							
$K'_a=0,e$		$K'_a=1,e$		$K'_a=2,e$		$K'_a=3,e$		$K'_a=1,f$		$K'_a=2,f$		$K'_a=3,f$		$K'_a=4,f$	
0_{00}	43464.40							1_{11}	465.78						
2_{02}	466.14	2_{11}	467.14	2_{20}	469.54			3_{13}	468.51	3_{22}	471.32	3_{31}	475.60		
4_{04}	470.20	4_{13}	471.58	4_{22}	473.78	4_{31}	477.93	5_{15}	473.35	5_{24}	476.61	5_{33}	480.94		
6_{06}	476.33	6_{15}	478.45	6_{24}	480.57	6_{33}	484.51	7_{17}	480.31	7_{26}	484.22	7_{35}	488.65	7_{44}	494.59
		8_{17}	487.68												
								(0,2,1)							
$K'_a=0,e$		$K'_a=1,e$		$K'_a=2,e$		$K'_a=3,e$		$K'_a=1,f$		$K'_a=2,f$		$K'_a=3,f$			
0_{00}	43522.58							1_{11}	524.04						
2_{02}	524.46	2_{11}	525.41	2_{20}	527.95			3_{13}	527.09	3_{22}	529.85	3_{31}	534.24		
4_{04}	528.88	4_{13}	530.02	4_{22}	532.42	4_{31}	536.78	5_{15}	532.54	5_{24}	535.59	5_{33}	539.95		
6_{06}	535.69	6_{15}	537.26	6_{24}	539.49	6_{33}	543.79	7_{17}	540.37	7_{26}	543.77	7_{35}	548.21		

Table F.1: (continued)

$J'_{K'_aK'_c}$	T	$J'_{K'_aK'_c}$	T	$J'_{K'_aK'_c}$	T	$J'_{K'_aK'_c}$	T	$J'_{K'_aK'_c}$	T	$J'_{K'_aK'_c}$	T	$J'_{K'_aK'_c}$	T	$J'_{K'_aK'_c}$	T
								(0,1,3)							
$K'_a = 0, e$		$K'_a = 1, e$		$K'_a = 2, e$		$K'_a = 3, e$		$K'_a = 1, f$		$K'_a = 2, f$		$K'_a = 3, f$			
0_{00}	43825.75							1_{11}	827.24						
2_{02}	827.76	2_{11}	828.66	2_{20}	831.05			3_{13}	830.44	3_{22}	833.11	3_{31}	837.13		
4_{04}	832.23	4_{13}	833.36	4_{22}	835.80			5_{15}	836.01	5_{24}	839.06	5_{33}	843.56		
6_{06}	839.19	6_{15}	840.70	6_{24}	843.06			7_{17}	843.88	7_{26}	847.38	7_{35}	852.07		
8_{08}	848.34	8_{17}	850.53	8_{26}	852.85	8_{35}	857.22	9_{19}	853.94	9_{28}	858.01				
								(0,3,1)							
$K'_a = 0, e$		$K'_a = 1, e$		$K'_a = 2, e$		$K'_a = 3, e$		$K'_a = 1, f$		$K'_a = 2, f$		$K'_a = 3, f$			
0_{00}	43886.71							1_{11}	888.22						
2_{02}	888.70	2_{11}	889.60	2_{20}	892.20			3_{13}	891.52	3_{22}	894.27	3_{31}	898.61		
4_{04}	893.36	4_{13}	894.37	4_{22}	896.92	4_{31}	901.33	5_{15}	897.41	5_{24}	900.25	5_{33}	904.70		
6_{06}	900.59	6_{15}	901.80	6_{24}	904.24			7_{17}	905.73	7_{26}	908.80	7_{35}	913.37		
								(1,0,1)							
$K'_a = 0, e$		$K'_a = 1, e$		$K'_a = 2, e$		$K'_a = 3, e$		$K'_a = 4, e$		$K'_a = 1, f$		$K'_a = 2, f$		$K'_a = 3, f$	
0_{00}	43834.76									1_{11}	836.16				
2_{02}	836.55	2_{11}	837.54	2_{20}	839.96					3_{13}	838.93	3_{22}	841.72	3_{31}	846.00
4_{04}	840.62	4_{13}	841.99	4_{22}	844.23	4_{31}	848.37			5_{15}	843.89	5_{24}	847.08	5_{33}	851.41
6_{06}	846.92	6_{15}	848.97	6_{24}	851.08	6_{33}	855.04			7_{17}	850.99	7_{26}	854.79	7_{35}	859.22
8_{08}	855.21	8_{17}	858.30	8_{26}	860.55	8_{35}	864.17	8_{44}	869.98	9_{19}	860.16	9_{28}	864.78		
								(0,0,5)							
$K'_a = 0, e$		$K'_a = 1, e$		$K'_a = 2, e$		$K'_a = 3, e$				$K'_a = 1, f$		$K'_a = 2, f$		$K'_a = 3, f$	
0_{00}	44169.21									1_{11}	170.59				
2_{02}	170.89	2_{11}	171.96	2_{20}	174.36					3_{13}	173.05	3_{22}	176.02	3_{31}	180.29
4_{04}	174.62	4_{13}	176.26	4_{22}	178.38	4_{31}	182.50			5_{15}	177.39	5_{24}	180.94	5_{33}	185.47
6_{06}	180.08	6_{15}	182.88	6_{24}	184.91	6_{33}	188.59			7_{17}	183.49	7_{26}	187.96	7_{35}	192.70
		8_{17}	191.56												
								(0,0,4)							
$K'_a = 1, e$		$K'_a = 2, e$		$K'_a = 3, e$		$K'_a = 0, f$		$K'_a = 1, f$		$K'_a = 2, f$		$K'_a = 3, f$		$K'_a = 4, f$	
2_{12}	43821.13	2_{21}	823.96			1_{01}	819.45[a]	1_{10}	820.39[a]						
4_{14}	824.40	4_{23}	827.71	4_{32}	831.95	3_{03}	822.07	3_{12}	823.46[a]	3_{21}	825.66	3_{30}	829.85		
6_{16}	829.49	6_{25}	833.55	6_{34}	837.93	5_{05}	826.50	5_{14}	828.85	5_{23}	830.94	5_{32}	834.71	5_{41}	840.42
8_{18}	836.54	8_{27}	841.49	8_{36}		7_{07}	832.70	7_{16}	836.41	7_{25}	838.88	7_{34}	842.15	7_{43}	847.47
						9_{09}	840.78	9_{18}	845.91			9_{36}	852.32		

---

[a] Ref. 43.

Bibliography

[1] Frank C. De Lucia. The submillimeter: A spectroscopist's view. *Journal of Molecular Spectroscopy*, 261:1–17, 2010.

[2] John Brown and Alan Carrington. *Rotational Spectroscopy of Diatomic Molecules*. Cambridge Molecular Science Series. Cambridge University Press, 2003.

[3] Walter Gordy and Robert L. Cook. *Microwave Molecular Spectra*. John Wiley and Sons, 1984.

[4] Thomas R. Gentile, Barbara J. Hughey, Daniel Kleppner, and Theodore W. Ducas. Microwave spectroscopy of calcium Rydberg states. *Physical Review A*, 42(1):440–451, 1990.

[5] A. Ganesh Vaidyanathan, William P. Spencer, Jan R. Rubbmark, Hajo Kuiper, Claude Fabre, and Daniel Kleppner. Experimental study of nonadiabatic core interactions in Rydberg states of calcium. *Physical Review A*, 26(6):3346–3350, 1982.

[6] F. Merkt and A. Osterwalder. Millimetre wave spectroscopy of high Rydberg states. *International Reviews in Physical Chemistry*, 21(3):385–403, 2002.

[7] A. Osterwalder, A. Wüest, and F. Merkt. High-resolution millimeter wave spectroscopy and multichannel quantum defect theory of the hyperfine structure in high Rydberg states of molecular hydrogen H_2. *The Journal of Chemical Physics*, 121(23):11810–11838, 2004.

[8] Jianing Han, Yasir Jamil, D. V. L. Norum, Paul J. Tanner, and T. F. Gallagher. Rb nf quantum defects from millimeter-wave spectroscopy of cold ^{85}Rb Rydberg atoms. *Physical Review A*, 74(5):054502, 2006.

[9] Kirill Prozument, Anthony Colombo, Yan Zhou, G. Barratt Park, Vladimir Petrović, Stephen Coy, and Robert Field. Chirped-pulse millimeter-wave spectroscopy of Rydberg-Rydberg transitions. *Physical Review Letters*, 107:143001, Sep 2011.

[10] Branko Leskovar and William F. Kolbe. Detection and measurements of air pollutants and constituents by millimeter-wave microwave spectroscopy. *IEEE Transactions on Nuclear Science*, 26(1):780–790, Feb. 1979.

[11] W. F. Kolbe, W. D. Zollner, and B. Lescovar. 140 GHz microwave spectrometer for the detection of gaseous chemical species. *International Journal of Infrared and Millimeter Waves*, 4(5):733–749, 1983.

[12] B. S. Dumesh, V. D. Gorbatenkov, V. G. Koloshnikov, V. A. Panfilov, and L. A. Surin. Application of highly sensitive millimeter-wave cavity spectrometer based on orotron for gas analysis. *Spectrochimica Acta. Part A: Molecular Spectroscopy*, 53:835, 1997.

[13] Jean Demaison, Kamil Sarka, and Edward A. Cohen, editors. *Spectroscopy From Space*, volume 20 of *NATO Science Series: II. Mathematics, Physics and Chemistry.* Kluwer Academic Publishers, 2000.

[14] F Wolf. Fast sweep experiments in microwave spectroscopy. *Journal of Physics D: Applied Physics*, 27(8):1774, 1994.

[15] Douglas T. Petkie, Thomas M. Goyette, Ryan P. A. Bettens, S. P. Belov, Sieghard Albert, Paul Helminger, and Frank C. De Lucia. A fast scan submillimeter spectroscopic technique. *Review of Scientific Instruments*, 68(4):1675–1683, 1997.

[16] Sieghard Albert, Douglas T. Petkie, Ryan P. A. Bettens, Sergei P. Belov, and Frank C. De Lucia. FASSST: A new gas-phase analytical tool. *Analytical Chemistry News and Features*, 70(21):719A–727A, 1998.

[17] Ivan Medvedev, Manfred Winnewisser, Frank C. De Lucia, Eric Herbst, Ewa Bialkowska-Jaworska, Lech Pszczólkowski, and Zbigniew Kisiel. The millimeter- and submillimeter-wave spectrum of the *trans–gauche* conformer of diethyl ether. *Journal of Molecular Spectroscopy*, 228(2):314–328, 2004. Special Issue Dedicated to Dr. Jon T. Hougen on the Occasion of His 68th Birthday.

[18] Ivan R. Medvedev, Markus Behnke, and Frank C. De Lucia. Fast analysis of gases in the submillimeter/terahertz with “absolute” specificity. *Applied Physics Letters*, 86(15):154105, 2005.

[19] B. A. McElmurry, R. R. Lucchese, J. W. Bevan, I. I. Leonov, S. P. Belov, and A. C. Legon. Studies of Ar:HBr using fast scan submillimeter-wave and microwave coaxial pulsed jet spectrometers with sub-kHz precision. *The Journal of Chemical Physics*, 119(20):10687–10695, 2003.

[20] S. P. Belov, B. A. McElmurry, R. R. Lucchese, J. W. Bevan, and I. Leonov. Testing the morphed potential of Ar:HBr using frequency and phase stabilized FASSST with a supersonic jet. *Chemical Physics Letters*, 370(3–4):528–534, 2003.

[21] Ralph M. Somers, T. O. Poehler, and P. E. Wagner. Microwave time domain Fabry-Perot emission spectrometer. *Review of Scientific Instruments*, 46(6):719–725, 1975.

[22] T. J. Balle, E. J. Campbell, M. R. Keenan, and W. H. Flygare. A new method for observing the rotational spectra of weak molecular complexes: KrHCl. *The Journal of Chemical Physics*, 71(6):2723–2724, 1979.

[23] T. J. Balle and W. H. Flygare. Fabry–Perot cavity pulsed Fourier transform microwave spectrometer with a pulsed nozzle particle source. *Review of Scientific Instruments*, 52(1):33–45, 1981.

[24] E. J. Campbell, L. W. Buxton, T. J. Balle, and W. H. Flygare. The theory of pulsed Fourier transform microwave spectroscopy carried out in a Fabry–Perot cavity: Static gas. *The Journal of Chemical Physics*, 74(2):813–828, 1981.

[25] Jens-Uwe Grabow, E. Samuel Palmer, Michael C. McCarthy, and Patrick Thaddeus. Supersonic-jet cryogenic-resonator coaxially oriented beam-resonator arrangement Fourier transform microwave spectrometer. *Review of Scientific Instruments*, 76(9):093106, 2005.

[26] W. F. Kolbe and B. Leskovar. 140-GHz pulsed Fourier transform microwave spectrometer. *Review of Scientific Instruments*, 56(1):97–102, 1985.

[27] W. F. Kolbe and B. Leskovar. Pulsed millimeter wave Fourier transform microwave spectrometer. *International Journal of Infrared and Millimeter Waves*, 7:1329–1338, 1986.

[28] D. Boucher, R. Bocquet, D. Petitprez, and L. Aime. Molecular beam millimeter sidebands fourier transform spectrometer (MB-MMSBFT). *International Journal of Infrared and Millimeter Waves*, 15(9):1481, 1994.

[29] Hideta Habara, Satoshi Yamamoto, Christian Ochsenfeld, Martin Head-Gordon, Ralf I. Kaiser, and Yuan T. Lee. Fourier transform millimeter-wave spectroscopy of the HCS radical in the $^2A'$ ground electronic state. *The Journal of Chemical Physics*, 108(21):8859–8863, 1998.

[30] Satoshi Yamamoto, Hideta Habara, Eunsook Kim, and Hiroyuki Nagasaka. Fourier transform millimeter-wave spectroscopy of chlorocarbene (HCCl). *The Journal of Chemical Physics*, 115(13):6007–6011, 2001.

[31] G. S. Grubbs II, C. T. Dewberry, and S. A. Cooke. A Fabry-Perot cavity pulsed Fourier transform W-band spectrometer with a pulsed nozzle source. 62nd Ohio State University International Symposium on Molecular Spectroscopy, 2008.

[32] G. G. Brown, B. C. Dian, K. O. Douglass, S. M. Geyer, S. T. Shipman, and B. H. Pate. A broadband Fourier transform microwave spectrometer based on microwave chirped pulse excitation. *Review of Scientific Instruments*, 79:053103, 2008.

[33] Gordon G. Brown, Brian C. Dian, Kevin O. Douglass, Scott M. Geyer, and Brooks H. Pate. The rotational spectrum of epifluorohydrin measured by

chirped-pulse Fourier transform microwave spectroscopy. *Journal of Molecular Spectroscopy*, 238(2):200–212, 2006.

[34] Brian C. Dian, Gordon G. Brown, Kevin O. Douglass, and Brooks H. Pate. Measuring picosecond isomerization kinetics via broadband microwave spectroscopy. *Science*, 320(5878):924–928, 2008.

[35] Brooks H. Pate. personal communication, 2011.

[36] J. C. McGurk, T. G. Schmalz, and W. H. Flygare. Fast passage in rotational spectroscopy: Theory and experiment. *The Journal of Chemical Physics*, 60:4181–4188, 1974.

[37] L. Allen and J. H. Eberly. *Optical Resonance and Two-Level Atoms.* John Wiley and Sons, Inc., New York, 1975.

[38] Hans A. Bechtel, Adam H. Steeves, , and Robert W. Field. Laboratory measurements of the hyperfine structure of $H^{14}N^{12}C$ and $D^{14}N^{12}C$. *The Astrophysical Journal Letters*, 649(1):L53–L56, 2006.

[39] S. G. Kukolich, D. J. Ruben, J. H. S. Wang, and J. R. Williams. High resolution measurements of ^{14}N, D quadrupole coupling in CH_3CN and CD_3CN. *The Journal of Chemical Physics*, 58(8):3155–3159, 1973.

[40] D. Boucher, J. Burie, A. Bauer, A. Dubrulle, and J. Demaison. Microwave spectra of molecules of astrophysical interest. XIX. Methyl cyanide. *Journal of Physical and Chemical Reference Data*, 9(3):659–720, 1980.

[41] H. A. Bechtel, A. H. Steeves, B. M. Wong, and R. W. Field. Evolution of chemical bonding during HCN/HNC isomerization as revealed through nuclear quadrupole hyperfine structure. *Angewandte Chemie International Edition*, 47(16):2969–2972, 2008.

[42] Masakazu Nakajima, Yoshihiro Sumiyoshi, and Yasuki Endo. Development of microwave-optical double-resonance spectroscopy using a Fourier-transform microwave spectrometer and a pulsed laser. *Review of Scientific Instruments*, 73(1):165–171, 2002.

[43] Kaoru Yamanouchi, Misaki Okunishi, Yasuki Endo, and Soji Tsuchiya. Laser induced fluorescence spectroscopy of the $\tilde{C}\ ^1B_2$—$\tilde{X}\ ^1A_1$ band of jet-cooled SO_2: rotational and vibrational analyses in the 235–210 nm region. *Journal of Molecular Structure*, 352/353:541–559, 1995. Molecular Structure and Spectroscopy.

[44] Adam H. Steeves, Hans A. Bechtel, Stephen L. Coy, and Robert W. Field. Millimeter-wave-detected, millimeter-wave optical polarization spectroscopy. *The Journal of Chemical Physics*, 123(14):141102, 2005.

[45] Lorene A. Samoska, Todd C. Gaier, Alejandro Peralta, Sander Weinreb, Jean Bruston, Imran Mehdi, Yaochung Chen, Hsin H. Liao, Matt Nishimoto, Richard Lai, Huei Wang, and Y. C. Leong. MMIC power amplifiers as local oscillator drivers for FIRST. *Proceedings of SPIE*, 4013(1):275–284, 2000.

[46] Th. de Graauw, N. Whyborn, E. Caux, T. Phillips, J. Stutzki, A. Tielens, T. Güsten, F. Helmich, W. Luinge, J. Martin-Pintado, J. Pearson, P. Planesas, P. Roelfsema, P. Saraceno, R. Schieder, K. Wildeman, and K. Wafelbakker. The Herschel-Heterodyne Instrument for the Far-Infrared (HIFI). In L. Pagani and M. Gerin, editors, *Astronomy in the submillimeter and far infrared domains with the Herschel space observatory*, volume 34 of *EAS Publication Series*, pages 3–20. European Astronomical Society, EDP Sciences, 2009.

[47] Cristóbal Pérez, Matt T. Muckle, Daniel P. Zaleski, Nathan A. Seifert, Berhane Temelso, George C. Shields, Zbigniew Kisiel, and Brooks H. Pate. Structures of cage, prism, and book isomers of water hexamer from broadband rotational spectroscopy. *Science*, 336(6083):897–901, 2012.

[48] Kirill Prozument, G. Barratt Park, Rachel G. Shaver, AnGayle K. Vasiliou, James M. Oldham, Donald E. David, John S. Muenter, John F. Stanton, Arthur G. Suits, G. Barney Ellison, and Robert W. Field. Chirped-pulse millimeter-wave spectroscopy for dynamics and kinetics studies of pyrolysis reactions. *Physical Chemistry Chemical Physics*, 16:15739–15751, 2014.

[49] James M. Oldham, Chamara Abeysekera, Baptiste Joalland, Lindsay N. Zack, Kirill Prozument, Ian R. Sims, G. Barratt Park, Robert W. Field, and Arthur G. Suits. A chirped-pulse Fourier-transform microwave/pulsed uniform flow spectrometer. I. The low-temperature flow system. *The Journal of Chemical Physics*, 141(15):154202, 2014.

[50] Chamara Abeysekera, Lindsay N. Zack, G. Barratt Park, Baptiste Joalland, James M. Oldham, Kirill Prozument, Nuwandi M. Ariyasingha, Ian R. Sims, Robert W. Field, and Arthur G. Suits. A chirped-pulse Fourier-transform microwave/pulsed uniform flow spectrometer. II. Performance and applications for reaction dynamics. *The Journal of Chemical Physics*, 141(21):214203, 2014.

[51] G. Barratt Park, Adam H. Steeves, Kirill Kuyanov-Prozument, Justin L. Neill, and Robert W. Field. Design and evaluation of a pulsed-jet chirped-pulse millimeter-wave spectrometer for the 70–102 GHz region. *The Journal of Chemical Physics*, 135(2):024202, 2011.

[52] Amanda L. Steber, Brent J. Harris, Justin L. Neill, and Brooks H. Pate. An arbitrary waveform generator based chirped pulse Fourier transform spectrometer operating from 260 to 295 GHz. *Journal of Molecular Spectroscopy*, 280(0):3–10, 2012.

[53] Justin L. Neill, Brent J. Harris, Amanda L. Steber, Kevin O. Douglass, David F. Plusquellic, and Brooks H. Pate. Segmented chirped-pulse Fourier transform submillimeter spectroscopy for broadband gas analysis. *Optics Express*, 21(17):19743–19749, Aug 2013.

[54] Anthony P. Colombo, Yan Zhou, Kirill Prozument, Stephen L. Coy, and Robert W. Field. Chirped-pulse millimeter-wave spectroscopy: Spectrum, dynamics, and manipulation of rydberg–rydberg transitions. *The Journal of Chemical Physics*, 138(1):014301, 2013.

[55] David Schmitz, V. Alvin Shubert, Thomas Betz, and Melanie Schnell. Multi-resonance effects within a single chirp in broadband rotational spectroscopy: The rapid adiabatic passage regime for benzonitrile. *Journal of Molecular Spectroscopy*, 280(0):77–84, 2012. Broadband Rotational Spectroscopy.

[56] V. V. Khodos, D. A. Ryndyk, and V. L. Vaks. Fast-passage microwave molecular spectroscopy with frequency sweeping. *The European Physical Journal: Applied Physics*, 25(3):203–208, 2004.

[57] J. C. McGurk, T. G. Schmalz, and W. H. Flygare. *Advances in Chemical Physics*, volume 25, chapter 1. Academic, New York, 1974.

[58] Jens-Uwe Grabow. Fourier transform microwave spectroscopy measurement and instrumentation. In Martin Quack and Frédéric Merkt, editors, *Handbook of High-Resolution Spectroscopy*, volume 2, pages 723–799. Wiley, 2011.

[59] G. W. King and C. K. Ingold. The bent excited state of acetylene. *Nature*, 169(4313):1101–1102, June 1952.

[60] C. K. Ingold and G. W. King. Excited states of acetylene. *Journal of the Chemical Society*, 1953:2702–2755, 1953.

[61] K. Keith Innes. Analysis of the near ultraviolet absorption spectrum of acetylene. *The Journal of Chemical Physics*, 22(5):863–876, 1954.

[62] E. K. Plyler, E. D. Tidwell, and T. A. Wiggins. Rotation-vibration constants of acetylene. *Journal of the Optical Society of America*, 53:589–593, 1963.

[63] Josef Plíva. Spectrum of acetylene in the 5-micron region. *Journal of Molecular Spectroscopy*, 44(1):145–164, 1972.

[64] Kent F. Palmer, Michael E. Mickelson, and K. Narahari Rao. Investigations of several infrared bands of $^{12}C_2H_2$ and studies of the effects of vibrational rotational interactions. *Journal of Molecular Spectroscopy*, 44(1):131–144, 1972.

[65] A. Baldacci, S. Ghersetti, and K. Narahari Rao. Interpretation of the acetylene spectrum at 1.5 μm. *Journal of Molecular Spectroscopy*, 68(2):183–194, 1977.

[66] Agostino Baldacci, Sergio Ghersetti, and K. Narahari Rao. Assignments of the $^{12}C_2H_2$ bands at 2.1–2.2μ. *Journal of Molecular Spectroscopy*, 41(1):222–225, 1972.

[67] L.N. Sinitsa. The C_2H_2 absorption spectrum in the Nd laser range. *Journal of Molecular Spectroscopy*, 84(1):57–59, 1980.

[68] Brian C. Smith and John S. Winn. The C–H overtone spectra of acetylene: Bend/stretch interactions below 10000 cm^{-1}. *The Journal of Chemical Physics*, 89(8):4638–4645, 1988.

[69] J. K. G. Watson, M. Herman, J. C. Van Craen, and R. Colin. The Ã–X̃ band system of acetylene: Analysis of long-wavelength bands, and vibration-rotation constants for the levels $n\nu_4''$ ($n = 0$–4), $n\nu_3'$ ($n = 0$–3), and $\nu_2' + n\nu_3'$ ($n = 0$–2). *Journal of Molecular Spectroscopy*, 95(1):101–132, 1982.

[70] J. C. Van Craen, M. Herman, R. Colin, and J. K. G. Watson. The Ã–X̃ band system of acetylene: Analysis of medium-wavelength bands, and vibration-rotation constants for the levels $n\nu_3'$ ($n = 4$–6), $\nu_2' + n\nu_3'$ ($n = 3$–5), and $\nu_1' + n\nu_3'$ ($n = 2$, 3). *Journal of Molecular Spectroscopy*, 111(1):185–197, 1985.

[71] J. C. Van Craen, M. Herman, R. Colin, and J. K. G. Watson. The Ã–X̃ band system of acetylene: Bands of the short-wavelength region. *Journal of Molecular Spectroscopy*, 119(1):137–143, 1986.

[72] M. Herman, T. R. Huet, and M. Vervloet. Spectroscopy and vibrational couplings in the $3\nu_3$ region of acetylene. *Molecular Physics*, 66(2):333–353, 1989.

[73] W. J. Lafferty and A. S. Pine. Spectroscopic constants for the 2.5 and 3.0 μm bands of acetylene. *Journal of Molecular Spectroscopy*, 141(2):223–230, 1990.

[74] Romola D'Cunha, Y. A. Sarma, G. Guelachvili, R. Farrenq, Qingli Kou, V. Malathy Devi, D. Chris Benner, and K. Narahari Rao. Analysis of the high-resolution spectrum of acetylene in the 2.4 μm region. *Journal of Molecular Spectroscopy*, 148(1):213–225, 1991.

[75] A.-M. Tolonen and S. Alanko. Investigations on the infrared spectrum of acetylene between 2500 cm^{-1} and 2800 cm^{-1} and studies of the resonance effects. *Molecular Physics*, 75(5):1155–1165, 1992.

[76] Y. Kabbadj, M. Herman, G. Di Lonardo, L. Fusina, and J. W. C. Johns. The bending energy levels of C_2H_2. *Journal of Molecular Spectroscopy*, 150(2):535–565, 1991.

[77] J. Vanderauwera, D. Hurtmans, M. Carleer, and M. Herman. The ν_3 fundamental in C_2H_2. *Journal of Molecular Spectroscopy*, 157(2):337–357, 1993.

[78] Q. Kou, G. Guelachvili, M. Abbouti Temsamani, and M. Herman. The absorption spectrum of C_2H_2 around $\nu_1 + \nu_3$: energy standards in the 1.5 μm region and vibrational clustering. *Canadian Journal of Physics*, 72(11–12):1241–1250, 1994.

[79] Mohammed Abbouti Temsamani and Michel Herman. The vibrational energy levels in acetylene $^{12}C_2H_2$: Towards a regular pattern at higher energies. *The Journal of Chemical Physics*, 102(16):6371–6384, 1995.

[80] Stephani Ann B. Solina, Jonathan P. O'Brien, Robert W. Field, and William F. Polik. Dispersed fluorescence spectrum of acetylene from the $\tilde{A}\ ^1A_u$ origin: Recognition of polyads and test of multiresonant effective Hamiltonian model for the $\tilde{X}$ state. *The Journal of Physical Chemistry*, 100(19):7797–7809, 1996.

[81] Mohammed Abbouti Temsamani, Michel Herman, Stephani A. B. Solina, Jonathan P. O'Brien, and Robert W. Field. Highly vibrationally excited $^{12}C_2H_2$ in the $\tilde{X}\ ^1\Sigma_g^+$ state: Complementarity of absorption and dispersed fluorescence spectra. *The Journal of Chemical Physics*, 105(24):11357–11359, 1996.

[82] Matthew P. Jacobson, Jonathan P. O'Brien, Robert J. Silbey, and Robert W. Field. Pure bending dynamics in the acetylene $\tilde{X}\ ^1\Sigma_g^+$ state up to 15000 cm^{-1} of internal energy. *The Journal of Chemical Physics*, 109(1):121–133, 1998.

[83] Matthew P. Jacobson, Christof Jung, Howard S. Taylor, and Robert W. Field. State-by-state assignment of the bending spectrum of acetylene at 15 000 cm^{-1}: A case study of quantum-classical correspondence. *The Journal of Chemical Physics*, 111(2):600–618, 1999.

[84] M. I. El Idrissi, J. Liévin, A. Campargue, and M. Herman. The vibrational energy pattern in acetylene (IV): Updated global vibration constants for $^{12}C_2H_2$. *The Journal of Chemical Physics*, 110(4):2074–2086, 1999.

[85] Matthew P. Jacobson and Robert W. Field. Acetylene at the threshold of isomerization. *The Journal of Physical Chemistry A*, 104(14):3073–3086, 03 2000.

[86] Kennosuke Hoshina, Atsushi Iwasaki, Kaoru Yamanouchi, Matthew P. Jacobson, and Robert W. Field. The infrared-ultraviolet dispersed fluorescence spectrum of acetylene: New classes of bright states. *The Journal of Chemical Physics*, 114(17):7424–7442, 2001.

[87] M. Herman, A. Campargue, M. I. El Idrissi, and J. Vander Auwera. Vibrational spectroscopic database on acetylene, $\tilde{X}\ ^1\Sigma_g^+$ ($^{12}C_2H_2$, $^{12}C_2D_2$, and $^{13}C_2H_2$). *Journal of Physical and Chemical Reference Data*, 32(3):921–1361, 2003.

[88] J. D. Tobiason, A. L. Utz, and F. F. Crim. The direct observation, assignment, and partial deperturbation of ν_5 and $\nu_3 + \nu_5$ in $\tilde{A}\ ^1A_u$ acetylene (C_2H_2). *The Journal of Chemical Physics*, 99(2):928–936, 1993.

[89] A. L. Utz, J. D. Tobiason, E. Carrasquillo M., L. J. Sanders, and F. F. Crim. The direct observation, assignment, and partial deperturbation of the ν_4 and ν_6 vibrational fundamentals in $\tilde{\mathrm{A}}\ {}^1\mathrm{A}_u$ acetylene ($\mathrm{C_2H_2}$). *The Journal of Chemical Physics*, 98(4):2742–2753, 1993.

[90] Miwako Mizoguchi, Nami Yamakita, Soji Tsuchiya, Atsushi Iwasaki, Kennosuke Hoshina, and Kaoru Yamanouchi. IR-UV double resonance spectroscopy of acetylene in the $\tilde{\mathrm{A}}\ {}^1\mathrm{A}_u$ $n\nu_3' + \nu_4'$ and $n\nu_3' + \nu_6'$ $(n = 2, 3)$ *ungerade* vibrational states. *The Journal of Physical Chemistry A*, 104(45):10212–10219, 2000.

[91] Anthony J. Merer, Nami Yamakita, Soji Tsuchiya, John F. Stanton, Zicheng Duan, and Robert W. Field. New vibrational assignments in the $\tilde{\mathrm{A}}\ {}^1\mathrm{A}_u$–$\tilde{\mathrm{X}}\ {}^1\Sigma_g^+$ electronic transition of acetylene, $\mathrm{C_2H_2}$: the ν_1' frequency. *Molecular Physics*, 101(4-5):663–673, 2003.

[92] A. H. Steeves, A. J. Merer, H. A. Bechtel, A. R. Beck, and R. W. Field. Direct observation of the symmetric stretching modes of $\tilde{\mathrm{A}}\ {}^1\mathrm{A}_u$ acetylene by pulsed supersonic jet laser induced fluorescence. *Molecular Physics*, 106(15):1867–1877, 2008.

[93] Anthony J. Merer, Nami Yamakita, Soji Tsuchiya, Adam H. Steeves, Hans A. Bechtel, and Robert W. Field. Darling–Dennison resonance and Coriolis coupling in the bending overtones of the $\tilde{\mathrm{A}}\ {}^1\mathrm{A}_u$ state of acetylene, $\mathrm{C_2H_2}$. *The Journal of Chemical Physics*, 129(5):054304, 2008.

[94] Adam H. Steeves, Hans A. Bechtel, Anthony J. Merer, Nami Yamakita, Soji Tsuchiya, and Robert W. Field. Stretch-bend combination polyads in the $\tilde{\mathrm{A}}\ {}^1\mathrm{A}_u$ state of acetylene, $\mathrm{C_2H_2}$. *Journal of Molecular Spectroscopy*, 256(2):256–278, 2009.

[95] Anthony J. Merer, Adam H. Steeves, Joshua H. Baraban, Hans A. Bechtel, and Robert W. Field. Cis-trans isomerization in the $\mathrm{S_1}$ state of acetylene: Identification of cis-well vibrational levels. *The Journal of Chemical Physics*, 134(24):244310, 2011.

[96] F. Duschinsky. *Acta Physicochimica URSS*, 7:551–556, 1937.

[97] B. A. Mamedov, H. Koc, and N Sunel. Unified treatment of Franck-Condon factors over harmonic oscillator wave function using binomial expansion theorems. *Journal of Molecular Structure*, 1048:301–307, 2013.

[98] T. E. Sharp and H. M. Rosenstock. Franck-Condon factors for polyatomic molecules. *The Journal of Chemical Physics*, 41(11):3453–3463, 1964.

[99] W. L. Smith and P. A. Warsop. Franck-Condon principle and large change of shape in polyatomic molecules. *Transactions of the Faraday Society*, 64:1165–1173, 1968.

[100] M. A. Kovner, A. V. Gorokhov, G. A. Gerasimov, and E. N. Bazarov. Calculation of the Franck-Condon integrals for a triatomic molecule. The $^1B_2 \rightarrow^1 \Sigma_g^+$ transition in the CO_2 molecule. *Optics and Spectroscopy*, 29(4):356–359, 1970.

[101] T. Müller, P. Dupre, P.H. Vaccaro, F. Pérez-Bernal, M. Ibrahim, and F. Iachello. Algebraic approach for the calculation of polyatomic Franck–Condon factors.: Application to the vibronically resolved emission spectrum of S_2O. *Chemical Physics Letters*, 292(3):243–253, 1998.

[102] H. Ishikawa, H. Toyosaki, N. Mikami, F. Pérez-Bernal, P.H. Vaccaro, and F. Iachello. Algebraic analysis of bent-from-linear transition intensities: The vibronically resolved emission spectrum of methinophosphide (HCP). *Chemical Physics Letters*, 365(1–2):57–68, 2002.

[103] Isao Kanesaka and Kiyoyasu Kawai. The Franck-Condon factor of a polyatomic molecule. Its method and application to acetylene and dideuteroacetylene. *Bulletin of the Chemical Society of Japan*, 48(10):2745–2750, 1975.

[104] James K.G Watson. Calculated vibrational intensities in the $\tilde{\mathrm{A}}$–$\tilde{\mathrm{X}}$ electronic transition of acetylene. *Journal of Molecular Spectroscopy*, 207(2):276–284, 2001.

[105] Johannes Weber and Georg Hohlneicher. Franck-Condon factors for polyatomic molecules. *Molecular Physics*, 101(13):2125–2144, 2003.

[106] J. T. Hougen and J. K. G. Watson. Anomalous rotational line intensities in electronic transitions of polyatomic molecules: Axis-switching. *Canadian Journal of Physics*, 43:298–320, 1965.

[107] J. H. Baraban, A. R. Beck, A. H. Steeves, J. F. Stanton, and R. W. Field. Reduced dimension discrete variable representation study of cis–trans isomerization in the S_1 state of C_2H_2. *The Journal of Chemical Physics*, 134(24):244311, 2011.

[108] Joshua H. Baraban. Personal communication. 2014.

[109] D. M. Jonas, S. A. B. Solina, B. Rajaram, R. J. Silbey, R. W. Field, K. Yamanouchi, and S. Tsuchiya. Intramolecular vibrational relaxation and forbidden transitions in the SEP spectrum of acetylene. *The Journal of Chemical Physics*, 97(4):2813–2816, 1992.

[110] İlker Özkan. Franck-Condon principle for polyatomic molecules: Axis-switching effects and transformations of normal coordinates. *Journal of Molecular Spectroscopy*, 139(1):147–162, 1990.

[111] E. Bright Wilson, J. C. Decius, and Paul C. Cross. *Molecular Vibrations: The Theory of Infrared and Raman Vibrational Spectra.* McGraw-Hill, New York, 1955.

[112] A. R. Hoy, I. M. Mills, and G. Strey. Anharmonic force constant calculations. *Molecular Physics*, 24(6):1265, 1972.

[113] Raffaele Borrelli and Andrea Peluso. The vibrational progressions of the $N \to V$ electronic transition of ethylene: A test case for the computation of Franck-Condon factors of highly flexible photoexcited molecules. *The Journal of Chemical Physics*, 125(19):194308, 2006.

[114] Raffaele Borrelli and Andrea Peluso. Erratum: "The vibrational progressions of the $N \to V$ electronic transition of ethylene: A test case for the computation of Franck-Condon factors of highly flexible photoexcited molecules" [J. Chem. Phys. 125, 194308 (2006)]. *The Journal of Chemical Physics*, 139(15):159902, 2013.

[115] Jeffrey R. Reimers. A practical method for the use of curvilinear coordinates in calculations of normal-mode-projected displacements and Duschinsky rotation matrices for large molecules. *The Journal of Chemical Physics*, 115(20):9103–9109, 2001.

[116] Amedeo Capobianco, Raffaele Borrelli, Canio Noce, and Andrea Peluso. Franck-Condon factors in curvilinear coordinates: the photoelectron spectrum of ammonia. *Theoretical Chemistry Accounts*, 131(3):1181, 2012.

[117] Raffaele Borrelli, Amedeo Capobianco, and Andrea Peluso. Franck-Condon factors—Computational approaches and recent developments. *Canadian Journal of Chemistry*, 91(7):495–504, 2013.

[118] R. Botter, V. H. Dibeler, J. A. Walker, and H. M. Rosenstock. Experimental and theoretical studies of photoionization-efficiency curves for C_2H_2 and C_2D_2. *The Journal of Chemical Physics*, 44:1271–1278, 1966.

[119] J. K. G. Watson. Vibration-rotation Hamiltonians of linear molecules. *Molecular Physics*, 79(5):943–951, 1993.

[120] David M. Jonas, Xueming Yang, and Alec M. Wodtke. Axis-switching transitions and the stimulated emission pumping spectrum of HCN. *The Journal of Chemical Physics*, 97(4):2284–2298, 1992.

[121] Claude Cohen-Tannoudji, Bernard Diu, and Franck Laloë. *Quantum Mechanics*. Hermann, Paris, France, 1977.

[122] Jun Jiang, Joshua H. Baraban, G. Barratt Park, Michelle L. Clark, and Robert W. Field. Laser-induced fluorescence study of the S_1 state of doubly-substituted ^{13}C acetylene and harmonic force field determination. *The Journal of Physical Chemistry A*, 117(50):13696–13703, 2013.

[123] L. Halonen, M. S. Child, and S. Carter. Potential models and local mode vibrational eigenvalue calculations for acetylene. *Molecular Physics*, 47(5):1097–1112, 1982.

[124] J. D. Tobiason, A. L. Utz, E. L. Sibert, and F. F. Crim. Normal modes analysis of $\tilde{\mathrm{A}}$-state acetylene based on directly observed fundamental vibrations. *The Journal of Chemical Physics*, 99(8):5762–5767, 1993.

[125] Matthew P. Jacobson, Jonathan P. O'Brien, and Robert W. Field. Anomalously slow intramolecular vibrational redistribution in the acetylene $\tilde{\mathrm{X}}\ {}^1\Sigma_g^+$ state above 10000 cm^{-1} of internal energy. *The Journal of Chemical Physics*, 109(10):3831–3840, 1998.

[126] Joshua H. Baraban, P. Bryan Changala, Anthony J. Merer, Adam H. Steeves, Hans A. Bechtel, and Robert W. Field. The $\tilde{\mathrm{A}}\ {}^1\mathrm{A}_u$ state of acetylene: ungerade vibrational levels in the region 45,800–46,550 cm^{-1}. *Molecular Physics*, 110(21–22):2707–2723, 2012.

[127] Joshua H. Baraban, Anthony J. Merer, John F. Stanton, and Robert W. Field. Anharmonic Force Fields for *cis* and *trans* S_1 $\mathrm{C}_2\mathrm{H}_2$. *Molecular Physics*, 110(21–22):2725–2733, 2012.

[128] Anthony J. Merer, Adam H. Steeves, H. A. Bechtel, Joshua H. Baraban, Peter Bryan Changala, and Robert W. Field. Unpublished results.

[129] Jonathan Paul O'Brien. *Acetylene: Dispersed Fluorescence Spectroscopy and Intramolecular Dynamics.* PhD thesis, Massachusetts Institute of Technology, 1991.

[130] Kent M. Ervin, Joe Ho, and W. C. Lineberger. A study of the singlet and triplet states of vinylidene by photoelectron spectroscopy of $\mathrm{H}_2\mathrm{C}{=}\mathrm{C}^-$, $\mathrm{D}_2\mathrm{C}{=}\mathrm{C}^-$, and $\mathrm{HDC}{=}\mathrm{C}^-$. Vinylidene-acetylene isomerization. *The Journal of Chemical Physics*, 91(10):5974–5992, 1989.

[131] S. Joseph and A. J. C. Varandas. Accurate MRCI and CC study of the most relevant stationary points and other topographical attributes for the ground-state $\mathrm{C}_2\mathrm{H}_2$ potential energy surface. *The Journal of Physical Chemistry A*, 114(50):13277–13287, 2010.

[132] Shengli Zou and Joel M Bowman. A new ab initio potential energy surface describing acetylene/vinylidene isomerization. *Chemical Physics Letters*, 368(3–4):421–424, 2003.

[133] Hyunwoo Lee, Joshua H. Baraban, Robert W. Field, and John F. Stanton. High-accuracy estimates for the vinylidene-acetylene isomerization energy and the ground state rotational constants of $:\mathrm{C}{=}\mathrm{CH}_2$. *The Journal of Physical Chemistry A*, 117(46):11679–11683, 2013.

[134] P. Bryan Changala, Joshua H. Baraban, John F. Stanton, Anthony J. Merer, and Robert W. Field. Reduced dimension rovibrational variational calculations of the S_1 state of $\mathrm{C}_2\mathrm{H}_2$. II. The S_1 rovibrational manifold and the effects of isomerization. *The Journal of Chemical Physics*, 140(2):024313, 2014.

[135] Kazuhide Tsuji, Chiaki Terauchi, Kazuhiko Shibuya, and Soji Tsuchiya. *Trans-cis* isomerization of acetylene in the state as studied by dispersed fluorescence spectroscopy. *Chemical Physics Letters*, 306(1-2):41–47, 1999.

[136] Matthew P. Jacobson, Robert J. Silbey, and Robert W. Field. Local mode behavior in the acetylene bending system. *The Journal of Chemical Physics*, 110(2):845–859, 1999.

[137] Vivian Tyng and Michael E. Kellman. Bending dynamics of acetylene: New modes born in bifurcations of normal modes. *The Journal of Physical Chemistry B*, 110(38):18859–18871, 2006.

[138] http://pages.uoregon.edu/meklab/migration2/.

[139] Bryan M. Wong, Adam H. Steeves, and Robert W. Field. Electronic signatures of large amplitude motions: Dipole moments of vibrationally excited local-bend and local-stretch states of S_0 acetylene. *The Journal of Physical Chemistry B*, 110(38):18912–18920, 2006.

[140] Kaoru Yamanouchi, Naru Ikeda, Soji Tsuchiya, David M. Jonas, James K. Lundberg, George W. Adamson, and Robert W. Field. Vibrationally highly excited acetylene as studied by dispersed fluorescence and stimulated emission pumping spectroscopy: Vibrational assignment of the feature states. *The Journal of Chemical Physics*, 95(9):6330–6342, 1991.

[141] Huixian Han, Anyang Li, and Hua Guo. Toward spectroscopically accurate global ab initio potential energy surface for the acetylene-vinylidene isomerization. *The Journal of Chemical Physics*, 141(24):244312, 2014.

[142] G. Barratt Park. Full dimensional Franck-Condon factors for the acetylene $\tilde{\mathrm{A}}\ {}^1\mathrm{A}_u$–$\tilde{\mathrm{X}}\ {}^1\Sigma_g^+$ transition. I. Method for calculating polyatomic linear–bent vibrational intensity factors and evaluation of calculated intensities for the *gerade* vibrational modes in acetylene. *The Journal of Chemical Physics*, 141(13):134304, 2014.

[143] G. Barratt Park, Joshua H. Baraban, and Robert W. Field. Full dimensional Franck-Condon factors for the acetylene $\tilde{\mathrm{A}}\ {}^1\mathrm{A}_u$–$\tilde{\mathrm{X}}\ {}^1\Sigma_g^+$ transition. II. Vibrational overlap factors for levels involving excitation in *ungerade* modes. *The Journal of Chemical Physics*, 141(13):134305, 2014.

[144] Jonathan P. O'Brien, Matthew P. Jacobson, Jennifer J. Sokol, Stephen L. Coy, and Robert W. Field. Numerical pattern recognition analysis of acetylene dispersed fluorescence spectra. *The Journal of Chemical Physics*, 108(17):7100–7113, 1998.

[145] Adam H. Steeves. *Electronic Signatures of Large Amplitude Motions*. PhD thesis, Massachusetts Institute of Technology, 2009.

[146] Anthony J. Merer, Zicheng Duan, Robert W. Field, and James K. G. Watson. Perturbations in the $4\nu_3$ level of the $\tilde{A}^1A_u$ state of acetylene, C_2H_2. *Canadian Journal of Physics*, 87:437–441, 2009.

[147] I.M. Mills, W.L. Smith, and J.L. Duncan. Coriolis perturbations in the infrared spectrum of allene. *Journal of Molecular Spectroscopy*, 16(2):349–377, 1965.

[148] W. M. Jackson, A. M. Mebel, S. H. Lin, and Y. T. Lee. Using *ab initio* MO calculations to understand the photodissociation dynamics of CH_2CCH_2 and CH_2C_2. *J. Phys. Chem. A*, 101(36):6638–6646, 1997.

[149] A. M. Mebel, M. Hayashi, K. K. Liang, and S. H. Lin. *Ab initio* calculations of vibronic spectra and dynamics for small polyatomic molecules: Role of Duschinsky effect. *J. Phys. Chem. A*, 103(50):10674–10690, 1999.

[150] Piero Altoæ, Fernando Bernardi, Irene Conti, Marco Garavelli, Fabrizia Negri, and Giorgio Orlandi. Light driven molecular switches: Exploring and tuning their photophysical and photochemical properties. *Theoretical Chemistry Accounts*, 117(5/6):1041–1059, 2007.

[151] Zicheng Duan. *Spectroscopic Study of the Acetylene Species*. PhD thesis, Massachusetts Institute of Technology, 2003.

[152] S. Becker, C. Braatz, J. Lindner, and E. Tiemann. Investigation of the predissociation of SO_2: state selective detection of the SO and O fragments. *Chemical Physics*, 196:275–291, 1995.

[153] Michael Ivanco, James Hager, Wayne Sharfin, and Stephen C. Wallace. Quantum interference phenomena in the radiative decay of the ($^1B_2$) state of SO_2. *The Journal of Chemical Physics*, 78:6531, 1983.

[154] Akihiro Okazaki, Takayuki Ebata, and Naohiko Mikami. Degenerate four-wave mixing and photofragment yield spectroscopic study of jet-cooled SO_2 in the $\tilde{C}\ ^1B_2$ state: Internal conversion followed by dissociation in the $\tilde{X}$ state. *The Journal of Chemical Physics*, 107(21):8752–8758, 1997.

[155] Tokuei Sako, Akiyoshi Hishikawa, and Kaoru Yamanouchi. Vibrational propensity in the predissociation rate of $SO_2(\tilde{C})$ by two types of nodal patterns in vibrational wavefunctions. *Chemical Physics Letters*, 294(6):571–578, 1998.

[156] Masahiro Kawasaki, Kazuo Kasatani, Hiroyasu Sato, Hisanori Shinohara, and Nobuyuki Nishi. Photodissociation of molecular beams of SO_2 at 193 nm. *Chemical Physics*, 73(3):377–382, 1982.

[157] Hideto Kanamori, James E. Butler, Kentarou Kawaguchi, Chikashi Yamada, and Eizi Hirota. Spin polarization in SO photochemically generated from SO_2. *The Journal of Chemical Physics*, 83(2):611–615, 1985.

[158] Kenshu Kamiya and Hiroyuki Matsui. Theoretical studies on the potential energy surfaces of SO_2: Electronic states for photodissociation from the $\tilde{C}^1B_2$ state. *Bulletin of the Chemical Society of Japan*, 64(9):2792–2801, 1991.

[159] Paresh C. Ray, Michael F. Arendt, and Laurie J. Butler. Resonance emission spectroscopy of predissociating SO_2 $\tilde{C}$ (1 $^1B_2$): Coupling with a repulsive $^1A_1$ state near 200 nm. *The Journal of Chemical Physics*, 109(13):5221–5230, 1998.

[160] Brad Parsons, Laurie J. Butler, Daiqian Xie, and Hua Guo. A combined experimental and theoretical study of resonance emission spectra of $SO_2(\tilde{C}^1B_2)$. *Chemical Physics Letters*, 320(5–6):499–506, 2000.

[161] Hideki Katagiri, Tokuei Sako, Akiyoshi Hishikawa, Takeki Yazaki, Ken Onda, Kaoru Yamanouchi, and Kouichi Yoshino. Experimental and theoretical exploration of photodissociation of SO_2 via the $\tilde{C}^1B_2$ state: identification of the dissociation pathway. *Journal of Molecular Structure*, 413–414(0):589–614, 1997.

[162] Bogdan R. Cosofret, Scott M. Dylewski, and Paul L. Houston. Changes in the vibrational population of $SO(^3\Sigma^-)$ from the photodissociation of SO_2 between 202 and 207 nm. *The Journal of Physical Chemistry A*, 104(45):10240–10246, 2000.

[163] A. R. Hoy and J. C. D. Brand. Asymmetric structure and force field of the $^1B_2(^1A')$ state of sulphur dioxide. *Molecular Physics*, 36(5):1409–1420, 1978.

[164] J. C. D. Brand, P. H. Chiu, A. R. Hoy, and H. D. Bist. Sulfur dioxide: Rotational constants and asymmetric structure of the $\tilde{C}^1B_2$ state. *Journal of Molecular Spectroscopy*, 60(1–3):43–56, 1976.

[165] Karl-Eliv Johann Hallin. *Some aspects of the electronic spectra of small triatomic molecules.* PhD thesis, The University of British Columbia, 1977.

[166] J. C. D. Brand, D. R. Humphrey, A. E. Douglas, and I. Zanon. The resonance fluorescence spectrum of sulfur dioxide. *Canadian Journal of Physics*, 51:530, 1973.

[167] Sylvestre Twagirayezu, Trocia N. Clasp, David S. Perry, Justin L. Neill, Matt T. Muckle, and Brooks H. Pate. Vibrational coupling pathways in methanol as revealed by coherence-converted population transfer fourier transform microwave infrared double-resonance spectroscopy. *The Journal of Physical Chemistry A*, 114(25):6818–6828, 2010.

[168] Sylvestre Twagirayezu, Xiaoliang Wang, David S. Perry, Justin L. Neill, Matt T. Muckle, Brooks H. Pate, and Li-Hong Xu. IR and FTMW-IR spectroscopy and vibrational relaxation pathways in the CH stretch region of CH_3OH and CH_3OD. *The Journal of Physical Chemistry A*, 115(34):9748–9763, 2011.

[169] Justin L. Neill, Kevin O. Douglass, Brooks H. Pate, and David W. Pratt. Next generation techniques in the high resolution spectroscopy of biologically relevant molecules. *Phys. Chem. Chem. Phys.*, 13:7253–7262, 2011.

[170] Brian C. Dian, Kevin O. Douglass, Gordon G. Brown, Jason J. Pajski, and Brooks H. Pate. Ultraviolet-chirped pulse Fourier transform microwave (UV-CPFTMW) double-resonance spectroscopy. 61st International Symposium on Molecular Spectroscopy, 2006.

[171] S.P. Belov, M.Y. Tretyakov, I.N. Kozin, E. Klisch, G. Winnewisser, W.J. Lafferty, and J.-M. Flaud. High frequency transitions in the rotational spectrum of SO_2. *Journal of Molecular Spectroscopy*, 191(1):17–27, 1998.

[172] Min Zhang and Hai-Lung Dai. Quantum state-resolved collision relaxation of highly vibrationally excited SO_2. *The Journal of Physical Chemistry A*, 111(38):9632–9639, 2007.

[173] Daiqian Xie, Hua Guo, Ota Bludský, and Petr Nachtigall. Absorption and resonance emission spectra of SO_2 $\tilde{X}^1A_1/\tilde{C}^1B_2$ calculated from ab initio potential energy and transition dipole moment surfaces. *Chemical Physics Letters*, 329(5–6):503–510, 2000.

[174] G. Barratt Park, J. Jiang, C. A. Saladrigas, and R. W. Field. Direct observation of the low-lying b_2 symmetry vibrational levels of the $\tilde{C}$ $^1B_2$ state of SO_2 by IR-UV double resonance: Characterization of the asymmetry staggering and the origin of unequal bond lengths. In preparation.

[175] Jun Jiang, G. Barratt Park, and Robert W. Field. Determination of internal force constants of $\tilde{C}$ state SO_2. In preparation.

[176] Jules Duchesne and B. Rosen. Contribution to the study of electronic spectra of bent triatomic molecules. *The Journal of Chemical Physics*, 15(9):631–644, 1947.

[177] V.T. Jones and J.B. Coon. The ultraviolet spectrum of SO_2 in matrix isolation and the vibrational structure of the 2348 Å system. *Journal of Molecular Spectroscopy*, 47(1):45–54, 1973.

[178] Michael Joseph Ivanco. *Quantum Interference Effects and Molecular Dynamics of the* $\tilde{C}(^1B_2)$ *State of Sulphur Dioxide*. PhD thesis, University of Toronto, 1985.

[179] R. S. Mulliken. The lower excited states of some simple molecules. *Canadian Journal of Chemistry*, 36(1):10–23, 1958.

[180] K.K Innes. SO_2: Origins of unequal bond lengths in the $\tilde{C}$ $^1B_2$ electronic state. *Journal of Molecular Spectroscopy*, 120(1):1–4, 1986.

[181] Petr Nachtigall, Jan Hrušák, Ota Bludský, and Suehiro Iwata. Investigation of the potential energy surfaces for the ground $\tilde{\mathrm{X}}^1\mathrm{A}_1$ and excited $\tilde{\mathrm{C}}^1\mathrm{B}_2$ electronic states of SO_2. *Chemical Physics Letters*, 303:441–446, 1999.

[182] Ota Bludský, Petr Nachtigall, Jan Hrušák, and Per Jensen. The calculation of the vibrational states of SO_2 in the $\tilde{\mathrm{C}}\ {}^1\mathrm{B}_2$ electronic state up to the $\mathrm{SO}(^3\Sigma^-) + \mathrm{O}^3(\mathrm{P})$ dissociation limit. *Chemical Physics Letters*, 318(6):607–613, 2000.

[183] G. Barratt Park, Caroline C. Womack, Andrew R. Whitehill, Jun Jiang, Shuhei Ono, and Robert W. Field. Millimeter-wave optical double resonance schemes for rapid rotationally-assigned spectral acquisition and Coriolis perturbations in the $(v_1', v_2', v_3') = (1, 3, 2)$ level of the $\tilde{\mathrm{C}}\ {}^1\mathrm{B}_2$ state of SO_2. In preparation.

[184] Takeshi Oka and Yonezo Morino. Calculation of inertia defect: Part II. Nonlinear symmetric XY_2 molecules. *Journal of Molecular Spectroscopy*, 8(1–6):9–21, 1962.

G. BARRATT PARK

Massachusetts Institute of Technology, 77 Massachusetts Ave. Room 6-022, Cambridge, MA 02139
Phone: (864) 554-0090 (cell), (617) 252-1975 (office); Email: barratt@mit.edu

At the time of the printing of this thesis, the following is a full list of publications and manuscripts in press or in preparation.

PUBLICATIONS:

G. B. Park, J. Jiang, C. A. Saladrigas, R. W. Field. "Direct observation of the low-lying b_2 symmetry vibrational levels of the $\tilde{C}\ ^1B_2$ state of SO_2 by IR-UV double resonance: Characterization of the asymmetry staggering and the origin of unequal bond lengths." In preparation.

J. Jiang, G. B. Park, R. W. Field. "Internal coordinate force field determination for the $\tilde{C}$ state of SO_2." In preparation.

G. B. Park, C. C. Womack, J. Jiang, A. R. Whitehill, S. Ono, R. W. Field. "Perturbations in the (v_1,v_2,v_3)=(1,3,2) band of $\tilde{C}$-state SO_2 and evaluation of millimeter-wave optical double resonance schemes." In preparation.

G. B. Park, R. W. Field. "Edge effects in chirped-pulse Fourier transform microwave spectra" (Submitted, *J. Mol. Spectrosc.*)

G. B. Park, J. H. Baraban, A. H. Steeves, R. W. Field "A simplified model for intrapolyad emission intensities in the acetylene $\tilde{A}\rightarrow\tilde{X}$ transition." (Accepted, *J. Phys. Chem. A*) http://dx.doi.org/10.1021/jp5113608

J. M. Oldham, C. Abaysekera, B. Joalland, L. N. Zack, K. Prozument, I. Sims, G. B. Park, R. W. Field, A. G. Suits "A chirped-pulse Fourier-transform microwave/pulsed uniform flow spectrometer: I. The low-temperature flow system." *J. Chem. Phys.*, **141**, 1545202 (2014). http://dx.doi.org/10.1063/1.4897979

C. Abeysekera, L. N. Zack, G. B. Park, B. Joalland, J. M. Oldham, K. Prozument, N. M. Ariyasingha, I. R. Sims, R. W. Field, A. G. Suits. "A chirped-pulse Fourier-transform microwave/pulsed uniform flow spectrometer: II. Performance and applications for reaction dynamics." *J. Chem. Phys.*, **141**, 214203 (2014). http://dx.doi.org/10.1063/1.4903253

G. B. Park. "Full dimensional Franck-Condon factors for the acetylene $\tilde{A}\ ^1A_u$—$\tilde{X}\ ^1\Sigma_g^+$ transition. I. Method for calculating polyatomic linear—bent vibrational intensity factors and evaluation of calculated intensities for the *gerade* vibrational modes in acetylene." *J. Chem. Phys.*, **141**, 134304 (2014).

G. B. Park, J. H. Baraban, R. W. Field. "Full dimensional Franck-Condon factors for the acetylene $\tilde{A}\ ^1A_u$—$\tilde{X}\ ^1\Sigma_g^+$ transition. II. Vibrational overlap factors for levels involving excitation in *ungerade* modes." *J. Chem Phys.*, **141**, 134305 (2014).

K. Prozument, G. B. Park, R. G. Shaver, A. K. Vasiliou, J. M. Oldham, D. E. David, J. S. Muenter, J. F. Stanton, A. G. Suits, G. B Ellison, R. W. Field. "Chirped-pulse millimeter-wave spectroscopy for dynamics and kinetics studies of pyrolysis reactions." *Phys. Chem. Chem. Phys.*, **16**, 15739, (2014).

J. Jiang, J. H. Baraban, G. B. Park, M. L. Clark, R. W. Field. "Laser-Induced Fluorescence Study of the S_1 State of Doubly-Substituted ^{13}C Acetylene and Harmonic Force Field Determination." *J. Phys. Chem. A*, **117**, 13696, (2013).

K. Prozument, R. G. Shaver, M. A. Ciuba, J. S. Muenter, G. B. Park, J. F. Stanton, H. Guo, B. M. Wong, D. S. Perry, R. W. Field. "A new approach toward transition state spectroscopy." *Faraday Discuss.* **163**, 33 (2013).

K. Prozument, A. P. Colombo, Y. Zhou, G. B. Park, V. S. Petrovic, S. L. Coy, R. W. Field. "Chirped-Pulse Millimeter-Wave Spectroscopy of Rydberg-Rydberg Transitions." *Phys. Rev. Lett.*, **107**, 143001 (2011).

G. B. Park, A. H. Steeves, K. Kuyanov-Prozument, J. L. Neill, R. W. Field. "Design and evaluation of a pulsed-jet chirped-pulse millimeter-wave spectrometer for the 70-102 GHz region." *J. Chem. Phys.*, **135**, 24202 (2011).

G. B. Park, D. M. Brown, M. D. Schuh. "Binary and Ternary Complexes Containing α-Cyclodextrin and Bromonaphthalene Derivatives: A Note of Caution in Interpreting UV Absorption Spectral Data." *J. Phys. Chem. B*, **110**, 22510-22516 (2006).